



Fabrication and electrical properties of advanced thin film materials for resistive switching memories

Li, Yang

Publication date:
2020

Document Version
Publisher's PDF, also known as Version of record

[Link back to DTU Orbit](#)

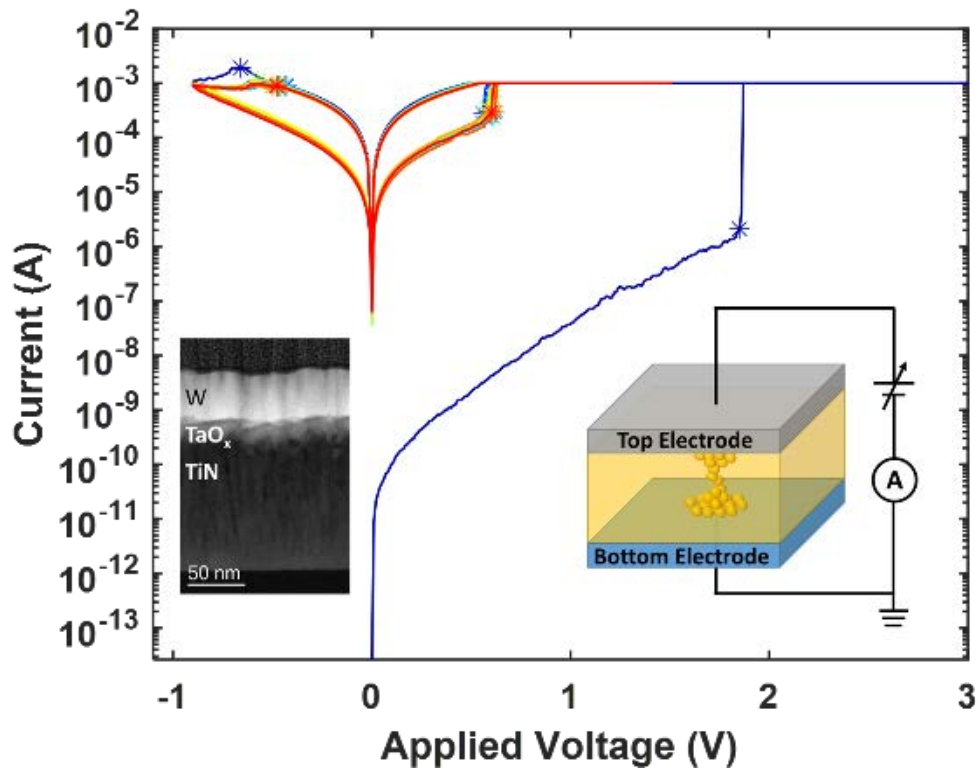
Citation (APA):
Li, Y. (2020). *Fabrication and electrical properties of advanced thin film materials for resistive switching memories*. Technical University of Denmark.

General rights

Copyright and moral rights for the publications made accessible in the public portal are retained by the authors and/or other copyright owners and it is a condition of accessing publications that users recognise and abide by the legal requirements associated with these rights.

- Users may download and print one copy of any publication from the public portal for the purpose of private study or research.
- You may not further distribute the material or use it for any profit-making activity or commercial gain
- You may freely distribute the URL identifying the publication in the public portal

If you believe that this document breaches copyright please contact us providing details, and we will remove access to the work immediately and investigate your claim.



DTU Energy
Department of Energy Conversion and Storage

Fabrication and electrical properties of advanced thin film materials for resistive switching memories

Yang Li

Lyngby
March 2020

Fabrication and electrical properties of advanced thin film materials for resistive switching memories

Supervisor: Prof. Dr Nini Pryds
Phone: +45 56 77 57 52
Email: nipr@dtu.dk

PhD thesis

By
Yang Li

Copyright: Reproduction of this publication in whole or in part must include the customary bibliographic citation, including author attribution, report title, etc.

Cover photo: Typical I - V curves of a TiN/TaO_x/W structured RRAM. (Left inset: A cross-sectional view of the device. Right inset: A schematic illustration of the device and testing set up.)

Published by: DTU, Department of Energy Conversion and Storage, Fysikvej, Building 310, 2800 Kg. Lyngby, Denmark
www.dtu.dk

ISSN: [0000-0000] (electronic version)

ISBN: [000-00-0000-000-0] (electronic version)

ISSN: [0000-0000] (printed version)

ISBN: [000-00-0000-000-0] (printed version)

Summary

The exponential growth of electronics and computing capacity has dramatically changed the way we live and can be envisioned even more in the future. This growth trend of electronics was predicted by Moore's law and driven by the device scaling down to 10 nm node. However, with the impending fundamental physical limits and increased fabrication cost, new technology routes need to be proposed to empower the development of even smaller, faster, and more energy-efficient devices. For memory devices, two technology routes were proposed. One is based on the 3D stacks of the traditional mainstream floating-gate based FLASH memory. The other is the new memory devices based on different storage mechanisms, such as resistive random access memory (RRAM). Compared to other emerging new memory technologies, such as ferroelectric random access memory (FeRAM), magnetoresistive random access memory (MRAM), and phase change memory (PCM), RRAM devices feature simple device structure, low fabrication cost, and easy 3D integration. RRAM devices were also reported to exhibit fast switching speed of less than 1 ns, superior endurance of 10^{12} cycles, and power consumption at several hundred pW. Yet combining all the excellent features within one material system is still an open challenge.

The performances that can be achieved in devices are determined by the materials. Understanding how to grow and control the properties of the materials is of great importance. Tantalum oxide (TaO_x) has been widely studied and reported to exhibit the fastest switching speed and the most superior endurance in RRAM applications. The use of pulsed laser deposition (PLD) technique to grow and control the TaO_x thin film materials for RRAM devices are less reported. In this thesis, I first describe the stoichiometry of the TaO_x thin films controlled by varying PLD conditions at room temperature and how it is related to the electrical properties, such as resistivity and resistive switching behaviour, of the TaO_x thin films. Second, I present how annealing effect can influence the TaO_x material and trigger the resistive switching behaviour in the $\text{TiN}/\text{TaO}_x/\text{W}$ structured RRAM devices. Also, the effect of strain on the $\text{Pt}/\text{TaO}_x/\text{Ta}$ structured RRAM devices were studied. The thesis ends with my view on how the understanding and the experiments can be improved further.

Resumé

Den eksponentielle vækst i elektronik og computerkapacitet har dramatisk ændret den måde, vi lever på, og vil forsætte med at ændre vores levemåde i fremtiden. Tendensen til vækst inden for elektronik blev forudsagt af Moore's lov og drevet af enkeltkomponenter, der skalerer ned til 10 nm. Men med de nuværende grundlæggende fysiske grænser samt øgede fabrikationsomkostninger, skal nye teknologiruter findes for at styrke udviklingen af endnu mindre, hurtigere og mere energieffektive enheder. For hukommelsesenheder er der foreslået to teknologiruter. Den ene er baseret på 3D-stablerne i den traditionelle mainstream flydende gate-baserede FLASH-hukommelse. Den anden er de nye hukommelsesenheder, der er baseret på forskellige lagringsmekanismer, såsom resistive random access memory (RRAM). Sammenlignet med andre nye hukommelsesteknologier, såsom ferroelektrisk random access memory (FeRAM), magnetoresistive random access memory (MRAM) og phase change memory (PCM), har RRAM-enheder en enkel enhedsstruktur, lave fabrikationsomkostninger og nem 3D-integration. RRAM-enheder er rapporteret til at udvise en hurtig skiftehastighed på mindre end 1 ns, overlegen udholdenhed på 10^{12} cyklusser og strømforbrug ved få hundrede pW. Alligevel er det stadig en storudfordring at kombinere alle disse fremragende funktioner i ét materialesystem.

De funktionaliteter, der kan opnås i apparater, bestemmes af materialerne. At forstå, hvordan man fremstiller materialerne og kontrollerer deres egenskaber, er af stor betydning. Tantaloxid (TaO_x) er undersøgt grundigt og rapporteret til at udvise den hurtigste skiftehastighed og den mest overlegne udholdenhed i RRAM-applikationer. Der rapporteres mindre om anvendelsen af en pulsed laser deposition (PLD) til at fremstille og kontrollere TaO_x -tyndfilmmaterialerne til RRAM-enheder. I denne afhandling beskriver jeg først samspillet mellem støkiometrien i TaO_x -tyndfilm og forskellige PLD-betingelser ved stuetemperatur, samt hvordan støkiometrien er relateret til de elektriske egenskaber, såsom resistivitet og resistiv skifteadfærd i TaO_x -tyndfilm. For det andet præsenterer jeg, hvordan temperaturbehandling kan påvirke TaO_x -materialet og udløse det resistive skift i $\text{TiN}/\text{TaO}_x/\text{W}$ strukturerede RRAM-enheder. Derudover blev effekten af tøjning på de $\text{Pt}/\text{TaO}_x/\text{Ta}$ strukturerede RRAM-apparater observeret. Specialet afsluttes med mit syn på, hvordan forståelsen og eksperimenterne kan forbedres yderligere.

Preface

This PhD thesis is submitted in the partial fulfilment of the requirements for acquiring the PhD degree at the Technical University of Denmark. The content of the thesis is based primarily on research collaborations between Department of Energy Conversion and Storage at the Technical University of Denmark, Max Planck Institute for Solid State Research, and Electronic Materials (PGI-7) at Forschungszentrum Jülich.

During this PhD project, I have worked with different material deposition, device fabrication, and material characterization technologies as reflected by the publication list provided in Appendix B. The thesis presents our main findings of the effect of deposition conditions, the annealing effect, and the strain effect on the electrical and resistive switching properties of tantalum oxide (TaO_x) thin films in the application for the resistive switching memories.

Principal supervisor:

Prof. Nini Pryds, Technical University of Denmark

Co-supervisors:

Prof. Vincenzo Esposito, Technical University of Denmark

Asst. Prof. Marie Lund Traulsen, Technical University of Denmark

Dr Simone Sanna, Technical University of Denmark

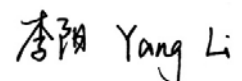
Assessment committee:

Assoc. Prof. Bhaskar Reddy Sudireddy (chairman), Technical University of Denmark

Prof. Daniel Ielmini, Politecnico di Milano

Prof. José Santiso López, Catalan Institute of Nanoscience and Nanotechnology

Lyngby, March 2020

 Yang Li

Yang Li

Acknowledgements

I would like to acknowledge the help, support and collaborations from my family, friends, colleagues, and supervisors:

I would like to thank the section leader and my main supervisor Nini Pryds for making this PhD project possible. I am particularly thankful for his guidance and support during my PhD project. I was given the freedom to carry out my PhD project and this process has developed my independence in the work, fostered my ability to grasp the main tasks and challenges I need to tackle, and deepened my way of critical thinking. Despite the freedom and trust given by him, he was always there ready to provide his support, guidance, knowledge, and insight. Help and support can also always be found from my co-supervisors, Simone Sanna, Marie Lund Traulsen, and Vincenzo Esposito. I am very grateful to have many nice supervisors at the same time. I would also like to thank Simone Sanna, Dennis Valbjørn Christensen, Marie Lund Traulsen and Eugen Stamate for the help in experiments and daily discussions. Mutual support was also provided within our group, in particular between my colleagues, Yu Zhang, Yulin Gan, Wei Niu, Simone Santucci, Haiwu Zhang, and Arindom Chatterjee.

I would like to thank our collaborators Y. Eren Suyolcu and Peter A. van Aken at Max Planck Institute for Solid State Research for the investigation of the TaO_x materials after annealing by TEM and EDX. I am very grateful for the discussion with Jennifer Rupp and her group at MIT for the material characterization by Raman spectroscopy and the effect of stain on materials' behaviour. I would also like to extend my sincere thanks to Regina Dittmann at Forschungszentrum Jülich for being my host during my external stay and also for her kind help and discussion. I would also like to thank Vikas Rana and Tim Kampen at Forschungszentrum Jülich for their help in assisting me in carrying out the device fabrication and electrical tests on the ultra-thin and fragile substrates.

A special thanks go to our technical administrative personnel including our skilled technicians Jørgen Geyti and Kristian Larsen, Secretary Anita Voss, Anne Heglingegård, and Heidi Adler Berggren.

I would like to thank my family and friends for their love and support.

17th March at Lyngby, Denmark

Contents

Summary.....	i
Resumé.....	iii
Preface.....	v
Acknowledgements.....	vii
Chapter 1.....	1
1.1 Control of oxide materials electrical properties by deposition.....	2
1.2 Effect of external stimulus on RRAM device performances.....	2
Chapter 2.....	3
2.1 Definition and history of RRAM.....	3
2.2 Operation Principles of RRAM.....	4
2.3 Applications RRAM.....	5
2.3.1 RRAM Application as Non-volatile Memories.....	5
2.3.2 RRAM Application in New Computing Diagrams.....	6
Chapter 3.....	7
3.1 TaO _x Stoichiometry and Crystal Structures Control by PLD.....	7
3.1.1 Stoichiometry and Crystal Structures of TaO _x	7
3.1.2 TaO _x Stoichiometry and Crystal Structure Controlled by PLD.....	9

3.2 TaO _x Electrical Properties Control by PLD.....	15
3.2.1 TaO _x Electrical Properties	15
3.2.2 TaO _x Electrical Properties Controlled by PLD.....	16
3.3 Resistive Switching Behaviours in TaO _x based RRAM.....	19
Chapter 4	29
4.1 Stoichiometry and Crystal Structure.....	29
4.2 Resistive Switching Behaviours of samples after post-deposition annealing.....	30
Chapter 5	39
5.1 The Effect of Strain on Metal Oxide Based RRAM Devices.....	40
5.2 The Effect of Strain on the TaO _x Thin Film and the TaO _x Based RRAM Devices.....	41
Chapter 6	51
Bibliography	55
Appendix A.....	69
A.1 List of Abbreviations.....	69
A.2 The Ta ₂ O ₅ target used in PLD	70
A.3 Typical <i>I-V</i> curves for TiN/TaO _x /W (tip probe) devices	71
A.4 Height deformation calibrated in 525 μm Si substrates	73
A.5 Typical <i>I-V</i> curves for Pt/TaO _x /Ta devices.....	74
Appendix B.....	77
List of Publications	77

Chapter 1

Motivation

The way we work, live, and communicate has been profoundly changed by the exponential growth of electronics and computing capacity. Driven by the need of the enterprise storage application, Big Data, Artificial Intelligence (AI), and Internet of Things (IoT), non-volatile memory devices with lower power consumption, faster-switching speed, and lower fabrication cost are highly desirable. Historically, the device scaling down process has led to less power consumption, improvement in speed, and reduction of fabrication cost. However, with the impending fundamental physical limits and increased fabrication cost as the fabrication technology reaches 10 nm node, new technology routes need to be proposed to empower the development of even smaller, faster, and more energy-efficient devices. Two technology routes were proposed. One is based on the 3D stacks of the traditional mainstream floating-gate based FLASH memory. The other is based on the new memory devices, such as ferroelectric random access memory (FeRAM), [1], [2] magnetoresistive random access memory (MRAM), [3], [4] phase change memory (PCM), [5], [6] and resistive switching memory (RRAM). [7]–[10] A comparison of the device behaviours among different memory technologies is as shown in Table 1. Compared with other emerging new memory technologies, RRAM devices feature in small device area, fast switching speed, and easy 3D integration.

Table 1 Comparison between different memory technologies. The data are based on Ref. [11]–[15].

Features	FLASH (NAND)	FeRAM	MRAM	PCM	RRAM
Cell size (F ²)	1-4	40 to 20	25	4 to 16	4
Read time (nm)	10 ⁵	20 to 80	3 to 20	20 to 50	<10
Write/erase time (ns)	10 ⁵	50/50	3 to 20	20 to 30	<10
Energy per bit (pJ)	2×10 ⁻⁵	3 to 20	<10	2 to 25	0.1 to 3
Endurance	10 ⁴	10 ¹²	>10 ¹⁵	>10 ¹⁶	10 ¹²
Non-volatility	Yes	Yes	Yes	Yes	Yes
Maturity	Commercialized	Limited production	Test chips	Test chips	Limited production
Applications	High density	Low density	Low density	High density	High density

1.1 Control of oxide materials electrical properties by deposition

RRAM devices were reported to exhibit excellent device performances, such as a small device size down to $2 \times 2 \text{ nm}^2$, [16] the fast switching speed of less than 1 ns, [17] superior endurance of 10^{12} cycles, [18] and power consumption of several hundred pW. [19] However, combining all these excellent performances within one material system remains an open challenge.

Many materials have been reported to exhibit resistive switching behaviours, such as solid-state electrolytes, [20]–[22] organic materials, [23]–[25] and metal oxides. [8], [26]–[28] A roadmap of electronic oxide materials has recently been reported in the scientific literature and specified the oxide materials application in non-volatile memory devices. [29] Transition metal oxide materials for RRAM application are of particular interest for their compatibility with complementary metal-oxide-semiconductor (CMOS) fabrication process. Full understanding of the resistive switching mechanisms in different RRAM material systems is still not achieved. Being able to finely control the materials composition/ properties as well as the statistical variation of the switching behaviour in RRAM devices is highly desirable. In this very relevant and interesting area, the use of different deposition techniques such as sputtering [8], [30]–[35], atomic layer deposition (ALD) [36]–[39] and pulsed laser deposition (PLD) [40], [41] techniques to be able to control the stoichiometry and properties of the film is very important. In the current work, I have used PLD to grow TaO_x thin film materials for RRAM devices. The use of PLD for growing this type of composition is less reported in the literature.

1.2 Effect of external stimulus on RRAM device performances

Memristive materials which are capable of responses to external stimuli represent one of the most exciting and emerging areas of scientific interest and unexplored commercial applications. This allows modifying the materials by imposing external stimuli, such as electrical field, magnetic field, temperature change, irradiation, and strain, on the device performance. Achieving this can provide new insights into the switching mechanisms of RRAM devices and can lead to new and yet unexplored properties for future memory and computing technologies. In a recent book chapter, we have highlighted the recent progress in stimuli-responsiveness of the metal oxide-based memristor (Appendix B, Article III). This research topic is to a large extent still unexplored both experimentally and theoretically and further research should be made in this direction.

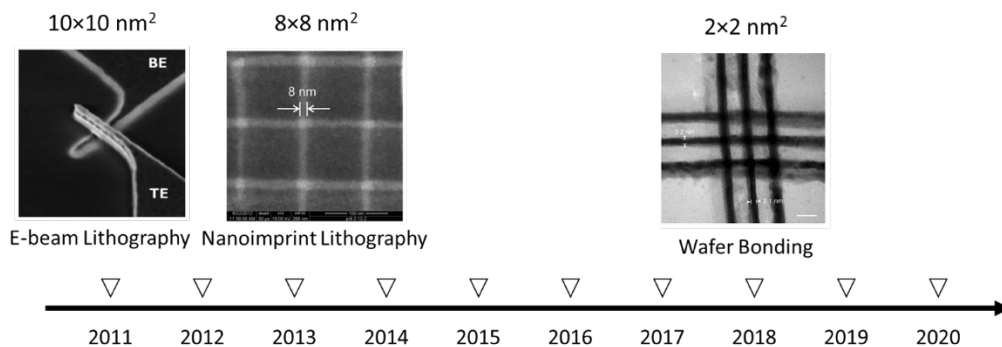


Figure 1 The scaling-down progress of RRAM devices. The figures are from Ref. [16], [42], [43].

Chapter 2

Basics of RRAM

2.1 Definition and history of RRAM

The resistive switching memory (RRAM) is a capacitor-like device structure with an insulating active layer (resistive switching layer) sandwiched between two metal electrodes. Resistive switching memory was first proposed by N. M. Bashara and P. H. Nielsen in a silicon monoxide thin film sandwiched between two gold electrodes (Au/SiO₂/Au) in 1963.[44] The resistance of the Au/SiO₂/Au can be tuned by an external electrical field and showed a low-frequency negative differential resistance.

	current i	voltage v	charge q	magnetic flux ϕ
current i		resistance $i = \frac{v}{R}$ 	$i = \frac{dq}{dt}$	inductance $i = \frac{\phi}{L}$ 
voltage v	resistance $v = iR$ 		capacitance $v = \frac{q}{C}$ 	$v = \frac{d\phi}{dt}$
charge q	$q = \int i dt$	capacitance $q = Cv$ 		memristance $q = \frac{\phi}{M}$ 
magnetic flux ϕ	inductance $\phi = iL$ 	$\phi = \int v dt$	memristance $\phi = Mq$ 	

Figure 2 The relationship between the four fundamental circuit variables of i (current), v (voltage), q (charge), and ϕ (magnetic flux). The combination of these four variables gives six relationships and the sixth one is the proposed concept of the memristor. The figure is updated from Ref.[45]. The memristor symbol in this figure is from <https://commons.wikimedia.org/wiki/File:Memristor-Symbol.svg>.

RRAM can arguably be viewed as memristors, a concept proposed by Leon Chua in 1971.[46], [47] The memristor as was predicated by Chua was considered as the fourth basic passive two-terminal element in the electric circuit. As the name of memristor implies, it is a combination of memory and resistor, which indicates that the same device behaves like a nonlinear resistor with a memory. Considering the relationship between the four fundamental circuit variables, i.e. i (current), v (voltage), q (charge), and ϕ (magnetic flux), there should be six possible combinations of these. Five of these six relationships are shown in Figure 2. Out of the six relationships, three of these represent the three basic passive two-terminal elements in the electric circuit, which are the **resistor**, the **capacitor**, and the **inductor**. Two other relationships are the ones: $i-q$ and $v-\phi$. Based on the symmetric intuition, a fundamental element representing the relationship between q and ϕ is missing, and this is the one that defines the memristor, $M(q) \equiv d\phi(q)/dq$, with the unit of resistance.[46] The device representing the relationship between q and ϕ is later named as an ideal memristor [48] and was generalized to a memristive device by Leon Chua and Sung Mo Kang in 1976.[49] In 2015, Leon Chua further claimed that any two-terminal device exhibiting a pinched hysteresis loop and passes through the origin in the voltage-current plane is called a memristor, which is the definition of the non-ideal memristor.

In 2008, R. Stanley Williams et al. from HP lab have shown experimentally the effect of resistive switching in TiO_2 and for the first time related this experimental observation to the memristor, claiming that the missing fourth element has been found.[50] RRAM devices have drawn much attention since 2008 and show huge potential in the application area of non-volatile memories[8], [10], [51], [52] and the new neuromorphic computing.[8], [53]–[56].

2.2 Operation Principles of RRAM

RRAM has a basic three-layered device structure with an insulating resistive switching layer sandwiched between two metal electrodes. The resistance of the device can be switched by an external electrical field and the device resistance upon removal of the field retained its resistance, i.e. exhibit a non-volatile behaviour. During switching, the external electrical field is applied between the top and bottom electrodes while the bottom electrode is grounded (Figure 3a). By switching the device into different high or low resistance states ('0' and '1'), information can be stored and readout, which enables the RRAM to be used as a non-volatile memory device.

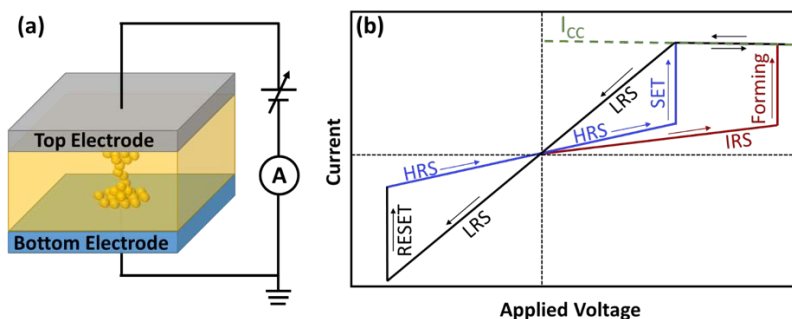


Figure 3 A schematic illustration of (a) metal-insulator-metal (MIM) structured RRAM device under electric field and (b) its switching process and the corresponding $I-V$ curve. The figures are from Appendix B, Article III.

The typical I - V curves of the RRAM device under the input of electrical voltage is shown in Figure 3b. The device usually starts from a high initial resistance state (IRS) without any conduction inside the resistive switching layer, i.e. conductive filaments. A Forming process is then required to trigger the resistive switching process. As the voltage reaches a threshold value, the insulating resistive switching layer becomes conductive by forming a filament and the current increases abruptly. To protect the device from breakdown, a compliance current (I_{CC}) is applied to limit the maximum current that can flow through the device. After the Forming process, and during the reversed cycle the device switches from initial resistance state to a low resistance state (LRS). In bipolar RRAM devices, a negative voltage ramp can switch the device from low resistance state back to a high resistance state (HRS). The process of switching the device from LRS into HRS is called RESET. The value of the high resistance state is usually smaller than the IRS. The process of switching the device from HRS to LRS is called SET. By alternating the polarity voltage, the device can be switched between low and high resistance states which can be maintained even upon removal of the power supply. The device can then store information at different resistance states and they can be read out at lower voltage values without disturbing the stored resistance states.

Material research and device characterization have shown that it is the ion migration and redistribution under the external electrical field which account for the resistive switching phenomenon.[33], [57]–[62] Based on the types of ions and the formed conductive filaments, the RRAM devices can be classified into two types. The first type is the electrochemical metallization memory (ECM) which has an electrochemically active top electrode, such as Ag or Cu.[63]–[65] The highly mobile metal drift from the top electrode under the external electrical field and discharge at the inert counter electrode, leading to the formation of conductive filaments consisting of the active metal electrode material. At this stage, the device is in LRS. Upon reversed polarity of the applied voltage, the formed conductive filaments electrochemically dissolve and the device switches back to HRS. The second type is the valence change memory (VCM) which relies on the migration of anions, such as oxygen anions, which occur in transition metal oxides. The migration of oxygen anions is usually described by the corresponding oxygen vacancies. The migration of oxygen anions (i.e., oxygen vacancies) corresponds to stoichiometry change of the transition metal oxide, leading to a valence change of the cation sublattice and a change in material resistivity. Direct observations of the conductive filaments in both ECM and VCM have been reported.[61], [63], [65], [66]

2.3 Applications RRAM

2.3.1 RRAM Application as Non-volatile Memories

One of the main driving forces for the development of non-volatile memories is the requirement for increasing storage density and reduction of the fabrication cost at the same time. As an example, for the recent achievement in this area, take the microSD card as an example, it is the smallest memory card that can be bought today and has a dimension of 15 mm × 11 mm × 1 mm. From 2005 to 2019, the storage density of micro SD storage card increased from 128 MB to 1 TB (SanDisk Company), which means in this 14 years, the storage density has increased by 10000

times (Figure 4). RRAM exhibits fast switching speed, small device area, and is easy for 3D integration, which makes RRAM a promising candidate for the next-generation storage.

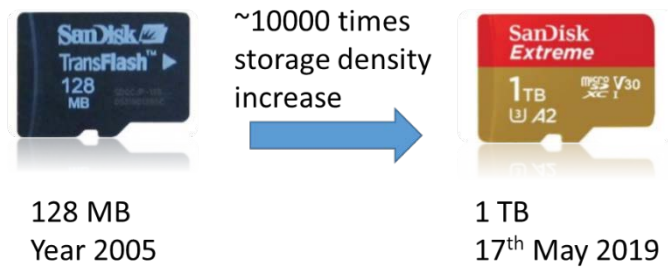


Figure 4 The storage density of MicroSD card has increased from 128 MB to 1 TB within a card dimension of 15 mm × 11 mm × 1 mm from 2005 to 2019. The products from SanDisk are taken as an example and figures are from the internet.

2.3.2 RRAM Application in New Computing Diagrams

Modern computers are based on von Neumann architecture using architecture proposed by John Von Neumann in 1945 in the *First Draft of a Report on the EDVAC*. The EDVAC (Electronic Discrete Variable Automatic Computer) was one of the earliest electronic computers. The term "von Neumann architecture" has evolved to describe any stored-program computer in which an instruction fetch and a data operation cannot occur at the same time because they share a common bus. This is referred to as the “von Neumann bottleneck” and often limits the performance of the system. Historically, the improvement of computing storage capability followed the prediction of Moore’s Law. The reduction of device sizes led to a reduction of power consumption, lowering of fabrication cost, and increase of computing speed. As the scaling of the devices run into its physical size limit and the increased fabrication cost, device scaling can no longer provide the desired performance improvement. The challenges of the classical von Neumann computing architecture are the memory bottleneck, high energy and speed costs, and device physical limits. New device structure, such as memristor (RRAM), and new computing diagram may provide a new method that enables hybrid memory–logic integration, bioinspired computing and efficient reconfigurable in-memory computing systems (Figure 5).[54], [56], [67][68], [69]

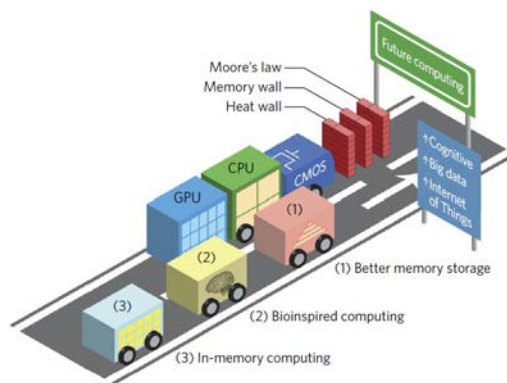


Figure 5 The race towards future computing solutions. The figure is from Ref. [54].

Chapter 3

Properties Control of TaO_x Thin Films by Pulsed Laser Deposition

Tantalum oxide (TaO_x) has a wide range of applications, such as waveguides and micro-resonators,[70] anti-reflective coating,[71] catalyst for hydrogen generation,[72] high-dielectric material [73]–[79], Cu diffusion barrier material [80] in microelectronics, and resistive switching memories.[17], [18], [81], [82] Many of its properties are highly dependent on its crystalline structure and material oxygen composition. In this chapter, I will provide experimental results that show the electrical resistivity and the resistive switching behaviour of the TaO_x controlled by changing the oxygen pressure during PLD.

3.1 TaO_x Stoichiometry and Crystal Structures Control by PLD

3.1.1 Stoichiometry and Crystal Structures of TaO_x

The stoichiometric Ta₂O₅ phase was the first phase that has been discovered back in the 1950s. In a review paper on the Ta-O system which was published in 1996 [83], it was pointed out that tantalum oxide (TaO_x) is a complex system that has more than twenty-five metastable sub-stoichiometry. Extensive research has been conducted since 1952 to understand/characterize the crystal structure of Ta₂O₅ and I will try to highlight only a small portion, but important, of these results in this part of the thesis. Various thermal-processing and stabilizing methods lead to different types of Ta₂O₅ structures, such as the tetragonal, orthorhombic, monoclinic, and hexagonal phases have been reported. Here, X-ray diffraction (XRD) [79], [83]–[88] and electron microscopy,[83], [86], [87], [89], [90] are extensively used to interpret the Ta₂O₅ crystal structures. The predictions of different phases were also done using calculations based on first-principle calculation.[91], [92]

The formation of amorphous Ta₂O₅ [76], [93], [94] and two other crystal structures, i.e. low-temperature β-phase and high temperature α-phase Ta₂O₅, were reported. The amorphous Ta₂O₅ crystallizes into low-temperature β-phase at elevated temperatures between 500 °C to 700 °C. This ordering process of the amorphous Ta₂O₅ induced by thermal annealing is a slow process, where the phase transition starts in the range of 500 °C to 600 °C and hardly completed even at 700 °C.[76], [93], [94] The crystal structures of the low-temperature β-phase Ta₂O₅ were reported to be orthorhombic but with different lattice parameters (Table 2).

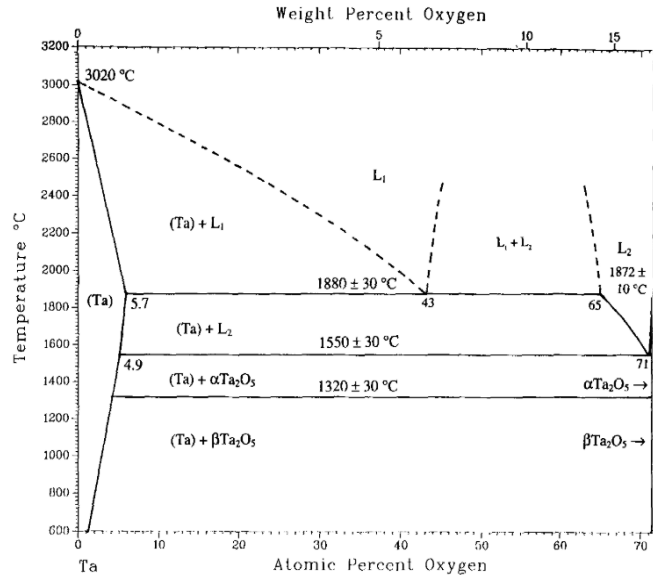


Figure 6 Phase diagram of Ta-O system. The figure is from Ref. [83].

Table 2 Reported experimental crystal structures of the low temperature β-phase Ta₂O₅

Year	Structure	Lattice Parameters	Ref.
1961	Orthorhombic	a=6.20 Å, b=69.6 Å, c=3.90 Å	[95]
1964	Orthorhombic	a=6.20 Å, b=3.66 Å, c=3.89 Å	[96]
1967	Orthorhombic	a=6.18 Å, b=3.66 Å, c=3.88 Å	[90]
1969	Orthorhombic	a=14.65 Å, b=9.395 Å, c=31.19 Å, Z=48	[84]
1971	Orthorhombic	a=6.198 Å, b=40.29 Å, c=3.888Å, 11 formula units	[85]
2002	Orthorhombic	a=6.217 Å, b=3.677 Å, and c=7.794 Å	[79]

Low temperature β-phase Ta₂O₅ can sluggishly transform into high temperature α-phase at about 1320 °C. The high temperature α-phase is stable at the temperature range between 1320 ± 30 °C and 1550 ± 30 °C.[83] The crystal structure of the high temperature α-phase Ta₂O₅ is shown in Table 3. Figure 6 shows the phase diagram of Ta-O system.

Table 3 Reported experimental crystal structures of the high temperature α-phase Ta₂O₅.

Year	Structure	Lattice Parameters	Ref.
1971 (2 mol% Sc ₂ O ₃)	Face-centred monoclinic C2	a=3.81 Å, b=3.81 Å, c=35.966 Å, β=96°42'	[97]
1997 & 2006 (8 mol% TiO ₂)	Monoclinic	a=3.79 Å, b=3.81 Å, c=35.7 Å, β=90°48'	[77], [98]
2007 (pure Ta ₂ O ₅)	Tetragonal	a=3.86 Å, c=36.18 Å	[89]

Other reports on the crystal structures of the tantalum oxide (TaO_x) system show additional phases such as the hexagonal δ-phase,[74], [91], [99] high-pressure modification of B-Ta₂O₅ and Z-Ta₂O₅,[86] rutile-type TaO₂ [100] and the orthorhombic λ-phase TaO_x with inter-plane oxygen vacancies.[101]

3.1.2 TaO_x Stoichiometry and Crystal Structure Controlled by PLD

Since the resistive switching depends very much on the stoichiometry and crystal structure, efforts have been made over the years to try to control the stoichiometry of the materials. One of the preferred deposition techniques to fabricate oxide and therefore these films is the PLD. By changing the PLD conditions, i.e. the oxygen pressure P_{O_2} in the deposition chamber and the deposition temperature T , the Ta/O composition and the crystallinity can be controlled.

(1) Composition: the ratio of Ta/O

For a constant deposition temperature, the Ta/O ratio decreases as the oxygen pressure in the chamber increases. For a constant oxygen pressure during deposition, the Ta/O ratio decreases as the deposition temperature increases. The ratio between Ta and O (Ta/O) depend on the deposition temperature and the deposition oxygen pressure and is shown in Figure 7, which was adapted from [102], [103]. The Ta/O ratio was determined by Rutherford backscattering spectrometry (RBS)¹ in Figure 7a and by Auger electron spectroscopy (AES)² in Figure 7b.

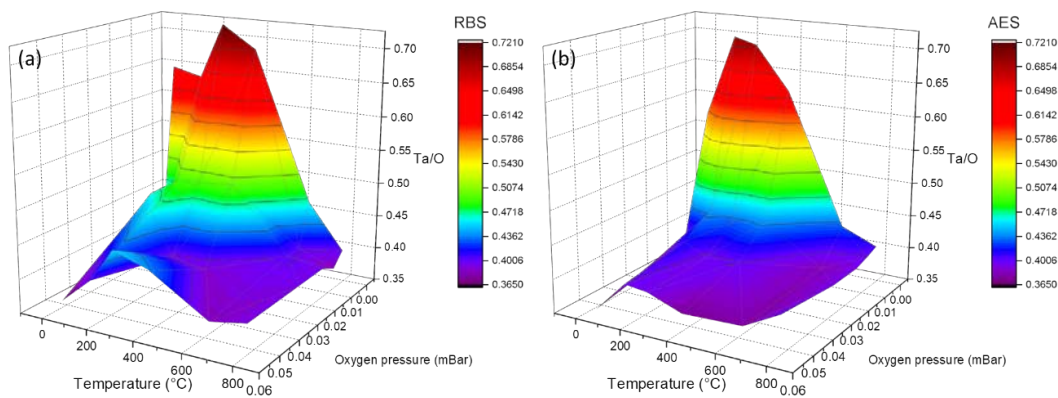


Figure 7 The TaO_x thin-film Ta/O dependency on the deposition temperature and the deposition oxygen pressures measured by (a) Rutherford backscattering spectrometry (RBS) and (b) Auger electron spectroscopy (AES). The figures are adapted from Ref. [102], [103].

(2) The crystallinity

The crystallinity of the TaO_x thin films is often characterized by X-ray diffraction (XRD).[103][102], [103] An interesting example of the evolution of the crystallinity is shown by the XRD spectra in Figure 8, where the XRD spectra were taken at Cu K_α radiation ($\lambda=1.5406 \text{ \AA}$) and the incident

¹ RBS, also referred to as high-energy ion scattering (HEIS) spectrometry, measures the backscattering of a beam of high energy ions (typically protons or alpha particles) impinging on a sample to determine the structure and composition of materials.

² AES is a common analytical technique used in the study of material surfaces and is based on the analysis of energetic electrons emitted from an excited atom after a series of internal relaxation events.

angle θ_0 fixed at 1° . The TaO_x thin films shown in Figure 8 were deposited at deposition temperatures of 400, 650, and 800 °C under the deposition oxygen pressure of 1 to 40 mTorr (1.3×10^{-3} to 5.3×10^{-2} mbar). For deposition temperature of $T \leq 400$ °C, the diffraction patterns of the TaO_x thin films consisted of a diffuse-scattering curve, indicating amorphous-like structures for all deposition oxygen pressures (Figure 8a). At the deposition temperature of $T \geq 650$ °C, amorphous TaO_x thin film transits from amorphous structure towards polycrystalline for the deposition oxygen pressure $P_{\text{O}_2} > 5$ mTorr (6.7×10^{-3} mbar). The peaks observed at an angle 2θ of 22.85°, 28.7°, 37°, and 49.3° can be assigned to the (001), (200), (201), and (1181) lines of the orthorhombic β -phase Ta_2O_5 structure, respectively (Figure 8b). At the deposition temperature of $T = 800$ °C, peaks at 2θ of 22.85°, 28.85°, 34° and 37° were observed, and can all be attributed to orthorhombic β -phase Ta_2O_5 structure (Figure 8c).

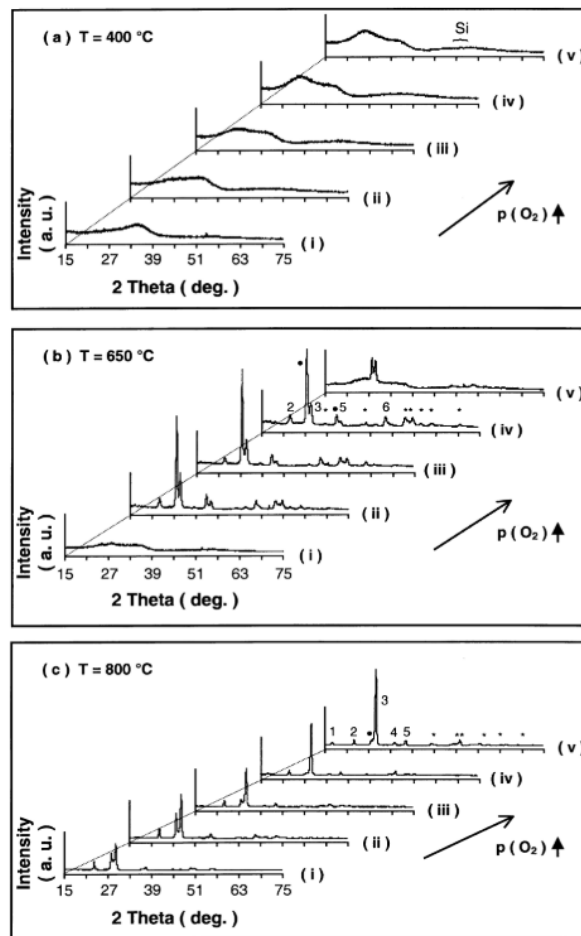


Figure 8 XRD spectra of TaO_x films deposited at (a) 400, (b) 650 and (c) 800 °C. For each temperature, the deposition oxygen pressure was: (i) 1 mTorr, (ii) 5 mTorr, (iii) 10 mTorr, (iv) 20 mTorr, and (v) 40 mTorr. (•) Not a β - Ta_2O_5 line; (*) broad, not well-defined peaks; (**) many β - Ta_2O_5 lines in this 2θ vicinity. Peak 1: (140); peak 2: (001); peak 3: (200); peak 4: (280); peak 5: (201); peak 6: (1181). The figures are from Ref.[103].

Previous studies only showed the dependence of Ta/O ratio on the deposition conditions. Since TaO_x is a complex system with many sub-stoichiometry states, the compositions of different

valence states of tantalum can be different even at the same Ta/O ratio. In my work, I therefore further investigated the composition of the TaO_x thin film and its relation to the deposition conditions. Part of my thesis, I studied a series of TaO_x thin films deposited at oxygen pressures from 10^{-6} mbar to 2×10^{-2} mbar by PLD and the effect of these deposition conditions on the composition and the physical properties.

The PLD system used in my experiments is provided by Surface PLD system (SURFACE & SURFACE systems + technology GmbH & Co. KG). The system consists of a KrF excimer laser (248 nm), a deposition chamber, and a process computer control as shown in Figure 9a. During the deposition of the TaO_x , the laser repetition rate was fixed at 10 Hz, the laser energy was fixed at 4 J/cm^2 , and the deposition temperature was kept at room temperature. The oxygen pressure in the chamber during the deposition was the only variable parameter and it was determined to be 10^{-6} , 5.6×10^{-4} , 2×10^{-3} , 5×10^{-3} , and 2×10^{-2} mbar. A commercial Ta_2O_5 ceramic target (99.99% purity, American Elements) with a diameter of 25.4 mm and a thickness of 6 mm was used. The target was investigated by XRD to ensure its phase purity before the deposition took place (Appendix A, Figure 55). The deposition was carried out by keeping the target-substrate distance constant at 7.5 cm. The target and the substrate were rotating in anti-clockwise and counter-clockwise, respectively, at a rate of 5 rpm during the deposition. Figure 9b shows a schematic illustration of the deposition process.

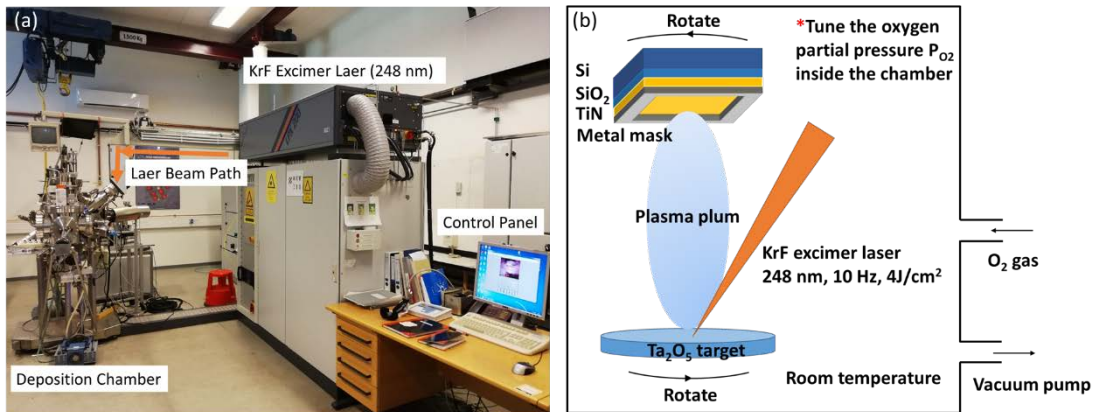


Figure 9 (a) A picture of the pulsed laser deposition (PLD) system, and (b) a schematic illustration of the PLD process of TaO_x thin films in our study.

XRD Bruker D8 Advanced diffractometer (Germany) with $Cu K\alpha$ ($\lambda=1.5406 \text{ \AA}$) radiation was used for the characterization of the films crystallinity. The XRD data in Figure 10a, c, and e were collected in theta-2 theta configuration scanning from 20° to 80° with a step size of 0.01° (0.2 seconds per step) at room temperature. Grazing-incidence small-angle scattering data in Figure 10b, d, and f were collected using the same diffractometer at room temperature. The X-ray incident angles θ_0 were set to 0.5° , 1° , and 2° , respectively. The detector scanned in 2 theta range $20^\circ \leq 2\theta \leq 90^\circ$ with a step size of 0.02° (0.5 seconds per step). The peaks observed in Figure 10 are attributed to the Si/SiO₂/TiN substrate. The peaks at 2θ of 32.9° and 69.1° can be attributed to (200) and (400) of Si.[104] The peaks at 2θ of 36.8° can be attributed to TiN (111).[105] No

obvious peaks from TaO_x were observed which indicates that all the TaO_x thin films deposited at room temperature were amorphous as indicated by XRD.

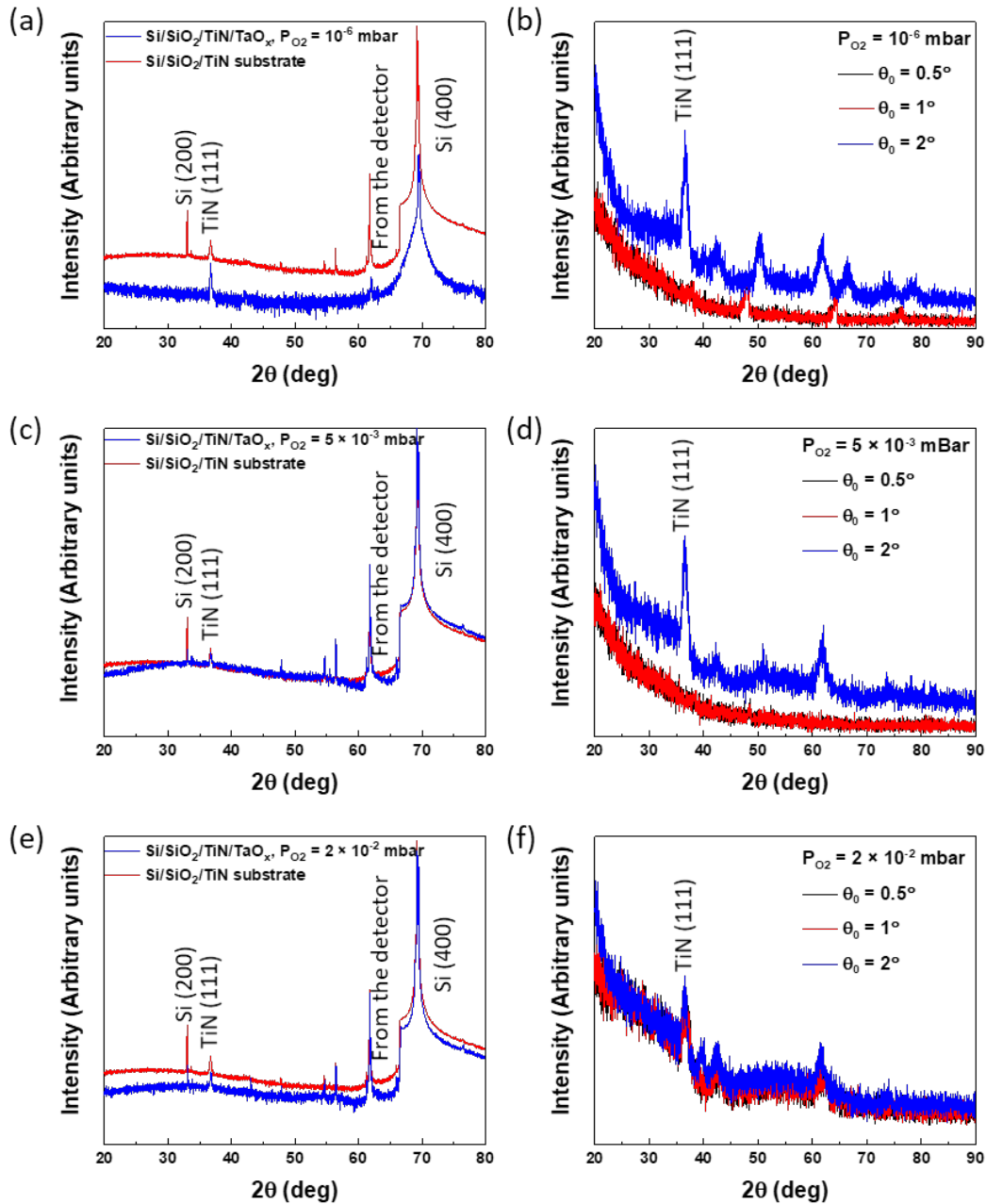


Figure 10 Morphology characterization of TaO_x thin films deposited at different oxygen partial pressures by using XRD. (a), (c), and (e) were characterized by stationary and horizontal sample position with the X-ray tube and the detector both move simultaneously over the angular range θ . (b), (d), and (f) were characterized using grazing incidence XRD with the incident angle θ_0 fixed to 0.5°, 1°, and 2°. The figures are adapted from Appendix B Article I.

The chemical composition of the TaO_x thin films was also examined using X-ray photoemission spectroscopy (XPS). The XPS analyses were performed on an ESCALAB XI⁺ X-ray photoelectron

spectrometer microprobe (Thermo Fisher Scientific, East Grinstead, U.K.) using a monochromatic Al-K α X-ray source with a 900 μm spot size. A combined ion/electron gun (i.e. a dual-beam source) was used to control sample charging. High resolution local binding energy spectra were obtained for Ta-4f using 20 eV detector pass energy, 50 ms dwell time, 0.02 energy step size, and collected over 5 scans. An emission angle of $\theta=0^\circ$ was used, which is relative to the perpendicular direction to the surface of the sample (i.e. maximum escape depth of ~ 10 nm). The spectra are the solid black lines as shown in Figure 11a to e. Figure 11f shows a schematic illustration of the XPS experiment set up.

The fitting analysis of the Ta-4f peaks and thus the quantification of the Ta oxidation states is based on the approach by Simpson et al.[106] Peaks were fitted using a 38% Lorentzian/Gaussian function, a 4f5/4f7 spin-orbit splitting of 1.9 eV, a 4f5/4f7 height ratio of 0.788, and a full width at half maximum (FWHM) fitting parameter of 1.2 ± 0.1 eV. The fitting envelopes are the solid red lines as shown in Figure 11a to e indicating almost a perfect fit.

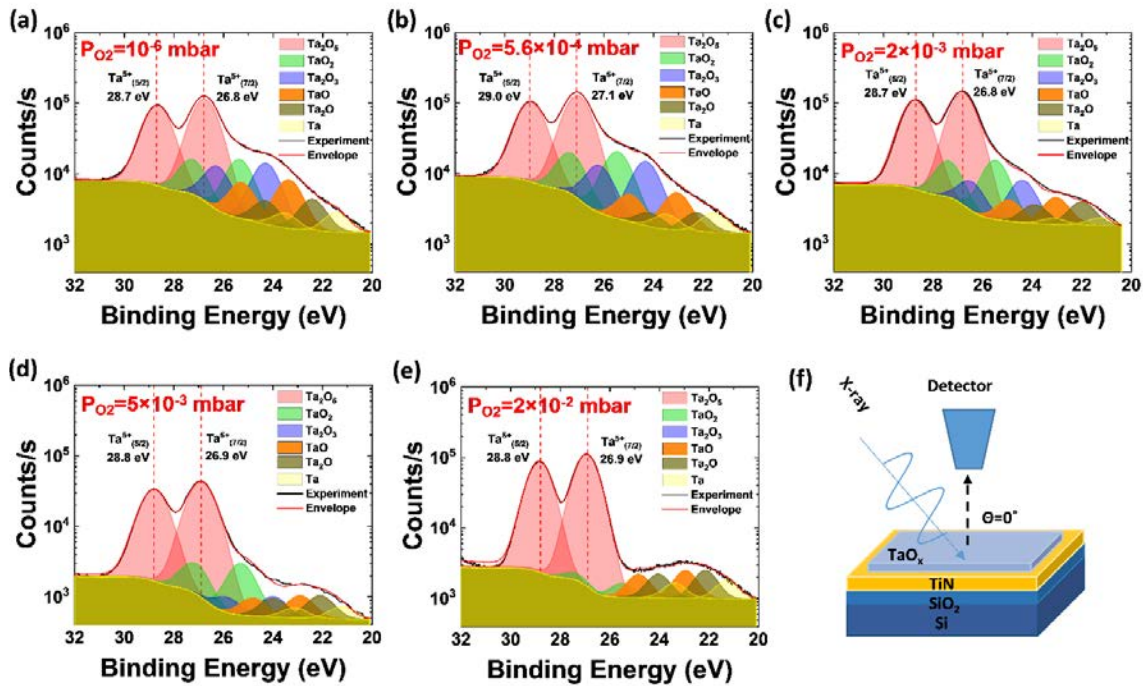


Figure 11 Ta 4f XPS spectra of TaO $_x$ thin films deposited for 60 min under different oxygen partial pressures of (a) $P_{O_2} = 10^{-6}$ mbar, (b) $P_{O_2} = 5.6 \times 10^{-4}$ mbar, (c) $P_{O_2} = 2 \times 10^{-3}$ mbar, (d) $P_{O_2} = 5 \times 10^{-3}$ mbar, and (e) $P_{O_2} = 2 \times 10^{-2}$ mbar. The solid black lines are the experiment XPS spectra data and the solid red lines are the fitting envelopes of the XPS spectra data. (f) A schematic illustration of the XPS experiment set up. The figures are from Appendix B Article I.

The results of the fitting show that the main peaks observed are the Ta 4f 7/2 and the Ta 4f 5/2 peaks of Ta $^{5+}$ (Ta $_2$ O $_5$) at binding energies of 26.9 ± 0.1 eV and 28.8 ± 0.1 eV, respectively. Besides the main peaks of Ta $^{5+}$ (Ta $_2$ O $_5$), there are the peaks of the lower oxidation states, which are Ta $^{4+}$, Ta $^{3+}$, Ta $^{2+}$, Ta $^{1+}$, and Ta 0 , representing TaO $_2$, Ta $_2$ O $_3$, TaO, Ta $_2$ O, and Ta metal, respectively. The

comparison between the binding energies for each oxidation states used in the work of Simpson et al.[106] and in my experimental results is shown in Table 4.

Table 4 The binding energies for each oxidation states used in the work of Simpson et al. and this paper. The table is from Appendix B Article I.

Oxide State	Binding Energy (eV)			
	Simpson <i>et al.</i> (Ref. [106])		my experiments	
	Ta4f 7/2	Ta4f 5/2	Ta4f 7/2	Ta4f 5/2
Ta ⁵⁺ (Ta ₂ O ₅)	27.0 ± 0.05	28.9 ± 0.05	26.9 ± 0.1	28.8 ± 0.1
Ta ⁴⁺ (TaO ₂)	25.7 ± 0.30	27.6 ± 0.30	25.5 ± 0.2	27.4 ± 0.2
Ta ³⁺ (Ta ₂ O ₃)	24.3 ± 0.20	26.2 ± 0.20	24.2 ± 0.2	26.1 ± 0.3
Ta ²⁺ (TaO)	23.3 ± 0.30	25.2 ± 0.30	23.1 ± 0.2	25.0 ± 0.2
Ta ¹⁺ (Ta ₂ O)	22.5 ± 0.10	24.4 ± 0.10	22.2 ± 0.2	24.1 ± 0.2
Ta ⁰ (metal)	21.50	23.42	21.3 ± 0.2	23.3 ± 0.3

Based on the fitting results (shown in Figure 11 with an emission angle of $\theta = 0^\circ$), the percentage change of each oxidation states of the tantalum oxide at a maximum detection depth (~10 nm) as a function of the deposition oxygen pressures was determined and is shown in Figure 12. At a detection depth of ~10 nm, the films were composed of Ta₂O₅ and the content of Ta₂O₅ seemed to increase from 75 at. % to 95 at. % as the deposition oxygen pressure increased from 10^{-6} mbar to 2×10^{-2} mbar. The percentage of the change of peaks with lower oxidation states found to decrease as the deposition oxygen pressure increased.

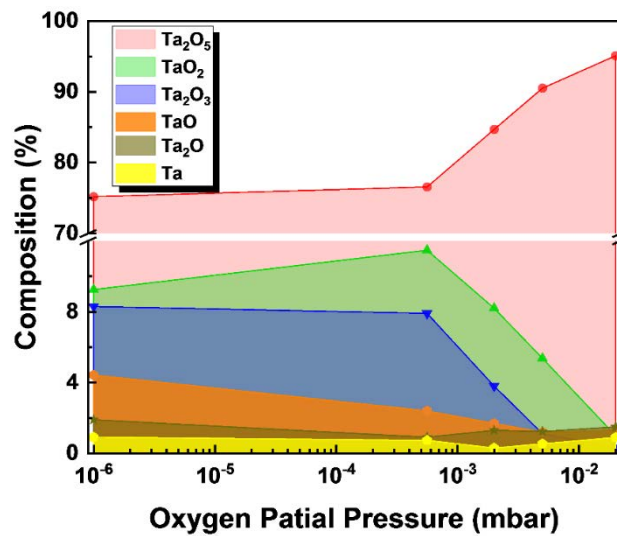


Figure 12 The composition of the TaO_x thin films deposited at different deposition oxygen pressures. The compositions were fitted according to the Ta 4f XPS spectra obtained at an emission angle of $\theta = 0^\circ$ relative to the perpendicular direction to the surface of the sample. The figures are from Appendix B Article I.

By using angle-resolved X-ray photoelectron spectroscopy (ARXPS), the composition homogeneity along the film growth direction and the surface

oxidation conditions of the TaO_x thin films were further studied. The emission angles θ , relative to the perpendicular direction of the surface of the sample, varied from 0° to 90° (grazing angle), which corresponds to the maximum probe depth of ~10 nm and the upper surface layer of the TaO_x thin films, respectively. As shown in Figure 13a, for TaO_x thin films deposited under high oxygen partial pressure (5×10^{-3} mbar) for a short time (10 min) corresponding to a film thickness of 23 ± 4 nm, the composition of TaO_x is found to be homogeneous for all emission angles, which means a homogeneous (similar) Ta oxidation states composition from the surface to approximately 10 nm deep under the surface. As compared to the TaO_x deposited for the same time but under a lower oxygen partial pressure (10^{-6} mbar) corresponding to a film thickness of 6 ± 1 nm, the composition of Ta₂O₅ increased as the emission angle increased, which indicate a higher Ta₂O₅ composition near the film surface, as shown in Figure 13b. These findings are

consistent with the work of Sharath et al.[107] Furthermore, as the thickness of the films increased, the composition of the films deposited at high oxygen partial pressure was not homogeneous any longer from the surface to approximately 10 nm deep under the surface. The composition along the film growth direction can be seen for films deposited at both high and low oxygen partial pressure in Figure 13c and d.

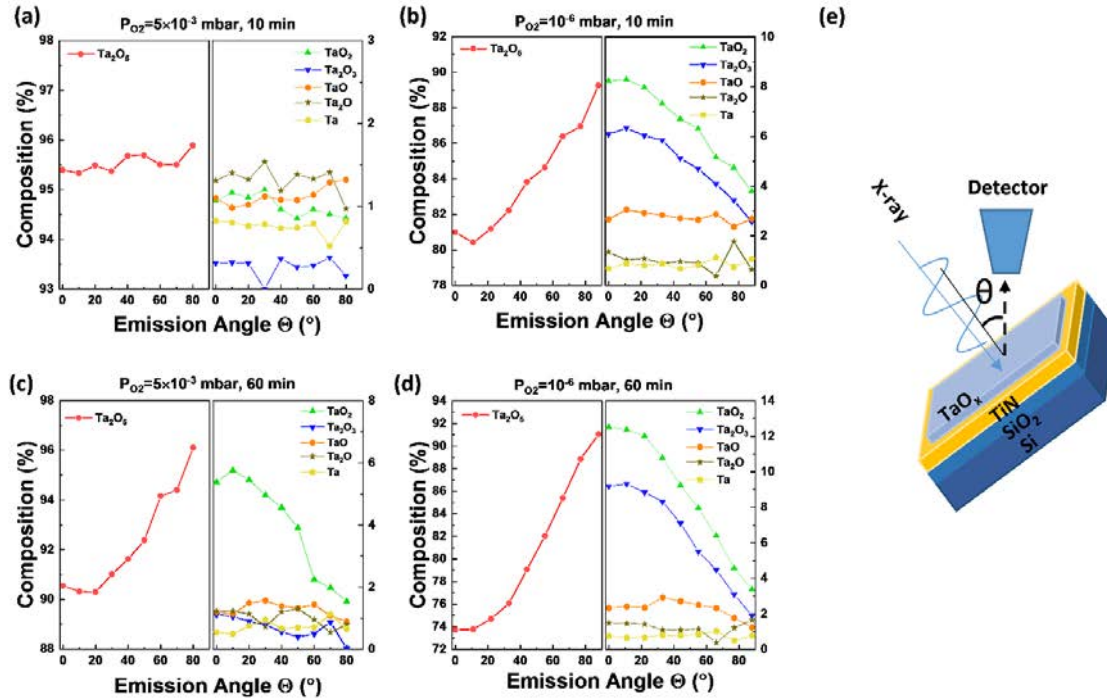


Figure 13 The Ta oxidation states of TaO_x films deposited under different deposition oxygen pressures revealed by XPS spectra. (a) oxygen partial pressure of $P_{O_2} = 5 \times 10^{-3}$ mbar for a deposition time of 10 min, (b) oxygen partial pressure of $P_{O_2} = 10^{-6}$ mbar for a deposition time of 10 min, (c) oxygen partial pressure of $P_{O_2} = 5 \times 10^{-3}$ mbar for a deposition time of 60 min, and (d) oxygen partial pressure of $P_{O_2} = 10^{-6}$ mbar for a deposition time of 60 min. (e) is a schematic illustration of the principle of ARXPS. The angle θ is the emission angle relative to the perpendicular direction of the surface of the sample. By changing the emission angle, the sampling depth decreases from ~ 10 nm at $\theta = 0^\circ$ to the very surface of the film at $\theta = 90^\circ$. The figures are from Appendix B Article I.

3.2 TaO_x Electrical Properties Control by PLD

The stoichiometry and the crystal structure of the TaO_x material are known to influence the electrical properties of the TaO_x film and the forming process of the TaO_x based RRAM devices.

3.2.1 The Electrical Properties of the TaO_x

Permittivity

Ta₂O₅ has been used as dielectric material in the microelectronics industry due to its high permittivity, i.e. the electric polarizability of a dielectric.[73]–[78] The relative permittivity of the Ta₂O₅ prepared by different methods were reported to be at a range of 10 to 610.[76], [78], [94], [108] The permittivity alters either due to the different crystal structures or due to the doping of the materials. The permittivity was found to be 25 in amorphous Ta₂O₅ and 50 to 59 in hexagonal crystalline Ta₂O₅ with a high anisotropic character.[74], [75], [95] Interestingly, it was also reported that an addition of 8 mol% TiO₂ can increase the permittivity of Ta₂O₅ by nearly a factor of four from 35 to 126.[6]

Resistivity

The electrical resistivity of TaO_x depends strongly on the degree of crystallinity of the material, the temperature during the test, and the oxygen pressure during the test.[78], [94], [97], [109]–[116] The resistivity of oxygen-deficient TaO_x can vary several orders of magnitude ranging from 1 to 10⁵ μΩ·cm (in magnitude) both of which predicted by calculation[117] and verified by experiments.[118] Neutral in-plane oxygen vacancies are responsible for the formation of a broad band in the gap of disordered Ta₂O₅ films and these defect levels serve as conduction centres for electron hopping in oxygen-deficient TaO_x films.[109], [116]

3.2.2 TaO_x Electrical Properties Controlled by PLD

Although tantalum oxide thin films deposited by PLD were widely studied,[102], [103], [119]–[129] focus was mainly put on the optical properties, [102], [103], [119], [120], [122], [124], [126], [128], [129] leakage current[119], [120], [122], [123], [126] and dielectric constant[122] of the TaO_x films. No direct link between the deposition condition, the thin film composition, and the thin film resistivity was reported. My work revealed a direct relationship between the oxygen pressure during PLD, the thin film composition, and the electrical resistivity.

Insulating MgO substrates were used to avoid any influences from the substrates and the resistivity of the TaO_x thin films were characterized by using Van der Pauw method.[130] The Van der Pauw method is suitable for a flat sample with arbitrary shape. Four successive contacts (1, 2, 3, and 4) were made by the Imina probe tip. The tips are at the circumstances of the sample and are sufficiently small. The sample is 1 cm × 1 cm and the probe tip is 500 nm in diameter. The resistance $R_{12,34}$ is defined as the potential difference $V_4 - V_3$ between the contacts 4 and 3 per unit current through the contacts 1 and 2. The current enters the sample through contact 1 and leaves the sample through contact 2. A schematic illustration of the testing configuration is as shown in Figure 14. The resistivity ρ is calculated according to the following equation [130]

$$\rho = \frac{\pi d}{\ln 2} \left(\frac{R_{12,34} + R_{23,41}}{2} \right) f \left(\frac{R_{12,34}}{R_{23,41}} \right), \quad (1)$$

where d is the film thickness, f is a function of the ratio $R_{12,34}/R_{23,41}$ only and satisfies the relation

$$\frac{R_{12,34} - R_{23,41}}{R_{12,34} + R_{23,41}} = f \operatorname{arcosh} \left\{ \frac{\exp(\ln 2 / f)}{2} \right\}. \quad (2)$$

The electrical tests were carried out using a test set up consisting of a Keithley 4200A semiconductor characterization system (SCS) and an Imina probe station. Figure 15 shows a picture of the whole electrical set up a zoomed-in view of the electrical contact to the sample under test.

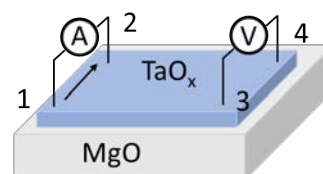


Figure 14 A schematic illustration of the resistivity testing set up using Van der Pauw method.

For the Keithley 4200A-SCS, the fundamental instrument modules used are four source-measurement units (SMU). The basic function of an SMU is to perform one of the following source-measure operations: (1) source voltage and measure current and voltage, or (2) source current and measure voltage and current. The source of the SMU can be configured to sweep or step voltages or currents, or to provide an output with a constant bias voltage or current. The 4200-SMU is a medium power (2 W) source-measure unit with a maximum voltage of 210 V and a maximum current of 105 mA. Two of the SUM were connected to two preamplifiers (4225-RPM) respectively. Without a preamplifier, the 100 nA range (100 fA resolution) is the lowest current source-measure range for an SMU. With a preamplifier installed, the 10 nA, 1 nA, 100 pA, 10 pA, and 1 pA source-measure ranges are available.

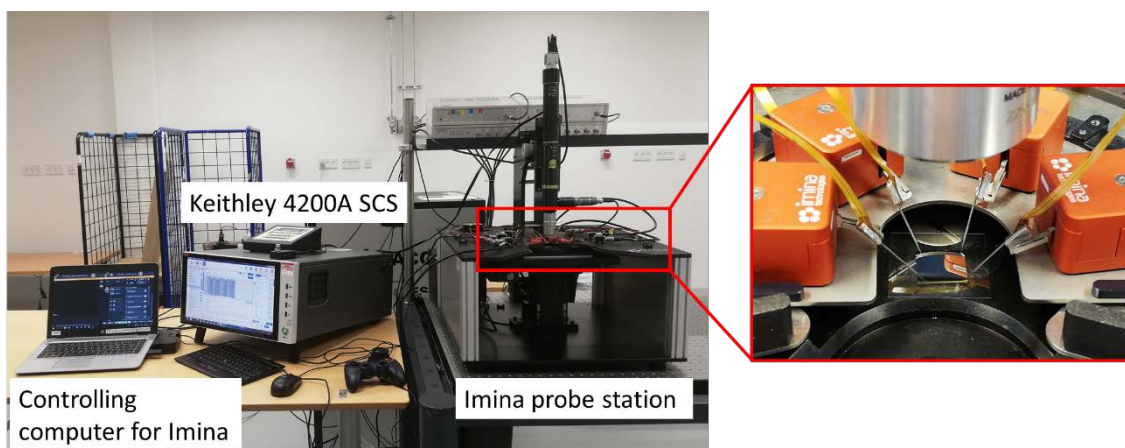


Figure 15 A picture of the electrical test setup of a Keithley 4200A SCS and an Imina probe station. The sample under test is Si/SiO₂/TiN substrate just as an example.

The Imina probe station mainly consists of one XYZ stage, one microscope, drivers, control handles, and six piezoelectric miBots. The miBot's are mobile robots and they are free to move over the stage surface. The Imina probe has 4 degrees of freedom, 2 translations (X and Y) and 2 rotations (in-plane of the miBot itself and out-of-plane of the tool holder tip). Figure 16a is a picture of the miBot with a probe tip installed on the tool holder tip. It is capable of nanometre resolution of positioning, 50 nm in stepping mode and 1.5 nm in scanning mode. The dimension of the miBot is 20.5 mm × 20.5 mm × 13.6 mm with a weight of 12 g (Figure 16b). Different probes, micro-tools and sensors, such as microgripper, micropipette, and optical fibre (Figure 16c to e), can be installed according to different applications. In the current study, I have used tungsten probe tip with a diameter of 500 nm (as illustrated in Figure 16a) for all my electrical testing experiments.

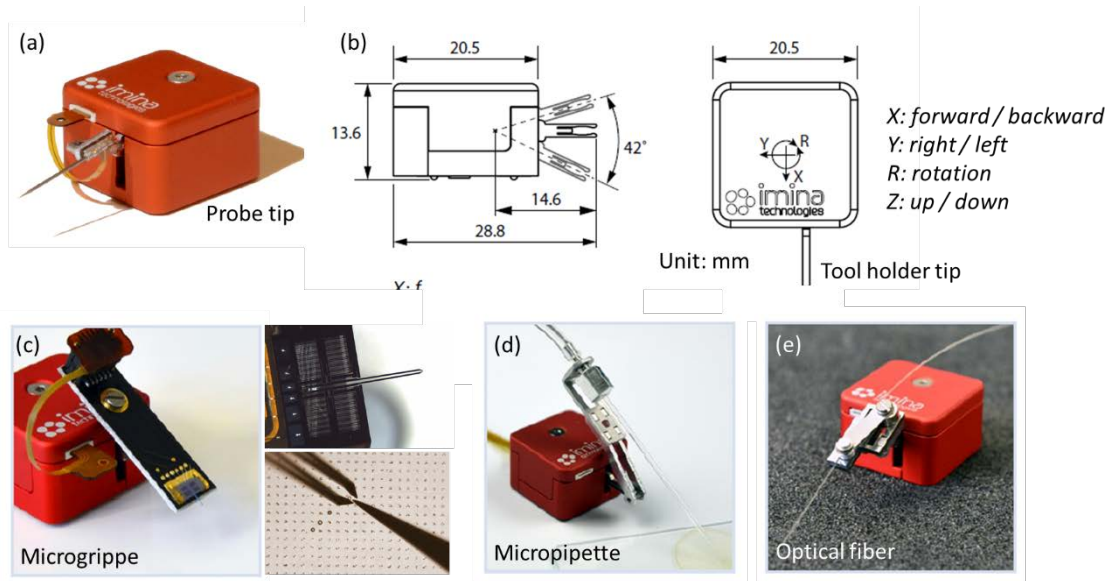


Figure 16 The applications and dimensions of the miBot robot. (a) A miBot with a probe tip on the tool-holder tip, (b) the miBot dimensions. According to different applications, the tool holder tip can hold different probes, micro-tools and sensors. The miBot with (c) microgripper, (d) micropipettes, and (e) optical fibre. The figures are from Imina's website <https://www.imina.ch/>.

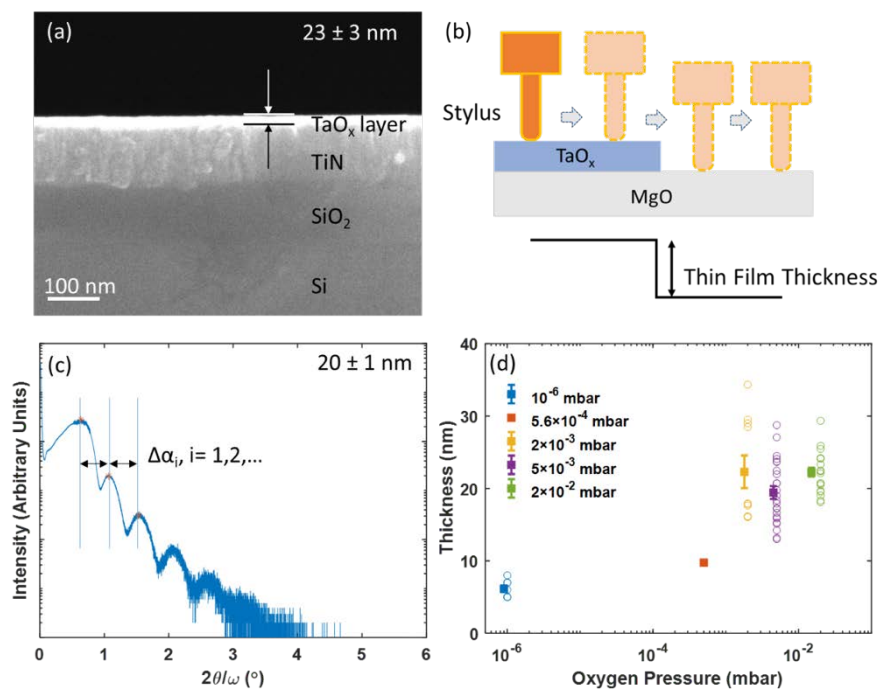


Figure 17 Examples of thin-film thickness determined by (a) scanning electron microscopy (SEM), (b) stylus profilometer, and (c) x-ray reflectivity (XRR). The relationship between oxygen pressure during PLD and the thin film thickness is given in (d). The results in this figure are based on TaO_x thin films grown by PLD at room temperature for 10 min (10 Hz, 4 J/cm²).

The thickness of the TaO_x thin films was determined either by using the scanning electron microscopy (SEM), Dektak stylus profilometer, or X-ray reflectivity (XRR). By using SEM, the

samples were cut along the middle line and the cross-sectional view was observed under SEM. The thickness of the TaO_x thin films was measured at several different positions by using the ruler in the SEM software and an average of the measured thickness was used (Figure 17a). By using Dektak stylus profilometer, the TaO_x thin film is determined by scanning along the TaO_x thin film edge using a stylus (Figure 17b). A Rigaku Smartlab (Cu K_α radiation with λ=1.5406 Å) is used for XRR determination of the films thicknesses. Interference occurs between the x-rays reflected from the surface of the TaO_x thin film and the interface between the TaO_x film and the substrate. Figure 17c is an example of the tested sample showing oscillations caused by this x-ray interference. The oscillation depends on the film thickness, and the thickness *d* can be calculated by

$$d = \frac{1}{n} \sum_{i=1}^n \frac{\lambda}{\Delta\alpha_i} \quad (3)$$

where *n* is the number of oscillations and Δα is the oscillation distance in radius. The results show that as the deposition oxygen pressure increased, the thickness of the TaO_x thin films (10 Hz, 4 J/cm², 10 min deposition) increased (Figure 17d). A similar observation of the increase in the TaO_x film growth rate as the PLD oxygen pressure increases was also reported in Ref. [119], [125], [129].

My results show that as the oxygen pressure increased from 10⁻⁶ mbar to 5 × 10⁻³ mbar, the resistivity of the TaO_x thin films increased from 0.33 Ω·cm up to 2.34 × 10³ Ω·cm. The resistivity of the TaO_x film grown at an oxygen pressure of 2 × 10⁻² mbar was high above the measurement limit (10⁹ Ω·cm). A relationship between the TaO_x resistivity and oxygen pressure during the growth in the PLD is shown in Figure 18.

3.3 Resistive Switching Behaviours in TaO_x based RRAM

TaO_x material is widely studied as the resistive switching layer in RRAM devices due to its excellent device performance, such as fast switching speed of about 100 ps [17] and high endurance cycles of 10¹² times.[18], [82], [131] Numerous TaO_x based single-layered [132], [133] or double-layered [134], [135] were reported to be ECM type [136], [137] or VCM type [135], [138] depending on the electrode materials.[132] Collection of the typical device configuration and their performances for the TaO_x based RRAM devices are shown in Table 5.

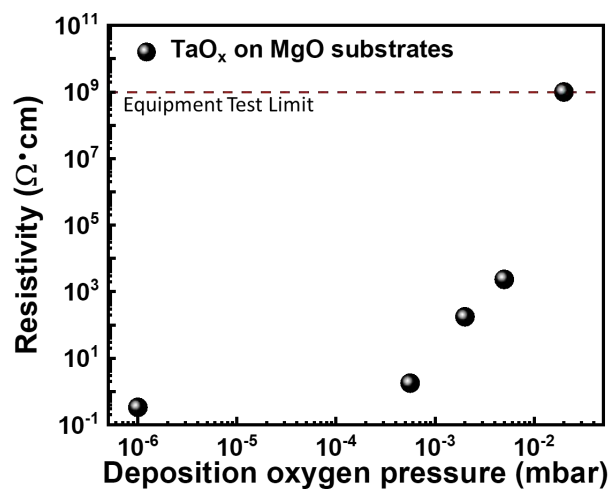


Figure 18 The relation between TaO_x thin film resistivity and the oxygen pressures during PLD. (b) This figure is adapted from Appendix B Article I.

Table 5 Device performances comparison in TaO_x based RRAM devices.

Device structure	Device size (μm ²)	SET/RES ET voltage (V)	Compliance Current (μA)	Retention (s)	Resistance Ratio	Endurance (cycles)	Ref
Ti/TiO ₂ /TaO _x /Ta	10 ⁴ (3D)	+4/-6	0.01	>10 ⁴	~10 ⁵	>10 ¹²	[18]
Pt/TaO _x /Ta/Pt	5 ² -20 ²	+1 to +2.5/-1 to -4	NR*	NR	NR	NR	[17]
BE/TaO _x /Ta ₂ O ₅ /TE	0.5 ²	-1/+2	200	>3×10 ⁸ , 85°C	~10 ³	10 ⁷	[82]
Pt/TaO _x /Ta ₂ O ₅ /Pt	30 ²	-4.5/+7	self-compliance	>10 ⁴ , 200°C	~300	>10 ¹²	[131]
Pt/TaO _x /Cu	NR	+2.3/+0.7	1000	>10 ⁴ , 85°C	~10	>100	[132]
Pt/TaO _x /Ta	50 ²	+0.6/-0.6	100	NR	~10	>10 ¹⁰	[133]
Pt/Ta ₂ O _{5-x} /TaO _{2-x} /Pt	50 ² -0.03 ²	-2.0/+2.0	40-200	>3×10 ⁸ , 85°C	~10	10 ¹²	[134]
W/WO _x /TaO _x /IrO _x	2 ²	-1.7/+1.1	500	>10 ⁴ , 85°C	~10 ³	>10 ⁵	[135]
Pt/Ta ₂ O ₅ /Cu	0.025 ² -5 ²	2.1/-0.5	100	NR	NR	NR	[136]
W/TaO _x /Cu	0.15 ²	0.6/-0.1	100	>10 ⁴	>10 ⁴	>10 ⁴	[137]
W/TiO _x /TaO _x /TiN	0.15 ²	3.0/-3.0	80	>10 ⁴ , 85°C	100	10 ⁴	[139]
Ir or Pt/Ta ₂ O _{5-δ} /Ta _{2-β} /Pt	0.5 ²	-1/+0.8	80/150	>10 ⁷	~10	10 ⁹	[138], [140]

*NR: not reported.

A schematic illustration of the possible electron conduction paths through a metal/insulator/metal stack is shown in Figure 19. The conduction of the thermally activated electrons injected over the barrier into the conduction band is termed Schottky emission. On the other hand, the emission of the trapped electrons to the conduction band is termed Pool-Frenkel emission. Most reported RRAM devices are based on amorphous TaO_x. The dominant conduction mechanism in amorphous Ta₂O₅ thin films is Schottky emission at a low electric field with a typical number between 0.1 to 2 MV/cm,[94], [111], [112] and Pool-Frenkel emission at a high electrical field with a typical threshold number of 0.35 to 2 MV/cm.[78], [94], [111] Similar results were also observed in TaO_x based VCM RRAM devices.

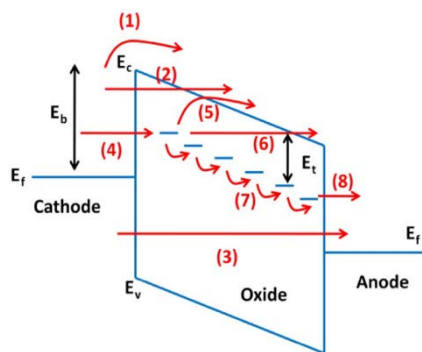


Figure 19 A schematic illustration of the possible electron conduction paths through a metal/insulator/metal stack. (1) Schottky emission, (2) Fowler-Nordheim (F-N) tunnelling, (3) direct tunnelling, (4) tunnelling from the cathode to the traps inside the insulator, (5) Poole-Frenkel emission, (6) F-N-like tunnelling from the traps inside the insulator to the conduction band, (7) trap to trap hopping or tunnelling, and (8) tunnelling from the traps inside the insulator to the anode. E_f: Fermi energy level; E_v: valence band; E_c: conduction band; E_b: Schottky barrier height; E_t: trap barrier height. The figure is from Ref.[8].

Figure 20a shows a Pt/TaO_x/Pt structured VCM RRAM where the log(*I*)-*V*^{1/2} for both HRS and LRS indicates a possible conduction mechanism of Schottky emission (Figure 20b).[138] Ohmic conduction mechanism at LRS [141], [142] and Poole-Frenkel conduction mechanism at HRS [141] were also reported in TaO_x based RRAM devices.

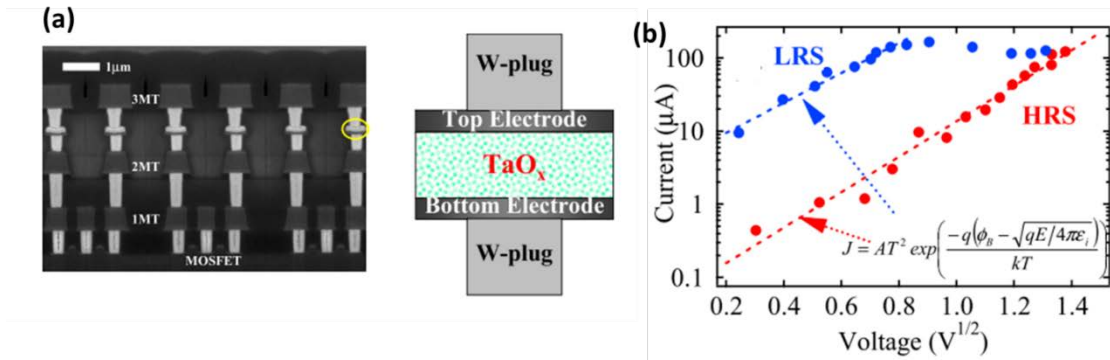


Figure 20 (a) A cross-sectional view of the fabricated 1T1R cells and an illustration of the Pt/TaO_x/Pt VCM RRAM, (b) the I-V characteristics indicating a Schottky emission conduction mechanism in both LRS and HRS states.[138]

In Pt/TaO_x/Pt RRAM device,[40] the TaO_x thin films, deposited by PLD at different temperatures, mainly consisted of Ta₂O₅ and TaO₂ according to the positions of the Ta4f peaks [106], [143] of the XPS spectra. The deconvolution of the XPS spectra shows that as the deposition temperature increased, the composition of TaO₂ increased, which indicate a decrease of the oxygen content inside the TaO_x thin film as shown in Figure 21a. Only films deposited at 600 °C showed resistive switching behaviour in Pt/TaO_x/Pt structured RRAM device (Figure 21b).[40] I will show and

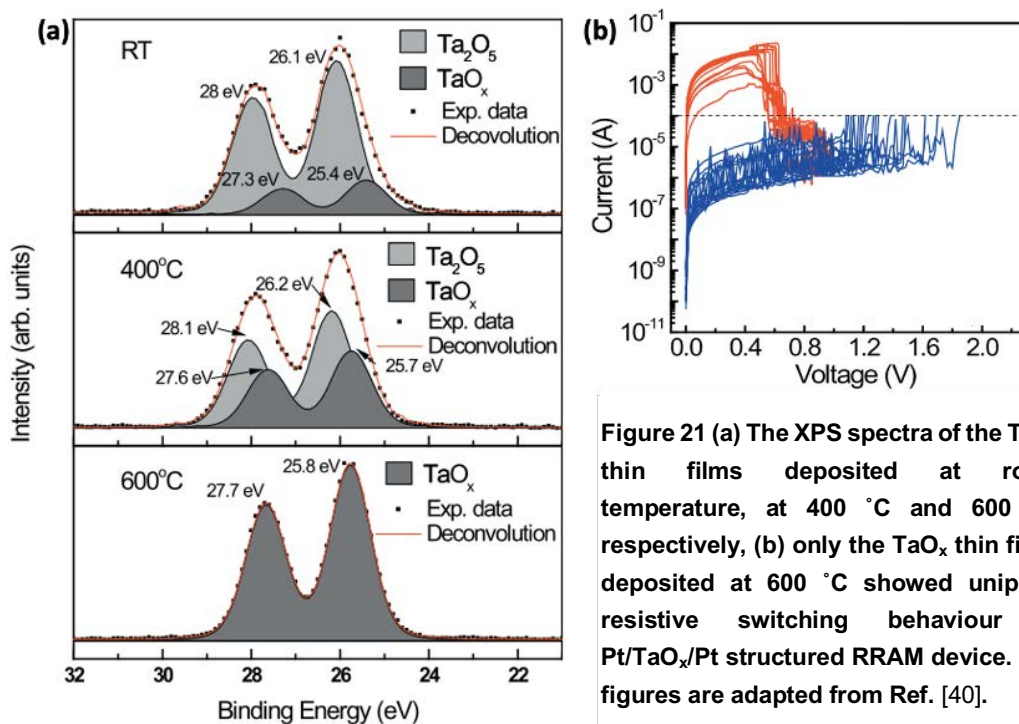


Figure 21 (a) The XPS spectra of the TaO_x thin films deposited at room temperature, at 400 °C and 600 °C, respectively, (b) only the TaO_x thin films deposited at 600 °C showed unipolar resistive switching behaviour in Pt/TaO_x/Pt structured RRAM device. The figures are adapted from Ref. [40].

explain later that if the oxygen deficiency of TaO_x thin film is large the films will not exhibit resistive switching. The results in the literature[40], as well as my results, indicate that the control over the oxygen content in the TaO_x thin films is crucial for the triggering the resistive switching of the TaO_x based RRAM devices.

My results have shown that the oxygen pressure during PLD can be an effective tuning knob to control the stoichiometry of the TaO_x thin film. We further studied the effect of the deposition conditions (i.e. the stoichiometry of the TaO_x thin film) on the resistive switching behaviours in different devices such as TiN/TaO_x/W. In my samples, all the TaO_x films were deposited at room temperature for 10 min by PLD (KrF excimer laser, 248 nm, 10 Hz, 4 J/cm²). TaO_x thin films with different stoichiometry were obtained by changing the oxygen pressure during PLD. The TaO_x films were all amorphous (similar to what have shown in Figure 10). Commercial silicon substrates (thickness of 525 ± 20 μm) in <100> orientation with 100 ± 10 nm silicon dioxide and 100 nm TiN film on top were used as the substrate (Figure 17a). The TaO_x thin films were deposited through a metal sample holder which covered part of the TiN bottom electrode layer and enabled the direct electrical contact to the bottom electrode after deposition. Two device configurations were used (Figure 22). The top electrode is either the tungsten probe tip (0.5 μm diameter, Figure 22a) or the sputtering deposited thin film tungsten electrodes. The sputtered tungsten (W) top electrode layer was deposited by DC magnetron sputtering without intentional substrate heating. The deposition conditions were set as 40 sccm Ar gas, 10⁻² Torr deposition pressure, 320 V discharge voltage and 0.2 A discharge current for a deposition time of 300 seconds. The sputtering deposited W top electrodes were patterned by Al₂O₃ shadow masks (LaserTech, Denmark) with diameters of 50 μm, 100 μm, 200 μm, and 500 μm, respectively (Figure 22b).

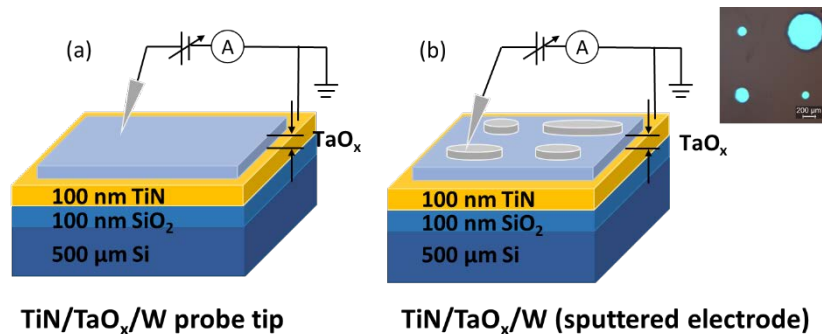


Figure 22 Device configurations: (a) using the W probe tip (0.5 μm in diameter) as the top electrode, and (b) using the sputtering deposited W layer as the top electrode (50 μm, 100 μm, 200 μm, and 500 μm in diameters).

All electrical tests were carried out using Keithley 4200A with an Imina probe station providing the contact through W needle probes (0.5 μm in diameter) (Figure 15). Our results show that as the oxygen pressure in the chamber during PLD (or the oxygen composition inside the TaO_x thin films) increases, the initial resistance of the devices increases. Figure 23a shows the relation between the initial resistance as a function of oxygen pressure measured at different electrode sizes. For devices with the same top electrode sizes, the initial resistance of the devices increased as the PLD oxygen pressure increased. For TaO_x films deposited at a similar PLD oxygen pressure, the initial resistances increased as the top electrode sizes decreased. Figure 23b shows

the relation between the initial resistances and the forming voltages. Most data points are from devices with the probe tip as the top electrode and the forming voltages linearly increased as the logarithm of the initial resistances increased.

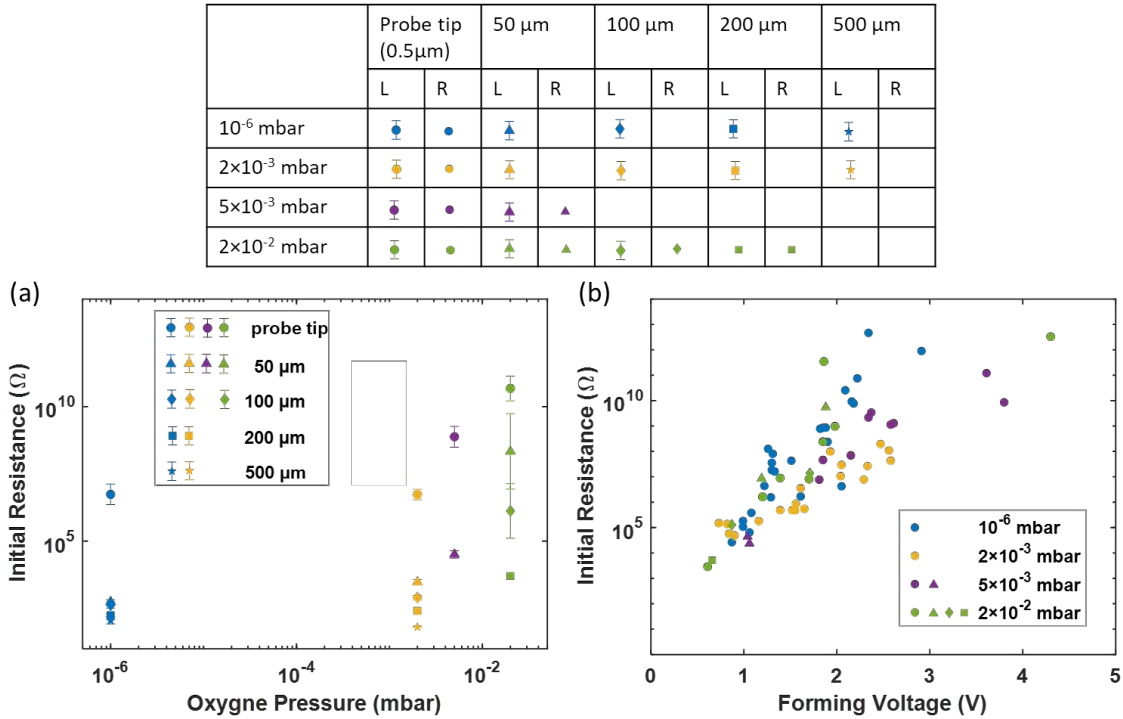


Figure 23 (a) The initial resistances dependency on the oxygen pressure during PLD, (b) the relationship of the initial resistances and the forming voltages in TiN/TaO_x/W structured devices with different top electrode diameters. Different colours represent different oxygen pressures. Different marker shapes represent different device sizes. Circle: probe tip, 0.5 μ m; triangle: sputtered top electrode, 50 μ m diameter; diamond: sputtered top electrode, 100 μ m diameter; square: sputtered top electrode, 200 μ m diameter; pentagram: sputtered top electrode, 500 μ m diameter.

For devices with W probe tip as the top electrode as illustrated in Figure 24a, all the TaO_x thin films deposited under different oxygen pressures showed resistive switching behaviours. (Typical *I-V* curves are shown in Appendix A, Figure 56.) Different colours represent different PLD oxygen pressures for the TaO_x thin films. Figure 24b and d are the SET and RESET voltages of the devices. Figure 24b shows the error bars (left side) along with the scatter points (right side) of the switching voltages. Figure 24d shows the cumulative probability of the switching voltages. Both the SET and RESET voltages showed no dependency on oxygen pressure. Figure 24c and e are the LRS and the HRS of the devices. Figure 24c shows the error bars (left side) along with the scatter points (right side) of the LRS and HRS. The LRS kept almost the same for different TaO_x thin films whereas the HRS increased as the oxygen pressure increased. Figure 24e shows the cumulative probability of LRS and HRS. The HRS showed larger variations than the LRS and the HRS of the devices based on the TaO_x deposited at an oxygen pressure $P_{O_2} = 2 \times 10^{-2}$ mbar showed the largest variation.

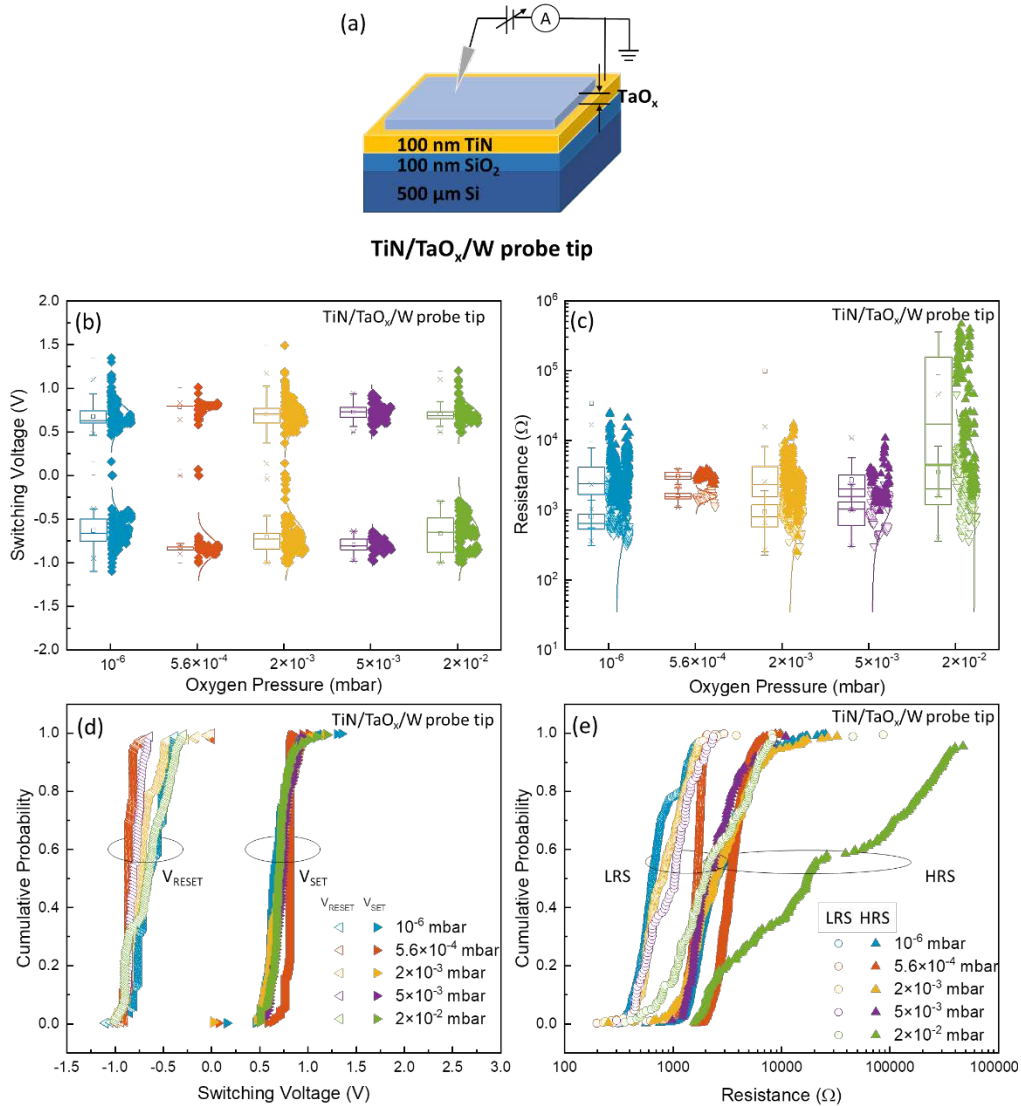


Figure 24 (a) is a schematic illustration of the TiN/TaO_x/W probe tip structured device. (b) and (d) show the SET and RESET voltages, (c) and (e) show the low state resistances (LRS) and the high resistance states (HRS).

The degradation behaviour of the TiN/TaO_x/W devices with TaO_x layer deposited at oxygen pressure of $P_{O_2} = 10^{-6}$ mbar for 10 min were tested over a time length of 117 days. Figure 25a shows the initial resistance, LRS, and HRS distribution along different testing time and Figure 25b shows the SET and REST voltages distribution along different testing time. No obvious degradation was observed, and the devices showed good stability over long time indicating minor effect owing to exposure to air. The devices were stored at room temperature in air.

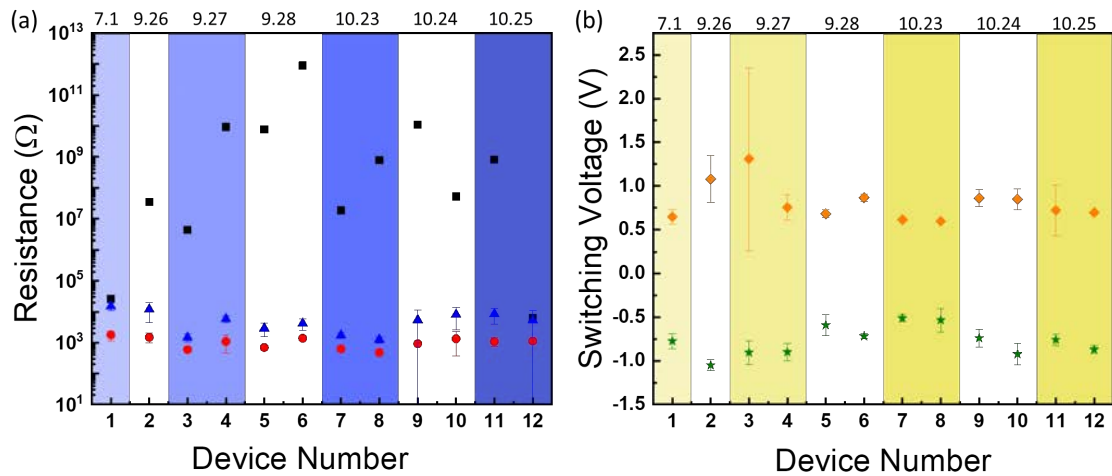


Figure 25 The degradation of the TiN/TaO_x/W probe tip structured devices tested over a time length of 117 days (from 1st July 2018 to 25th October 2018), (a) The distribution of the initial resistance (black square), LRS (red circle), and HRS (blue triangle), and (b) The distribution of SET (orange diamond) and RESET (green pentagram) voltages.

The volatile behaviours were also observed for the TiN/TaO_x/W devices with TaO_x layer deposited at oxygen pressure of $P_{O_2} = 10^{-6}$ mbar for 10 min. The Successive SET operations can be achieved within one device without any RESET operation, as shown in Figure 26a. After the SET process, the device is set to LRS and the resistance retention is read. The current drops from high current value of 10^{-4} A to low current of about 10^{-10} A, which means the device resistance turned from LRS to HRS, within 150 s spontaneously without any RESET operation, as shown in Figure 26b.

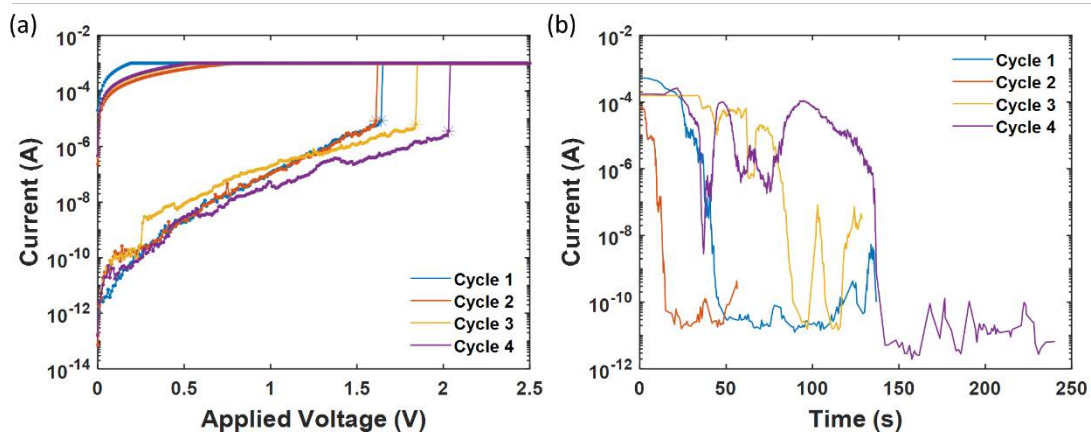


Figure 26 The volatile behaviours were observed in TiN/TaO_x/W probe tip structured devices. (a) Successive SET operations can be achieved within one device without any RESET operation. (b) The current drops from high current value of 10^{-4} A to low current of about 10^{-10} A spontaneously within 150 s.

W probe tip as the top electrode can provide a flexibility to have many ‘devices’ within one sample and the fabrication process is easier since no additional sputtering process is needed for the top electrode. The disadvantage when using the probe tip as top electrodes is that the distribution of the initial resistances is wide.

For TiN/TaO_x/W devices with TaO_x layer deposited at oxygen pressure of $P_{O_2} = 10^{-6}$ mbar for 10 min, the initial resistances of the devices can have a wide distribution from about 10 Ω to 10⁹ Ω as shown in Figure 27a. Devices with initial resistances lower than 10³ Ω were too conductive and showed no Forming or any resistive switching behaviours. Only devices with initial resistances from 10⁴ Ω to 10⁹ Ω showed resistive switching behaviours. Not all the devices with initial resistances falling within this range were switchable, some devices electrically broke down during the Forming process, which cannot RESET back to HRS, and some devices showed volatile SET. Figure 27b only shows the initial resistances and the Forming voltages of the devices (TiN/TaO_x/W with TaO_x layer deposited at oxygen pressure of $P_{O_2} = 10^{-6}$ mbar for 10 min) with many switching cycles. The percentage of the switchable devices out of all tested devices is 38.7% (12 out of 31 devices).

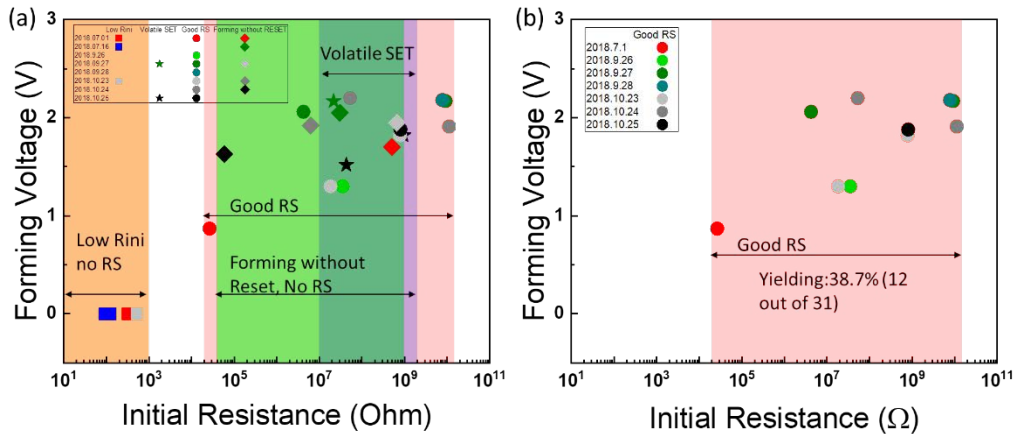


Figure 27 The initial resistances and the Forming voltages of (a) all tested TiN/TaO_x/W probe tip structured devices. (b) TiN/TaO_x/W (probe tip as top electrode) devices with many switching cycles. Several different device behaviours were observed: too low initial resistances without any Forming or resistive switching behaviour, break down after Forming, volatile SET, and many resistive switching (RS) cycles. The yielding of the devices with many switching cycles were 38.7% (12 out of 31 devices). The TaO_x film was deposited at oxygen pressure $P_{O_2} = 10^{-6}$ mbar for 10 min.

The wide distribution of the initial resistances in TiN/TaO_x/W devices may be due to the vertical position of the probe tip when it is brought into contact with the TaO_x film surface. When placing the probe tip on the TaO_x surface, since there is no force feedback function of the probe tip, the extent of the approaching process is not always the same for each device. Figure 28 shows the relationship between the initial resistances and the probe tip approaching process. The resistances were recorded at the same position and the probe tip was lifted up and lowered down using different number of steps per move. When using stepping mode to manipulate the probe approaching to the surface, the number of steps per move can be changed. For 300, 200, 100, 50, and 10 steps per move, the results obviously show a large difference of resistance distributions from about 100 Ω to 10¹⁰ Ω. However, it is worth noting that, as also shown in Figure

25 and Figure 27, this will not affect the LRS and HRS or the SET and REEST voltages. Another disadvantage of using probe tip as top electrode is that the device cannot be tested again after the probe is lifted up for there is no mark to trace the device position again.

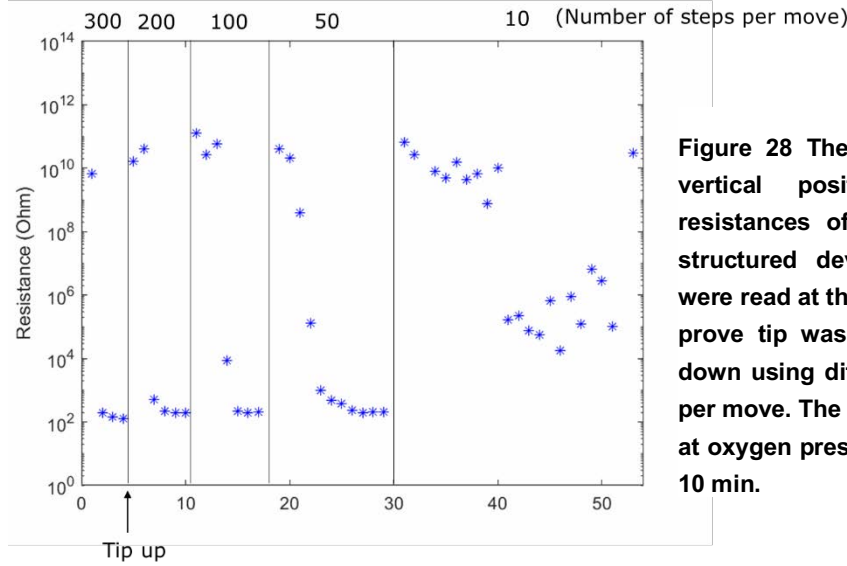


Figure 28 The effect of W probe tip vertical position on the initial resistances of TiN/TaO_x/W probe tip structured devices. The resistances were read at the same position and the probe tip was lifted up and lowered down using different number of steps per move. The TaO_x film was deposited at oxygen pressure $P_{O_2} = 10^{-6}$ mbar for 10 min.

Based on these results, we have decided to concentrate on the devices with the top electrodes of 50 μm diameters which showed a resistance resistive switching compared to other devices with larger top electrode sizes. Figure 29a shows the initial resistance of the TiN/TaO_x/W (50 μm diameter) devices and the initial resistances seems to increase as the PLD oxygen pressure increase. Figure 29b shows typical I - V curves of different devices. Only devices based on TaO_x films deposited at an oxygen pressure $P_{O_2} > 2 \times 10^{-3}$ mbar showed resistive switching. The devices based on the TaO_x thin films deposited at an oxygen pressure $P_{O_2} \leq 2 \times 10^{-3}$ mbar were very conductive and cannot be switched to lower resistance states or be RESET to higher resistance states.

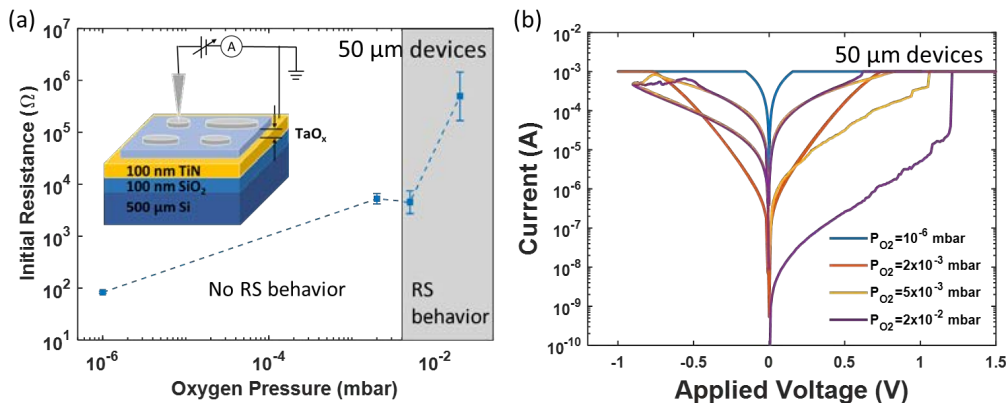


Figure 29 Resistive switching behaviours of the TiN/TaO_x/W (sputtered W electrodes with 50 μm diameter) structured device: (a) shows the initial resistance dependency on the oxygen pressure, (b) shows the typical I - V curves of different devices. The figures are adapted from Appendix B Article II.

Summary

1. The oxygen pressure in the PLD chamber during the growth was used as a tuning knob to control the TaO_x thin films oxygen content and the resistivity. As the deposition oxygen pressure increased from 10⁻⁶ mbar to 2 × 10⁻² mbar, the Ta₂O₅ inside the TaO_x thin films increased from 75 at.% to 95 at.% and the resistivity of the TaO_x thin films increased from 0.33 Ω·cm to higher than the equipment test limit (10⁹ Ω·cm).
2. For TiN/TaO_x/W (probe tip, 0.5 μm diameter) structured RRAM devices, the devices initial resistances increased as the deposition oxygen pressures increased and all devices showed resistive switching behaviours. The switching voltages are independent on the deposition oxygen pressure of the TaO_x thin films. The LRS kept almost the same for different TaO_x thin films whereas the HRS increased as the oxygen pressure increased. The HRS showed larger variations than the LRS and the HRS of the devices based on the TaO_x deposited at an oxygen pressure of 2 × 10⁻² mbar showed the largest variation.
3. For TiN/TaO_x/W (sputtered, 50 μm diameter) structured RRAM devices, the device initial resistances also increased as the deposition oxygen pressures increased. Only devices with TaO_x deposited at oxygen pressure higher than 2 × 10⁻³ mbar showed resistive switching behaviour.

Chapter 4

Phase and Device Behaviour Control by Annealing

So far, I have been discussing the effect of being able to control the performance of the TaO_x based device by controlling the fabrication conditions. However, there is another way to control the device behaviours and this is via post-deposition annealing. Post-deposition annealing is often used to further improve the mechanical, electrical or optical properties of thin films by structural relaxation and stoichiometry change.[93], [144] In this chapter I will provide the results which show the behaviour of the TaO_x materials under post-deposition annealing.

4.1 Stoichiometry and Crystal Structure

Both the stoichiometry and the crystal structure of the TaO_x films can be influenced by the post-deposition annealing process. Annealing in different gas atmospheres at elevated temperatures can be an effective way to tune the stoichiometry of tantalum oxide.[132], [145] [146] Compositions dependence on the post-deposition annealing temperature and time were studied by O. K.

Donaldson et al.[146] Figure 30 shows the TaO_x thin films stoichiometry change as a function of the post-deposition annealing time and temperature. Figure 30a and b show the TaO_x films

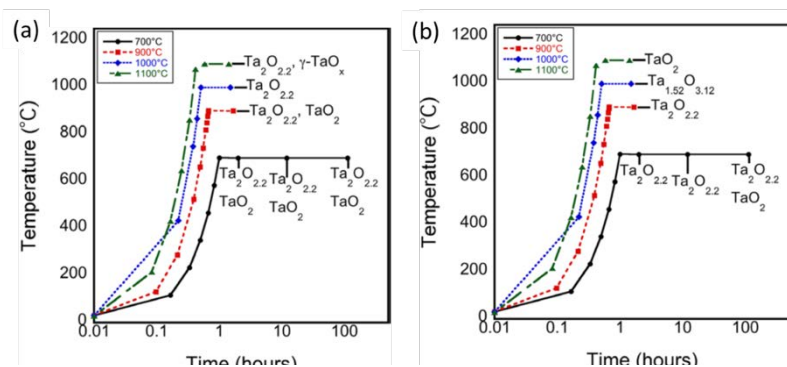


Figure 30 The stoichiometry retained in the TaO_x thin films during the annealing at different temperatures: (a) TaO_x thin films deposited at low vacuum condition (1.3×10^{-4} mbar), and (b) TaO_x thin films deposited at high vacuum condition (1.3×10^{-7} mbar). The figures are from Ref. [146].

deposited at low vacuum condition (1.3×10^{-4} mbar) and high vacuum condition (1.3×10^{-7} mbar), respectively. The TaO_x films deposited at low vacuum condition (1.3×10^{-4} mbar) showed devitrification after annealing 1 hr at 700 °C and the TaO_x films deposited at vacuum condition (1.3×10^{-7} mbar) showed an increase devitrification temperature of 900 °C.[146]

As for the development of crystal structure as a function of temperature and time, the amorphous Ta₂O₅ transfer into the low temperature β-phase Ta₂O₅ at elevated temperatures between 500 °C to 700 °C. This ordering process of the amorphous Ta₂O₅ induced by thermal annealing is a slow process, where the phase transition starts in the range of 500 °C to 600 °C and hardly completed even at 700 °C.[93] For comparison, the low temperature β-phase can sluggishly transform into high temperature α-phase at a very high temperature of about 1320 °C.[83] [76], [93], [94]

4.2 Resistive Switching Behaviours of samples after post-deposition annealing

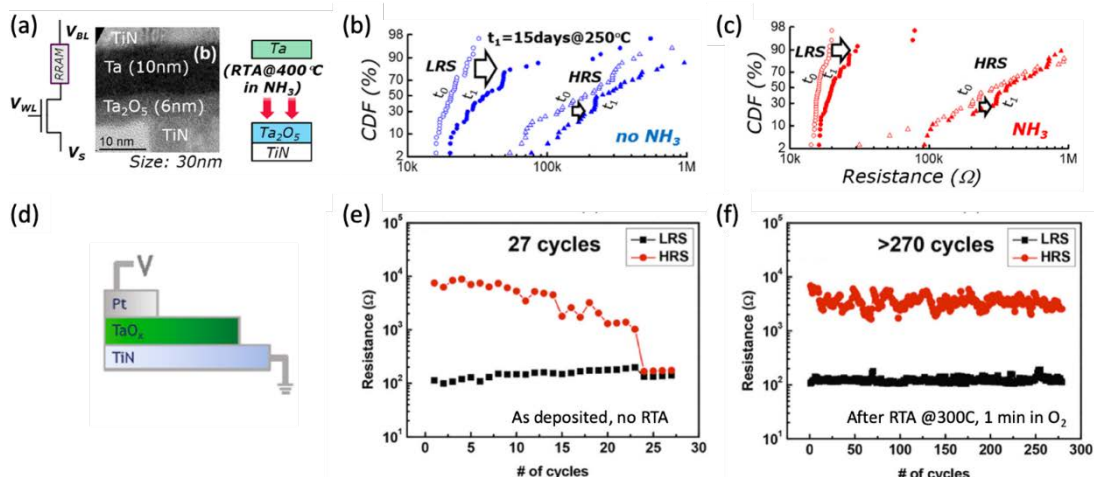


Figure 31 Rapid thermal annealing effect in TaO_x based RRAM devices. (a) Schematic illustration of TiN/Ta₂O₅/Ta RRAM and a TEM cross-sectional view of the RRAM device, (b) resistance retention behaviour in devices without NH₃ annealing, (c) resistance retention behaviour in devices with NH₃ annealing.[147] (d) Schematic illustration of Pt/TaO_x/TiN RRAM, (e) endurance behaviour without rapid thermal annealing (RTA), (f) endurance behaviour after rapid thermal annealing.[145]

The annealing process can influence the behaviours of the TaO_x based RRAM devices depending on the atmosphere, temperature and time. Rapid thermal annealing (RTA) process of the TaO_x films in NH₃ at 400 °C for 5 min results in the incorporation of hydrogen (H) species in the TaO_x (Figure 31a), which lowered both the forming voltage and the low resistance states (LRS) of TiN/Ta₂O₅/Ta structured RRAM devices. This also shifted HRS and LRS to higher values after heating the device at 250 °C for 15 days (Figure 31b and c). The improved thermal stability of the device was attributed to the O-H bonds formed in Ta₂O₅ after RTA. This effect can be described by the Kröger–Vink notation as



This process shows that the formed O-H bonds act as donors and lead to the generation of electrons (e^-). The formation of the O-H bonds stabilized the $V_{\dot{O}}$ defects and improved the stability of the conductive filaments.[147] Another work showed that annealing TiN/TaO_x/Pt structured RRAM devices in an oxygen atmosphere at 300 °C for 1 min changed the TaO_x thin film oxygen stoichiometry from TaO_{2-y} to Ta₂O_{5-z} and improved the device endurance from 27 cycles to more than 270 cycles (Figure 31d to e).[145]

In Pt/TaO_x/W structured RRAM devices, annealing the device in the air at 964 °C for 30 min led to a change of the TaO_x layer from amorphous (blue) to polycrystalline β -phase (red), as indicated by the XRD in Figure 21a. But the resistive switching of the Pt/TaO_x/W device showed negligible difference (Figure 32b).[148] This indicates that for this device configuration the crystallinity of the films (seen only from XRD) maybe does not affect the electrical characteristics of the device.

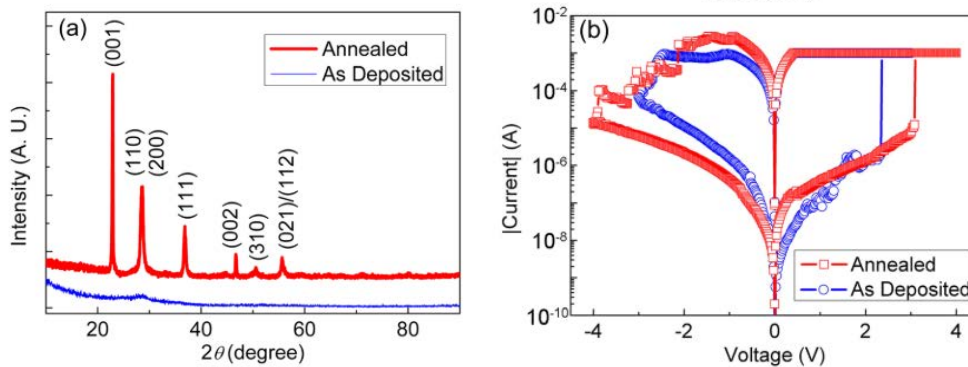


Figure 32 Annealing effect on Pt/TaO_x/W RRAM. (a) XRD patterns showed amorphous phase for the as-deposited TaO_x and β -phase Ta₂O₅ after annealing in air at 964 °C for 30 min. (b) No obvious resistive switching difference was observed after the annealing process. The figures are from Ref. [148].

I studied the effect of post-deposition annealing on the TiN/TaO_x/W devices. The active TaO_x layer was deposited by PLD under oxygen pressure $P_{O_2} = 2 \times 10^{-3}$ mbar. The top electrodes were deposited by sputtering and patterned by an Al₂O₃ shadow mask with diameters of 50 μ m, 100 μ m, 200 μ m, and 500 μ m, respectively. Each sample (525 μ m $1 \times$ cm 1 cm) had 16 devices for each size, respectively to get more statistics in the measurements.

Two different annealing methods were used in these experiments: (1) annealing the devices in air at 100 °C and 150 °C for 1 min, 5 min, and 30 min, continuously, which means the devices under test undergone 6 annealing processes and 72 min annealing time in total as shown in Figure 33a; (2) annealing the devices in air at different temperatures for 4 hr, respectively, with a heating up and cooling process of 200 °C/hr as shown in Figure 33b. All the electrical measurements were carried out at room temperature.

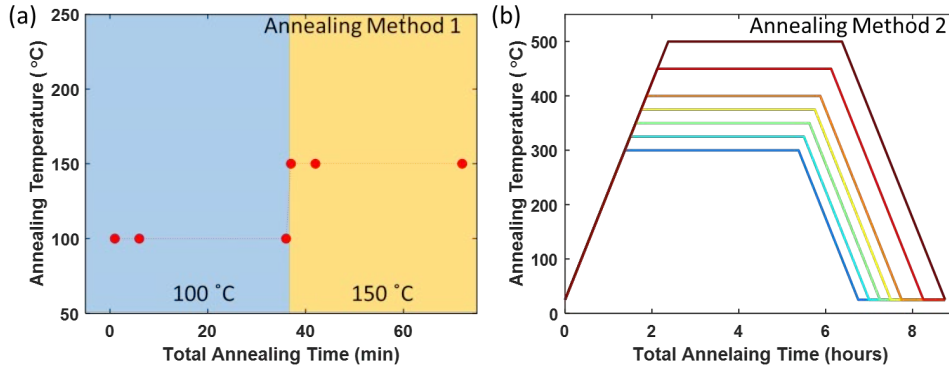


Figure 33 The temperature change as a function of the total annealing time: (1) annealing method 1 and (2) annealing method 2.

(1) Method 1 for annealing temperatures $T \leq 150$ °C: the devices showed good thermal stability.

In the first annealing procedure, a hot plate (Cossim, China) was used for annealing the devices in the air. The heater has a heating temperature range from room temperature to 400 °C with a maximum heating speed of 10 °C/min, temperature fluctuation of ± 0.5 °C, and measurement accuracy of $\leq \pm 0.5\%$. The heating plate is 109 mm in diameter with a heating area of 31.5 mm in diameter. The hot plate is as shown in Figure 34. After the temperature is stabilized at the desired value, the samples were placed onto the heating plate. After each annealing process, the samples were cooled down to room temperature and the resistance of the devices were measured at room temperature. Since the volume of the sample used was $525 \mu\text{m} \times 1 \text{ cm} \times 1 \text{ cm}$, the heating and the cooling process were regarded as fast and negligible.



Figure 34 A picture of the hot plate used in the first annealing method. The heating plate is 109 mm in diameter with a heating area of 31.5 mm in diameter. The sample is $525 \mu\text{m} \times 1 \text{ cm} \times 1 \text{ cm}$.

Low annealing temperatures of 100 °C and 150 °C were chosen to have better control of the annealing process and the annealing time was used as another parameter to control the annealing process. The as-fabricated samples with TaO_x deposited at an oxygen pressure $P_{O_2} = 2 \times 10^{-3}$ mbar did not show resistive switching initially with low initial resistances with an average below $10^4 \Omega$ magnitude.

Figure 35 shows the resistance change in the first annealing process. The left column shows the resistance changes for each device with different top electrode diameters. The right column shows the relative resistance changes to the initial resistance state. Due to the relatively low annealing temperatures (36 min at 100 °C and 36 min at 150 °C in the air), the resistances of most devices kept stable after the whole annealing process, which indicates the thermal stability of the devices.

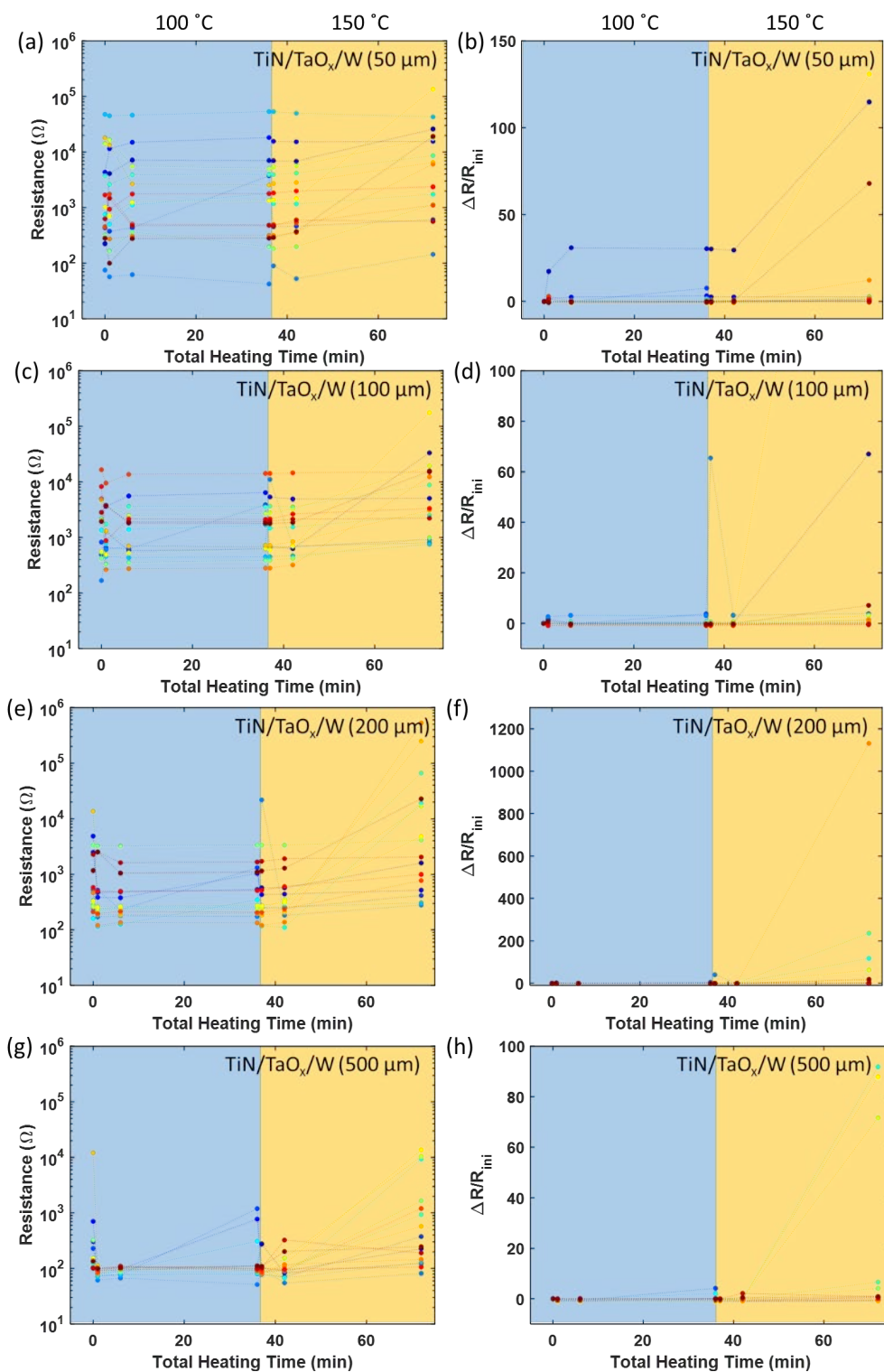


Figure 35 The resistance change of TiN/TaO_x/W structured devices after annealing in air at 100 C (36 min) and 150 C (36 min) for 72 min in total. Left column figures (a, c, e, and g) are the resistance changes for 50 μm, 100 μm, 200 μm, and 500 μm devices, respectively. Right column figures (b, d, f, and h) are the relative resistance changes to the initial resistance state for 50 μm, 100 μm, 200 μm, and 500 μm devices, respectively.

(2) Method 2 for annealing temperatures $300\text{ }^{\circ}\text{C} \leq T \leq 500\text{ }^{\circ}\text{C}$

In the second annealing procedure, a furnace was used to anneal the samples in the air at the annealing temperatures of $300\text{ }^{\circ}\text{C}$ to $500\text{ }^{\circ}\text{C}$. The temperatures were raised to accelerate the process. The samples were heated up in the furnace at a heating up rate of $200\text{ }^{\circ}\text{C/hr}$ to the desired annealing temperatures, annealed at the desired temperatures for 4hr, and then cooled down to room temperature at a cooling rate of $200\text{ }^{\circ}\text{C/hr}$. Figure 36 shows that the devices initial resistance increases as the annealing temperatures increases. Since the devices with $50\text{ }\mu\text{m}$ diameter showed the highest resistances among all devices, for simplicity, the focus was put on the devices with $50\text{ }\mu\text{m}$ diameter top electrodes.

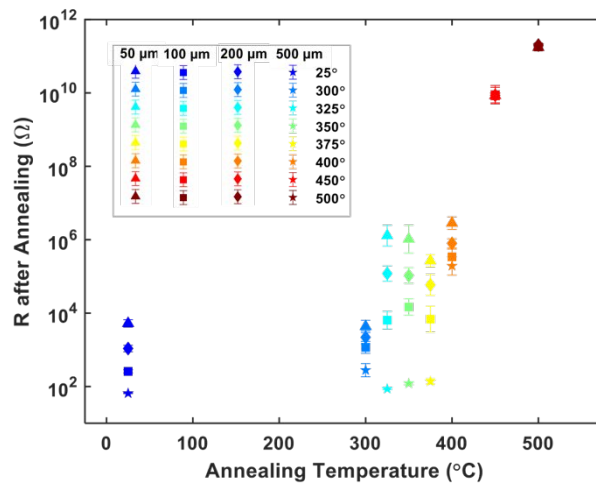


Figure 36 The devices resistances change after the annealing in the air for 4 hr at different annealing temperatures. The inset shows the devices area and annealing temperatures for each symbol.

For the annealing temperature up to $300\text{ }^{\circ}\text{C}$, the resistances showed no obvious change after the annealing process and the devices kept non-switchable after the annealing process.

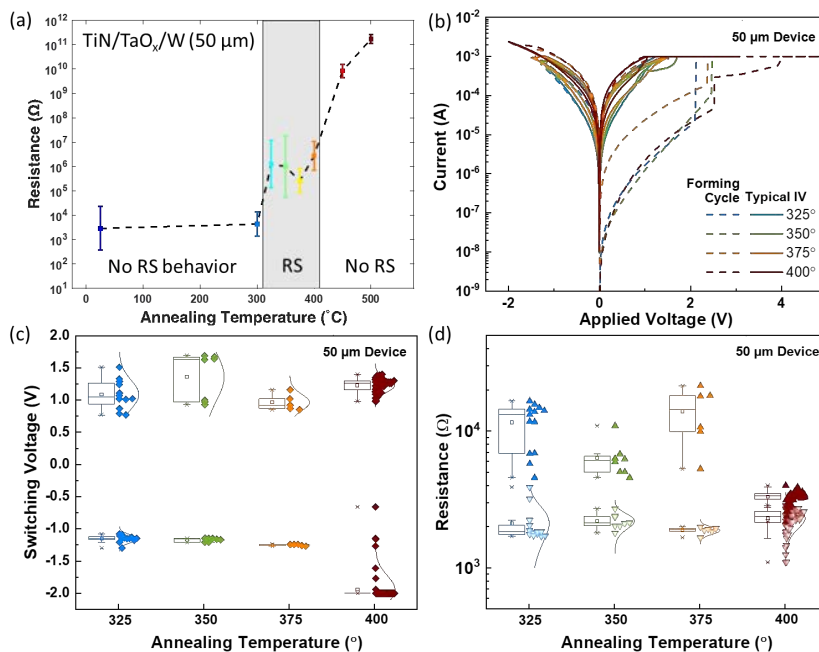


Figure 37 (a) The devices resistances change after annealing in air at different temperatures for 4 hr. The resistive switching behaviours were triggered in initially non-switching devices after annealing at $325\text{ }^{\circ}\text{C} \leq T \leq 400\text{ }^{\circ}\text{C}$. (b) Typical I-V curves, (c) the switching voltages, and (d) the resistance states of the devices whose resistive switching behaviours were triggered by annealing. (a) and (b) are adapted from Appendix B Article II.

For the annealing temperatures between $325\text{ }^{\circ}\text{C} \leq T \leq 400\text{ }^{\circ}\text{C}$, the results show that the devices initial resistances increased from about $5.6\text{ k}\Omega$ to about $10^3\text{ k}\Omega$ after the annealing process as shown in Figure 37a. At this temperature range, the resistive switching behaviours were triggered after the annealing process. Typical I-V curves of the devices with resistive switching behaviours

are shown in Figure 37b. Different colours represent different annealing temperatures. The dash lines are the Forming cycle and the solid lines are typical following switching cycles. The SET voltages showed no obvious dependency on the annealing temperatures and the absolute value of the RESET voltage increased as the annealing temperature increased, as shown in Figure 37c. The LRS and HRS for devices after different annealing at different temperatures are shown in Figure 37d and the resistance window decreased as the annealing temperatures increased.

For annealing temperatures of $400\text{ }^{\circ}\text{C} < T \leq 500\text{ }^{\circ}\text{C}$, the devices initial resistances exceeds $10^{10}\text{ }\Omega$, showing an insulating state with no resistive switching.

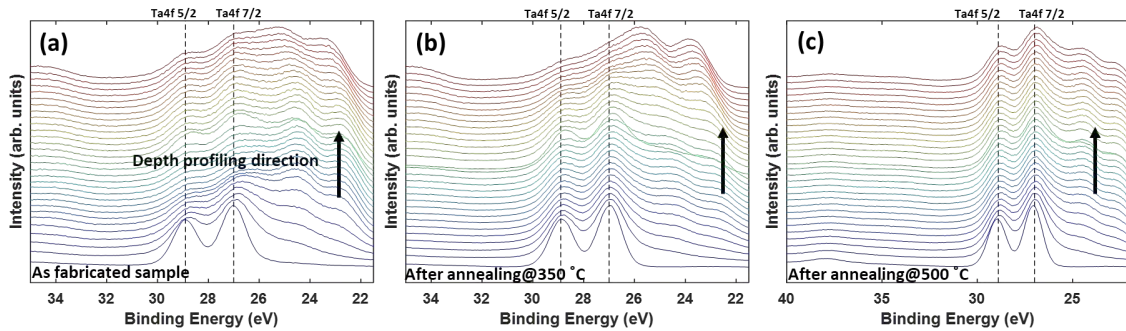


Figure 38 XPS depth profiles of the TaO_x thin films (a) as fabricated, (b) after annealing at 350 °C, and (c) after annealing at 500 °C. The black arrows indicate the etching direction from the surface of TaO_x to the inner part of TaO_x thin film. The dashed lines represent the binding energy for Ta⁵⁺. The figures are adapted from Appendix B Article II.

To understand the oxidation state and stoichiometry of the TaO_x thin films after annealing using the second annealing method and their relation to the resistive switching, I studied the following three samples: (1) as-deposited sample, (2) sample after annealing at 350 °C, and (3) sample after annealing at 500 °C, using XPS depth profiling. The conditions for the XPS depth profiling were: a spot size of 650 μm and a take-off angle of 90° from the surface plane on a fraction of the area of 0.7 × 0.7 mm² with monoatomic Ar⁺ Ion Beam. The kinetic energy of the beam was set to 3 keV (10 s/each level with 30 levels in total). The analysis chamber pressure was 4×10^{-8} mbar. For obtaining high resolution local binding energy spectra for the Ta-4f, a 20 eV detector pass energy, a dwelling time of 50 ms, and an energy step size of 0.05 eV were used. To control the sample charging, a combined ion/electron gun (i.e., a dual-beam source) was used. According to the O1s spectra peak position of the second spectrum of the as-deposited sample, all Ta-4f spectra were shifted accordingly.

Figure 38a to c are the XPS depth profiles of the sample as-deposited, sample after annealing at 350 °C, and sample after annealing at 500 °C. The black arrows in each figure represent the depth profiling direction from the TaO_x surface to the inner part of the TaO_x. Since the analysed times for each set of profiles were similar, the profiling depths for each sample were also similar. In the as-deposited sample (Figure 38a), the Ta 4f peaks shifted to a lower binding energy direction. This means that from the surface to the inner part of the TaO_x thin films, a stoichiometric to less stoichiometric composition gradient was observed. In the sample after annealing at 500 °C (Figure 38c), Ta₂O₅ was the dominant composition independent of the profiling depth. In the sample after annealing at 350 °C (Figure 38b), the results show a mixture of both stoichiometric and non-stoichiometric compositions through the depth profiling direction. Relating the XPS results in Figure 38 and the resistive switching behaviours in Figure 37, the results indicate that to trigger the resistive switching behaviour, the TaO_x layer of the devices should be partially insulating and partially conductive, i.e. as observed in Figure 38b of the sample after annealing at 350 °C.

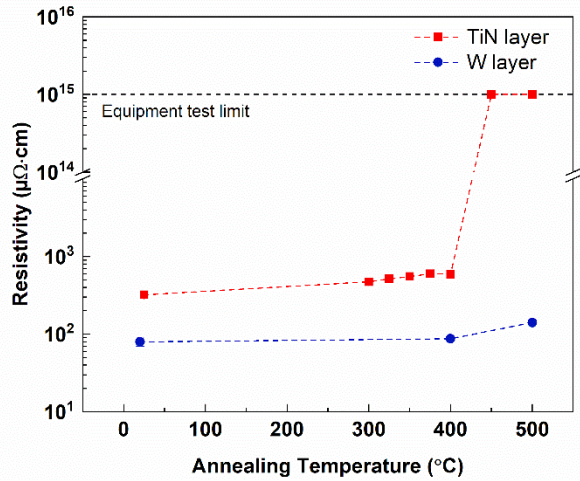


Figure 39. Resistivity change of TiN and W layer after annealing at different temperatures. The resistivity was tested by using Van der Pauw configuration on 1 cm×1 cm samples. The figure is from Appendix B Article II.

Besides the stoichiometry of the TaO_x layers, other sources influencing the resistive switching behaviour are the electrodes and the interfaces. The resistivity of the TiN layer (red line in Figure 39) was $320 \pm 19 \mu\Omega \cdot \text{cm}$ to $592 \pm 61 \mu\Omega \cdot \text{cm}$ for annealing temperatures up to 400 °C, which showed a no obvious resistivity increase. After annealing at 450 °C and 500 °C, the TiN layer became insulating with a resistivity higher than the equipment test limit. The oxidation of the TiN layer led to the non-switching of the devices after annealing at temperatures at 450 °C and 500 °C. The resistivity of W (blue line in Figure 39) kept stable for all annealing temperatures up to 500 °C.

The samples were studied by scanning tunnelling electron microscopy (STEM) analysis using a probe-aberration corrected JEOL JEM-ARM200F microscope. A probe semi-convergence angles of 20 and 28 mrad (probe sizes of 0.8 and 1.0 Å) and collection angles for HAADF images of 75–310 mrad were used. The out-of-plane elemental intermixing at both TiN/TaO_x and TaO_x/W interfaces increased as the annealing temperature increased, as observed by the STEM-HAADF imaging profiles and STEM-EDX chemical investigations (Figure 40). For the as-deposited sample, Figure 40d shows that the TiN/TaO_x interface and the TaO_x/W interface had an intermixing width of about 5 nm and 10 nm, respectively. Samples after annealing at 350 °C, shows that the intermixing at both interfaces increased and the presence of Ta in the nominal W layer suggests Ta diffusion into the W layer, see Figure 40e. An additional (W, Ta)O_x layer over the nominal W layer was observed and the W layer thickness (~20 nm) was less than expected.

For the sample after annealing at 500 °C, the elemental intermixing was the highest at both interfaces. The TiN layer was found to be completely oxidized, which was also indicated by the high resistivity of the TiN layer at this temperature.

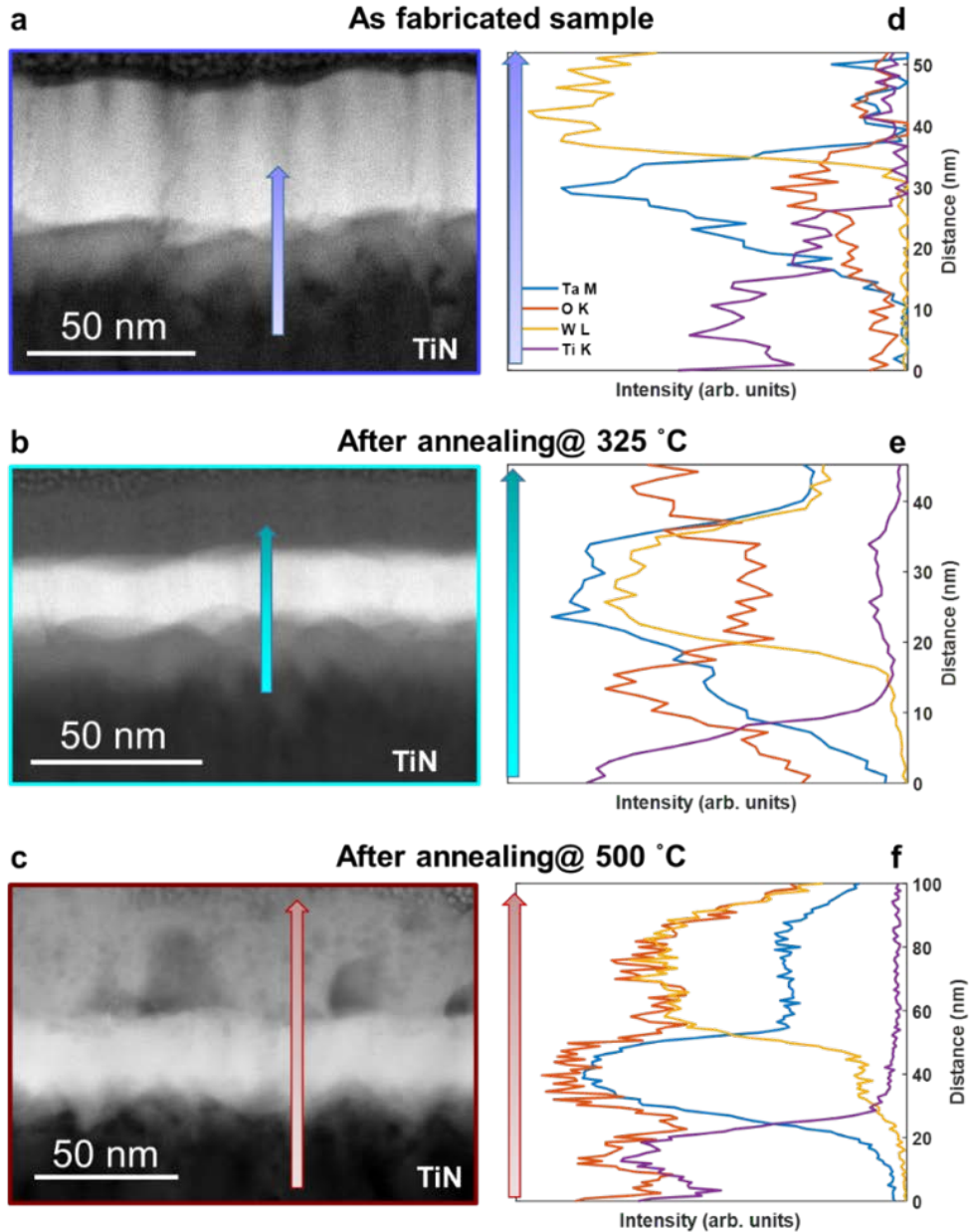


Figure 40 STEM investigations of TiN/TaO_x/W interfaces annealed under different conditions. Representative STEM-HAADF images of (a) an as-fabricated device, (b) a device after annealing at 325 °C, and (c) a device after annealing at 500 °C. The arrows on the STEM-HAADF images indicate both the growth direction and the EDX line scan positions acquired across the interfaces of (d) an as-fabricated device, (e) a device after annealing at 325 °C, and (f) a device after annealing at 500 °C. The elemental profiles in (d-f) are obtained using Ta M (blue), O K (orange), W L (yellow) and Ti K (purple) X-ray emission lines. The figures are from Appendix B Article II.

Summary

1. Post-deposition annealing can trigger the resistive switching behaviours inside the initially non-switching TiN/TaO_x/W devices and two annealing methods were carried out.
2. For the annealing temperatures $T \leq 300$ °C, the devices initial resistances kept stable and showed no resistive switching behaviour after annealing using both annealing methods.
3. For the annealing temperatures 300 °C $\leq T \leq 400$ °C, the devices initial resistances increased from about 5.6 k Ω to about 10^3 k Ω and the resistive switching behaviours were triggered after the annealing process using method 2. As indicated by XPS depth profiling, the TaO_x layer became more stoichiometric after annealing, which contributed to the emergence of the resistive switching behaviour, compared to the as-deposited sample. The resistivity of both TiN and W electrodes kept stable after annealing.
4. For the annealing temperatures $T > 400$ °C, the TaO_x became more stoichiometric and TiN bottom electrode became fully oxidized and insulating. As the TiN layer became insulating, the devices were non-switchable, indicating that both the stoichiometry and the TaO_x/electrode interface played an essential role in triggering resistive switching behaviour.

Chapter 5

Effect of Strain on the Device Behaviour

The RRAM devices have a potential application in flexible electronics, such as roll-up displays and wearable devices. Exploring the feasibility of printable, foldable and stretchable devices and the effect of strain on the device is of particular interest and is a key parameter for tuning the functionality of the devices.[149] RRAM devices have been reported to be fabricated on many different flexible or foldable substrates, such as paper,[150], [151] plastic,[152]–[155] mica,[156] water-soluble substrates[157] polyimide,[158]–[160] polyethersulfone (PES),[161]–[166] polyethylene-naphthalate (PEN),[22] poly-ethylene-terephthalate (PET),[167]–[174] parylene,[175] and polydimethylsiloxane (PDMS).[176]

Three types of strain can be applied to an RRAM device: (1) mechanical deformation,[164] (2) interface mismatch induced strain (heterostructure interfaces [149], [177], [178] and weak points at grain boundaries [179]), and (3) doping induced strain.[180] The strain induced by the

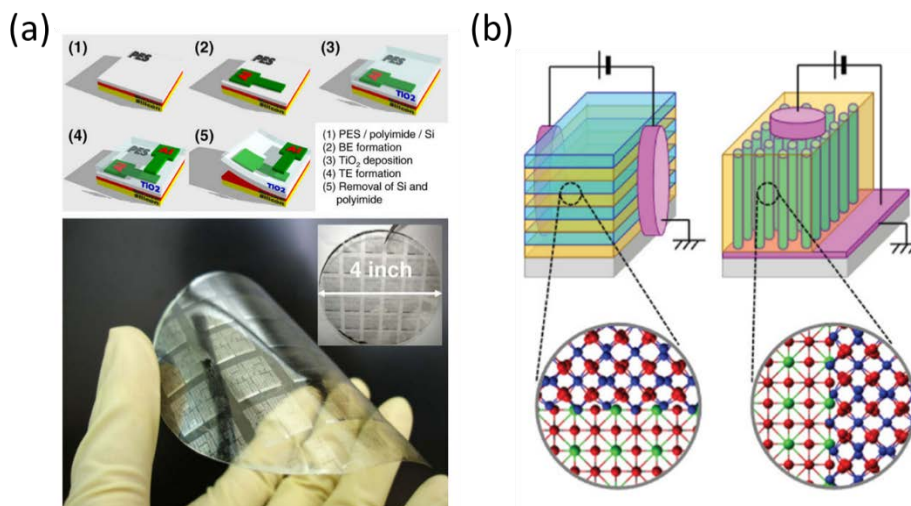


Figure 41 Two sources of stress applied to RRAM device: (a) the fabrication process flow of Al/TiO₂/Al structured RRAM on polyethersulfone (PES) and a photograph of the mechanical bending stress applied to RRAM devices; (b) illustration of stress introduced by heterostructure interfaces inside RRAM device. The figures are adapted from Ref. [149], [164].

mechanical deformation [164] and at the heterostructure interfaces [149] is shown in Figure 41a and b, respectively. Figure 41a shows the Al/TiO₂/Al structured RRAM fabricated on polyethersulfone (PES) and the sample is under strain induced by the mechanical bending.[164] Figure 41b shows schematic illustrations of the RRAM devices with multilayer films and nano scaffold film as the resistive switching layer. The strain can be induced at the lateral or the vertical hetero-interfaces of dissimilar crystal structures.[149] Doping can also induce strain by modifying the lattice with elements of different sizes, since the effect of doping induced strain on the RRAM devices are less reported, the doping induced strain will not be discussed here.[181]–[194]

5.1 The Effect of Strain on Metal Oxide Based RRAM Devices

The mechanical deformation using bending is the most widely reported strain applied to the RRAM devices. Under repetitive bending, the strain often results in detachment of the films or formation of cracks in the metal oxide-based RRAM devices.[163], [170], [195] In ITO/ZnO/ITO RRAM fabricated on PES substrate, after bending for 10 times at a bending radius of 20 mm, both the LRS and HRS of the device increased due to the cracking of the ITO bottom electrode layer. It was observed that the crack density increased as the strain increased.[172] The number of bending cycles was improved from 10 to 10⁴ cycles for the PES/ITO/ZnO/ITO RRAM by inserting a ductile Ag layer between the ITO bottom electrode and the ZnO layer (Figure 42a). A record of 10⁵ bending cycles was measured for the Ni/GeO/HfON/TaN system and both the LRS and HRS remained stable after 10⁵ bending cycles (Figure 42 b).[159] Other works [151], [156], [168], [170], [172], [195]–[197] also reported the mechanical robustness of the device by showing stable resistance states after many cycles of bending, yet currently, the maximum bending cycles is still limited to 10⁵.

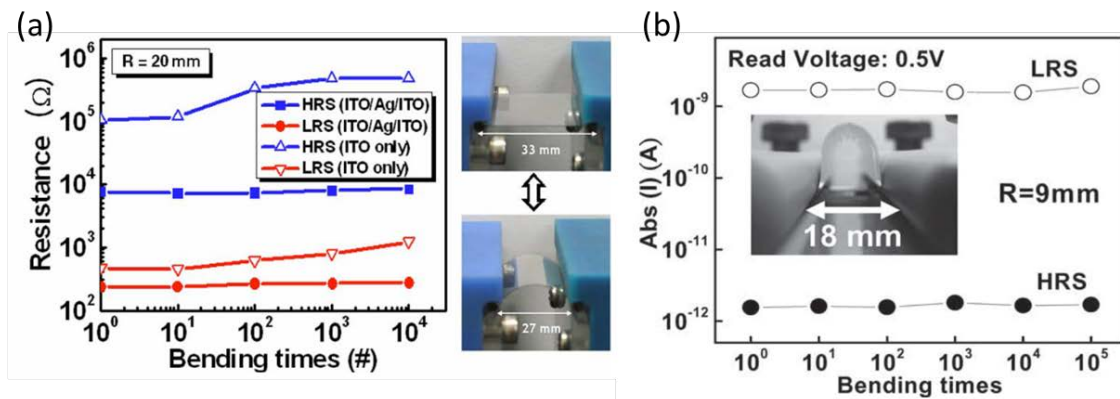


Figure 42 Mechanical endurance of RRAM devices. (a) ITO/ZnO/ITO structured RRAM devices showed severe resistance degradation when exceeding 10 times of bending due to the bottom electrode cracking. Improved mechanical endurance was achieved by inserting Ag into the bottom electrode. (b) TaN/HfON/GeO/Ni structured RRAM device showed robust LRS and HRS after 10⁵ times of bending. The figures are from Ref. [159], [163]

Another source of strain comes from the interface mismatch between the layers, which causes lattice compressive or tensile strain depending on the type of materials used. [198], [199] These studies focused mainly on the tuning of the ionic conductivity at such interfaces.[200]–[203] S.

Schweiger et al. [204] reported an RRAM device based on $Gd_{0.1}Ce_{0.9}O_{2-\delta}/Er_2O_3$ heterostructure as shown in Figure 43a. A compressive strain is induced in $Gd_{0.1}Ce_{0.9}O_{2-\delta}$ by the lattice mismatch between the $Gd_{0.1}Ce_{0.9}O_{2-\delta}$ and the Er_2O_3 interface as shown in Figure 43b.[178], [204] As the number of interfaces within a constant total thickness increased, the compressive strain in the $Gd_{0.1}Ce_{0.9}O_{2-\delta}$ increased from unstrained state (single layer $Gd_{0.1}Ce_{0.9}O_{2-\delta}$) to -1.26% (60 interfaces). As the strain increased, the concentration of oxygen vacancies and the electrons increased. The mobility of the oxygen vacancies decreased in the Er_2O_3 layer and the mobility of electrons increased. The effect of concentration and the mobility of oxygen vacancies and the electrons together decreased the LRS as the strain increased and resulted in an increase of the HRS/LRS ratio by one order of magnitude as shown in Figure 43c.

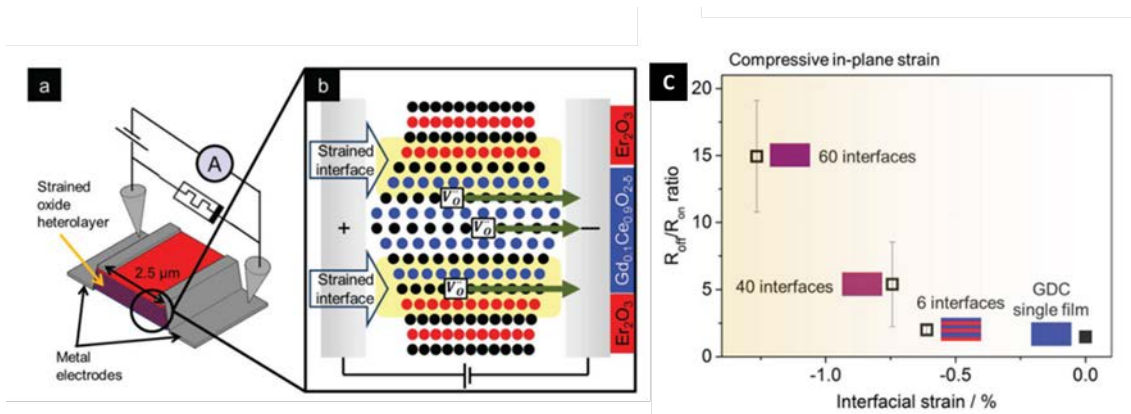


Figure 43 (a) a schematic illustration of the device composed of $Gd_{0.1}Ce_{0.9}O_{2-\delta}/Er_2O_3$ heterostructures and the testing set up, (b) schematic view of one of the $Gd_{0.1}Ce_{0.9}O_{2-\delta}/Er_2O_3$ interface showing the lattice mismatch induced strain and the conduction channels of oxygen vacancies V_o , (c) the HRS/LRS ratio under different strain conditions. The figures are from Ref.[204].

5.2 The Effect of Strain on the TaO_x Thin Film and the TaO_x Based RRAM Devices

For the TaO_x , in particular, Y.Jia et al. reported the change in the electrical properties induced by the strain.[205] The hexagonal δ -phase Ta_2O_5 showed a large change in the resistance and capacitance under mechanical strain. In that work, a hexagonal δ -phase Ta_2O_5 thin film deposited on Si was glued to an Ag/PMN-PT/Ag piezoelectric stack that imposes strain to the thin film using an applied electrical field. Two Al circular electrodes (3 mm thick) were deposited on to the Ta_2O_5 thin film with a 4 mm spacing between the electrodes to characterize its resistance change under strain (Figure 44).

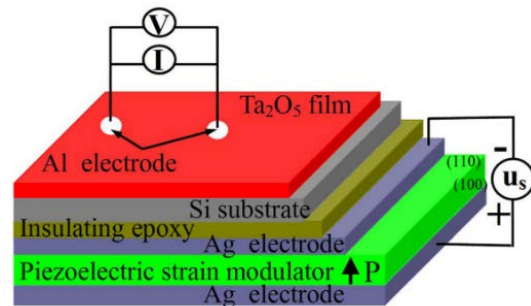


Figure 44 The geometry of the strain modulation of the Ta_2O_5 film by the converse piezoelectric effect. The arrow in the PMN-PT layer represents the poling direction. The figure is from Ref. [205].

Table 6 gives a detailed material and deposition parameters of the reported δ -phase Ta_2O_5 thin film.

Table 6 Properties of the hexagonal δ -phase Ta_2O_5 in Ref. [205].

Crystalline phase	Hexagonal structure δ - Ta_2O_5
Lattice constant	$a=6.2 \text{ \AA}$, $b=3.66 \text{ \AA}$, $c=3.89 \text{ \AA}$
Substrate	(001)-oriented Si, 500 μm in thickness
Deposition method	DC magnetron sputtering
Deposition conditions	Ar ₂ and O ₂ , 0.5 Pa (0.005 mbar) Deposition temperature unknown
Film thickness	200 nm
Post deposition treatment	In situ annealing, 700 °C, 30 min

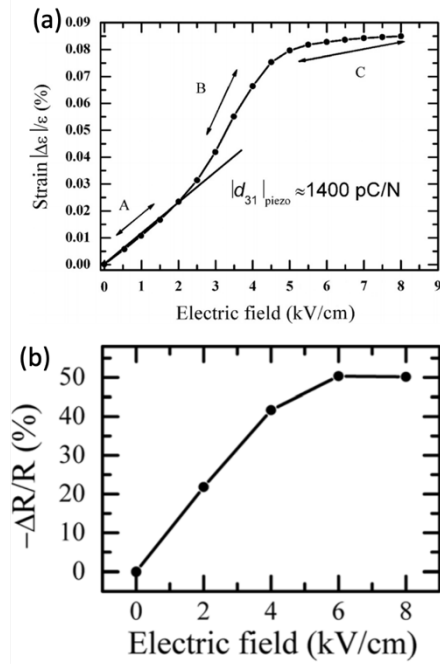


Figure 45 The relationship between (a) electrical field U_s and induced transverse strain in whole film stack, and (b) electrical field U_s and the relative resistance change in Ta_2O_5 thin film (200 nm). The figure is from Ref. [205].

By applying an electric field U_s to the Ag/PMN-PT/Ag piezoelectric stack, a strain is induced to the whole film stack. Three steps of strain change were observed in the piezoelectric stack: (1) In stage A ($0 \text{ V/mm} < U_s < 250 \text{ V/mm}$), the PMN-PT undergoes a rhombohedral lattice distortion; (2) In stage B ($250 \text{ V/mm} < U_s < 500 \text{ V/mm}$), the PMN-PT undergoes a rhombohedral to a tetragonal phase transition; (3) In stage C ($500 \text{ V/mm} < U_s < 800 \text{ V/mm}$), the strain in the electric-field induced tetragonal phase of PMN-PT is saturated. These three steps of strain change under the electrical field is as shown in Figure 45a. The maximum strain induced in the Ta_2O_5 layer is 0.09% which resulted in a 50% resistance change as shown in Figure 45b.

Another study by C. Chou et al. reported that in Ti/TiO₂/TaO_x/Ta RRAM, both the LRS and HRS increased by almost an order of magnitude as the bending radius decreased from a flat initial state (infinite bending radius) to 10 mm.[160] Figure 46a shows a schematic illustration of the device structure, Figure 46b shows the mechanical bending of the devices, and Figure 46c shows the resistance change of the devices under different strain conditions.

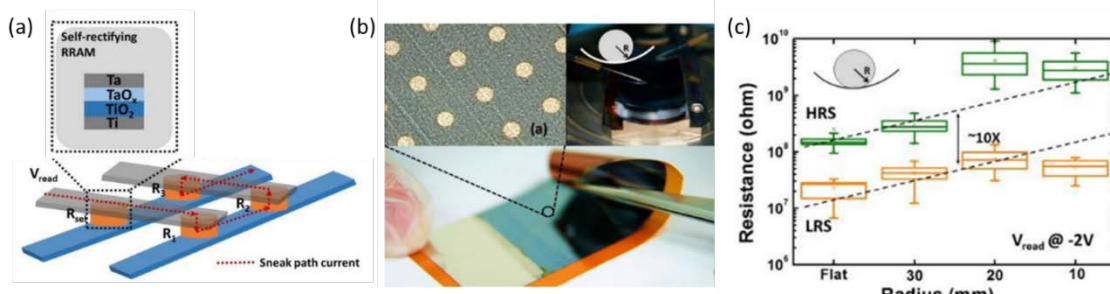


Figure 46 (a) Schematic illustration of the device structure. (b) Image of fabricated RRAM devices, electrical measurement setup and flexible RRAM device. (c) Resistance evolution as the bending radius decreased. The figure is from Ref. [160].

Since the strain has already been shown to strongly affect both the mobility of the oxygen vacancies V_o in metal oxide materials and the resistance in TaO_x thin films and TaO_x based RRAM, it is of interest to further investigate the effect of strain on the TaO_x-based RRAM device behaviour by in-situ materials characterization. Aiming at this purpose, I, therefore, studied the strain effect on the Pt/TaO_x/Ta RRAM fabricated on 50 μm thick Si substrates.

A mechanical strainer with a cylinder to introduce strain to the devices was used in my experiments. Figure 47a is a picture of the sample under strain on the mechanical strainer and Figure 47b shows a schematic illustration of a simplified mechanical strainer and the sample. The sample under test is fixed by two clamps at both sides. By turning the screw under the cylinder, the height of the cylinder can be adjusted, which induces a mechanical deformation of the sample and introduce strain.

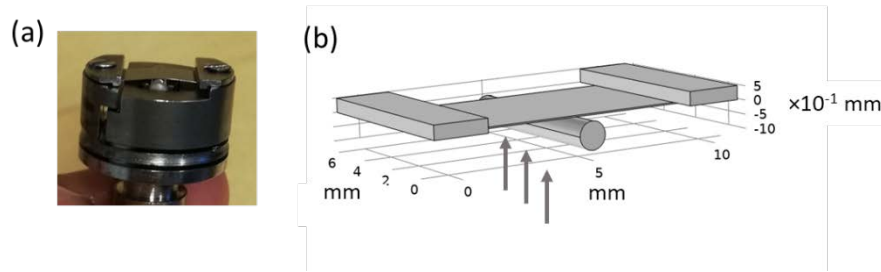


Figure 47 (a) A picture of the mechanical strainer with a 50 μm thick Si substrate inserted. (b) A schematic illustration of the strainer and the 50 μm thick Si substrate. The arrows indicate the cylinder movement direction.

The substrate deformation was characterized by a laser profilometer (cyberTECHNOLOGIES, GmbH). The profilometer scans the morphology of the sample surface with a measurement range of 600 μm, a spot size of 1.8 μm, and a Z-resolution of 0.01 μm. Both the deformation of the 525 μm thick Si substrates (Appendix A, Figure 57) and the 50 μm thick Si substrates were measured. The 50 μm thick Si substrates were used in my strain related experiments for they are more flexible than the thick Si substrates.

Figure 48a and c show the mechanical deformation of 50 μm Si under no strain and the mechanical deformation of 50 μm Si under maximum strain. The maximum height displacement, h , in the 50 μm Si substrates induced by the strainer is $h = 325.9 \pm 10.9 \mu\text{m}$ which corresponds to the maximum strain condition with a strain of 0.14%. The sample length projection d on the XY plane is $d = 6.8 \text{ mm}$. The bending radius R of the substrate can be calculated by solving the equation

$$R^2 = (d/2)^2 + (R - h)^2, \quad (5)$$

with $R = 17.9 \text{ mm}$. According to [172], the strain ε induced can be simply estimated by

$$\varepsilon = t/2R, \quad (6)$$

where t is the thickness of the substrate and R is the bending radius. The maximum strain ε we can apply to the 50 μm thick Si substrate can be estimated as $\varepsilon = 0.14\%$. As indicated in [205], the maximum strain induced by a piezoelectric stack was 0.09%, which means our method can induce large enough strain inside the TaO_x based RRAM fabricated on 50 μm Si.

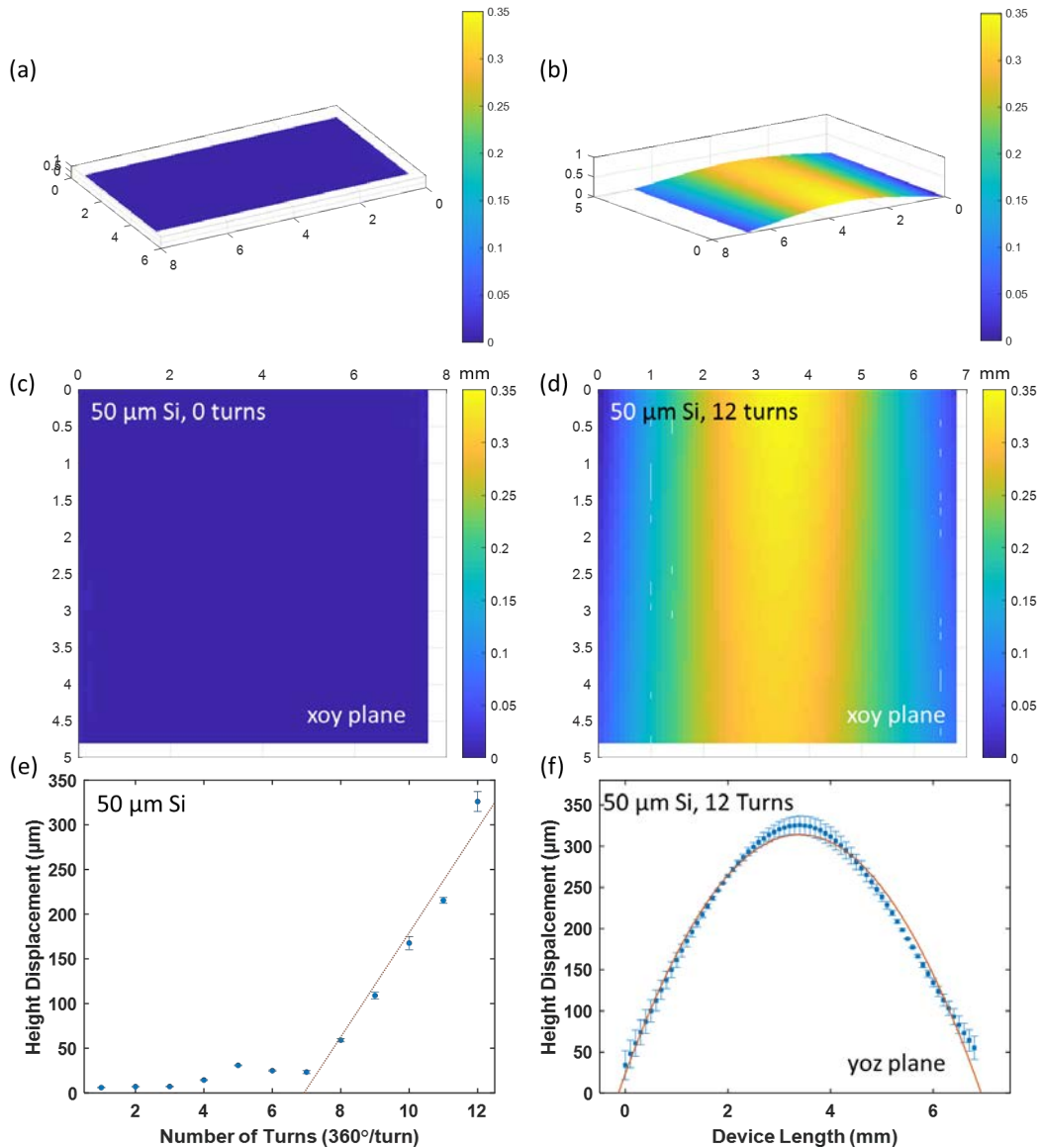


Figure 48 The mechanical deformation of 50 μm thick Si under strain. (a) and (c) No deformation of the Si substrate, (b) and (d) the maximum deformation of the Si substrate, (e) the relationship between the number of turns of the strew in the strainer and the maximum height deformation in Si, (f) the yoz plane view of the Si under maximum strain. The 50 μm Si did not break under the maximum strain which the mechanical strainer can induce.

A COMSOL model for the 50 μm Si substrate under strain was built. A block of 10 mm \times 5 mm \times 50 μm was used to represent the Si substrate. The strainer was simplified as the boundary conditions. Two clamps with a distance of 1.5 mm from the substrate edges were set as fixed

constraints (red lines indicated in Figure 49). The left bottom corner and right upper corner (blue circles labelled in Figure 49) of the clamps were set with a prescribed displacement of 0 μm . The cylinder is represented by the prescribed displacement at the centre of the substrate (blue dash line as indicated in Figure 49). The Young's modulus is defined as the

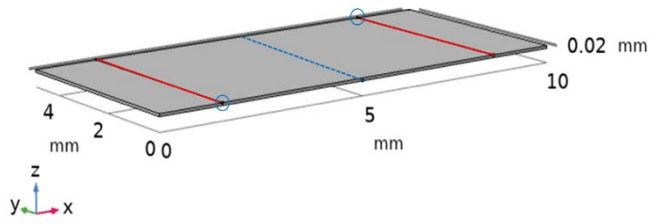


Figure 49 A simplified strainer model in the COMSOL software.

relationship between the force per unit area (stress) and proportional deformation (strain) in a material in the linear elasticity regime of uniaxial deformation. The Young's modulus of Si used in

this model is 1.7×10^{11} Pa which is the embedded value of Si in the COMSOL software.

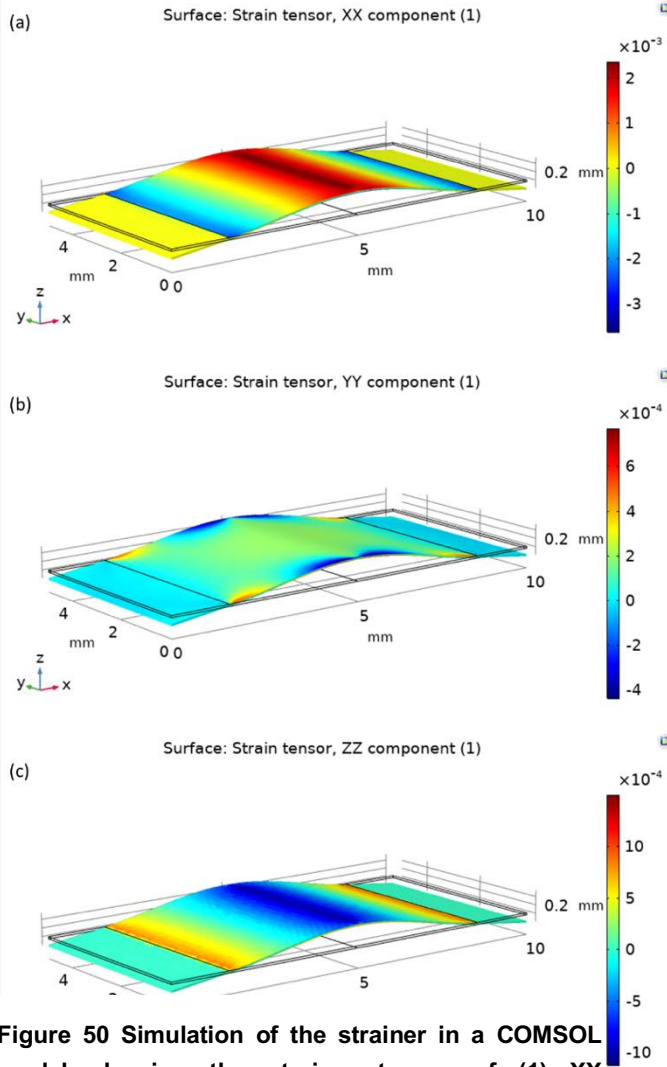


Figure 50 Simulation of the strainer in a COMSOL model showing the strainer tensor of (1) XX component, (b) YY component, and (c) ZZ component.

By setting the prescribed displacement of the cylinder to different values, the strain induced in the substrate can be simulated. Figure 50a to c show the XX, YY, ZZ strain components induced in the substrate under maximum deformation. The maximum strain induced in the substrate is the XX component with a strain of about 0.2%, which is similar to the previously estimated value of 0.14%.

For the strain experiments, the Si/Ti/Pt/TaO_x/Ta structured devices were fabricated on 50 μm Si substrates. The experimental fabrication of these films was carried out using sputtering at Forschungszentrum Jülich where Prof. Regina Dittmann's group is a worldwide leading group of RRAM. The deposition conditions for the layers are described in Table 7.

Table 7 Sputtering deposition conditions for each layer in Si/Ti/Pt/TaO_x/Ta structured devices.

Material	Thickness (nm)	Deposition Condition
Ti (adhesion layer)	5	30% Ar (60 sccm), 2.33×10^{-2} mbar, 299 W, 265 V, DC
Pt (bottom electrode)	100	30% Ar (60 sccm), 1.44×10^{-2} mbar, 375W, 330 V, DC
TaO _x (resistive switching layer)	7, 14, or 25	23% Ar (46 sccm), 7% O ₂ (14 sccm), 2.2×10^{-2} mbar, RF
Ta (top electrode)	14, 28, or 50	30% Ar (60 sccm), 2.3×10^{-2} mbar, RF
Pt (protective layer)	50	30% Ar (60 sccm), 1.44×10^{-2} mbar, 375W, 330 V, DC

Different TaO_x thin films (7 nm, 14 nm, and 25 nm) were used. The top Ta electrode thickness was chosen in the way to be twice the thickness of the TaO_x layer. This is because the Forming voltage was reported to decrease as the Ta electrode thickness increase and the decrease of the Forming voltage saturated when the Ta electrode thickness is twice of the TaO_x layer.[206] Figure 51a shows the device configuration with an example of different thickness of layers. Figure 51b shows a relationship between the Forming voltages and the initial resistances. Typical *I-V* curves of the devices were shown in Appendix A, Figure 58.

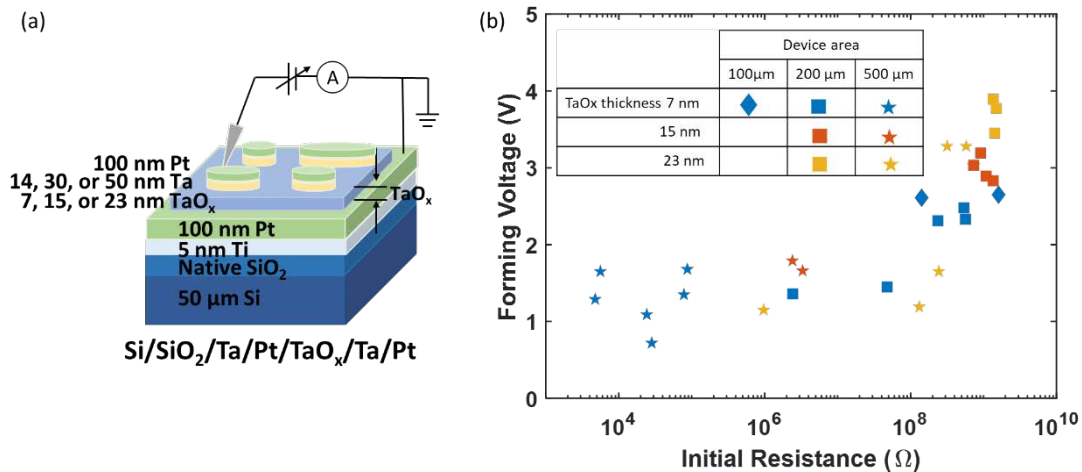


Figure 51 (a) A schematic illustration of the Pt/TaO_x/Ta structured RRAM device, (b) the forming voltages and the initial resistances of devices with different TaO_x thicknesses.

For the devices under no strain condition, both the initial resistances and the Forming voltages increased (decreased) as the TaO_x layer thickness increased (the device area increased). Figure 52a shows that the initial resistances of 200 μm devices increases from about $10^8 \Omega$ to $10^9 \Omega$ as the TaO_x layer thickness increases from 7 nm to 23 nm. Figure 52b shows that the Forming voltages of 200 μm devices increase from about 2 V to 3.5 V as the TaO_x layer thickness increases from 7 nm to 23 nm. This is in agreement with the report in the literature [206] where the forming voltage of Pt/TaO_x/Ta devices increases from about 2 V to 3V as the TaO_x layer thickness increases from 7 nm to 13 nm in a $2 \mu\text{m} \times 2 \mu\text{m}$ Pt/TaO_x/Ta devices. A similar trend of increased Forming voltages and initial resistances as the TaO_x thickness increase was also observed in 500 μm devices as shown in Figure 53a and b, respectively. For both 200 μm and 500 μm devices,

the LRS was at $10^3 \Omega$ magnitude and the HRS were at $10^4 \Omega$ magnitude, independent of the TaO_x thickness, as shown in Figure 52a (200 μm) and Figure 53a (500 μm). The SET and RESET voltages for both 200 μm devices and 500 μm devices also showed no obvious dependency on the TaO_x layer thickness, as shown in Figure 52b (200 μm) and Figure 53b (500 μm).

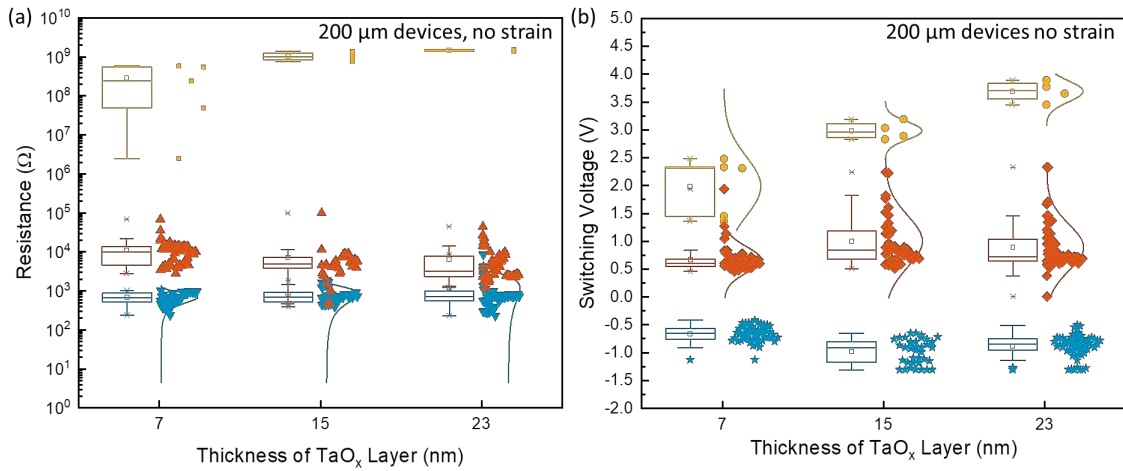


Figure 52 Device size of 200 μm in diameter: (1) the initial resistances (yellow), LRS (light red), and HRS (blue), (b) the Forming voltages (yellow), SET voltages (light red), and RESET voltages (blue) for devices with different TaO_x thicknesses.

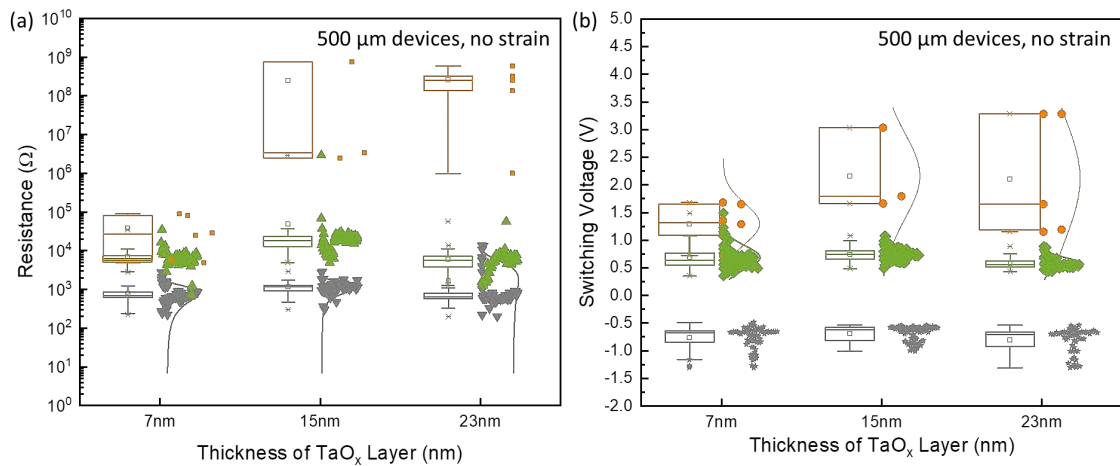


Figure 53 Device size of 500 μm in diameter: (1) the initial resistances (orange), LRS (green), HRS (grey), (b) the Forming voltages (orange), SET voltages (green), and RESET voltages (grey) for devices with different TaO_x thicknesses.

For devices under maximum strain condition, the effect of strain was tested in 500 μm diameter devices with 7 nm thick TaO_x resistive layer. Comparison of the resistances and switching voltages under no strain and maximum strain conditions were made. Preliminary results indicate that the initial resistances increased under the strain condition and the LRS and HRS showed no dependency on the strain effect as shown in Figure 54a. The Forming, SET, and RESET voltages

showed no obvious change under no strain and the maximum strain conditions as shown in Figure 54b. However, due to the stochastic nature of the RRAM devices, additional experiments are needed to be carried out before any concrete conclusions can be drawn out of these experiments.

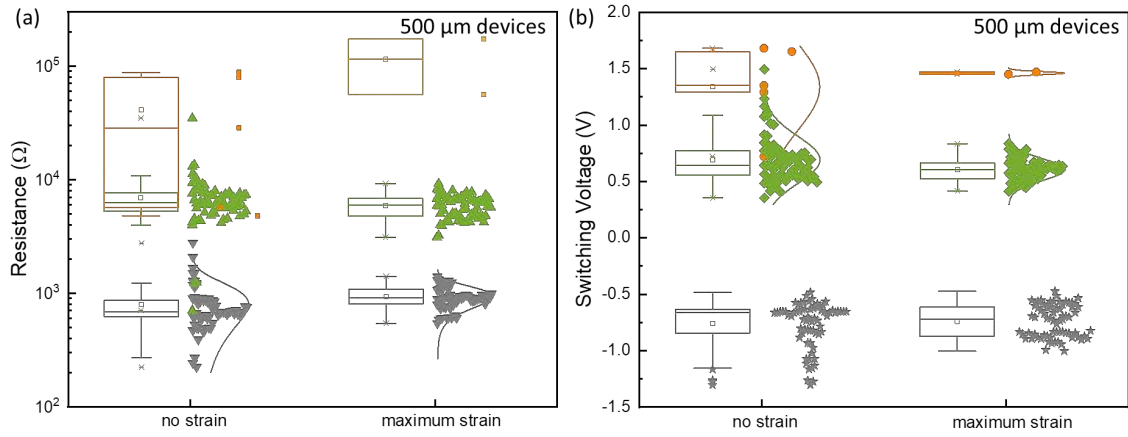


Figure 54 The comparison between no strain and maximum strain conditions on Pt/TaO_x (7nm)/Ta devices with 500 μm diameters: (a) the distribution of the initial resistances (orange), LRS (green), and HRS (grey), (b) the distribution of the Forming voltages (orange), SET voltages (green), and RESET voltages (grey).

Summary

1. The deformation of the 50 μm Si substrates induced by the mechanical strainer was characterized by using a laser profilometer and the maximum height displacement was $325.9 \pm 10.9 \mu\text{m}$, which corresponds to an estimated maximum strain condition with a strain of 0.14%.
2. A simplified model of the sample under strain was simulated by using COMSOL software and the maximum strain component was simulated to be about 0.2%.
3. Pt/TaO_x/Ta devices were fabricated on 50 μm Si substrates. Different TaO_x layer thickness of 7 nm, 15 nm, and 23 nm with Ta top electrode layer thickness of double the thickness of the TaO_x layer were used.
4. For the devices under no strain condition, both the initial resistances and the Forming voltages increased (decreased) as the TaO_x layer thickness increased (the device area increased).
5. For the devices under maximum strain condition, the initial resistances increased and the LRS and HRS showed no obvious change. The Forming, SET, and RESET voltages showed no obvious change under strain. However, due to the stochastic nature of the RRAM devices, additional experiments are needed to be carried out before any concrete conclusions can be drawn out of these experiments.

Chapter 6

Conclusions

This thesis focused on the electrical properties of the TaO_x materials and the TaO_x based RRAM devices during the fabrication, post-fabrication and under external strain. Three main areas of research were reported in this thesis and the conclusions are:

- (1) By controlling the deposition parameters during the pulsed laser deposition (PLD), the stoichiometry of the TaO_x was controlled by the deposition conditions, such as the oxygen pressure and the deposition temperature. Both the stoichiometry and the resistivity of the TaO_x thin films increased as the oxygen pressure increased. A direct link between the deposition condition and the electrical resistivity was given. In TiN/TaO_x/W (W is the probe tip) devices, all the TaO_x thin films deposited under different oxygen pressures showed resistive switching. Both the SET and RESET voltages showed no dependency on the oxygen pressures during PLD. The value of the low state resistance (LRS) kept almost the same for different TaO_x thin films whereas the value of the high resistance state (HRS) increased as the oxygen pressure increased. In TiN/TaO_x/W (sputtered W thin film) devices, the TaO_x deposited at oxygen pressures $P_{O_2} < 5 \times 10^{-3}$ mbar showed Ohmic *I-V* relationship without any resistive switching behaviour. The TaO_x deposited at oxygen pressures $P_{O_2} \geq 5 \times 10^{-3}$ mbar showed resistive switching behaviour. The results show that the amount of oxygen content is critical for the triggering of the resistive switching behaviour.
- (2) By post thermal annealing the TiN/TaO_x/W (sputtered W thin film) devices (TaO_x deposited at an oxygen pressure of $P_{O_2} = 2 \times 10^{-3}$ mbar) in the air between 325 °C and 400 °C for 4 hr, the resistive switching behaviour was successfully triggered in the devices with no switching behaviour at the beginning.
- (3) The effect of strain on the Pt/TaO_x/Ta devices on 50 μm Si substrates was studied. The hypothesis is that the strain may influence the mobility of the oxygen vacancies, which are also the ions contributing to the filament formed in the Pt/TaO_x/Ta VCM RRAM. Influencing the mobility may be used as a tuning knob to control the switching parameters change. Primary results show that the strain has an effect on the Forming process but further tests and investigations are needed to be conducted due to the stochastic nature of the devices.

Chapter 7

Outlook

The effect of external stimuli on the RRAM devices represent one of most exciting and emerging areas of scientific interest with possible commercial applications. Strain is an interesting external stimuli which can either be induced by external stress or by inducing strain via heterostructures interfaces. Preliminary experiments were carried out during my work to study the strain effect on TaO_x based RRAM devices by using voltage sweep external electrical field. It is early to conclude that but the Forming process showed some dependence on the strain effect. More devices could be tested for a better understanding of the stochastic nature of the resistive switching behaviour under strain. Further in-situ characterizations of the TaO_x materials change by the Raman spectroscopy or XPS under strain can be a good way to interpret and understand the effect of strain on the resistive switching. Achieving this can provide new insights into the switching mechanisms of RRAM devices and can lead to new and yet unexplored properties for future memory and computing technologies.

Another interesting possibility for future work will be to conduct a dedicated experiment to study the crystallization of the amorphous TaO_x films and the effect on the resistive switching. Since most TaO_x based RRAM devices are amorphous the effect of crystallinity of TaO_x on the resistive switching behaviours would important both from fundamental point of view but also commercially.

The effect of electrode geometry and position can be another interesting topic to study in the future. It would be interesting to study the effect of multiple electrodes on one single device. This will enable understanding the role of position of the electrodes with respect to each other and with respect to the counter electrodes on the device states.

Bibliography

- [1] Y. Arimoto and H. Ishiwara, "Current Status of Ferroelectric Random-Access Memory," *MRS Bull.*, vol. 29, no. 11, pp. 823–828, 2004.
- [2] H. Ishiwara, M. Okuyama, and Y. Arimoto, *Ferroelectric random access memories: fundamentals and applications*, vol. 93. Springer Science & Business Media, 2004.
- [3] Z. H. U. Jian-Gang, "Magnetoresistive random access memory: The path to competitiveness and scalability," *Proc. IEEE*, vol. 96, no. 11, pp. 1786–1798, 2008. DOI:10.1109/JPROC.2008.2004313.
- [4] D. Apalkov, B. Dieny, and J. M. Slaughter, "Magnetoresistive Random Access Memory," *Proc. IEEE*, vol. 104, no. 10, pp. 1796–1830, 2016. DOI:10.1109/JPROC.2016.2590142.
- [5] M. Salinga, B. Kersting, I. Ronneberger, V. P. Jonnalagadda, X. T. Vu, M. Le Gallo, I. Giannopoulos, O. Cojocar-Mirédin, R. Mазzarello, and A. Sebastian, "Monatomic phase change memory," *Nat. Mater.*, vol. 17, no. 8, pp. 681–685, 2018. DOI:10.1038/s41563-018-0110-9.
- [6] G. W. Burr, M. J. BrightSky, A. Sebastian, H. Y. Cheng, J. Y. Wu, S. Kim, N. E. Sosa, N. Papandreou, H. L. Lung, H. Pozidis, E. Eleftheriou, and C. H. Lam, "Recent Progress in Phase-Change Memory Technology," *IEEE J. Emerg. Sel. Top. Circuits Syst.*, vol. 6, no. 2, pp. 146–162, 2016. DOI:10.1109/JETCAS.2016.2547718.
- [7] B. Mohammad, M. A. Jaoude, V. Kumar, D. M. Al Homouz, H. A. Nahla, M. Al-Qutayri, and N. Christoforou, "State of the art of metal oxide memristor devices," *Nanotechnol. Rev.*, vol. 5, no. 3, pp. 311–329, 2016. DOI:10.1515/ntrev-2015-0029.
- [8] H. S. P. Wong, H. Y. Lee, S. Yu, Y. S. Chen, Y. Wu, P. S. Chen, B. Lee, F. T. Chen, and M. J. Tsai, "Metal-oxide RRAM," *Proc. IEEE*, vol. 100, no. 6, pp. 1951–1970, 2012. DOI:10.1109/JPROC.2012.2190369.
- [9] Y. Li, S. Long, Y. Liu, C. Hu, J. Teng, Q. Liu, H. Lv, J. Suñé, and M. Liu, "Conductance Quantization in Resistive Random Access Memory," *Nanoscale Res. Lett.*, vol. 10, no. 1, 2015. DOI:10.1186/s11671-015-1118-6.
- [10] R. Waser, R. Dittmann, C. Staikov, and K. Szot, "Redox-based resistive switching memories nanoionic mechanisms, prospects, and challenges," *Adv. Mater.*, vol. 21, no. 25–26, pp. 2632–2663, 2009. DOI:10.1002/adma.200900375.
- [11] J. S. Meena, S. M. Sze, U. Chand, and T. Y. Tseng, "Overview of emerging nonvolatile memory technologies," *Nanoscale Res. Lett.*, vol. 9, no. 1, pp. 1–33, 2014. DOI:10.1186/1556-276X-9-526.
- [12] H. S. Mram, P. K. Amiri, Z. M. Zeng, P. Upadhyaya, G. Rowlands, H. Zhao, I. N. Krivorotov, J. Wang, H. W. Jiang, J. A. Katine, S. Member, J. Langer, K. Galatsis, and K. L. Wang, "Low Write-Energy Magnetic Tunnel Junctions for," vol. 32, no. 1, pp. 2010–2012, 2011.
- [13] S. W. Zheng, J. S. Bi, K. Xi, J. Liu, M. Liu, and L. Luo, "A 28 nm full-margin, high-reliability, and ultra-low-power consumption sense amplifier for STT-MRAM," *Microelectron. Reliab.*, vol. 100–101, no. May, 2019. DOI:10.1016/j.microrel.2019.113465.
- [14] M. Qazi, A. Amerasekera, and A. P. Chandrakasan, "CMOS for Nonvolatile Processing in Digital Systems," vol. 49, no. 1, pp. 202–211, 2014.
- [15] M. Qazi, M. Clinton, S. Bartling, and A. P. Chandrakasan, "A low-voltage 1Mb FeRAM in 0.13 μ m CMOS featuring time-to-digital sensing for expanded operating margin in scaled CMOS," *Dig. Tech. Pap. - IEEE Int. Solid-State Circuits Conf.*, pp. 208–209, 2011. DOI:10.1109/ISSCC.2011.5746285.
- [16] S. Pi, C. Li, H. Jiang, W. Xia, H. Xin, J. J. Yang, and Q. Xia, "Memristor crossbar arrays with 6-nm half-pitch and 2-nm critical dimension," *Nat. Nanotechnol.*, vol. 14, no. 1, pp. 35–39, 2018. DOI:10.1038/s41565-018-0302-0.

- [17] A. C. Torrezan, J. P. Strachan, G. Medeiros-Ribeiro, and R. S. Williams, "Sub-nanosecond switching of a tantalum oxide memristor," *Nanotechnology*, vol. 22, no. 48, p. 485203, 2011. DOI:10.1088/0957-4484/22/48/485203.
- [18] C.-W. Hsu, I.-T. Wang, C.-L. Lo, M. Chiang, W. Jang, C.-H. Lin, and T.-H. Hou, "Self-Rectifying Bipolar TaO_x/TiO₂ RRAM with Superior Endurance over 10¹² Cycles for 3D High-Density Storage-Class Memory," in *2013 Symposium on VLSI Circuits (VLSI)*, 2013, pp. T166–T167.
- [19] C. H. Cheng, A. Chin, and F. S. Yeh, "Novel ultra-low power RRAM with good endurance and retention," *Dig. Tech. Pap. - Symp. VLSI Technol.*, no. 5, pp. 85–86, 2010. DOI:10.1109/VLSIT.2010.5556180.
- [20] W. Zhang, Y. Hu, T. Chang, K. Chang, T. Tsai, H. Chen, Y. Su, T. Chu, M. Chen, H. Huang, and W. Su, "An Electronic Synapse Device Based on Solid Electrolyte Resistive Random Access Memory," *IEEE Electron Device Lett.*, vol. 36, no. 8, pp. 772–774, 2015.
- [21] J. Sun, Q. Liu, H. Xie, X. Wu, and F. Xu, "In situ observation of nickel as an oxidizable electrode material for the solid-electrolyte-based resistive random access memory," *Appl. Phys. Lett.*, vol. 102, no. 5, p. 053502, 2013. DOI:10.1063/1.4790837.
- [22] J. Jang, F. Pan, K. Braam, and V. Subramanian, "Resistance switching characteristics of solid electrolyte chalcogenide Ag₂Se nanoparticles for flexible nonvolatile memory applications," *Adv. Mater.*, vol. 24, no. 26, pp. 3573–3576, 2012. DOI:10.1002/adma.201200671.
- [23] B. Lee, H. Bae, H. Seong, D. Lee, H. Park, Y. J. Choi, S. Im, S. O. Kim, Y. Choi, and L. E. E. T. Al, "Direct Observation of a Carbon Filament in Water-Resistant Organic Memory," *ACS Nano*, vol. 9, no. 7, pp. 7306–7313, 2015. DOI:10.1021/acsnano.5b02199.
- [24] H. Ling, M. Yi, M. Nagai, L. Xie, L. Wang, and B. Hu, "Controllable Organic Resistive Switching Achieved by One-Step Integration of Cone-Shaped Contact," *Adv. Mater.*, vol. 29, no. 35, p. 1701333, 2017. DOI:10.1002/adma.201701333.
- [25] Y. Cai, J. Tan, L. Yefan, M. Lin, and R. Huang, "A flexible organic resistance memory device for wearable biomedical applications," *Nanotechnology*, vol. 27, no. 27, p. 275206, 2016.
- [26] D. Kumar, R. Aluguri, U. Chand, and T. Y. Tseng, "Metal oxide resistive switching memory : Materials , properties and switching mechanisms," *Ceram. Int.*, vol. 43, no. May, pp. S547–S556, 2017. DOI:10.1016/j.ceramint.2017.05.289.
- [27] M. Prezioso, F. Merrih-Bayat, B. D. Hoskins, G. C. Adam, K. K. Likharev, and D. B. Strukov, "Training and operation of an integrated neuromorphic network based on metal-oxide memristors," *Nature*, vol. 521, pp. 61–64, 2015. DOI:10.1038/nature14441.
- [28] S. Bagdzevicius, M. Boudard, J. M. Caicedo, L. Rapenne, X. Mescot, R. Rodríguez-Lamas, F. Robaut, J. Santiso, and M. Burriel, "Superposition of interface and volume type resistive switching in perovskite nanoionic devices," *J. Mater. Chem. C*, vol. 7, no. 25, pp. 7580–7592, 2019. DOI:10.1039/c9tc00609e.
- [29] M. Lorenz, M. S. Ramachandra Rao, T. Venkatesan, E. Fortunato, P. Barquinha, R. Branquinho, D. Salgueiro, R. Martins, E. Carlos, A. Liu, F. K. Shan, M. Grundmann, H. Boschker, J. Mukherjee, M. Priyadarshini, N. Dasgupta, D. J. Rogers, ... N. Pryds, "The 2016 oxide electronic materials and oxide interfaces roadmap," *J. Phys. D: Appl. Phys.*, vol. 49, no. 43, 2016. DOI:10.1088/0022-3727/49/43/433001.
- [30] N. Ge, M. X. Zhang, L. Zhang, J. J. Yang, Z. Li, and R. S. Williams, "Electrode-material dependent switching in TaO_x memristors," *Semicond. Sci. Technol.*, vol. 29, no. 10, 2014. DOI:10.1088/0268-1242/29/10/104003.
- [31] A. J. Lohn, J. E. Stevens, P. R. Mickel, and M. J. Marinella, "Optimizing TaO_x memristor performance and consistency within the reactive sputtering 'forbidden region,'" *Appl. Phys. Lett.*, vol. 103, no. 6, 2013. DOI:10.1063/1.4817927.
- [32] X. Chen, J. Feng, and D. Bae, "Drastic reduction of RRAM reset current via plasma oxidization of TaO_x film," *Appl. Surf. Sci.*, vol. 324, pp. 275–279, 2015. DOI:10.1016/j.apsusc.2014.10.133.
- [33] G.-S. Park, Y. B. Kim, S. Y. Park, X. S. Li, S. Heo, M.-J. Lee, M. Chang, J. H. Kwon, M. Kim, U.-I. Chung, R. Dittmann, R. Waser, and K. Kim, "In situ observation of filamentary

- conducting channels in an asymmetric Ta₂O_{5-x}/TaO_{2-x} bilayer structure," *Nat. Commun.*, vol. 4, pp. 1–9, 2013. DOI:10.1038/ncomms3382.
- [34] H. Jeon, J. Park, W. Jang, H. Kim, H. Song, H. Kim, H. Seo, and H. Jeon, "Resistive switching behaviors of Cu/TaO_x/TiN device with combined oxygen vacancy/copper conductive filaments," *Curr. Appl. Phys.*, vol. 15, no. 9, pp. 1005–1009, 2015. DOI:10.1016/j.cap.2015.06.002.
- [35] J. Hong, W. Jang, H. Song, C. Kang, H. Jeon, H. Jeon, J. Park, H. Kim, and H. Kim, "Endurance Improvement due to Rapid Thermal Annealing (RTA) of a TaO_x Thin Film in an Oxygen Ambient," *J. Korean Phys. Soc.*, vol. 66, no. 5, pp. L721–L725, 2015. DOI:10.3938/jkps.66.721.
- [36] L. Goux, A. Fantini, Y. Y. Chen, A. Redolfi, R. Degraeve, and M. Jurczak, "Evidences of Electrode-Controlled Retention Properties in Ta₂O₅-Based Resistive-Switching Memory Cells," *ECS Solid State Lett.*, vol. 3, no. 11, pp. Q79–Q81, 2014. DOI:10.1149/2.0011412ssl.
- [37] L. Goux, J. Y. Kim, B. Magyari-Kope, Y. Nishi, A. Redolfi, and M. Jurczak, "H-treatment impact on conductive-filament formation and stability in Ta₂O₅-based resistive-switching memory cells," *J. Appl. Phys.*, vol. 117, no. 12, 2015. DOI:10.1063/1.4915946.
- [38] W. Jiyong, L. Wootae, P. Sangsu, K. Seonghyun, L. Daeseok, C. Godeuni, C. Euijun, L. Ji Hyun, J. Woo Young, P. Chan Gyung, and H. Hyunsang, "Multi-layer Tunnel Barrier (Ta₂O₅/TaO_x/TiO₂) Engineering for Bipolar RRAM Selector Applications," in *2013 Symposium on VLSI Circuits (VLSI)*, 2013, pp. T168–T169.
- [39] L. Goux, A. Fantini, A. Redolfi, C. Y. Chen, F. F. Shi, R. Degraeve, Y. Y. Chen, T. Witters, G. Groeseneken, and M. Jurczak, "Role of the Ta scavenger electrode in the excellent switching control and reliability of a scalable low-current operated TiN/Ta₂O₅/Ta RRAM device," *Dig. Tech. Pap. - Symp. VLSI Technol.*, vol. 10, no. 2011, pp. 2013–2014, 2014. DOI:10.1109/MLSIT.2014.6894401.
- [40] F. Kurnia, Hadiyawarman, C. U. Jung, R. Jung, and C. Liu, "Composition dependence of unipolar resistance switching in TaO_x thin films," *Phys. Status Solidi - Rapid Res. Lett.*, vol. 5, no. 7, pp. 253–255, 2011. DOI:10.1002/pssr.201105253.
- [41] T. Kundozeroova and G. Stefanovich, "Resistance switching in metal oxide thin films and its memory application," *Appl. Mech. Mater.*, vol. 346, no. Modern Development in Materials, Machinery and Automation, pp. 29–34, 7 pp., 2013. DOI:10.4028/www.scientific.net/AMM.346.29.
- [42] B. Govoreanu, G. S. Kar, Y. Y. Chen, V. Paraschiv, S. Kubicek, A. Fantini, I. P. Radu, L. Goux, S. Clima, R. Degraeve, N. Jossart, O. Richard, T. Vandeweyer, K. Seo, P. Hendrickx, G. Pourtois, H. Bender, ... M. Jurczak, "10×10nm² Hf/HfO_x crossbar resistive RAM with excellent performance, reliability and low-energy operation," in *International Electron Devices Meeting, IEDM*, 2011, pp. 729–732. DOI:10.1109/IEDM.2011.6131652.
- [43] S. Pi, P. Lin, and Q. Xia, "Cross point arrays of 8 nm × 8 nm memristive devices fabricated with nanoimprint lithography," *J. Vac. Sci. Technol. B, Nanotechnol. Microelectron. Mater. Process. Meas. Phenom.*, vol. 31, no. 6, p. 06FA02, 2013. DOI:10.1116/1.4827021.
- [44] N. M. Bashara and P. H. Nielsen, "Memory effects in thin film negative resistance structures," in *Annual Report 1963 Conference on Electrical Insulation*, 1963, pp. 29–32. DOI:10.1109/EIC.1963.7466544.
- [45] B. Hayes, "The memristor," *Am. Sci.*, vol. 99, no. 2, pp. 106–110, 2011. DOI:10.1511/2011.89.106.
- [46] L. O. Chua, "Memristor—The Missing Circuit Element," *IEEE Trans. Circuit Theory*, vol. 18, no. 5, pp. 507–519, 1971. DOI:10.1109/TCT.1971.1083337.
- [47] L. Chua, "Everything you wish to know about memristors but are afraid to ask," *Radioengineering*, vol. 24, no. 2, pp. 319–368, 2015. DOI:10.13164/re.2015.0319.
- [48] P. Mazumder, S. M. Kang, and R. Waser, "Memristors: Devices, models, and applications," *Proc. IEEE*, vol. 100, no. 6, pp. 1911–1919, 2012. DOI:10.1109/JPROC.2012.2190812.

- [49] L. O. Chua and S. M. Kang, "Memristive Devices and Systems," *Proc. IEEE*, vol. 64, no. 2, pp. 209–223, 1976. DOI:10.1109/PROC.1976.10092.
- [50] D. B. Strukov, G. S. Snider, D. R. Stewart, and R. S. Williams, "The missing memristor found," *Nature*, vol. 453, no. 7191, pp. 80–83, 2008. DOI:10.1038/nature08166.
- [51] Y. Xie, "Emerging Memory Technologies - Springer," *Springer*, pp. 43–56, 2014. DOI:10.1007/978-1-4419-9551-3_1.
- [52] B. Hudec, C. W. Hsu, I. T. Wang, W. L. Lai, C. C. Chang, T. Wang, K. Frohlich, C. H. Ho, C. H. Lin, and T. H. Hou, "3D resistive RAM cell design for high-density storage class memory- a review," *Sci. China Inf. Sci.*, vol. 59, no. 6, pp. 1–21, 2016. DOI:10.1007/s11432-016-5566-0.
- [53] Q. Xia and J. J. Yang, "Memristive crossbar arrays for brain-inspired computing," *Nat. Mater.*, vol. 18, no. 4, pp. 309–323, 2019. DOI:10.1038/s41563-019-0291-x.
- [54] M. A. Zidan, J. P. Strachan, and W. D. Lu, "The future of electronics based on memristive systems," *Nat. Electron.*, vol. 1, no. 1, pp. 22–29, 2018. DOI:10.1038/s41928-017-0006-8.
- [55] J. J. Yang, D. B. Strukov, and D. R. Stewart, "Memristive devices for computing," *Nat. Nanotechnol.*, vol. 8, no. 1, pp. 13–24, 2013. DOI:10.1038/nnano.2012.240.
- [56] D. Ielmini and S. Ambrogio, "Emerging neuromorphic devices," *Nanotechnology*, vol. 31, no. 9, 2020. DOI:10.1088/1361-6528/ab554b.
- [57] D.-H. Kwon, K. M. Kim, J. H. Jang, J. M. Jeon, M. H. Lee, G. H. Kim, X.-S. Li, G.-S. Park, B. Lee, S. Han, M. Kim, and C. S. Hwang, "Atomic structure of conducting nanofilaments in TiO₂ resistive switching memory," *Nat. Nanotechnol.*, vol. 5, no. 2, pp. 148–153, 2010. DOI:10.1038/nnano.2009.456.
- [58] U. Celano, L. Goux, A. Belmonte, A. Schulze, K. Opsomer, C. Detavernier, O. Richard, H. Bender, M. Jurczak, and W. Vandervorst, "Conductive-AFM tomography for 3D filament observation in resistive switching devices," *Tech. Dig. - Int. Electron Devices Meet. IEDM*, pp. 574–577, 2013. DOI:10.1109/IEDM.2013.6724679.
- [59] Z. Xu, Y. Bando, W. Wang, X. Bai, and D. Golberg, "Real-Time In Situ HRTEM-Resolved Resistance Switching of Ag₂S Nanoscale Ionic Conductor," *ACS Nano*, vol. 4, no. 5, pp. 2515–2522, 2010. DOI:10.1021/nn100483a.
- [60] Q. Liu, J. Su, H. Lv, S. Long, K. Yin, N. Wan, Y. Li, L. Sun, and M. Liu, "Real-time observation on dynamic growth/dissolution of conductive filaments in oxide-electrolyte-based ReRAM," *Adv. Mater.*, vol. 25, no. 2, pp. 162–164, 2013. DOI:10.1002/adma.201104104.
- [61] C. Li, B. Gao, Y. Yao, X. Guan, X. Shen, Y. Wang, P. Huang, L. Liu, X. Liu, J. Li, C. Gu, J. Kang, and R. Yu, "Direct Observations of Nanofilament Evolution in Switching Processes in HfO₂-Based Resistive Random Access Memory by In Situ TEM Studies," *Adv. Mater.*, vol. 29, no. 10, pp. 1–8, 2017. DOI:10.1002/adma.201602976.
- [62] Q. Liu, J. Sun, H. Lv, S. Long, K. Yin, N. Wan, Y. Li, L. Sun, and M. Liu, "Real-time observation on dynamic growth/dissolution of conductive filaments in oxide-electrolyte-based ReRAM," *Adv. Mater.*, vol. 24, no. 14, pp. 1844–1849, 2012.
- [63] Q. Liu, S. Long, H. Lv, W. Wang, J. Niu, Z. Huo, J. Chen, and M. Liu, "Controllable growth of nanoscale conductive filaments in solid-electrolyte-based ReRAM by using a metal nanocrystal covered bottom electrode," *ACS Nano*, vol. 4, no. 10, pp. 6162–6168, 2010. DOI:10.1021/nn1017582.
- [64] X. Xu, H. Lv, H. Liu, T. Gong, G. Wang, M. Zhang, Y. Li, Q. Liu, S. Long, and M. Liu, "Superior retention of low-resistance state in conductive bridge random access memory with single filament formation," *IEEE Electron Device Lett.*, vol. 36, no. 2, pp. 129–131, 2015. DOI:10.1109/LED.2014.2379961.
- [65] U. Celano, L. Goux, A. Belmonte, K. Opsomer, A. Franquet, A. Schulze, C. Detavernier, O. Richard, H. Bender, M. Jurczak, and W. Vandervorst, "Three-dimensional observation of the conductive filament in nanoscaled resistive memory devices," *Nano Lett.*, vol. 14, no. 5, pp. 2401–2406, 2014. DOI:10.1021/nl500049g.
- [66] G. S. Park, X. S. Li, D. C. Kim, R. J. Jung, M. J. Lee, and S. Seo, "Observation of electric-field induced Ni filament channels in polycrystalline Ni Ox film," *Appl. Phys. Lett.*, vol. 91,

- no. 22, pp. 1–4, 2007. DOI:10.1063/1.2813617.
- [67] R. Carboni and D. Ielmini, “Stochastic Memory Devices for Security and Computing,” *Adv. Electron. Mater.*, vol. 5, no. 9, pp. 1–27, 2019. DOI:10.1002/aelm.201900198.
- [68] W. Wang, G. Pedretti, V. Milo, R. Carboni, A. Calderoni, N. Ramaswamy, A. S. Spinelli, and D. Ielmini, “Learning of spatiotemporal patterns in a spiking neural network with resistive switching synapses,” *Sci. Adv.*, vol. 4, no. 9, pp. 1–9, 2018. DOI:10.1126/sciadv.aat4752.
- [69] Z. Sun, G. Pedretti, E. Ambrosi, A. Bricalli, W. Wang, and D. Ielmini, “Solving matrix equations in one step with cross-point resistive arrays,” *Proc. Natl. Acad. Sci. U. S. A.*, vol. 116, no. 10, pp. 4123–4128, 2019. DOI:10.1073/pnas.1815682116.
- [70] T. C. Sverre, J. R. C. Woods, E. A. Shaw, P. Hua, V. Apostolopoulos, J. S. Wilkinson, and A. C. Tropper, “Tantalum Pentoxide Waveguides and Microresonators for VECSEL-based Frequency Combs,” in *Proceedings of SPIE*, 2018, no. February. DOI:10.1117/12.2289773.
- [71] I. G. E. Gore, N. Branch, T. Roman, E. Orange, K. Wayne, and R. A. Gore, “Tantalum oxide anti-reflective coating (ARC) integrated with a metallic transistor gate electrode and method of formation,” 6,004,850, 1998.
- [72] V. S. Souza, J. D. Scholten, D. E. Weibel, D. Eberhardt, D. L. Baptista, S. R. Teixeira, and J. Dupont, “Hybrid tantalum oxide nanoparticles from the hydrolysis of imidazolium tantalate ionic liquids: efficient catalysts for hydrogen generation from ethanol/water solutions,” *J. Mater. Chem. A*, vol. 4, no. 19, pp. 7469–7475, 2016. DOI:10.1039/C6TA02114J.
- [73] H. Shinriki, T. Kisu, S. I. Kimura, Y. Nishioka, Y. Kawamoto, and K. Mukai, “Promising Storage Capacitor Structures with Thin Ta₂O₅ Film for Low-Power High-Density DRAM’s,” *IEEE Trans. Electron Devices*, vol. 37, no. 9, pp. 1939–1947, 1990. DOI:10.1109/16.57154.
- [74] M. Hiratani, S. Kimura, T. Hamada, S. Iijima, and N. Nakanishi, “Hexagonal polymorph of tantalum-pentoxide with enhanced dielectric constant,” *Appl. Phys. Lett.*, vol. 81, no. 13, pp. 2433–2435, 2002. DOI:10.1063/1.1509861.
- [75] C. Chaneliere, S. Four, J. L. Autran, and R. A. B. Devine, “Dielectric permittivity of amorphous and hexagonal electron cyclotron resonance plasma deposited Ta₂O₅ thin films,” *Electrochem. Solid-State Lett.*, vol. 2, no. 6, pp. 291–293, 1999. DOI:10.1149/1.1390814.
- [76] C. Chaneliere, J. L. Autran, R. A. B. Devine, and B. Balland, “Tantalum pentoxide (Ta₂O₅) thin films for advanced dielectric applications,” *Mater. Sci. Eng. R Reports*, vol. 22, no. 6, pp. 269–322, 1998. DOI:10.1016/S0927-796X(97)00023-5.
- [77] J. F. Meng, B. K. Rai, R. S. Katiyar, and A. S. Bhalla, “Raman investigation on (Ta₂O₅)_{1-x}(TiO₂)_x system at different temperatures and pressures,” *J. Phys. Chem. Solids*, vol. 58, no. 10, pp. 1503–1506, 1997. DOI:10.1016/S0022-3697(97)00180-7.
- [78] C. Chaneliere, S. Four, J. L. Autran, and R. A. B. Devine, “Comparison between the properties of amorphous and crystalline Ta₂O₅ thin films deposited on Si,” *Microelectron. Reliab.*, vol. 39, no. 2, pp. 261–268, 1999. DOI:10.1016/S0026-2714(98)00218-2.
- [79] L. A. Aleshina and S. V. Loginova, “Rietveld analysis of X-ray diffraction pattern from β-Ta₂O₅ oxide,” *Crystallogr. Reports*, vol. 47, no. 3, pp. 415–419, 2002. DOI:10.1134/1.1481927.
- [80] A. L. Salaün, A. Mantoux, E. Blanquet, and E. Djurado, “ESD and ALD Depositions of Ta₂O₅ Thin Films Investigated as Barriers to Copper Diffusion for Advanced Metallization,” *J. Electrochem. Soc.*, vol. 156, no. 5, p. H311, 2009. DOI:10.1149/1.3086781.
- [81] J. S. Park, W. J. Maeng, H. S. Kim, and J. S. Park, “Review of recent developments in amorphous oxide semiconductor thin-film transistor devices,” *Thin Solid Films*, vol. 520, no. 6, pp. 1679–1693, 2012. DOI:10.1016/j.tsf.2011.07.018.
- [82] S. R. Lee, Y. B. Kim, M. Chang, K. K. M. Kim, C. B. Lee, J. H. Hur, G. S. Park, D. Lee, M. J. Lee, C. J. Kim, U. I. Chung, I. K. Yoo, and K. K. M. Kim, “Multi-level switching of triple-

- layered TaOx RRAM with excellent reliability for storage class memory,” in *2012 Symposium on VLSI Technology*, 2012, vol. 52, no. 2011, pp. 71–72. DOI:10.1109/VLSIT.2012.6242466.
- [83] S. P. Garg, N. Krishnamurthy, A. Awasthi, and M. Venkatraman, “The O-Ta (Oxygen-Tantalum) system,” *J. Phase Equilibria*, vol. 17, no. 1, pp. 63–77, 1996. DOI:10.1007/BF02648373.
- [84] G. M. Wolten and A. B. Chase, “Single-crystal data for β Ta₂O₅ and A KPO₃,” *Zeitschrift fur Krist. - New Cryst. Struct.*, vol. 129, no. 5–6, pp. 365–368, 1969. DOI:10.1524/zkri.1969.129.5-6.365.
- [85] N. C. Stephenson and R. S. Roth, “Structural systematics in the binary system Ta₂O₅–WO₃. V. The structure of the low-temperature form of tantalum oxide L-Ta₂O₅,” *Acta Crystallogr. Sect. B Struct. Crystallogr. Cryst. Chem.*, vol. 27, no. 5, pp. 1037–1044, 1971. DOI:10.1107/s056774087100342x.
- [86] I. P. Zibrov, V. P. Filonenko, M. Sundberg, and P. E. Werner, “Structures and phase transitions of B-Ta₂O₅ and Z-Ta₂O₅: Two high-pressure forms of Ta₂O₅,” *Acta Crystallogr. Sect. B Struct. Sci.*, vol. 56, no. 4, pp. 659–665, 2000. DOI:10.1107/S0108768100005462.
- [87] C. Askeljung, B. O. Marinder, and M. Sundberg, “Effect of heat treatment on the structure of L-Ta₂O₅: A study by XRPD and HRTEM methods,” *J. Solid State Chem.*, vol. 176, no. 1, pp. 250–258, 2003. DOI:10.1016/j.jssc.2003.07.003.
- [88] N. Schonberg, “An X-Ray Investigation of the Tantalum Oxygen System,” *Acta Chemica Scandinavica*, vol. 8, no. 2, pp. 240–245, 1954. DOI:10.3891/acta.chem.scand.08-0240.
- [89] X. Q. Liu, X. D. Han, Z. Zhang, L. F. Ji, and Y. J. Jiang, “The crystal structure of high temperature phase Ta₂O₅,” *Acta Mater.*, vol. 55, no. 7, pp. 2385–2396, 2007. DOI:10.1016/j.actamat.2006.11.031.
- [90] J. Spyridelis, P. Delavignette, and S. Amelinckx, “On the Superstructures of Ta₂O₅ and Nb₂O₅,” *Phys. Status Solidi*, vol. 19, no. 2, pp. 683–704, 1967. DOI:10.1002/pssb.19670190220.
- [91] A. Fukumoto and K. Miwa, “Prediction of hexagonal structure by first-principles calculations,” *Phys. Rev. B - Condens. Matter Mater. Phys.*, vol. 55, no. 17, pp. 11155–11160, 1997. DOI:10.1103/PhysRevB.55.11155.
- [92] B. R. Sahu and L. Kleinman, “Theoretical study of structural and electronic properties of β -Ta₂O₅ and δ -Ta₂O₅,” *Phys. Rev. B - Condens. Matter Mater. Phys.*, vol. 69, no. 16, pp. 1–6, 2004. DOI:10.1103/PhysRevB.69.165202.
- [93] C. Joseph, P. Bourson, and M. D. Fontana, “Amorphous to crystalline transformation in Ta₂O₅ studied by Raman spectroscopy,” *J. Raman Spectrosc.*, vol. 43, no. 8, pp. 1146–1150, 2012. DOI:10.1002/jrs.3142.
- [94] F.-C. Chiu, J.-J. Wang, J. Y. Lee, and S. C. Wu, “Leakage currents in amorphous Ta₂O₅ thin films,” *J. Appl. Phys.*, vol. 81, no. 10, pp. 6911–6915, 1997. DOI:10.1063/1.365252.
- [95] J. Harvey and H. Wilman, “The crystallisation of thin amorphous tantalum oxide films heated in air or vacuo, and the structure of the crystalline oxide,” *Acta Crystallogr.*, vol. 14, no. 12, pp. 1278–1281, 1961. DOI:10.1107/s0365110x61003703.
- [96] K. Lehovc, “Lattice structure of β -Ta₂O₅,” *J. Less-Common Met.*, vol. 7, no. 6, pp. 397–410, 1964. DOI:10.1016/0022-5088(64)90036-0.
- [97] A. E. Michale and H. L. Tuller, “Defects and charge transport in stabilized α -Ta₂O₅,” *Radiat. Eff.*, vol. 75, no. 1–4, pp. 267–281, 1982. DOI:10.1080/00337578308224711.
- [98] D. Makovec, J. M. Zuo, R. Twisten, and D. A. Payne, “A high-temperature structure for Ta₂O₅ with modulations by TiO₂ substitution,” *J. Solid State Chem.*, vol. 179, no. 6, pp. 1782–1791, 2006. DOI:10.1016/j.jssc.2006.03.014.
- [99] O. Yamaguchi, D. Tomihisa, T. Uegaki, and K. Shimizu, “Formation and Transformation of δ -Ta₂O₅ Solid Solution in the System Ta₂O₅-Al₂O₃,” *J. Am. Ceram. Soc.*, vol. 70, no. 11, pp. C–335, 1987.
- [100] Y. Syono, M. Kikuchi, T. Goto, and K. Fukuoka, “Formation of rutile-type Ta(IV)O₂ by shock reduction and cation-deficient Ta_{0.8}O₂ by subsequent oxidation,” *J. Solid State Chem.*, vol. 50, no. 2, pp. 133–137, 1983. DOI:10.1016/0022-4596(83)90180-9.

- [101] Y. Guo and J. Robertson, "Oxygen vacancy defects in Ta₂O₅ showing long-range atomic re-arrangements," *Appl. Phys. Lett.*, vol. 104, no. 11, 2014. DOI:10.1063/1.4869553.
- [102] S. Boughaba, M. U. Islam, G. I. Sproule, and M. J. Graham, "Characterization of tantalum oxide films grown by pulsed laser deposition," *Surf. Coatings Technol.*, vol. 120–121, pp. 757–764, 1999. DOI:10.1016/S0257-8972(99)00371-0.
- [103] S. Boughaba, G. I. Sproule, J. P. McCaffrey, M. Islam, and M. J. Graham, "Synthesis of tantalum pentoxide films by pulsed laser deposition: material characterization and scale-up," *Thin Solid Films*, vol. 358, pp. 104–113, 2000.
- [104] K. Okamura, B. Nasr, R. A. Brand, and H. Hahn, "Solution-processed oxide semiconductor SnO in p-channel thin-film transistors," *J. Mater. Chem.*, vol. 22, no. 11, pp. 4607–4610, 2012. DOI:10.1039/c2jm16426d.
- [105] B. M. Gray, A. L. Hector, M. Jura, J. R. Owen, and J. Whittam, "Effect of oxidative surface treatments on charge storage at titanium nitride surfaces for supercapacitor applications," *J. Mater. Chem. A*, vol. 5, no. 9, pp. 4550–4559, 2017. DOI:10.1039/C6TA08308K.
- [106] R. Simpson, R. G. White, J. F. Watts, and M. A. Baker, "XPS investigation of monatomic and cluster argon ion sputtering of tantalum pentoxide," *Appl. Surf. Sci.*, vol. 405, pp. 79–87, 2017. DOI:10.1016/j.apsusc.2017.02.006.
- [107] S. U. Sharath, M. J. Joseph, S. Vogel, E. Hildebrandt, P. Komissinskiy, J. Kurian, T. Schroeder, and L. Alff, "Impact of oxygen stoichiometry on electroforming and multiple switching modes in TiN/TaO_x/Pt based ReRAM," *Appl. Phys. Lett.*, vol. 109, no. 173503, 2016. DOI:10.1063/1.4965872.
- [108] H. Search, C. Journals, A. Contact, and M. Iopscience, "Structure and Electrical Properties of Thin Ta₂O₅ Deposited on Metal Electrodes," *Jpn. J. Appl. Phys.*, vol. 37, 1998. DOI:10.1143/JJAP.37.1336.
- [109] I. Goldfarb, F. Miao, J. J. Yang, W. Yi, J. P. Strachan, M. X. Zhang, M. D. Pickett, G. Medeiros-Ribeiro, and R. S. Williams, "Electronic structure and transport measurements of amorphous transition-metal oxides: Observation of Fermi glass behavior," *Appl. Phys. A Mater. Sci. Process.*, vol. 107, no. 1, pp. 1–11, 2012. DOI:10.1007/s00339-012-6856-z.
- [110] D. R. Kudrak and M. J. Sienko, "Solid-State Studies of Oxygen-Deficient Tantalum Pentoxide," *Inorg. Chem.*, vol. 6, no. 5, pp. 880–884, 1967. DOI:10.1021/ic50051a006.
- [111] S. Ezhilvalavan and T. Y. Tseng, "Conduction mechanisms in amorphous and crystalline Ta₂O₅ thin films," *J. Appl. Phys.*, vol. 83, no. 9, pp. 4797–4801, 1998. DOI:10.1063/1.367272.
- [112] C. L. Standley and L. I. Maissel, "Some observations on conduction through thin tantalum oxide films," *J. Appl. Phys.*, vol. 35, no. 5, pp. 1530–1534, 1964. DOI:10.1063/1.1713661.
- [113] J. E. STROUD, W. C. TRIPP, and J. M. WIMMER, "Defect Structure of Ta₂O₅," *J. Am. Ceram. Soc.*, vol. 57, no. 4, pp. 172–175, 1974. DOI:10.1111/j.1151-2916.1974.tb10848.x.
- [114] P. Kofstad, "On The Defect Structure of Ta₂O₅," *J. Electrochem. Soc.*, vol. 109, no. 9, p. 776, 1962. DOI:10.1149/1.2425554.
- [115] U. Balachandran and N. G. Eror, "Electrical Conductivity in Ta₂O₅," *Mat. Res. Bull.*, vol. 17, pp. 151–160, 1982.
- [116] I. Goldfarb and R. S. Williams, "Conduction centers in a Ta₂O₅-δ Fermi glass," *Appl. Phys. A Mater. Sci. Process.*, vol. 114, no. 2, pp. 287–289, 2014. DOI:10.1007/s00339-013-8162-9.
- [117] R. J. Bondi, M. P. Desjarlais, A. P. Thompson, G. L. Brennecka, and M. J. Marinella, "Electrical conductivity in oxygen-deficient phases of tantalum pentoxide from first-principles calculations," *J. Appl. Phys.*, vol. 114, no. 20, 2013. DOI:10.1063/1.4829900.
- [118] C. D. Landon, R. H. T. Wilke, M. T. Brumbach, G. L. Brennecka, M. Blea-kirby, J. F. Ihlefeld, M. J. Marinella, T. E. Beechem, C. D. Landon, R. H. T. Wilke, M. T. Brumbach, G. L. Brennecka, M. Blea-kirby, J. F. Ihlefeld, M. J. Marinella, and T. E. Beechem, "Thermal transport in tantalum oxide films for memristive applications," *Appl. Phys. Lett.*, vol. 107, no. 2, 2015. DOI:10.1063/1.4926921.

- [119] J.-Y. Zhang, Q. Fang, and I. W. Boyd, "Growth of tantalum pentoxide film by pulsed laser deposition," *Appl. Surf. Sci.*, vol. 138–139, pp. 320–324, 1999. DOI:10.1016/S0169-4332(98)00413-9.
- [120] J.-Y. Zhang and I. W. Boyd, "Pulsed laser deposition of tantalum pentoxide film," *Appl. Phys. A Mater. Sci. Process.*, vol. 70, no. 6, pp. 657–661, 2000.
- [121] O. K. Donaldson, K. Hattar, and J. R. Trelewicz, "Metastable Tantalum Oxide Formation During the Devitrification of Amorphous Tantalum Thin Films," *J. Am. Ceram. Soc.*, vol. 99, no. 11, pp. 3775–3783, 2016. DOI:10.1111/jace.14384.
- [122] Zhou Mingfei, Fu Zhengwen, Yang Haijun, Zhang Zhuangjian, and Qin Qizong, "Pulsed laser deposition of tantalum oxide thin films," *Appl. Surf. Sci.*, vol. 108, no. 3, pp. 399–403, 1997. DOI:10.1016/S0169-4332(96)00605-8.
- [123] Q. Qin and Z. Fu, "Processing and Characterization of Ta₂O₅ Films by Pulsed Laser Ablation," *Adv. Mater.*, vol. 11, no. 13, pp. 1119–1123, 1999.
- [124] J.-Y. Zhang and I. W. Boyd, "Thin tantalum and tantalum oxide films grown by pulsed laser deposition," *Appl. Surf. Sci.*, vol. 168, no. 1–4, pp. 234–238, 2000. DOI:10.1016/S0169-4332(00)00605-X.
- [125] T. Hino, M. Nishida, and T. Araki, "Crystallization of tantalum oxide formed by PLD," *Surf. Coatings Technol.*, vol. 149, no. 1, pp. 1–6, 2002. DOI:10.1016/S0257-8972(01)01408-6.
- [126] T. Hino, S. Mustofa, M. Nishida, and T. Araki, "The effect of 5 mass% O₃ gas on PLD of tantalum oxide," *Appl. Surf. Sci.*, vol. 189, no. 1–2, pp. 1–6, 2002. DOI:10.1016/S0169-4332(01)00395-6.
- [127] F. Kurnia, Hadiywarman, C. U. Jung, R. Jung, and C. Liu, "Composition dependence of unipolar resistance switching in TaO_x thin films," *Phys. Status Solidi - Rapid Res. Lett.*, vol. 5, no. 7, pp. 253–255, 2011. DOI:10.1002/pssr.201105253.
- [128] G. W., "Deposition of Optical Thin Films by Pulsed Laser Assisted Evaporation," *Appl. Opt.*, vol. 28, no. 14, p. 2806, 1989.
- [129] Y. Nishimura, U. Hiroki, T. Ochiai, and M. Tsuji, "Tantalum oxide film deposition by laser ablation," *Appl. Surf. Sci.*, vol. 79–80, no. C, pp. 165–170, 1994. DOI:10.1016/0169-4332(94)90406-5.
- [130] L. J. van der PAUW, "A Method of Measuring Specific Resistivity and Hall Effect of Discs of Arbitrary Shape," *Semiconductor Devices: Pioneering Papers*. pp. 174–182, 1991. DOI:10.1142/9789814503464_0017.
- [131] Y.-B. Kim, S. R. Lee, D. Lee, C. B. Lee, M. Chang, J. H. Hur, M.-J. Lee, G.-S. Park, C. J. Kim, U.-I. Chung, I.-K. Yoo, and K. Kim, "Bi-layered RRAM with Unlimited Endurance and Extremely Uniform Switching," in *2011 Symposium on VLSI Technology (VLSIT)*, 2011, pp. 52–53.
- [132] L. Zhang, S. Member, R. Huang, S. Member, M. Zhu, and S. Qin, "Unipolar TaO_x-based Resistive Change Memory Realized with Electrode Engineering," *IEEE Electron Device Lett.*, vol. 31, no. 9, pp. 966–968, 2010. DOI:10.1109/LED.2010.2052091.
- [133] J. J. Yang, M.-X. Zhang, J. P. Strachan, F. Miao, M. D. Pickett, R. D. Kelley, G. Medeiros-Ribeiro, and R. S. Williams, "High switching endurance in TaO_x memristive devices," *Appl. Phys. Lett.*, vol. 97, no. 23, p. 232102, 2010. DOI:10.1063/1.3524521.
- [134] M.-J. Lee, C. B. Lee, D. Lee, S. R. Lee, M. Chang, J. H. Hur, Y. B. Kim, C. J. Kim, D. H. Seo, S. Seo, U.-I. Chung, I.-K. Yoo, and K. Kim, "A fast, high-endurance and scalable non-volatile memory device made from asymmetric Ta₂O_{5-x}/TaO_{2-x}," *Nat. Mater.*, vol. 10, no. 8, pp. 625–630, 2011. DOI:10.1038/nmat3070.
- [135] A. Prakash, S. Maikap, C. S. Lai, T. C. Tien, W. S. Chen, H. Y. Lee, F. T. Chen, M. J. Kao, and M. J. Tsai, "Bipolar resistive switching memory using bilayer TaO_x/WO_x films," *Solid. State. Electron.*, vol. 77, pp. 35–40, 2012. DOI:10.1016/j.sse.2012.05.028.
- [136] T. Sakamoto, K. Lister, N. Banno, T. Hasegawa, K. Terabe, and M. Aono, "Electronic transport in Ta₂O₅ resistive switch," *Appl. Phys. Lett.*, vol. 91, no. 9, p. 092110, 2007. DOI:10.1063/1.2777170.
- [137] S. Rahaman, S. Maikap, T.-C. Tien, H.-Y. Lee, W.-S. Chen, F. T. Chen, M.-J. Kao, and M.-J. Tsai, "Excellent resistive memory characteristics and switching mechanism using a Ti nanolayer at the Cu/TaO_x interface," *Nanoscale Res. Lett.*, vol. 7, no. 1, p. 345, 2012.

- DOI:10.1186/1556-276X-7-345.
- [138] Z. Wei, Y. Kanzawa, K. Arita, Y. Katoh, K. Kawai, S. Muraoka, S. Mitani, S. Fujii, K. Katayama, M. Iijima, T. Mikawa, T. Ninomiya, R. Miyanaga, Y. Kawashima, K. Tsuji, A. Himeno, T. Okada, ... M. Oshima, "Highly reliable TaO_x ReRAM and direct evidence of redox reaction mechanism," *2008 IEEE Int. Electron Devices Meet.*, pp. 1–4, 2008. DOI:10.1109/IEDM.2008.4796676.
- [139] A. Prakash, S. Maikap, H. Chiu, T. Tien, and C. Lai, "Enhanced resistive switching memory characteristics and mechanism using a Ti nanolayer at the W/TaO_x interface," *Nanoscale Res. Lett.*, no. Cc, pp. 1–9, 2014.
- [140] T. Ninomiya, Z. Wei, S. Muraoka, R. Yasuhara, K. Katayama, and T. Takagi, "Conductive filament scaling of TaO_x bipolar ReRAM for improving data retention under low operation current," *IEEE Trans. Electron Devices*, vol. 60, no. 4, pp. 1384–1389, 2013. DOI:10.1109/TED.2013.2248157.
- [141] H. Jeon, J. Park, W. Jang, H. Kim, C. Kang, H. Song, H. Kim, H. Seo, and H. Jeon, "Stabilized resistive switching behaviors of a Pt/TaO_x/TiN RRAM under different oxygen contents," *Phys. Status Solidi Appl. Mater. Sci.*, vol. 211, no. 9, pp. 2189–2194, 2014. DOI:10.1002/pssa.201431260.
- [142] Y. Zhang, N. Deng, H. Wu, Z. Yu, J. Zhang, and H. Qian, "Metallic to hopping conduction transition in Ta₂O_{5-x}/TaO_y resistive switching device," *Appl. Phys. Lett.*, vol. 105, no. 6, p. 063508, 2014. DOI:10.1063/1.4893325.
- [143] Y. Li, S. Sanna, K. Norrman, D. V. Christensen, C. S. Pedersen, J. M. G. Lastra, M. L. Traulsen, V. Esposito, and N. Pryds, "Tuning the stoichiometry and electrical properties of tantalum oxide thin films," *Appl. Surf. Sci.*, vol. 470, no. November 2018, pp. 1071–1074, 2019. DOI:10.1016/j.apsusc.2018.11.153.
- [144] D. V. Christensen, M. von Soosten, F. Trier, T. S. Jespersen, A. Smith, Y. Chen, and N. Pryds, "Controlling the Carrier Density of SrTiO₃-Based Heterostructures with Annealing," *Adv. Electron. Mater.*, vol. 3, no. 8, pp. 1–7, 2017. DOI:10.1002/aelm.201700026.
- [145] J. Hong, W. Jang, H. Song, C. Kang, and H. Jeon, "Endurance improvement due to rapid thermal annealing (RTA) of a TaO_x thin film in an oxygen ambient," *J. Korean Phys. Soc.*, vol. 66, no. 5, pp. 721–725, 2015. DOI:10.3938/jkps.66.721.
- [146] O. K. Donaldson, K. Hattar, J. R. Trelewicz, and E. I. C. Johnson, "Metastable Tantalum Oxide Formation During the Devitrification of Amorphous Tantalum Thin Films," *J. Am. Ceram. Soc.*, vol. 99, no. 11, pp. 3775–3783, 2016. DOI:10.1111/jace.14384.
- [147] L. Goux, J. Y. Kim, B. Magyari-Kope, Y. Nishi, A. Redolfi, and M. Jurczak, "H-treatment impact on conductive-filament formation and stability in Ta₂O₅-based resistive-switching memory cells," *J. Appl. Phys.*, vol. 117, no. 12, p. 124501, 2015. DOI:10.1063/1.4915946.
- [148] C. Chen, C. Song, J. Yang, F. Zeng, and F. Pan, "Oxygen migration induced resistive switching effect and its thermal stability in W/TaO_x/Pt structure," *Appl. Phys. Lett.*, vol. 100, no. 25, 2012. DOI:10.1063/1.4730601.
- [149] S. Lee, A. Sangle, P. Lu, A. Chen, W. Zhang, J. S. Lee, H. Wang, Q. Jia, and J. L. MacManus-Driscoll, "Novel electroforming-free nanoscaffold memristor with very high uniformity, tunability, and density," *Adv. Mater.*, vol. 26, no. 36, pp. 6284–6289, 2014. DOI:10.1002/adma.201401917.
- [150] B. H. Lee, D. H. Lee, H. Bae, H. Seong, S. B. Jeon, M. L. Seol, J. W. Han, M. Meyyappan, S. G. Im, and Y. K. Choi, "Foldable and Disposable Memory on Paper," *Sci. Rep.*, vol. 6, no. December, pp. 1–8, 2016. DOI:10.1038/srep38389.
- [151] D. H. Lien, Z. K. Kao, T. H. Huang, Y. C. Liao, S. C. Lee, and J. H. He, "All-printed paper memory," *ACS Nano*, vol. 8, no. 8, pp. 7613–7619, 2014. DOI:10.1021/nn501231z.
- [152] Y. C. Liu, Z. Q. Wang, Y. X. Liu, X. H. Li, H. Y. Xu, and X. T. Zhang, "Flexible Resistive Switching Memory Device Based on Amorphous InGaZnO Film With Excellent Mechanical Endurance," *IEEE Electron Device Lett.*, vol. 32, no. 10, pp. 1442–1444, 2011. DOI:10.1109/led.2011.2162311.
- [153] S. Kim, H. Y. Jeong, S. K. Kim, S. Y. Choi, and K. J. Lee, "Flexible memristive memory

- array on plastic substrates," *Nano Lett.*, vol. 11, no. 12, pp. 5438–5442, 2011. DOI:10.1021/nl203206h.
- [154] Y. W. Dai, L. Chen, W. Yang, Q. Q. Sun, P. Zhou, P. F. Wang, S. J. Ding, D. W. Zhang, and F. Xiao, "Complementary resistive switching in flexible RRAM devices," *IEEE Electron Device Lett.*, vol. 35, no. 9, pp. 915–917, 2014. DOI:10.1109/LED.2014.2334609.
- [155] H. G. Yoo, S. Kim, and K. J. Lee, "Flexible one diode-one resistor resistive switching memory arrays on plastic substrates," *RSC Adv.*, vol. 4, no. 38, pp. 20017–20023, 2014. DOI:10.1039/c4ra02536a.
- [156] X. Yan, Z. Zhou, J. Zhao, Q. Liu, H. Wang, G. Yuan, and J. Chen, "Flexible memristors as electronic synapses for neuro-inspired computation based on scotch tape-exfoliated mica substrates," *Nano Res.*, vol. 11, no. 3, pp. 1183–1192, 2018. DOI:10.1007/s12274-017-1781-2.
- [157] H. Bae, B. H. Lee, D. Lee, M. L. Seol, D. Kim, J. W. Han, C. K. Kim, S. B. Jeon, D. Ahn, S. J. Park, J. Y. Park, and Y. K. Choi, "Physically Transient Memory on a Rapidly Dissolvable Paper for Security Application," *Sci. Rep.*, vol. 6, no. December, pp. 1–7, 2016. DOI:10.1038/srep38324.
- [158] J. J. Huang, Y. M. Tseng, W. C. Luo, C. W. Hsu, and T. H. Hou, "One selector-one resistor (1S1R) crossbar array for high-density flexible memory applications," *Tech. Dig. - Int. Electron Devices Meet. IEDM*, pp. 31.7.1-31.7.4, 2011. DOI:10.1109/IEDM.2011.6131653.
- [159] C. H. Cheng, F. S. Yeh, and A. Chin, "Low-power high-performance non-volatile memory on a flexible substrate with excellent endurance," *Adv. Mater.*, vol. 23, no. 7, pp. 902–905, 2011. DOI:10.1002/adma.201002946.
- [160] C. Chou, C. Hsu, C. Chang, and T. Hou, "Self-Rectifying Ta/TaO_x/TiO₂/Ti Cell for High-Density Flexible RRAM," in *2014 International Conference on Solid State Devices and Materials*, 2014, pp. 422–423.
- [161] S. Kim and Y. K. Choi, "Resistive switching of aluminum oxide for flexible memory," *Appl. Phys. Lett.*, vol. 92, no. 22, pp. 1–4, 2008. DOI:10.1063/1.2939555.
- [162] S. Kim, H. Moon, D. Gupta, S. Yoo, and Y. K. Choi, "Resistive switching characteristics of Sol-Gel Zinc oxide films for flexible memory applications," *IEEE Trans. Electron Devices*, vol. 56, no. 4, pp. 696–699, 2009. DOI:10.1109/TED.2009.2012522.
- [163] J. Won Seo, J. W. Park, K. S. Lim, S. J. Kang, Y. H. Hong, J. H. Yang, L. Fang, G. Y. Sung, and H. K. Kim, "Transparent flexible resistive random access memory fabricated at room temperature," *Appl. Phys. Lett.*, vol. 95, no. 13, pp. 1–4, 2009. DOI:10.1063/1.3242381.
- [164] S. Kim, O. Yarimaga, S. J. Choi, and Y. K. Choi, "Highly durable and flexible memory based on resistance switching," *Solid. State. Electron.*, vol. 54, no. 4, pp. 392–396, 2010. DOI:10.1016/j.sse.2009.10.021.
- [165] H. Y. Jeong, J. Y. Kim, J. W. Kim, J. O. Hwang, J. E. Kim, J. Y. Lee, T. H. Yoon, B. J. Cho, S. O. Kim, R. S. Ruoff, and S. Y. Choi, "Graphene oxide thin films for flexible nonvolatile memory applications," *Nano Lett.*, vol. 10, no. 11, pp. 4381–4386, 2010. DOI:10.1021/nl101902k.
- [166] H. Y. Jeong, Y. I. Kim, J. Y. Lee, and S. Y. Choi, "A low-temperature-grown TiO₂ based device for the flexible stacked RRAM application," *Nanotechnology*, vol. 21, no. 11, p. 115203, 2010. DOI:10.1088/0957-4484/21/11/115203.
- [167] R.-C. Fang, Q.-Q. Sun, P. Zhou, W. Yang, P.-F. Wang, and D. W. Zhang, "High-performance bilayer flexible resistive random access memory based on low-temperature thermal atomic layer deposition," *Nanoscale Res. Lett.*, vol. 8, no. 1, p. 92, 2013. DOI:10.1186/1556-276x-8-92.
- [168] S. Kim, J. H. Son, S. H. Lee, B. K. You, K.-I. Park, H. K. Lee, M. Byun, and K. J. Lee, "Flexible Crossbar-Structured Resistive Memory Arrays on Plastic Substrates via Inorganic-Based Laser Lift-Off," *Adv. Mater.*, vol. 26, no. 44, pp. 7418–7418, 2014. DOI:10.1002/adma.201470300.
- [169] A. Midya, N. Gogurla, and S. K. Ray, "Flexible and transparent resistive switching devices using Au nanoparticles decorated reduced graphene oxide in polyvinyl alcohol matrix,"

- Curr. Appl. Phys.*, vol. 15, no. 6, pp. 706–710, 2015. DOI:10.1016/j.cap.2015.03.008.
- [170] L. Liang, K. Li, C. Xiao, S. Fan, J. Liu, W. Zhang, W. Xu, W. Tong, J. Liao, Y. Zhou, B. Ye, and Y. Xie, “Vacancy associates-rich ultrathin nanosheets for high performance and flexible nonvolatile memory device,” *J. Am. Chem. Soc.*, vol. 137, no. 8, pp. 3102–3108, 2015. DOI:10.1021/jacs.5b00021.
- [171] K. N. Pham, V. D. Hoang, C. V. Tran, and B. T. Phan, “TiO₂ thin film based transparent flexible resistive switching random access memory,” *Adv. Nat. Sci. Nanosci. Nanotechnol.*, vol. 7, no. 1, p. 015017, 2016. DOI:10.1088/2043-6262/7/1/015017.
- [172] J. Shang, W. Xue, Z. Ji, G. Liu, X. Niu, X. Yi, L. Pan, Q. Zhan, X. H. Xu, and R. W. Li, “Highly flexible resistive switching memory based on amorphous-nanocrystalline hafnium oxide films,” *Nanoscale*, vol. 9, no. 21, pp. 7037–7046, 2017. DOI:10.1039/c6nr08687j.
- [173] B. Sun, X. Zhang, G. Zhou, T. Yu, S. Mao, S. Zhu, Y. Zhao, and Y. Xia, “A flexible nonvolatile resistive switching memory device based on ZnO film fabricated on a foldable PET substrate,” *J. Colloid Interface Sci.*, vol. 520, pp. 19–24, 2018. DOI:10.1016/j.jcis.2018.03.001.
- [174] L. Wu, J. Guo, W. Zhong, W. Zhang, X. Kang, W. Chen, and Y. Du, “Flexible, multilevel, and low-operating-voltage resistive memory based on MoS₂-rGO hybrid,” *Appl. Surf. Sci.*, vol. 463, no. July 2018, pp. 947–952, 2019. DOI:10.1016/j.apsusc.2018.09.022.
- [175] X. Zhao, R. Wang, X. Xiao, C. Lu, F. Wu, R. Cao, C. Jiang, and Q. Liu, “Flexible cation-based threshold selector for resistive switching memory integration,” *Sci. China Inf. Sci.*, vol. 61, no. 6, pp. 0–8, 2018. DOI:10.1007/s11432-017-9352-0.
- [176] M. Yang, X. Zhao, Q. Tang, N. Cui, Z. Wang, Y. Tong, and Y. Liu, “Stretchable and conformable synapse memristors for wearable and implantable electronics,” *Nanoscale*, vol. 10, no. 38, pp. 18135–18144, 2018. DOI:10.1039/c8nr05336g.
- [177] C. A. M. van den Bosch, A. Cavallaro, R. Moreno, G. Cibin, G. Kerherve, J. M. Caicedo, T. K. Lippert, M. Doebeli, J. Santiso, S. J. Skinner, and A. Aguadero, “Revealing Strain Effects on the Chemical Composition of Perovskite Oxide Thin Films Surface, Bulk, and Interfaces,” *Adv. Mater. Interfaces*, vol. 7, no. 2, pp. 1–10, 2020. DOI:10.1002/admi.201901440.
- [178] S. Schweiger, M. Kubicek, F. Messerschmitt, C. Murer, and J. L. M. Rupp, “A microdot multilayer oxide device: Let us tune the strain-ionic transport interaction,” *ACS Nano*, vol. 8, no. 5, pp. 5032–5048, 2014. DOI:10.1021/nn501128y.
- [179] Y. Shi, Y. Ji, F. Hui, M. Nafria, M. Porti, G. Bersuker, and M. Lanza, “In Situ Demonstration of the Link Between Mechanical Strength and Resistive Switching in Resistive Random-Access Memories,” *Adv. Electron. Mater.*, vol. 1, no. 4, p. 1400058, 2015. DOI:10.1002/aelm.201400058.
- [180] S. Ambrogio, S. Balatti, S. Choi, and D. Ielmini, “Impact of the mechanical stress on switching characteristics of electrochemical resistive memory,” *Adv. Mater.*, vol. 26, no. 23, pp. 3885–3892, 2014. DOI:10.1002/adma.201306250.
- [181] Y. Y. Chen, R. Roelofs, A. Redolfi, R. Degraeve, D. Crotti, A. Fantini, S. Clima, B. Govoreanu, M. Komura, L. Goux, L. Zhang, A. Belmonte, Q. Xie, J. Maes, G. Pourtois, and M. Jurczak, “Tailoring switching and endurance / retention reliability characteristics of HfO₂ / Hf RRAM with Ti, Al, Si dopants,” *Dig. Tech. Pap. - Symp. VLSI Technol.*, no. 59, pp. 1–2, 2014. DOI:10.1109/VLSIT.2014.6894403.
- [182] B. Traore, P. Blaise, E. Vianello, H. Grampeix, S. Jeannot, L. Perniola, B. De Salvo, and Y. Nishi, “On the Origin of Low-Resistance State Retention Failure in HfO₂-Based RRAM and Impact of Doping/Alloying,” *IEEE Trans. Electron Devices*, vol. 62, no. 12, pp. 4029–4036, 2015. DOI:10.1109/TED.2015.2490545.
- [183] H. Zhang, L. Liu, B. Gao, Y. Qiu, X. Liu, J. Lu, R. Han, J. Kang, and B. Yu, “Gd-doping effect on performance of HfO₂ based resistive switching memory devices using implantation approach,” *Appl. Phys. Lett.*, vol. 98, no. 4, pp. 1–4, 2011. DOI:10.1063/1.3543837.
- [184] C. S. Peng, W. Y. Chang, Y. H. Lee, M. H. Lin, F. Chen, and M. J. Tsai, “Improvement of

- resistive switching stability of HfO₂ films with Al doping by atomic layer deposition,” *Electrochem. Solid-State Lett.*, vol. 15, no. 4, pp. 88–90, 2012. DOI:10.1149/2.011204esl.
- [185] K. C. Chang, T. M. Tsai, T. C. Chang, Y. E. Syu, S. L. Chuang, C. H. Li, D. S. Gan, and S. M. Sze, “The effect of silicon oxide based RRAM with tin doping,” *Electrochem. Solid-State Lett.*, vol. 15, no. 3, pp. 65–68, 2012. DOI:10.1149/2.013203esl.
- [186] N. Raghavan, R. Degraeve, A. Fantini, L. Goux, D. J. Wouters, G. Groeseneken, and M. Jurczak, “Stochastic variability of vacancy filament configuration in ultra-thin dielectric RRAM and its impact on OFF-state reliability,” *Tech. Dig. - Int. Electron Devices Meet. IEDM*, pp. 21.1.1-21.1.4, 2013. DOI:10.1109/IEDM.2013.6724674.
- [187] S. H. Misha, N. Tamanna, J. Woo, S. Lee, J. Song, J. Park, S. Lim, J. Park, and H. Hwang, “Effect of nitrogen doping on variability of TaO_x-RRAM for low-power 3-bit MLC applications,” *ECS Solid State Lett.*, vol. 4, no. 3, pp. P25–P28, 2015. DOI:10.1149/2.0011504ssl.
- [188] H. Xu, D. H. Kim, Z. Xiahou, Y. Li, M. Zhu, B. Lee, and C. Liu, “Effect of Co doping on unipolar resistance switching in Pt/Co:ZnO/Pt structures,” *J. Alloys Compd.*, vol. 658, pp. 806–812, 2016. DOI:10.1016/j.jallcom.2015.11.018.
- [189] N. Sedghi, H. Li, I. F. Brunell, K. Dawson, R. J. Potter, Y. Guo, J. T. Gibbon, V. R. Dhanak, W. D. Zhang, J. F. Zhang, J. Robertson, S. Hall, and P. R. Chalker, “The role of nitrogen doping in ALD Ta₂O₅ and its influence on multilevel cell switching in RRAM,” *Appl. Phys. Lett.*, vol. 110, no. 10, pp. 1–6, 2017. DOI:10.1063/1.4978033.
- [190] L. F. Liu, J. F. Kang, N. Xu, X. Sun, C. Chen, B. Sun, Y. Wang, X. Y. Liu, X. Zhang, and R. Q. Han, “Gd doping improved resistive switching characteristics of TiO₂-based resistive memory devices,” *Jpn. J. Appl. Phys.*, vol. 47, no. 4 PART 2, pp. 2701–2703, 2008. DOI:10.1143/JJAP.47.2701.
- [191] B. Gao, H. W. Zhang, S. Yu, B. Sun, L. F. Liu, X. Y. Liu, Y. Wang, R. Q. Han, J. F. Kang, B. Yu, and Y. Y. Wang, “Oxide-based RRAM: Uniformity improvement using a new material-oriented methodology,” *Dig. Tech. Pap. - Symp. VLSI Technol.*, pp. 30–31, 2009.
- [192] H. Zhang, B. Gao, B. Sun, G. Chen, L. Zeng, L. Liu, X. Liu, J. Lu, R. Han, J. Kang, and B. Yu, “Ionic doping effect in ZrO₂ resistive switching memory,” *Appl. Phys. Lett.*, vol. 96, no. 12, pp. 98–101, 2010. DOI:10.1063/1.3364130.
- [193] C. Y. Liu, X. J. Lin, H. Y. Wang, and C. H. Lai, “Improved resistive switching dispersion of NiO_x thin film by Cu-doping Method,” *Jpn. J. Appl. Phys.*, vol. 49, no. 5 PART 1, pp. 0565071–0565074, 2010. DOI:10.1143/JJAP.49.056507.
- [194] B. Gao, J. F. Kang, H. W. Zhang, B. Sun, B. Chen, L. F. Liu, X. Y. Liu, R. Q. Han, Y. Y. Wang, B. Yu, Z. Fang, H. Y. Yu, and D. L. Kwong, “Oxide-based RRAM: Physical based retention projection,” *2010 Proc. Eur. Solid State Device Res. Conf. ESSDERC 2010*, pp. 392–395, 2010. DOI:10.1109/ESSDERC.2010.5618200.
- [195] F. M. Simanjuntak, D. Panda, K. H. Wei, and T. Y. Tseng, “Status and Prospects of ZnO-Based Resistive Switching Memory Devices,” *Nanoscale Res. Lett.*, vol. 11, no. 1, 2016. DOI:10.1186/s11671-016-1570-y.
- [196] W. Duan, Y. Tang, X. Liang, C. Rao, J. Chu, G. Wang, and Y. Pei, “Solution processed flexible resistive switching memory based on Al-In-O self-mixing layer,” *J. Appl. Phys.*, vol. 124, no. 10, pp. 1–10, 2018. DOI:10.1063/1.5041469.
- [197] Y. Cai, J. Tan, L. Yefan, M. Lin, and R. Huang, “A flexible organic resistance memory device for wearable biomedical applications,” *Nanotechnology*, vol. 27, no. 27, 2016. DOI:10.1088/0957-4484/27/27/275206.
- [198] C. Korte, J. Keppner, A. Peters, N. Schichtel, H. Aydin, and J. Janek, “Coherency strain and its effect on ionic conductivity and diffusion in solid electrolytes - an improved model for nanocrystalline thin films and a review of experimental data,” *Phys. Chem. Chem. Phys.*, vol. 16, no. 44, pp. 24575–24591, 2014. DOI:10.1039/c4cp03055a.
- [199] S. Schweiger and J. L. M. Rupp, *Strain and interfaces for metal oxide-based memristive devices*. Elsevier Inc., 2018. DOI:10.1016/b978-0-12-811166-6.00014-5.
- [200] J. L. M. Rupp, S. Schweiger, and F. Messerschmitt, “Strained multilayer resistive-switching memory elements.” Washington, DC: U.S. Patent and Trademark Office, Aug-2017.
- [201] S. Azad, O. A. Marina, C. M. Wang, L. Saraf, V. Shutthanandan, D. E. McCready, A. El-

- Azab, J. E. Jaffe, M. H. Engelhard, C. H. F. Peden, and S. Thevuthasan, "Nanoscale effects on ion conductance of layer-by-layer structures of gadolinia-doped ceria and zirconia," *Appl. Phys. Lett.*, vol. 86, no. 13, p. 131906, 2005. DOI:10.1063/1.1894615.
- [202] J. Garcia-Barriocanal, A. Rivera-Calzada, M. Varela, Z. Sefrioui, E. Iborra, C. Leon, S. J. Pennycook, and J. Santamaria, "Colossal Ionic Conductivity at Interfaces of Epitaxial $ZrO_2:Y_2O_3/SrTiO_3$ Heterostructures," *Science*, vol. 321, no. 5889, pp. 676–680, 2008. DOI:10.1126/science.1156393.
- [203] S. Sanna, V. Esposito, A. Tebano, S. Licocchia, E. Traversa, and G. Balestrino, "Enhancement of ionic conductivity in sm-doped ceria/yttria-stabilized zirconia heteroepitaxial structures," *Small*, vol. 6, no. 17, pp. 1863–1867, 2010. DOI:10.1002/smll.200902348.
- [204] S. Schweiger, R. Pfenninger, W. J. Bowman, U. Aschauer, and J. L. M. Rupp, "Designing Strained Interface Heterostructures for Memristive Devices," *Adv. Mater.*, vol. 29, no. 15, 2017. DOI:10.1002/adma.201605049.
- [205] Y. Jia, X. Tian, J. Si, S. Huang, Z. Wu, and C. Zhu, "Modulation of strain, resistance, and capacitance of tantalum oxide film by converse piezoelectric effect," *Appl. Phys. Lett.*, vol. 99, no. 1, pp. 1–4, 2011. DOI:10.1063/1.3609012.
- [206] W. Kim, D. J. Wouters, S. Menzel, C. Rodenbucher, R. Waser, and V. Rana, "Lowering forming voltage and forming-free behavior of Ta_2O_5 ReRAM devices," *Eur. Solid-State Device Res. Conf.*, vol. 2016-Octob, pp. 164–167, 2016. DOI:10.1109/ESSDERC.2016.7599612.
- [207] A. Demont, C. Prestipino, O. Hernandez, E. Elkaim, S. Paofai, N. Naumov, B. Fontaine, R. Gautier, and S. Cordier, "Unprecedented electron-poor octahedral Ta_6 clusters in a solid-state compound: Synthesis, characterisations and theoretical investigations of $Cs_2BaTa_6Br_{15}O_3$," *Chem. - A Eur. J.*, vol. 19, no. 38, pp. 12711–12719, 2013. DOI:10.1002/chem.201300777.

Appendix A

A.1 List of Abbreviations

AI	Artificial Intelligence
IoT	Internet of Things
FeRAM	Ferroelectric Random Access Memory
MRAM	Magnetoresistive Random Access Memory
PCM	Phase Change Memory
RRAM	Resistance (Switching) Random Access Memory
COMS	Complementary Metal-Oxide-Semiconductor
PLD	Pulsed Laser Deposition
MIM	Metal-insulator-metal
IRS	Initial Resistance State
LRS/RON	Low Resistance State
HRS/ROFF	High Resistance State
ECM	Electrochemical Metallization Memory
VCM	Valance Change Memory
RBS	Rutherford backscattering spectrometry
AES	Auger electron spectroscopy
XRD	X-ray diffraction
XPS	X-ray photoemission spectroscopy
FWHM	the full width at half maximum
ARXPS	angle-resolved X-ray photoelectron spectroscopy
SCS	semiconductor characterization system
SMU	source-measurement unit
SEM	scanning electron microscopy
XRR	X-ray reflectivity
RTA	rapid thermal annealing
STEM	scanning tunnelling electron microscopy
EDX	Energy Dispersive X-Ray Spectroscopy
PEN	Poly-Ethylene-Naphthalate
PET	Poly-Ethylene-Terephthalate
PDMS	Polydimethylsiloxane

A.2 The Ta₂O₅ target used in PLD

The commercial Ta₂O₅ target (99.99% purity, American Elements) has a diameter of 25.4 mm and a thickness of 6 mm. The target was investigated by X-ray diffraction (XRD) to ensure their phase purity before the deposition (Figure 55a and b). The XRD pattern of the as bought Ta₂O₅ is consistent with the reported literature,[207] with an orthorhombic structure of $a=6.1886(3)$ Å, $b=3.66227(13)$ Å, and $c=7.7838(2)$ Å, space group Pccm (49). The Ta₂O₅ target changed from white colour (Figure 55b and c) to black colour (Figure 55d) after being ablated by the laser, but the XRD patterned remained constant (Figure 55a to d), which indicated no change of the target itself.

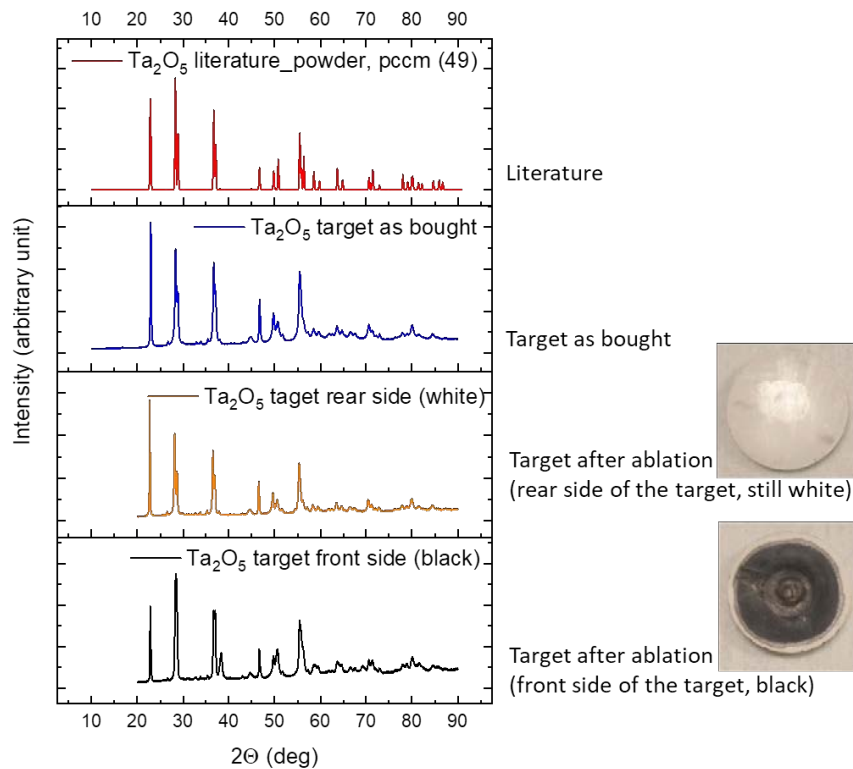
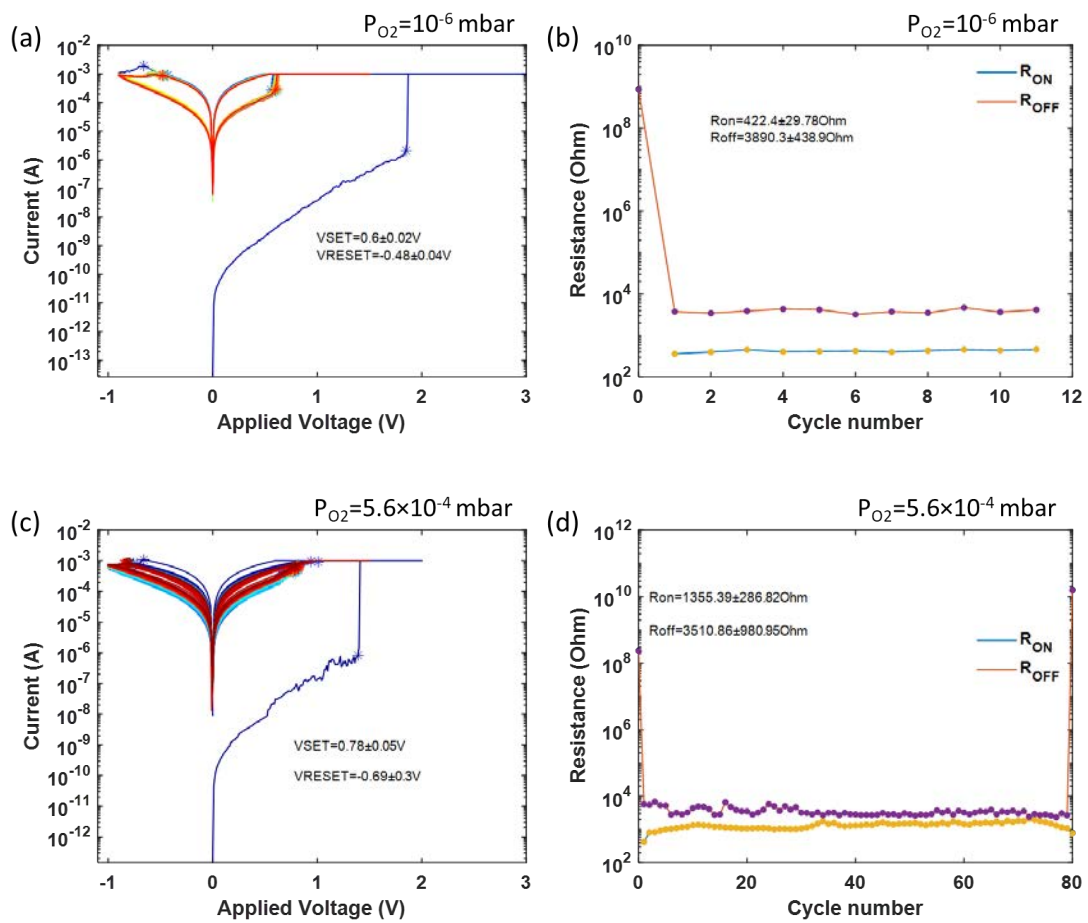
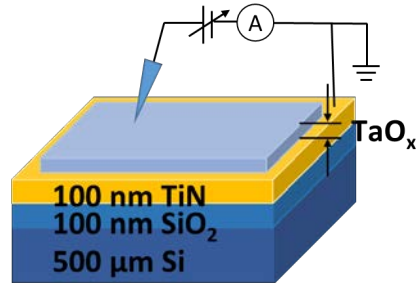


Figure 55 The XRD spectra of (a) the Ta₂O₅ from literature (ICSD database),[207] (b) the as-bought Ta₂O₅ target (white), (c) the rear side of the Ta₂O₅ after PLD laser ablation (white), and (d) the front side of the Ta₂O₅ after PLD laser ablation (black).

A.3 Typical I - V curves for TiN/TaO_x/W (tip probe) devices

TiN/TaO_x/W probe tip (top electrode, 500 nm diameter)



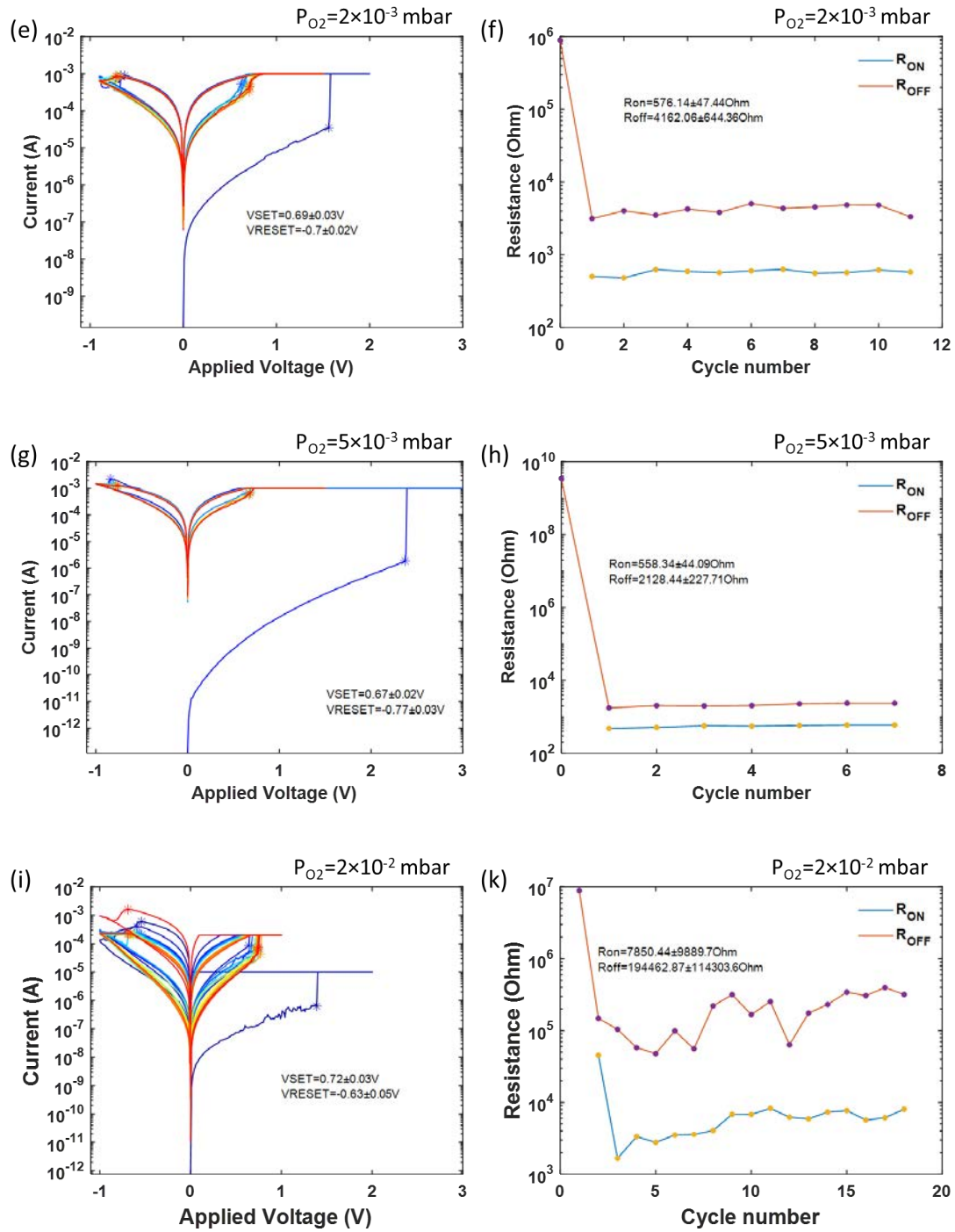


Figure 56 Typical resistive switching behaviour of the TiN/TaO_x/W probe tip structured device. The left column is the typical IV curves and the right column is the initial resistance, LRS and HRS resistances. The TaO_x thin films used in the devices were deposited at 10⁻⁶, 5.6 × 10⁻⁴, 2 × 10⁻³, 5 × 10⁻³, and 2 × 10⁻² mbar, respectively (from top to down). All the TaO_x thin films were deposited at room temperature, with laser energy of 4 J/cm² (10 Hz) for 10 min. The W probe tip acted as the top electrode and has a diameter of 500 nm.

A.4 Height deformation calibrated in 525 μm Si substrates

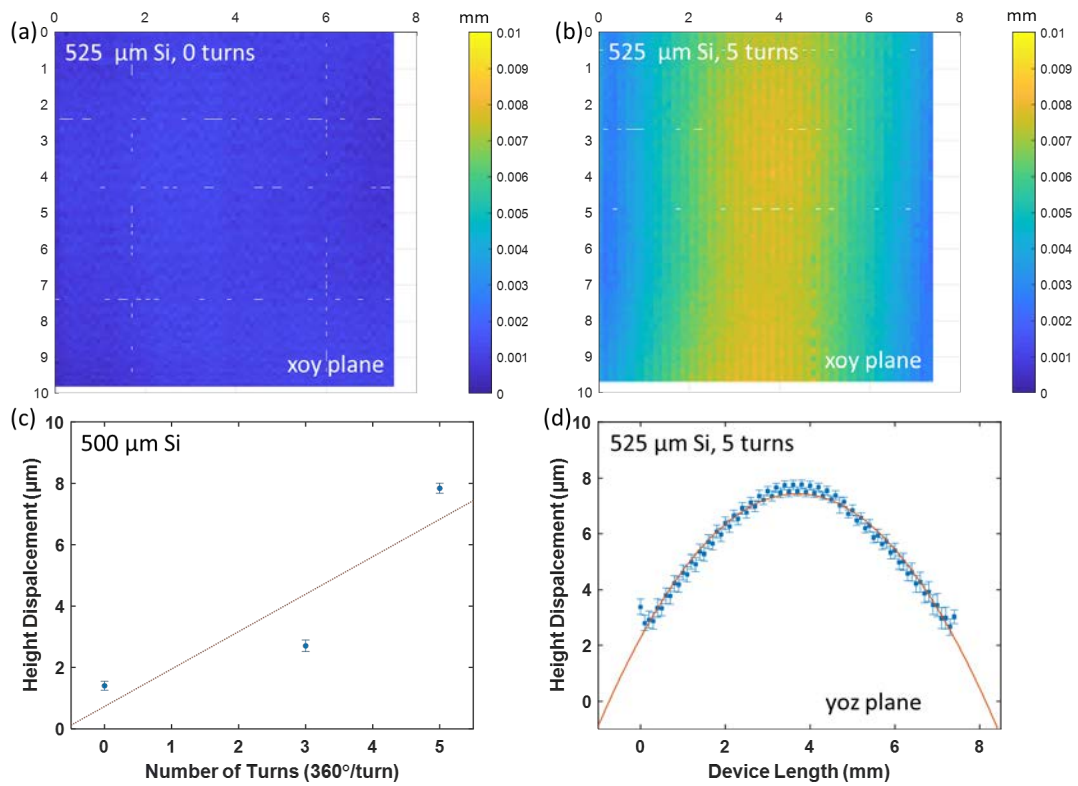
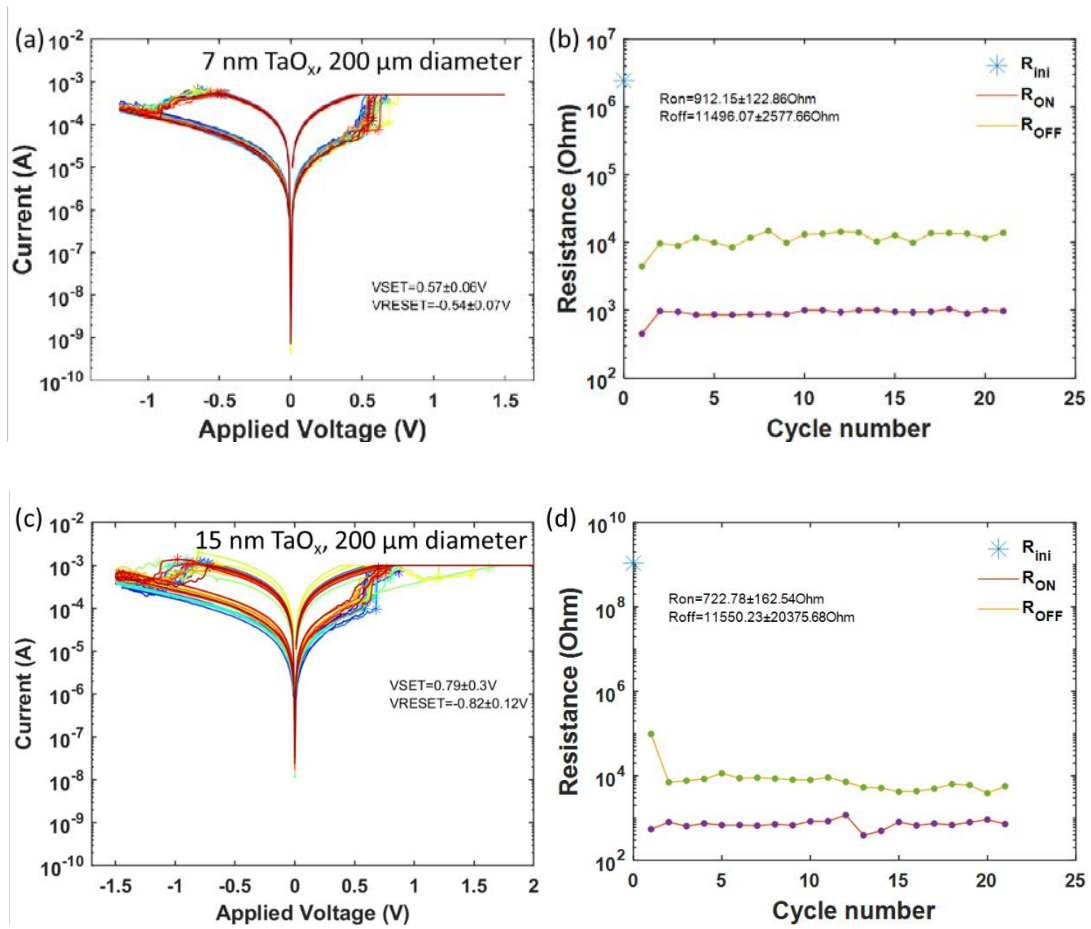
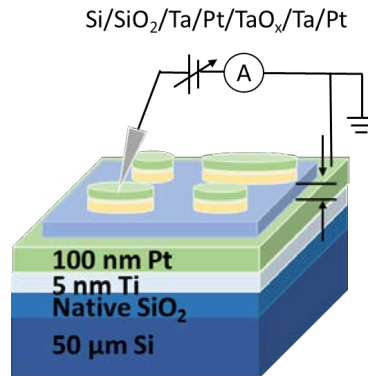


Figure 57 The mechanical deformation of 525 \pm 20 μm thick Si under strain. (a) No deformation of the Si substrate, (b) the maximum deformation of the Si substrate before breaking, (c) the relationship between the number of turns of the strew in the strainer and the maximum height deformation in Si, (d) the yoz plane view of the Si under maximum strain.

A.5 Typical I - V curves for Pt/TaO_x/Ta devices



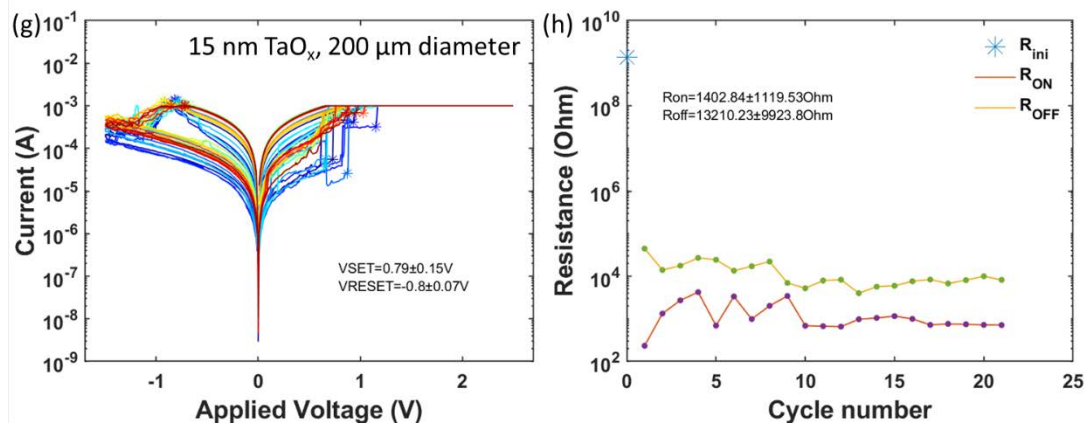


Figure 58 Typical resistive switching behaviour of the Pt/TaO_x/Ta devices. The left column is the typical IV curves and the right column is the initial resistance state, LRS and HRS. The TaO_x thin films used in the devices were deposited at the same conditions by sputtering with different thicknesses of 7n, 14 nm, and 25 nm.

Appendix B

List of Publications

The following articles are published, submitted or under preparation during this PhD project.



Y. Li, S. Sanna, K. Norrman, D. V. Christensen, C. S. Pedersen, J. M. G. Lastra, M. L. Traulsen, V. Esposito, and N. Pryds, “Tuning the stoichiometry and electrical properties of tantalum oxide thin films,” *Appl. Surf. Sci.*, vol. 470, no. November 2018, pp. 1071–1074, 2019. DOI:10.1016/j.apsusc.2018.11.153. [143]



Y. Li, Y. E. Suyolcu, S. Sanna, D. V. Christensen, M. L. T., E. Stamate, C. S. Pedersen, P. A. van Aken, J. M. G. Lastra, V. Esposito, and Nini Pryds, “Tuning the Resistive Switching in Tantalum Oxide Based Memristors by Annealing”, under review for AIP Advances (2020).



Y. Li, D. V. Christensen, S. Sanna, V. Esposito, and N. Pryds, “The effect of external stimuli on the performance of memristive oxides”, book chapter in “Metal Oxides for Non-volatile Memory: Technology and Applications”, Elsevier (2020).



C. S. Pedersen, J. H. Chang, **Y. Li**, N. Pryds, and J. M. G. Lastra, “Phase separation and mixing in amorphous tantalum-oxide from first principles”, submitted to Nanoscale (2020).

Y. Li, S. Sanna, K. Norrman, D. V. Christensen, C. S. Pedersen, J. M. G. Lastra, M. L. Traulsen, V. Esposito, and N. Pryds
Tuning the stoichiometry and electrical properties of tantalum oxide thin films
Appl. Surf. Sci., vol. 470, no. November 2018, pp. 1071–1074, 2019.
DOI:10.1016/j.apsusc.2018.11.153.



Copenhagen Harbour (19th August 2017)
Photo: Yang Li



Contents lists available at ScienceDirect

Applied Surface Science

journal homepage: www.elsevier.com/locate/apsusc

Short Communication

Tuning the stoichiometry and electrical properties of tantalum oxide thin films



Yang Li^a, Simone Sanna^a, Kion Norrman^a, Dennis Valbjørn Christensen^a,
Christian Søndergaard Pedersen^b, Juan María García Lastra^b, Marie Lund Traulsen^a,
Vincenzo Esposito^a, Nini Pryds^{a,*}

^a Department of Energy Conversion and Storage, Technical University of Denmark, Roskilde, 4000, Denmark

^b Department of Energy Conversion and Storage, Technical University of Denmark, Kgs. Lyngby, 2800, Denmark

ABSTRACT

Tantalum oxide has a wide range of applications and has drawn much attention especially for its useful properties in resistive random-access memories, in which the Ta oxide composition plays an important role to control the electrical properties of the TaO_x thin films. In this paper, we present a way to tune the composition of TaO_x thin films by varying the oxygen partial pressure during growth using pulsed laser deposition. TaO_x thin films were deposited at room temperature, under oxygen partial pressures ranging from 10⁻⁶ mbar to 2 × 10⁻² mbar. Using angle resolved X-ray photoelectron spectroscopy, we show that the composition of the film varies systematically with the oxygen partial pressure during the film growth. We then correlate the oxygen content with the electrical properties of the film and the results show that the composition has a great influence on the resistivity of the TaO_x thin films. As the oxygen partial pressure during deposition increases, the percentage of tantalum pentoxide (Ta₂O₅) as well as the resistivity of the films increases. This experimental approach provides a pathway to control the TaO_x thin film stoichiometry and its electrical properties during growth.

Tantalum oxide (TaO_x) is a promising candidate for a wide range of applications such as antireflection coatings [1,2], optical waveguides [3,4], hydrogen generation photocatalysts [5,6], and dielectric materials in the microelectronic industry [7,8]. TaO_x thin film has recently drawn much attention as a non-volatile memory material which makes it suitable for resistive random access memories (RRAMs) [9–12]. Due to the excellent performances of TaO_x based RRAMs such as a large endurance of 10¹² cycles [11] and a fast switching speed of sub-nano second [12], it becomes one of the promising materials for memory application. Seen from fabrication point of view, since a high-temperature process is not preferable in complementary metal oxide semiconductor (CMOS) fabrication process, TaO_x deposited at room temperature is often preferred. The resistive switching phenomenon in this family of materials is usually achieved by partially switching the TaO_x thin film between a highly resistive state of tantalum pentoxides (Ta₂O₅) and a more conductive state of TaO_{x < 2.5} under external electrical field [10,11]. Understanding the parameters influencing the different phases of TaO_x and their electrical characteristics is thus essential for memristor device design. The electrical properties of TaO_x have been found to be greatly influenced by the oxygen content and often very small changes in the deposition parameters cause profound change in the functionality of the film. Tantalum oxide films with different stoichiometry have been reported by using several methods,

including thermal oxidation [13], sputtering [14–20], chemical vapor deposition (CVD) [21,22], photolysis [23], atomic layer deposition (ALD) [24,25], sol-gel method [26], and pulsed laser deposition (PLD) [27–34]. A direct detailed dependence between the stoichiometry of the film and the resistivity of tantalum oxide were so far reported mainly for sputtering deposition method [17–20], but there are no reports on the relation between the deposition condition and the film performance for PLD based samples. Although tantalum oxide thin films deposited by PLD were widely studied [27–39], focus was mainly put on the optical properties, [27,28,30,31,33,35,36,38,39] leakage current [27,29,33,35,36] and dielectric constant [27] of the oxide films. In order to be able to control the exact phases formed during the deposition, understanding of the relation between the film stoichiometry and the deposition conditions, especially the oxygen partial pressure, are desirable. Here we conduct a systematic experimental study to determine and understand the relationship between the Ta oxidation state and the electrical properties of the film. Understanding this will provide a tool to fabricate highly controlled TaO_x films with tailored properties at room temperature.

TaO_x films were deposited using a PLD setup as described elsewhere [40]. A KrF excimer laser (248 nm, 10 Hz, 4 J/cm²) was used to ablate a commercial ceramic target of Ta₂O₅ (American Elements) with 99.99% purity and dimensions of 25.4 mm in diameter and 6 mm in thickness.

* Corresponding author.

E-mail address: nipr@dtu.dk (N. Pryds).

<https://doi.org/10.1016/j.apsusc.2018.11.153>

Received 27 June 2018; Received in revised form 6 November 2018; Accepted 19 November 2018

Available online 23 November 2018

0169-4332/ © 2018 Elsevier B.V. All rights reserved.

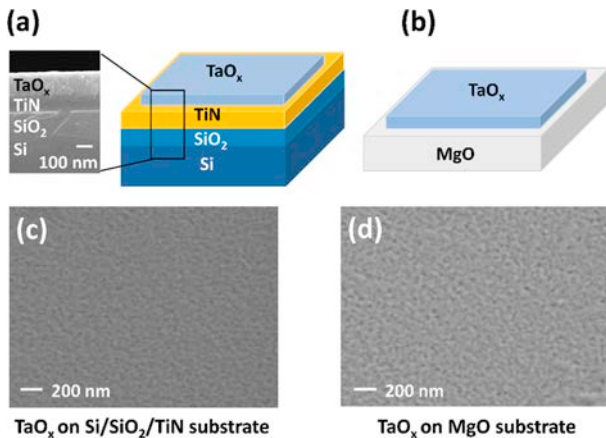


Fig. 1. (a) A schematic illustration of TaO_x film deposited on Si/SiO₂/TiN substrate. The inset shows a cross sectional SEM image of the film stack. (b) A schematic illustration of TaO_x film deposited on MgO (100) substrate. (c) SEM picture showing the surface of TaO_x film deposited on Si/SiO₂/TiN substrate. (d) SEM picture showing the surface of TaO_x film deposited on MgO (100) substrate. The TaO_x films shown here are all deposited under 10^{-6} mbar at room temperature.

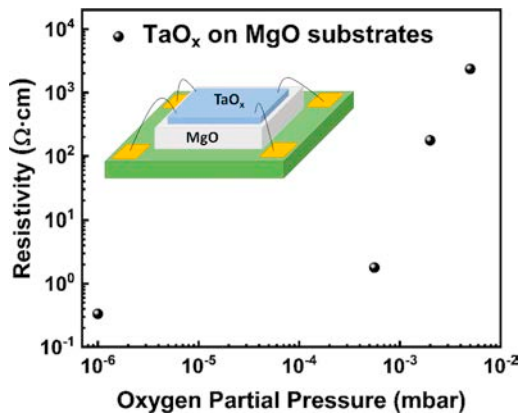


Fig. 2. The relation between TaO_x thin film resistivity and oxygen partial pressure during deposition. The inset figure shows the van der Pauw configuration for resistivity test. Since the figure is plotted in double logarithmic coordinates, the error bars are not included due to lack of visibility. The relative standard deviation (σ/μ) of the resistivity is smaller than 13%.

Two types of commercial substrates were used in this study: (1) (100) silicon substrates with 100 ± 10 nm silicon di-oxide and 100 nm sputtered TiN film on top, labeled as Si/SiO₂/TiN substrates and (2) single crystal (100) MgO substrates. The TiN layer in the Si/SiO₂/TiN substrate acts as a conducting layer, whereas the MgO substrates were insulating. Both substrates and target were investigated with X-ray diffraction (XRD) to ensure their phase purity prior to the deposition. The deposition was carried out by keeping the target-substrate distance constant at 7.5 cm, while the deposition time was chosen to be either 10 or 60 min at room temperature. The oxygen partial pressure was varied from 10^{-6} mbar (base pressure) to 2×10^{-2} mbar and five different values of oxygen partial pressures were used in total. X-ray diffraction (XRD) and scanning electron microscope (SEM) were employed on all films to characterize the crystalline quality and the morphology of the films. The oxidation states of Ta in the TaO_x films were determined by angle resolved X-ray photoelectron spectroscopy (ARXPS). The ARXPS analyses were performed on a ESCALAB XI⁺ X-ray photoelectron spectrometer microprobe (Thermo Fisher Scientific, East Grinstead, U.K.) using a monochromatic Al-K α X-ray source with a 900 nm spot size. A combined ion/electron gun (i.e. a dual beam source) was used to

control sample charging. The electrical conductivity was measured on a rectangular shaped sample (10 mm \times 10 mm) in a Van der Pauw configuration using a station probe (Imina).

Fig. 1(a) and **(b)** show the schematic configurations of the deposited films together with a micrograph showing a cross-sectional SEM image of the TaO_x film deposited on TiN substrate (at $P_{O_2} = 10^{-6}$ mbar, room temperature). The TaO_x thin films deposited at $P_{O_2} = 10^{-6}$ mbar on Si/SiO₂/TiN and MgO substrates show a typical similar surface morphology, as illustrated in **Fig. 1(c)** and **(d)**, respectively. TaO_x thin films grown at different oxygen partial pressures all show similar microstructures. XRD of TaO_x films deposited at different oxygen partial pressure shows that all the films deposited on top of the Si/SiO₂/TiN substrate have no distinct diffraction peak other than the one belong to substrate peaks, indicating the existence of an amorphous structure (**supplementary material, Fig. S1**).

Since the memristors operate at room temperature, the resistivity of different TaO_x films were measured at this temperature. **Fig. 2** shows the results of the room-temperature resistivity of TaO_x thin films grown on MgO substrates for 60 min as a function of oxygen partial pressure in the PLD chamber. The resistivity of the films did not show very minor anisotropy in the plane of the film. The result shows that the resistivity increases from 0.33 Ω -cm up to 2.34 k Ω -cm as the oxygen partial pressure increases from 10^{-6} mbar to 5×10^{-3} mbar. The resistivity of the TaO_x film grown at an oxygen partial pressure of 2×10^{-2} mbar was high above the measurement limit. The oxygen partial pressure can therefore be used as a convenient knob to tune the conductivity towards a more insulating phase as the pressure is increased.

The chemical composition of the TaO_x thin films were examined by ARXPS. High resolution local binding energy spectra, as shown in **Fig. 3**, were obtained for Ta-4f using 20 eV detector pass energy, 50 ms dwell time, 0.02 eV energy step size, and collected over 5 scans. Fitting analysis of the Ta 4f peaks and thus quantification of the Ta oxidation states is based on the approach by Simpson et al. [41]. Peaks were fitted using a 38% Lorentzian/Gaussian function, a 4f5/4f7 spin orbit splitting of 1.9 eV, and a 4f5/4f7 height ratio of 0.788. **Fig. 3** presents Ta 4f ARXPS spectra obtained at an emission angle of $\theta = 0^\circ$ relative to the perpendicular direction to the surface of the sample (i.e. maximum escape depth), showing the main Ta⁵⁺ peak together with lower oxidation states. These are Ta⁴⁺, Ta³⁺, Ta²⁺, Ta¹⁺, and Ta⁰ representing TaO₂, Ta₂O₃, TaO, Ta₂O, and Ta metal, respectively. The main peaks observed are the Ta 4f 7/2 and the Ta 4f 5/2 peaks at binding energies of 26.9 ± 0.1 eV and 28.8 ± 0.1 eV, respectively. This confirms that most of the deposited thin films are composed of Ta₂O₅. The fit of the Ta 4f peaks and thus quantification of the Ta oxidation states is based on the approach by Simpson et al. [41]. (The comparison between the binding energies for each oxidation states used in the work of Simpson et al. [41] and this paper is shown in the **supplementary material Table S1**.)

In order to investigate the composition homogeneity along the film growth direction and the surface oxidation conditions of the TaO_x thin films, ARXPS were carried out and the emission angles θ , relative to the perpendicular direction of the surface of the sample, vary from 0° to 90° (grazing angle), which corresponds to the maximum probe depth of ~ 10 nm and the upper surface layer of the TaO_x thin films, respectively. As show in **Fig. 4(a)**, for TaO_x thin films deposited under high oxygen partial pressure (5×10^{-3} mbar) for a short time (10 min) corresponding to a film thickness of 23 ± 4 nm, the composition of TaO_x thin film is homogeneous for all emission angles, which means a homogeneous Ta oxidation states composition from surface to approximately 10 nm deep under the surface. As compared to the TaO_x deposited for the same time but under a lower oxygen partial pressure (10^{-6} mbar) corresponding to a film thickness of 6 ± 1 nm, the composition of Ta₂O₅ increases as the emission angle increases, which indicate a higher Ta₂O₅ composition near the film surface, as shown in **Fig. 4(b)**. This finding is in consistency with the work of Sharath et al. [42] Furthermore, as the thickness of the films increase, the

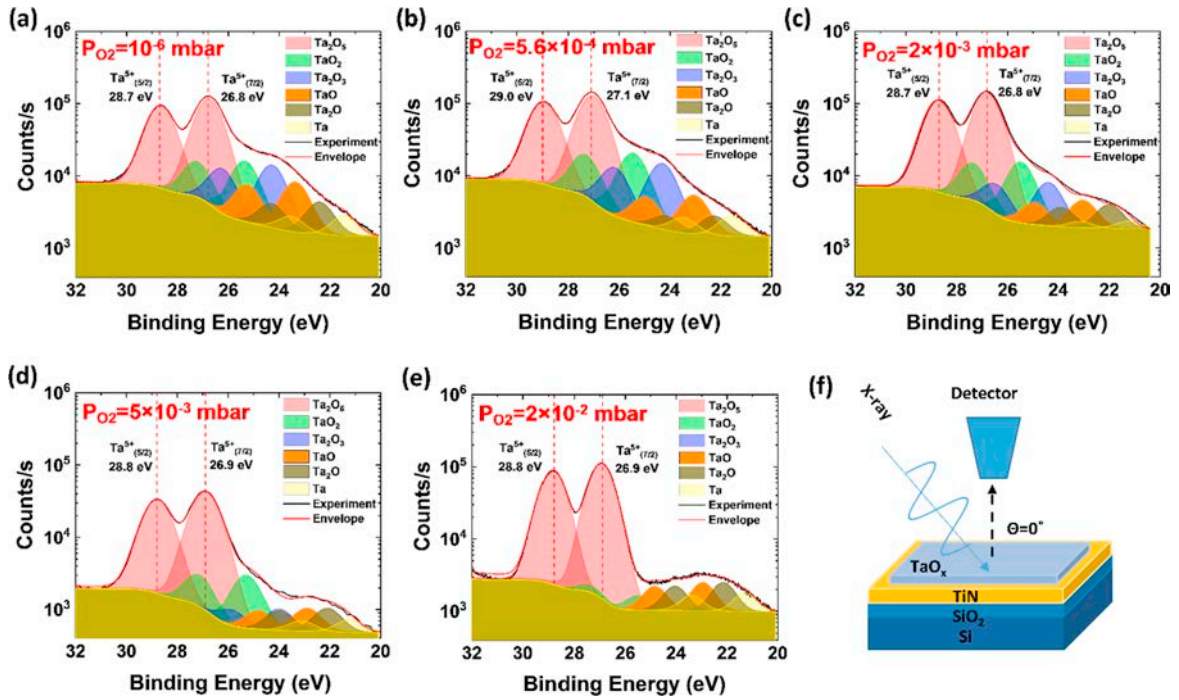


Fig. 3. Ta 4f XPS spectra of TaO_x thin films deposited for 60 min under different oxygen partial pressure of: (a) $P_{\text{O}_2} = 10^{-6}$ mbar, (b) $P_{\text{O}_2} = 5.6 \times 10^{-4}$ mbar, (c) $P_{\text{O}_2} = 2 \times 10^{-3}$ mbar, (d) $P_{\text{O}_2} = 5 \times 10^{-3}$ mbar, and (e) $P_{\text{O}_2} = 2 \times 10^{-2}$ mbar. The solid black lines are the experiment XPS spectra data and the solid red lines are the fitting envelopes of the XPS spectra data.

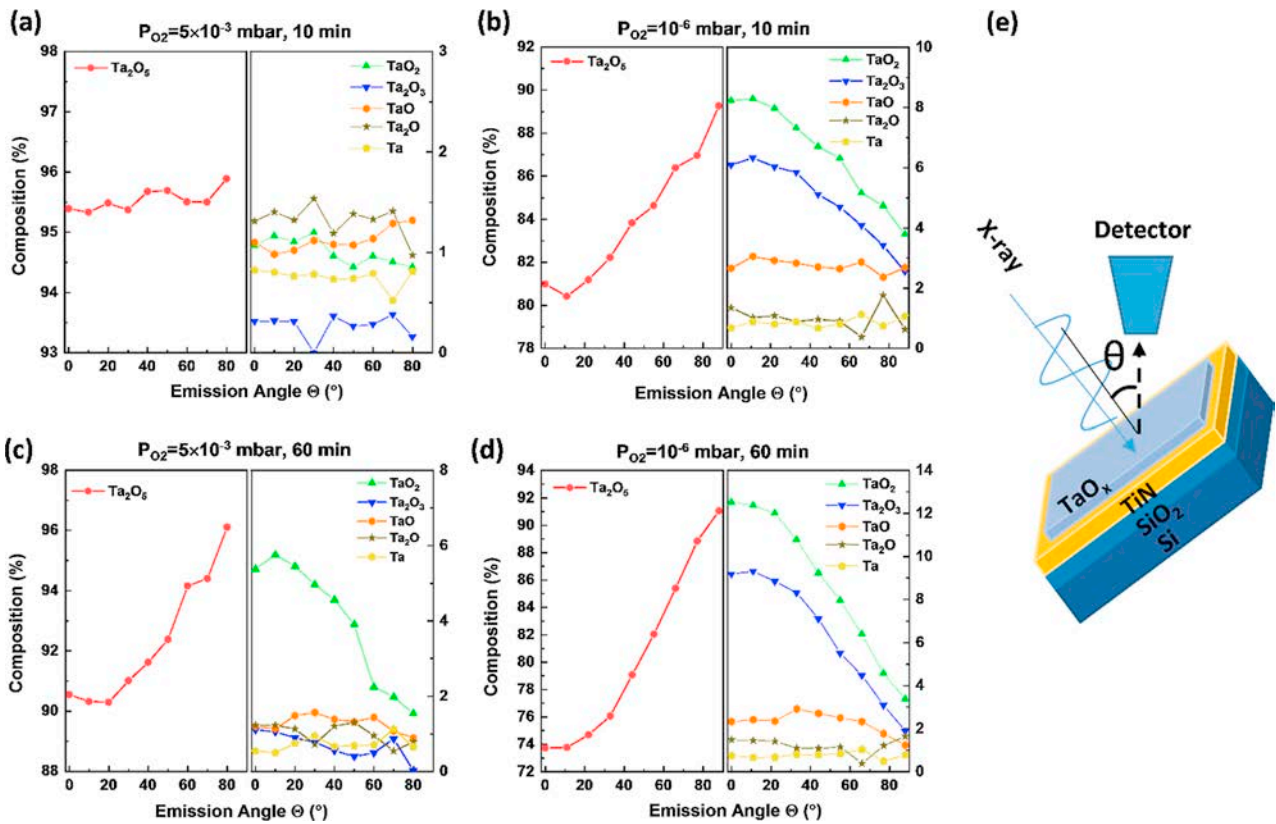


Fig. 4. The Ta oxidation states of TaO_x films deposited under different conditions revealed by ARXPS spectra. (a) oxygen partial pressure of $P_{\text{O}_2} = 5 \times 10^{-3}$ mbar for deposition time of 10 min, (b) oxygen partial pressure of $P_{\text{O}_2} = 10^{-6}$ mbar for deposition time of 10 min, (c) oxygen partial pressure of $P_{\text{O}_2} = 5 \times 10^{-3}$ mbar for deposition time of 60 min, and (d) oxygen partial pressure of $P_{\text{O}_2} = 10^{-6}$ mbar for deposition time of 60 min. (e) is a schematic illustration of the principle of ARXPS. The angle θ is the emission angle relative to the perpendicular direction of the surface of the sample. By changing the emission angle, the sampling depth decreases from ~ 10 nm at $\theta = 0^\circ$ to the very surface of the film at $\theta = 90^\circ$.

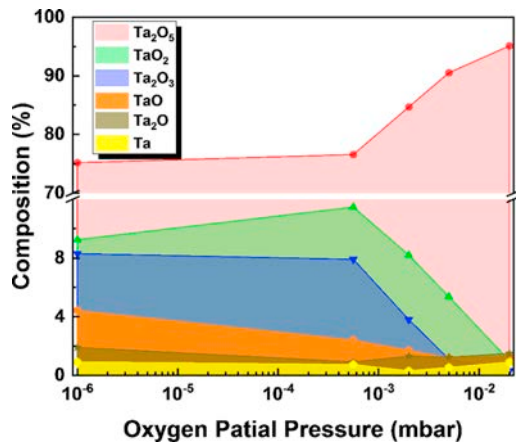


Fig. 5. The Ta oxidation states inside TaO_x thin films deposited under different oxygen partial pressure for 60 min at room temperature.

composition of the thin films deposited at high oxygen partial pressure is not homogeneous any longer from surface to approximately 10 nm deep under the surface and a composition gradient along the film growth direction can be seen for films deposited at both high and low oxygen partial pressure, as shown in Fig. 4(c) and (d), respectively.

Fig. 5 illustrates the Ta oxidation states in the TaO_x films as a function of oxygen partial pressure. The percentage of Ta oxidation states in the TaO_x films are obtained from the XPS data taken at an emission angle of 0°. The percentage of Ta⁵⁺ (Ta₂O₅) increases from 75 at.% to 95 at.% as the oxygen partial pressure increases from 10⁻⁶ mbar to 2 × 10⁻² mbar while the contribution from the lower oxidation state reduces. By comparing the XPS results, it is clear that it requires very low oxygen partial pressures to form lower oxidation state than the Ta⁵⁺ in a significant concentration. Comparing the XPS results of samples deposited at the same oxygen partial pressure, but different deposition duration of 60 min and 10 min (supplementary material S2), the results indicate that combining long deposition duration with low oxygen partial pressure provides the most efficient way to form lower oxidation states in significant concentrations.

In summary, we demonstrated the influence of oxygen partial pressure during PLD growth on the properties and stoichiometry of TaO_x films. This was used to tune the oxygen content in the film and therefore the resistivity of the TaO_x films. Our approach suggests that the future design of the desired initial state of the memory devices which depend very much of the phases used can be attained by choosing the right deposition parameters.

Acknowledgment

The authors thank the support from the Independent Research Fund Denmark, Grant No. 6111-00145B.

Appendix A. Supplementary material

Supplementary data to this article can be found online at <https://doi.org/10.1016/j.apsusc.2018.11.153>.

References

- [1] C.T. Wu, F.H. Ko, C.H. Lin, Appl. Phys. Lett. 90 (2007) 2005.
- [2] F. Rubio, J. Denis, J.M. Albella, J.M. Martinez-Duart, Thin Solid Films 90 (1982) 405.
- [3] T. Chen Sverre, J.R.C. Woods, P. Hua, J.S. Wilkinson, A.C. Tropper, V. Apostolopoulos, E.A. Shaw, Vert. Extern. Cavity Surf. Emit. Lasers VIII 29 (2018).
- [4] A. Aghajani, G.S. Murugan, N.P. Sessions, V. Apostolopoulos, J.S. Wilkinson, Opt. Lett. 40 (2015) 2549.
- [5] V.S. Souza, J.D. Scholten, D.E. Weibel, D. Eberhardt, D.L. Baptista, S.R. Teixeira, J. Dupont, J. Mater. Chem. A 4 (2016) 7469.
- [6] M.M. Momeni, M. Mirhosseini, M. Chavoshi, A. Hakimzade, J. Mater. Sci. Mater. Electron. 27 (2016) 3941.
- [7] A.I. Kingon, J.P. Maria, S.K. Streiffer, Nature 406 (2000) 1032.
- [8] C. Chanelliere, J.L. Autran, R.A.B. Devine, B. Bolland, Mater. Sci. Eng. R Reports 22 (1998) 269.
- [9] I.T. Wang, Y.C. Lin, Y.F. Wang, C.W. Hsu, T.H. Hou, Tech. Dig. - Int. Electron Devices Meet. IEDM 2015-Febru, 28.5.1 (2015).
- [10] M.J. Lee, C.B. Lee, D. Lee, S.R. Lee, M. Chang, J.H. Hur, Y.B. Kim, C.J. Kim, D.H. Seo, S. Seo, U.I. Chung, I.K. Yoo, K. Kim, Nat. Mater. 10 (2011) 625.
- [11] Y.-B. Kim, S.R. Lee, D. Lee, C.B. Lee, M. Chang, J.H. Hur, M.-J. Lee, G.-S. Park, C.J. Kim, U.-I. Chung, I.-K. Yoo, K. Kim, in: Symp. VLSI Technol. - Dig. Tech. Pap., vol. 52, 2011.
- [12] A.C. Torrezan, J.P. Strachan, G. Medeiros-Ribeiro, R.S. Williams, Nanotechnology 22 (2011).
- [13] G.S. Oehrlein, F.M. D'Heurle, A. Reisman, J. Appl. Phys. 55 (1984) 3715.
- [14] H. Demiryont, J.R. Sites, K. Geib, Appl. Opt. 24 (1985) 490.
- [15] A.J. Lohn, J.E. Stevens, P.R. Mickel, M.J. Marinella, Appl. Phys. Lett. 103 (2013).
- [16] M.T. Brumbach, P.R. Mickel, A.J. Lohn, A.J. Mirabal, M.A. Kalan, J.E. Stevens, M.J. Marinella, J. Vac. Sci. Technol. A Vacuum, Surfaces, Film 32 (2014) 051403.
- [17] D. Gerstenberg, C.J. Calbick, J. Appl. Phys. 35 (1964) 402.
- [18] I. Goldfarb, F. Miao, J.J. Yang, W. Yi, J.P. Strachan, M.X. Zhang, M.D. Pickett, G. Medeiros-Ribeiro, R.S. Williams, Appl. Phys. A Mater. Sci. Process. 107 (2012) 1.
- [19] F. Miao, W. Yi, I. Goldfarb, J.J. Yang, M.X. Zhang, M.D. Pickett, J.P. Strachan, G. Medeiros-Ribeiro, R.S. Williams, ACS Nano 6 (2012) 2312.
- [20] J.E. Stevens, A.J. Lohn, S.A. Decker, B.L. Doyle, P.R. Mickel, M.J. Marinella, J. Vac. Sci. Technol. A Vacuum, Surfaces, Film. 32 (2014) 021501.
- [21] L. Corp, S. Joseph, J. Wiley, N. York, W.R. Hitchens, W.C. Krusell, D.M. Dobkin, Mater. Sci. Eng. R 22 (1993) 269.
- [22] S.R. Jeon, S.W. Han, J.W. Park, J. Appl. Phys. 77 (1995) 5978.
- [23] Y. Imai, A. Watanabe, M. Mukaida, K. Osato, T. Kameyama, Thin Solid Film 261 (261) (1995) 76.
- [24] K. Kukli, M. Ritala, M. Leskela, J. Electrochem. Soc. 142 (1995) 1670.
- [25] K. Kukli, J. Aarik, A. Aidla, O. Kohan, T. Uustare, V. Sammelselg, Thin Solid Films 260 (1995) 135.
- [26] T. Ohishi, S. Maekawa, A. Katoh, J. Non. Cryst. Solids 147–148 (1992) 493.
- [27] Fu. Zhou Mingfei, Yang Haijun Zhengwen, Zhang Zhuangjian, Qin Qizong, Appl. Surf. Sci. 108 (1997) 399.
- [28] S. Boughaba, M.U. Islam, G.I. Sproule, M.J. Graham, Surf. Coatings Technol. 120–121 (1999) 757.
- [29] Q. Qin, Z. Fu, Adv. Mater. 11 (1999) 1119.
- [30] J.-Y. Zhang, I.W. Boyd, Appl. Surf. Sci. 168 (2000) 234.
- [31] S. Boughaba, G.I. Sproule, J.P. McCaffrey, M. Islam, M.J. Graham, Thin Solid Films 358 (2000) 104.
- [32] T. Hino, M. Nishida, T. Araki, Surf. Coatings Technol. 149 (2002) 1.
- [33] T. Hino, S. Mustofa, M. Nishida, T. Araki, Appl. Surf. Sci. 189 (2002) 1.
- [34] F. Kurnia, Hadiyawanman, C.U. Jung, R. Jung, C. Liu, Phys. Status Solidi - Rapid Res. Lett. 5 (2011) 253.
- [35] J.-Y. Zhang, Q. Fang, I.W. Boyd, Appl. Surf. Sci. 138–139 (1999) 320.
- [36] J.-Y. Zhang, I.W. Boyd, Appl. Phys. A Mater. Sci. Process. 70 (2000) 657.
- [37] O.K. Donaldson, K. Hattar, J.R. Trelewicz, E.I.C. Johnson, J. Am. Ceram. Soc. 99 (2016) 3775.
- [38] H.O. Sankur, W. Gunning, Appl. Opt. 28 (1989) 2806.
- [39] Y. Nishimura, U. Hiroki, T. Ochiai, M. Tsuji, Appl. Surf. Sci. 79–80 (1994) 165.
- [40] D.V. Christensen, F. Trier, M. Von Soosten, G.E.D.K. Prawiroatmodjo, T.S. Jespersen, Y.Z. Chen, N. Pryds, Appl. Phys. Lett. 109 (2016).
- [41] R. Simpson, R.G. White, J.F. Watts, M.A. Baker, Appl. Surf. Sci. 405 (2017) 79.
- [42] S.U. Sharath, M.J. Joseph, S. Vogel, E. Hildebrandt, P. Komissinskiy, J. Kurian, T. Schroeder, L. Alff, Appl. Phys. Lett. 109 (2016) 1.

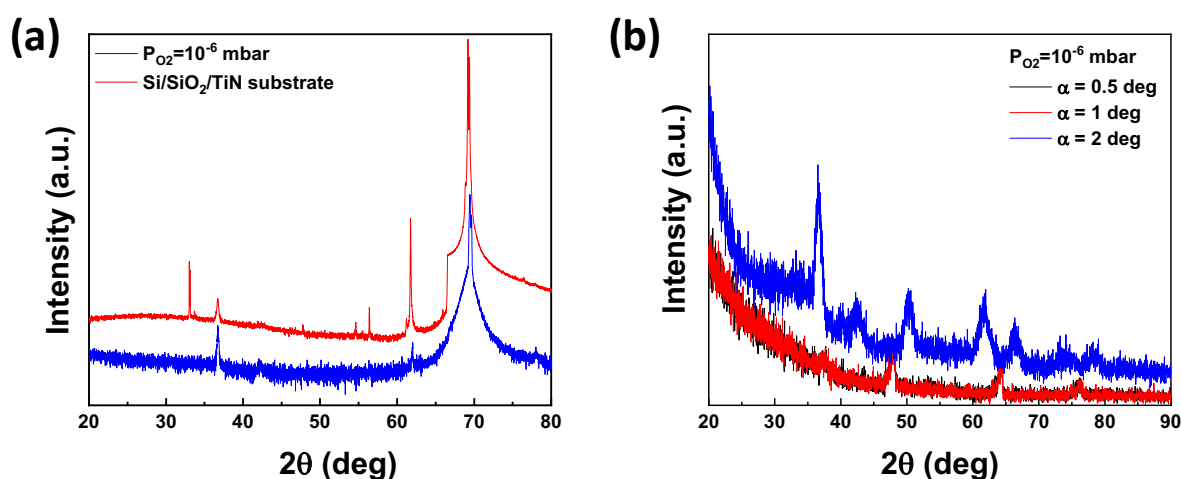
Tuning the stoichiometry and electrical properties of tantalum oxide thin films– Supplementary material

Yang Li,¹ Simone Sanna,¹ Kion Norrman,¹ Dennis Valbjørn Christensen,¹ Christian Søndergaard Pedersen,² Juan Maria García Lastra,² Marie Lund Traulsen,¹ Vincenzo Esposito,¹ and Nini Pryds^{1*}

¹ Department of Energy Conversion and Storage, Technical University of Denmark, Roskilde, 4000, Denmark

² Department of Energy Conversion and Storage, Technical University of Denmark, Kgs. Lyngby, 2800, Denmark

XRD Bruker D8 Advanced diffractometer (Germany) with Cu K α ($\lambda=1.5406$ Å) radiation was used for XRD characterization. The XRD data in Figure S1 (a), (c), and (e) were collected in theta-2 theta configuration scanning from 20° to 80° with a step size of 0.01° (0.2 seconds per step) at room temperature. The grazing-incidence small-angle scattering data in Figure S1 (b), (d), and (f) were collected using the same diffractometer at room temperature. The X-ray incident angles were set to 0.5°, 1°, and 2°, respectively. The detector scanned in 2 theta range 20° \leq 2 θ \leq 90° with a step size of 0.02° (0.5 seconds per step).



*Email: nipr@dtu.dk

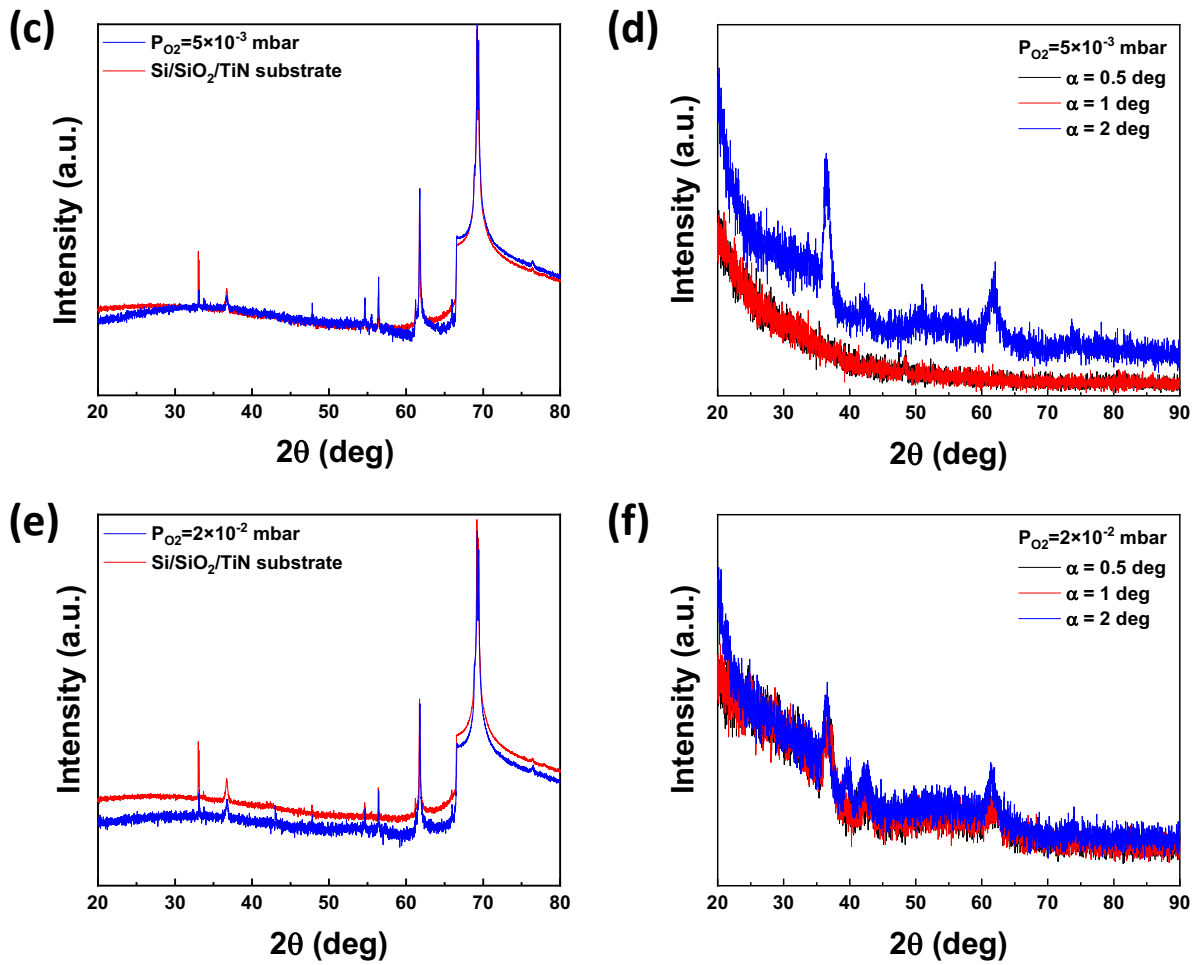


Figure S1 Morphology characterization of TaO_x thin films deposited at different oxygen partial pressure by using X-ray diffraction (XRD). (a), (c), and (e) were characterized with stationary and horizontal sample position with the X-ray tube and the detector both move simultaneously over the angular range θ . (b), (d), and (f) were characterized using grazing incidence XRD.

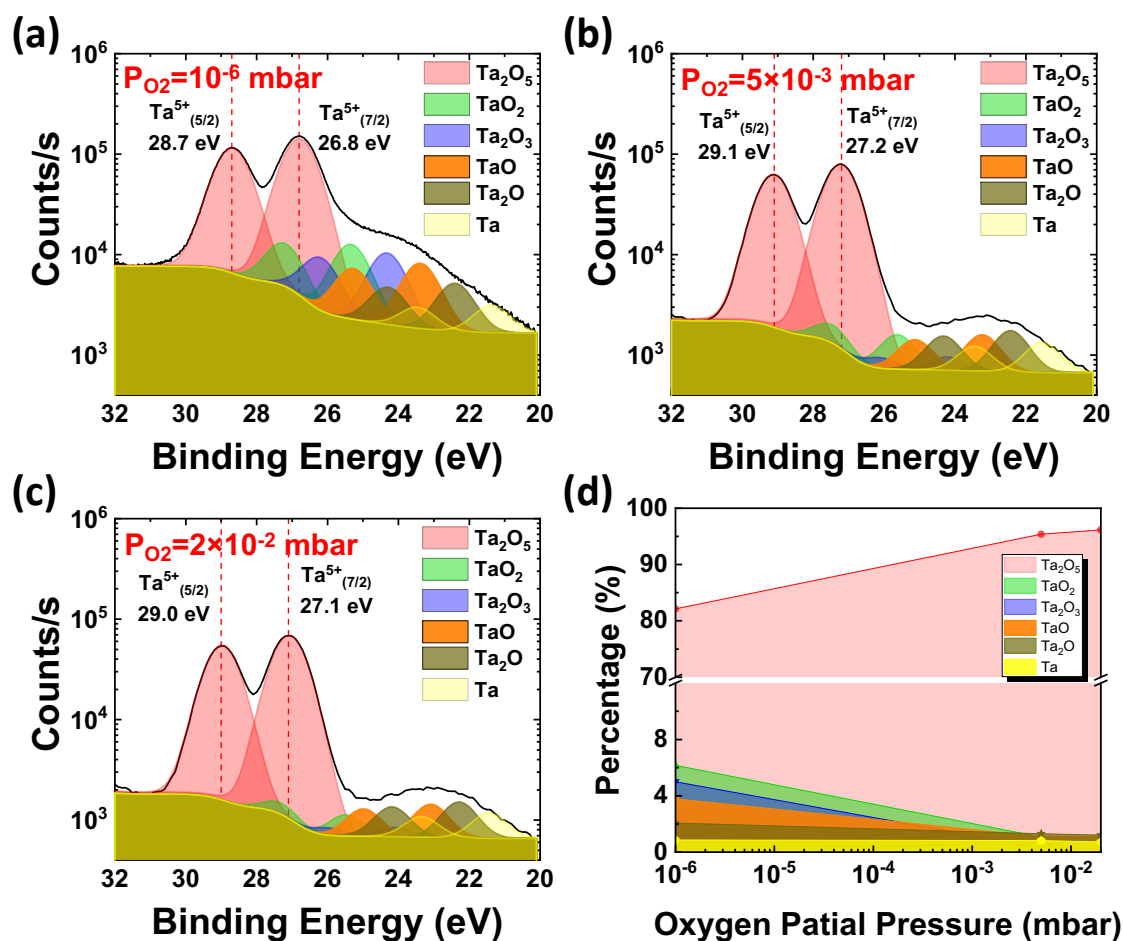


Figure S2 Ta 4f XPS spectra of TaO_x thin films deposited for 10 min under different oxygen partial pressures of: (a) P_{O₂}= 10⁻⁶ mbar, (b) P_{O₂}=5×10⁻³ mbar, and (c) P_{O₂}=2×10⁻² mbar. (d) The Ta oxide states composition inside TaO_x thin films deposited under different oxygen partial pressure for 10 min at room temperature.

During the XPS data analysis, the Ta 4f_{5/2}/4f_{7/2} height ratio was fixed to 0.788, which was automatically chosen by the Avantage software. The Ta 4f_{5/2}/4f_{7/2} binding energy splitting is fixed to 1.9 eV and the full width at half maximum (FWHM) fitting parameter used for all XPS spectrum is 1.2 ± 0.1 eV. Table 1 shows the comparison between the binding energies for each oxidation states used in the work of Simpson et al. and this paper. Table 2 is an example of the fitting parameters used for XPS spectra analysis and the data is of the sample for TaO_x film grown under P_{O₂}=10⁻⁶ mbar for 60 min.

Table 1 The binding energies for each oxidation states used in the work of Simpson et al. and this paper.

Oxide State	Binding Energy (eV)			
	Simpson <i>et al.</i> (Ref. 41 in main text)		this paper	
	Ta4f 7/2	Ta4f 5/2	Ta4f 7/2	Ta4f 5/2
Ta ⁵⁺ (Ta ₂ O ₅)	27.0± 0.05	28.9± 0.05	26.9± 0.1	28.8±0.1
Ta ⁴⁺ (TaO ₂)	25.7± 0.30	27.6± 0.30	25.5±0.2	27.4± 0.2
Ta ³⁺ (Ta ₂ O ₃)	24.3± 0.20	26.2± 0.20	24.2± 0.2	26.1± 0.3
Ta ²⁺ (TaO)	23.3± 0.30	25.2± 0.30	23.1± 0.2	25.0± 0.2
Ta ¹⁺ (Ta ₂ O)	22.5± 0.10	24.4± 0.10	22.2± 0.2	24.1± 0.2
Ta ⁰ (metal)	21.50	23.42	21.3± 0.2	23.3± 0.3

Table 2 An example of the fitting parameters used for XPS spectra analysis. The data is of the sample for TaO_x film grown under P_{O₂}=10⁻⁶ mbar for 60 min.

	Peak BE (eV)	Height CPS	Height Ratio	Area CPS (eV)	Area Ratio	FWHM Fit Parameter (eV)		Percentage (%)	4f5/4f7 Height Ratio	4f5/4f7 BE Splitting (eV)
Ta 4f7 Ta ₂ O ₅	26.78	110948.04	1	139461.49	1	1.2				
Ta 4f5 Ta ₂ O ₅	28.68	87469.41	0.79	109729.01	0.79	1.2	Ta ₂ O ₅	75.7	0.788	1.9
Ta 4f7 TaO ₂	25.3	13901.3	0.13	17501.13	0.13	1.2				
Ta 4f5 TaO ₂	27.2	10959.53	0.1	13770.02	0.1	1.2	TaO ₂	9.5	0.788	1.9
Ta 4f7 Ta ₂ O ₃	24.23	11991.4	0.11	15113.78	0.11	1.2				
Ta 4f5 Ta ₂ O ₃	26.13	9453.8	0.09	11891.66	0.09	1.2	Ta ₂ O ₃	8.2	0.788	1.9
Ta 4f7 TaO	23.38	5105.89	0.05	6441.06	0.05	1.2				
Ta 4f5 TaO	25.28	4025.39	0.04	5067.9	0.04	1.2	TaO	3.5	0.788	1.9
Ta 4f7 Ta ₂ O	22.58	2893.05	0.03	3652.62	0.03	1.2				
Ta 4f5 Ta ₂ O	24.48	2280.83	0.02	2873.94	0.02	1.2	Ta ₂ O	2.0	0.788	1.9
Ta 4f7 Ta	21.56	1665.87	0.02	2101.29	0.02	1.2				
Ta 4f5 Ta	23.46	1313.34	0.01	1656.64	0.01	1.2	Ta	1.1	0.788	1.9
							Sum=	100		

Y. Li et al.
Tuning the Resistive Switching in Tantalum Oxide Based
Memristors by Annealing
Under review for AIP Advances (2020).



Midsummer Day Sunset at Roskilde Fjord (23rd June 2019)
Photo: Yang Li

Tuning the Resistive Switching in Tantalum Oxide Based Memristors by Annealing

Yang Li¹, Y. Eren Suyolcu², Simone Sanna¹, Dennis Valbjørn Christensen¹, Marie Lund Traulsen¹, Eugen Stamate¹, Christian Søndergaard Pedersen¹, Peter A. van Aken², Juan Maria García Lastra¹, Vincenzo Esposito¹, and Nini Pryds¹

¹Department of Energy Conversion and Storage, Technical University of Denmark, Lyngby, 2800, Denmark

²Max Planck Institute for Solid State Research, Heisenbergstraße 1, Stuttgart, 70569, Germany

ABSTRACT

A key step in engineering resistive switching is the ability to control the device switching behavior. Here, we investigate the possibility to tune the resistive switching of tantalum oxide-based memristors from a non-switchable state to a switchable state by applying post-fabrication annealing of the devices. The switching of the devices was found to be related to: (1) The oxidation state changes in the TaO_x thin film after annealing as well as (2) The local variations in oxygen stoichiometry in the vicinity of the interface between the TiN electrode and the TaO_x active resistive layer. We further discuss the possible mechanism behind the resistive switching after annealing. This experimental approach provides a simple but powerful pathway to trigger the resistive switching behavior in devices that do not show any resistive switching behavior initially.

1. INTRODUCTION

Tantalum oxide (TaO_x) is widely used as resistive switching material in memristors as it exhibits excellent features such as superior endurance of more than 10¹² cycles¹ and ultra-fast switching speed of sub-nanosecond.² Tantalum oxide is a complex system that includes more than 20 non-equilibrium phases and two equilibrium Ta₂O₅ (tantalum pentoxide) phases.³ Being able to control these phases is an essential step in achieving highly controllable resistive switching behaviors in tantalum oxide memristors.

Two simple but effective methods enable to tune and control the tantalum oxide (TaO_x) based memristor behaviors are: (1) by manipulating the TaO_x thin film growth conditions⁴⁻⁷ or/and (2) by annealing TaO_x thin film after deposition.⁸⁻¹¹ We have shown in our previous work⁴ that we can finely tune and control the resistivity of the TaO_x thin film during the growth using Pulsed Laser Deposition (PLD). By varying the oxygen pressure during deposition from 10⁻⁶ mbar to 2×10⁻² mbar, the resistivity of deposited tantalum oxide can be altered by more than six orders of magnitude as a result of a controlled oxygen stoichiometry. This, in turn, led to different resistive switching behavior of memristors. Memristors with TaO_x deposited at low oxygen pressure below and equal to 2×10⁻³ mbar showed no resistive switching, whereas TaO_x deposited at oxygen pressures above 2×10⁻³ mbar showed resistive switching character.

Besides varying the oxygen pressure during thin film deposition, the temperature is another critical factor influencing TaO_x phases. For example, Ta₂O₅ pellet after been sintered at 1400 to 1600 °C for 24 hours, shows a monoclinic to orthorhombic phase transition by Raman scattering at about

327 °C.¹² Ta₂O₅ in the amorphous state (a-Ta₂O₅) transfer into low-temperature (LT) crystalline state (orthorhombic β-phase) at approximately 650 °C. The orthorhombic β-phase can reversibly transfer into the high temperature (HT) crystalline tetragonal α-phase at approximately 1320 ± 20 °C.^{3,12,13}

Beside controlling the Ta₂O₅ phases by annealing at different temperatures, annealing in different gas atmospheres at elevated temperatures can also be an effective way to tune the stoichiometry of tantalum oxide.^{8,11} This approach is also often used to further improve the mechanical, electrical or optical properties of thin films by structural relaxation and stoichiometry change.^{14,15}

Altogether, annealing is an effective way to tune the properties of TaO_x based memristors.^{8,11,16} For example, annealing a TaO_x-based memristor in oxygen atmosphere at 300 °C can affect the oxygen stoichiometry, which has been found to improve the device endurance.⁸ Annealing in NH₃ at 400 °C, on the other hand, resulted in the incorporation of hydrogen (H) species into TaO_x,¹⁰ which improved the device endurance, lowered the forming voltage, and enhanced the retention lifetime of formed conductive filaments. Besides the effect of annealing on the active TaO_x layer, the electrode materials may also be affected by the annealing process. For example, Raman scattering spectra indicated the presence of rutile TiO₂ signals in 1 μm thick TiN after annealing in air at 500 °C for 2 hours.¹⁷

So far, most studies on the annealing of TaO_x based memristors were carried out on TaO_x films deposited either by sputtering or by atomic layer deposition (ALD). No systematic work on the effect of post-deposition annealing on the resistive switching behavior of TaO_x films fabricated by PLD has so far been reported. PLD is a powerful technique for fabrication of complex oxide while preserving the stoichiometry. In this work, we focus on utilizing post-deposition annealing method to tune the stoichiometry and resistive switching behaviors of tantalum oxide-based memristors. By using isochronal annealing steps imposed with controlled heating and cooling, we successfully trigger the switching behavior in devices which did not show any switching initially. We also reveal the stoichiometry change of TaO_x after annealing and propose a possible mechanism for the triggering of the switching behavior.

2. EXPERIMENT

The configuration of the device film stack used in this study was Si/SiO₂/TiN/TaO_x/W with TiN and W serving as the electrodes and TaO_x being the active memristor layer. The substrates are commercially available (100) silicon substrates with 100 ± 10 nm native silicon dioxide, and 100 nm sputtered TiN film on top (Prime Wafers), labeled as Si/SiO₂/TiN substrates. The TiN layer in the Si/SiO₂/TiN substrate acts as the bottom electrode. An active oxide layer of TaO_x thin films was deposited using pulsed laser deposition (PLD) through a square-shaped shadow mask in order to expose the TiN bottom electrode. A KrF excimer laser (248 nm, 10 Hz, 4 J/cm²) was used to ablate a commercial ceramic target of Ta₂O₅ (American Elements) with 99.99% purity and dimensions of 25.4 mm in diameter and 6 mm in thickness. The deposition was carried out keeping the target-substrate distance constant at 7.5 cm. The TaO_x thin films were deposited with a thickness of approximately 20 nm at room temperature (RT) with an oxygen pressure P_{O₂}=2×10⁻³

mbar inside the chamber. The tungsten (W) top electrode layer was deposited by DC magnetron sputtering without intentional substrate heating, using the following parameters: 40 sccm Ar gas, 10^{-2} Torr deposition pressure, 320 V discharge voltage and 0.2 A discharge current for a deposition time of 300 seconds. The top electrodes were patterned into a circular shape with a diameter of 50 μm and a thickness of about 150 nm using an Al_2O_3 shadow mask.

All electrical tests were carried out using Keithley 4200A with an Imina probe station providing the contact to the W and TiN electrodes through W needle probes. During the two terminal electrical tests, voltages were applied to the W top electrodes, and the TiN bottom electrodes were grounded. The voltage ramp with 10 mV per step was used in both SET and RESET processes. A compliance current of 1 mA was used in the SET process. The resistances of the devices follow lognormal distribution, which means the log of the resistances follow normal distribution. In Figure 1, the mean values are of the log of the resistances and the error bars are the standard deviations of the mean. The electrical conductivity was measured on rectangular-shaped samples ($1 \times 1 \text{ cm}^2$) in a van der Pauw configuration.

Chemical and structural changes in the materials induced by the annealing were characterized by x-ray photoelectron spectroscopy (XPS), x-ray diffraction (XRD), scanning transmission electron microscopy (STEM), and energy-dispersive x-ray spectroscopy (EDX). The XPS analyses were performed on an ESCALAB XI⁺ X-ray photoelectron spectrometer (Thermo Fisher Scientific, East Grinstead, U.K.) using a monochromatic Al-K α X-ray source with a 650 μm spot size and a take-off angle of 90° from the surface plane. A combined ion/electron gun (i.e., a dual-beam source) was used to control sample charging. The pressure in the analysis chamber was 4×10^{-8} mbar. High resolution local binding energy spectra were obtained for Ta-4f using 20 eV detector pass energy, dwelling time 50 ms, and energy step size 0.05 eV. The sputter depth profiling was performed on fraction of the area of $0.7 \times 0.7 \text{ mm}^2$ with monoatomic Ar⁺ Ion Beam. The beam has a kinetic energy of 3 KeV, for 10 sec each level and with 30 levels in total. All spectra were shifted according to the O1s spectra peaks position using the second O1s spectrum of the as-deposited sample. For the XRD analysis, Bruker D8 Advanced diffractometer (Germany) with Cu K α ($\lambda=1.5406 \text{ \AA}$) radiation was used. For the STEM analyses, a probe-aberration corrected JEOL JEM-ARM200F microscope equipped with a cold field-emission electron source, a probe Cs-corrector (DCOR, CEOS GmbH), and a large solid-angle JEOL Centurio SDD-type EDX detector was used. STEM imaging and EDX analyses were performed at probe semi-convergence angles of 20 and 28 mrad, resulting in probe sizes of 0.8 and 1.0 \AA , respectively. Collection angles for HAADF images were 75–310 mrad.

3. RESULTS AND DISCUSSION

A set of seven samples were fabricated under the same conditions as described in the experimental part. Each sample contains 16 devices defined by a circular W top-electrode with a diameter of 50 μm and a 20 nm active TaO_x layer. A schematic illustration of the device is shown in the inset of Figure 1a. Initially, all devices showed no resistive switching with an average low initial resistance of approximately 5.26 k Ω (Figure 1a). We annealed the memristors at different temperatures

ranging from 300 °C to 500 °C in air. Seven annealing temperatures were used: 300, 325, 350, 375, 400, 450, and 500 °C, with a fixed annealing time of 4 hours and ramping rate of 200 °C/hr during heating and cooling (inset of Figure 1b). After the annealing process, the ability of the samples to resistive switch were tested at room temperature.

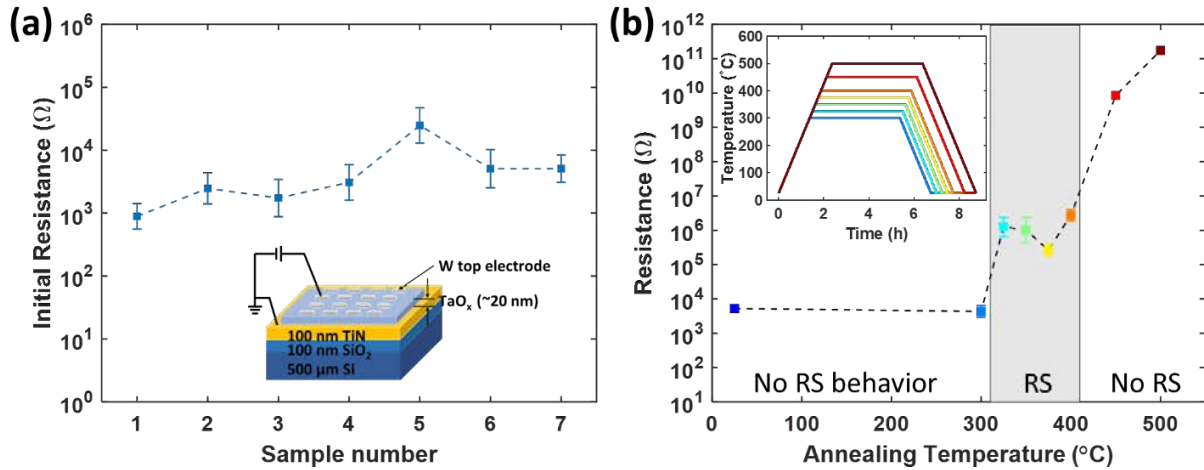


Figure 1. (a) Initial resistance distribution for seven as-fabricated samples. Each sample contains 16 devices. The diameter of the top electrodes is 50 μm . The thickness of the TaO_x layer is about 20 nm. The inset shows a schematic illustration of the devices under test and the two terminal electrical test setup. (b) Change of resistances after the annealing process at different temperatures. The inset shows the temperature change during the annealing process. RS stands for resistive switching. The error bars represent the standard deviation of the mean.

The results of the annealing revealed the following: (1) For annealing temperature smaller than or equal to 300 °C, no resistive switching was observed inside the devices (Figure 2a to b), (2) From 325 °C to 400 °C, the resistive switching was triggered (Figure 2c to f) and (3) Above 400 °C, the average resistance of devices exceeds 10^{10} Ω , showing an insulating state with no resistive switching (Figure 2g to h).

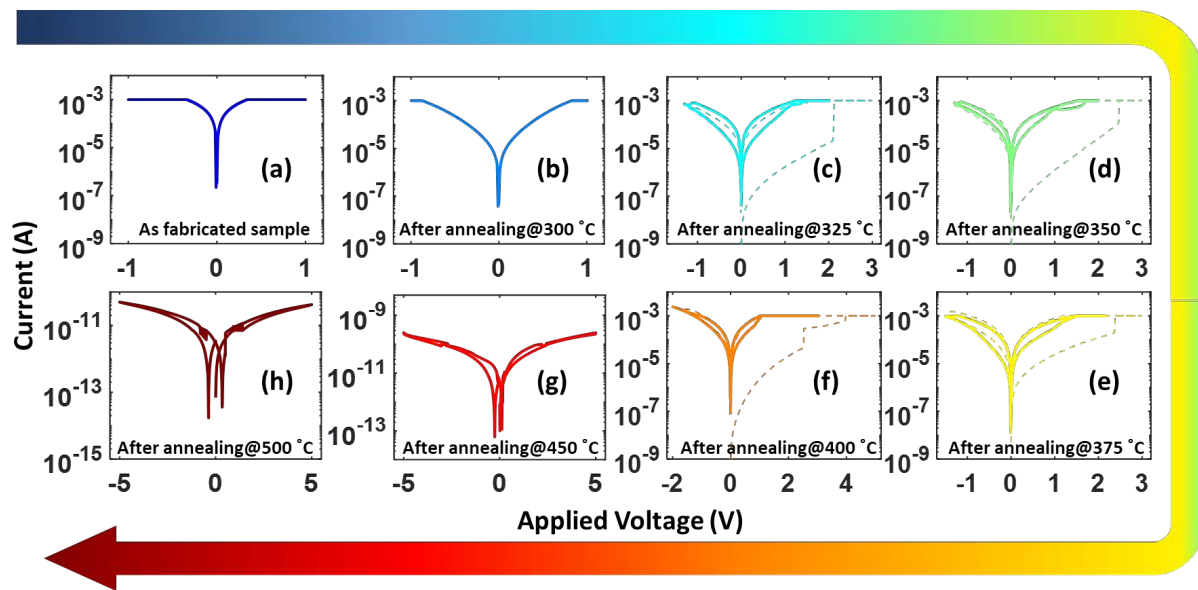


Figure 2. Typical I-V relation for (a) as-fabricated devices and (b) to (h) devices after annealing at 300 °C, 325 °C, 350 °C, 375 °C, 400 °C, 450 °C, and 500 °C, respectively. The dashed lines in (c) to (f) represent the corresponding Forming and the first RESET processes.

Thus, only in a limited window, between 325 °C and 400 °C, could we trigger resistive switching behaviors in TiN/TaO_x/W structured devices. In the following, we, therefore, investigate the underlying origins responsible for enabling of the resistive switching within this window and the reasons for terminating the resistive switching when annealed outside this window.

Oxidation and crystallinity of the TaO_x resistive switching layer

In order to understand the oxidation state and stoichiometry of film and their relation to the resistive switching, we have studied three samples: (1) as-deposited sample, (2) annealed at 350 °C and (3) annealed at 500 °C, using XPS depth profiling (Figure 3). The black arrows in Figure 3 represent the XPS depth profile direction from the surface of the TaO_x to the inner part of the TaO_x. The depth profiles taken from these samples have a similar analysis time, i.e. approximately similar depth length. From these profiles we can conclude the following: (1) For the as-deposited samples, the position of Ta4f peaks shift to the lower binding energy as the profiling depth increases, which means that there is a gradient of composition starting from the stoichiometric composition at the surface towards less stoichiometric composition at the inner part of the film, (2) For the samples annealed at 500 °C, the dominant phase is the Ta₂O₅ independent of the depth. This indicate that the films are completely oxidized, and (3) Samples annealed at 350 °C show a mixture of both stoichiometric and non-stoichiometric compositions along the depth.

Comparing the XPS results to the corresponding resistive switching of the heat-treated devices, it indicates that, in order to restive switch the devices the samples should be partially resistive and partially conductive, i.e. as observed in the samples annealed at 350 °C. In other words, the resistive switching depends on the right amount of oxygen vacancies in the device. Note that after being annealed at 500 °C, the devices were also non-switchable, but this is related to the sample

being fully oxidized but also to the oxidation of the TiN bottom electrode. This will be discussed in the following paragraph.

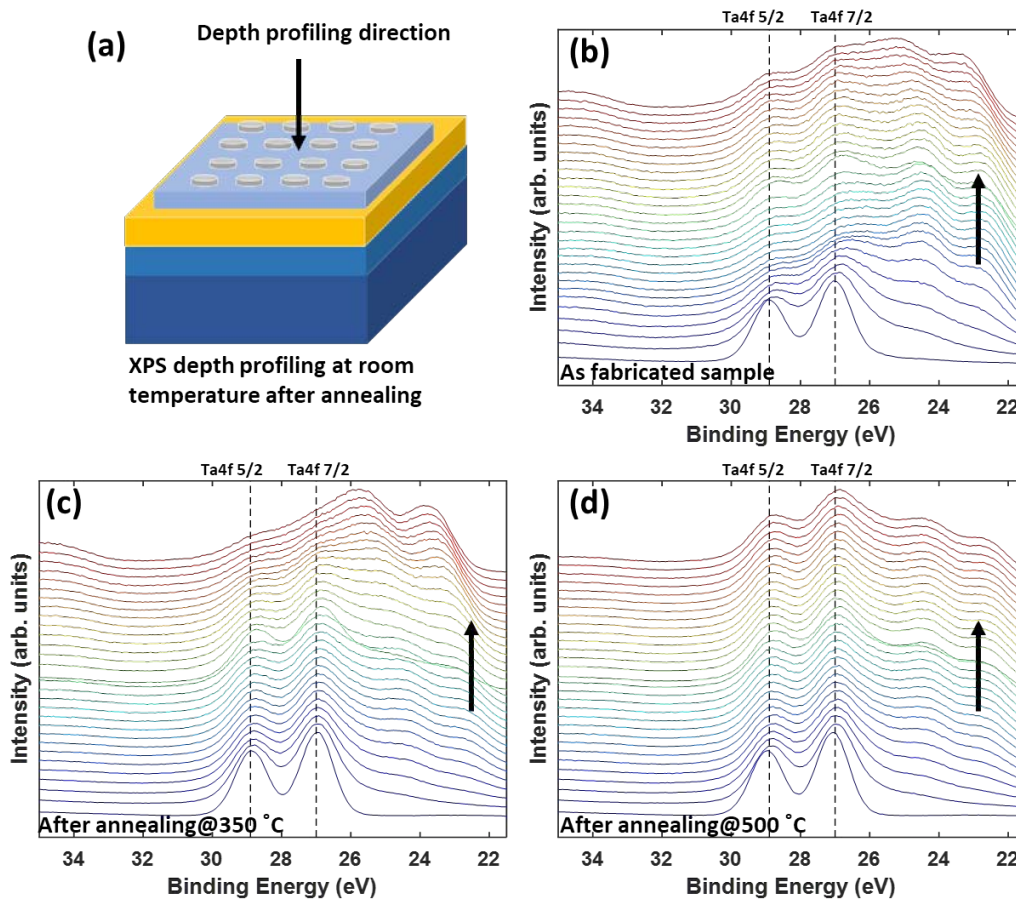


Figure 3. (a) An illustration of the XPS depth profiling direction. XPS depth profiles of devices (b) as fabricated, (b) after annealing at 350 °C, and (c) after annealing at 500 °C. The black arrows indicate the etching direction from the surface of TaO_x to the inner part of TaO_x thin film. The dashed lines represent the binding energy for Ta⁵⁺.

The devices which showed resistive switching i.e., the samples annealed in air between 325 °C and 400 °C, show also amorphous structure which seems to be robust and stable without any changes, at least in this temperature interval and time, as indicated by x-ray diffraction (XRD) (Supplementary materials, **Error! Reference source not found.**).

The effect of electrodes and interfaces

As mentioned before, another source of possible absence of resistive switching is the degradation of the electrodes during annealing. Besides the oxidation process of TaO_x, we also observe an indication of oxidation of the TiN electrode materials, i.e. by transport measurements. After the annealing process (on samples similar to the one shown in Figure 3), the resistivity of both the TiN bottom electrode layer and the W top electrode layer were tested using four-probe van der Pauw configuration. The four-probe test was carried out on the TiN layer of the devices, and on a new

set of samples only consisting of bare W electrode. All tests were carried out at room temperature after the annealing process. The resistivity of the TiN layers show an increase from $320 \pm 19 \mu\Omega\cdot\text{cm}$ without any post-annealing process to $592 \pm 61 \mu\Omega\cdot\text{cm}$ after being annealed at 400°C . As the annealing temperatures increased above 400°C , the TiN layer became very insulating with a resistivity above the detection limit of our equipment (Figure 4). On the other hand, the W layer kept a stable resistivity even after being annealed at 500°C .

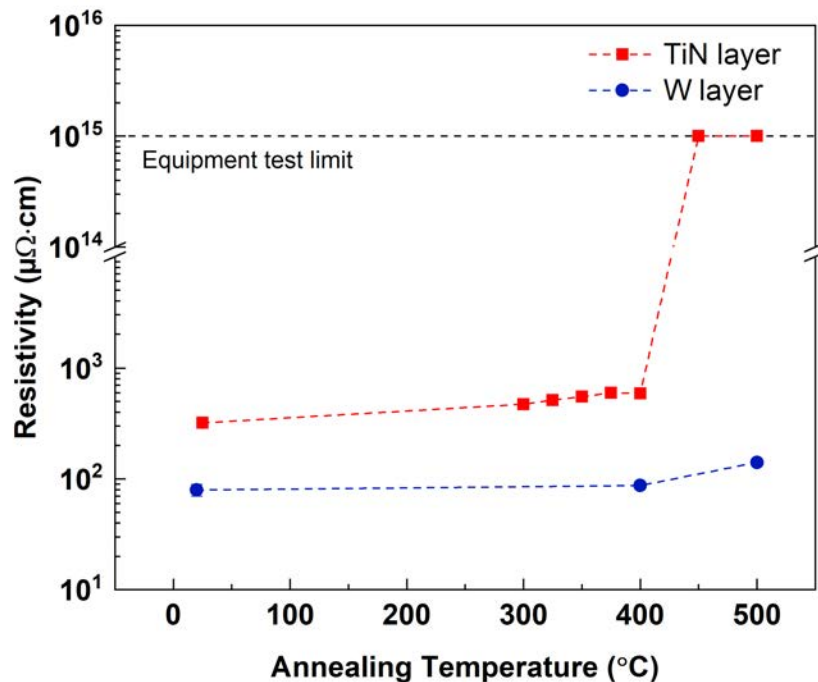


Figure 4. Resistivity change of TiN and W layer after annealing at different temperatures. The resistivity was tested by using four-probe van der Pauw configuration on $1\text{ cm}\times 1\text{ cm}$ samples.

In addition to the stoichiometry control of the TaO_x layer, one need also to ensure the right choice of electrode combination which is also a crucial factor for the resistive switching. By inserting a layer of W between the TiN and the TaO_x layer ($\text{Si}/\text{SiO}_2/\text{TiN}/\text{W}/\text{TaO}_x/\text{W}$), as a “blocking” layer for oxygen, the resistance increased from $10^2 \Omega$ to $10^7 \Omega$, see Figure 5a. However, no resistive switching was triggered in these samples (Figure 5b). The devices showed Ohmic I - V relationship for the annealing temperature up to 400°C . Devices after being annealed at 500°C showed a Forming/SET process but cannot be switched back to the high resistance state at negative voltage side.

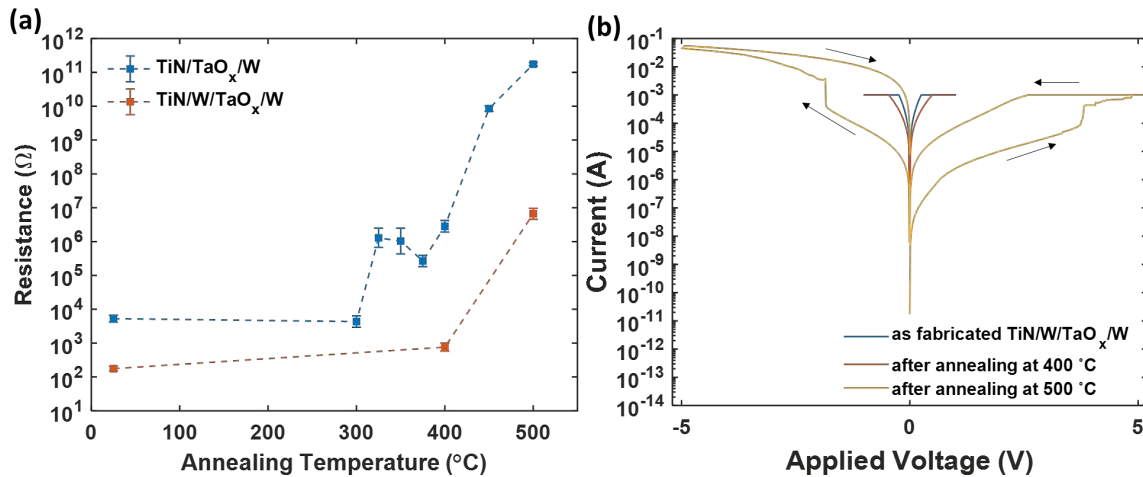


Figure 5. (a) Resistance change of TiN/TaO_x/W and TiN/W/TaO_x/W structured devices after the annealing process. (b) Typical IV curves for TiN/W/TaO_x/W structured devices.

In order to understand the influence of annealing on the interface profiles, detailed STEM investigations were carried out on similar samples (Figure 3). Figure 6 a-c show STEM-HAADF imaging profiles of the layered structure. From STEM-EDX chemical investigations, it was clear also that the out-of-plane elemental intermixing at both TiN/TaO_x and TaO_x/W interfaces was observed (Figure 6d-f). Concerning the as-fabricated sample, the interfaces between TaO_x and W are relatively sharper and show an intermixing width of about ~ 5 nm, while the elemental intermixing at the TiN-TaO_x interfaces show much larger intermixing width of about ~ 10 nm (Figure 6d). For the sample annealed at 325 $^{\circ}\text{C}$, the intermixing of the elements at both interfaces are more pronounced compared to the as-fabricated sample, i.e. the presence of Ta in the nominal W layer suggests Ta diffusion into the W layer. Besides, the observation of an emergence of an additional (W, Ta)O_x layer over the nominal W layer, the thickness of the W layer (~ 20 nm) was in fact less than what expected, which is explained by the formation of a (W, Ta)O_x layer. After annealing at 500 $^{\circ}\text{C}$ (Figure 6c and f), the elemental intermixing across the interfaces was observed to be highest among all samples. Here, the TiN layer is found to be completely oxidized, which is also indicated by the high resistivity of the TiN layer as indicated by transport measurements.

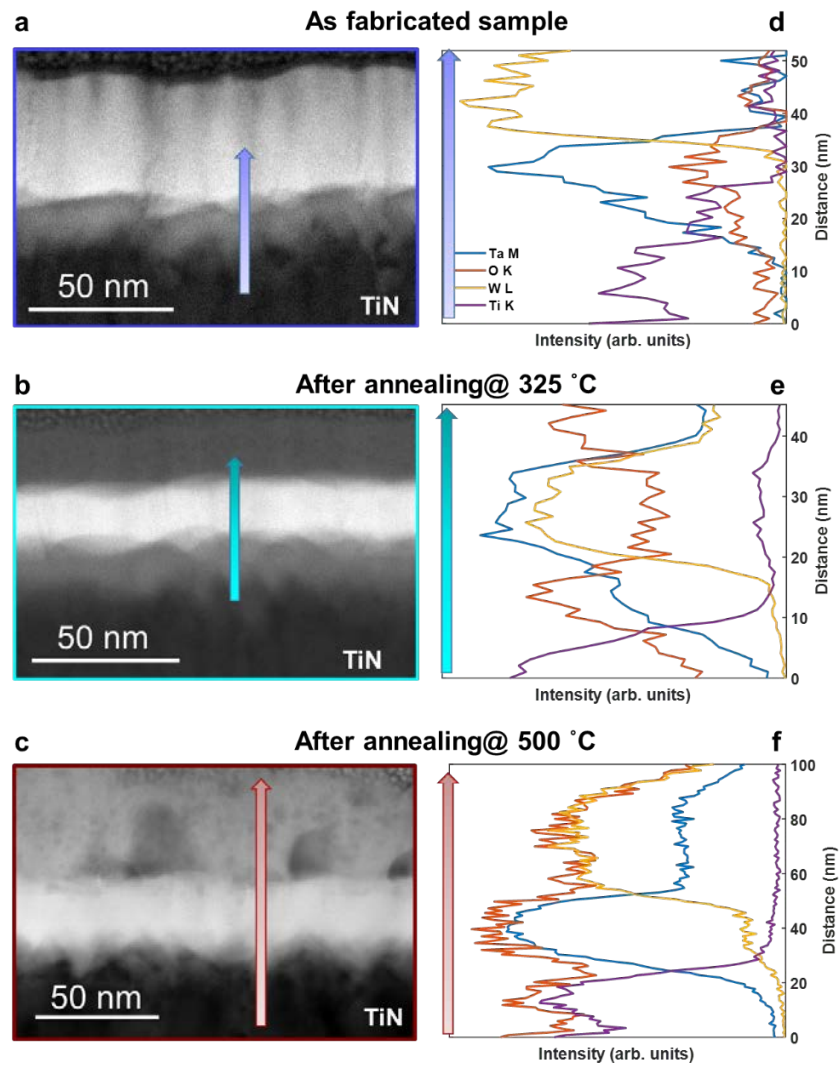


Figure 6. STEM investigations of TiN/TaO_x/W interfaces annealed under different conditions. Representative STEM-HAADF images of (a) an as-fabricated device, (b) a device after annealing at 325 °C, and (c) a device after annealing at 500 °C. The arrows on the STEM-HAADF images indicate both the growth direction and the EDX line scan positions acquired across the interfaces of (d) an as-fabricated device, (e) a device after annealing at 325 °C, and (f) a device after annealing at 500 °C. The elemental profiles in (d-f) are obtained using Ta M (blue), O K (orange), W L (yellow) and Ti K (purple) X-ray emission lines.

4. CONCLUSION

In this work, we were able to trigger the resistive switching in TiN/TaO_x/W devices by applying post-annealing procedure. We identify three different temperature regimes:

- $T \leq 300$ °C: The devices are thermally stable when exposed to annealing in air up to 300 °C for 4 hours. With the given deposition parameters used for the TaO_x deposition, no resistive switching was observed at room temperature.
- 300 °C $\leq T \leq 400$ °C: The devices showed resistive switching after annealing within this temperature window. As indicated by the XPS depth profiling, the TaO_x layer became more stoichiometric after annealing compared to the as-deposited sample. Electrical resistivity measurements of the electrodes indicate that both the TiN and W layer showed stability within this temperature range. Based on these observations, we argue that the shift towards the stoichiometric sample of TaO_x, which indicates the decrease of the oxygen vacancies content inside the films, contributed to the emergence of resistive switching behavior. This is consistent with TaO_x layers deposited by PLD at different oxygen partial pressures, as shown in **Error! Reference source not found.**, where using a higher oxygen pressure led to an enabling of the resistive switching behavior.
- $T > 400$ °C: The TaO_x becomes more oxides, i.e. towards stoichiometric composition, leading to more insulating films. Furthermore, the TiN bottom electrode layer became oxidized after annealing at temperatures above 400 °C and the resistivity of TiN layer increased abruptly. As the TiN layer became insulating, the devices lost resistance switching behavior. This indicates that both stoichiometry of TaO_x and TaO_x/electrode interface played an essential role in triggering resistive switching behavior.

We have shown that post-annealing can enable resistive switching and allow studying the switching behavior in samples which otherwise did not show resistive switching. Annealing can then be a simple yet powerful method in triggering the resistive switching. By post-annealing the devices at a temperature range between 325 °C and 400 °C, the initial resistances of the TiN/TaO_x/W structured devices increased from 10³ Ω to 10⁶ Ω resulting in the resistive switching. The temperature range observed in these experiments related to the stability of the electrodes and the active layer. Both the stoichiometric TaO_x layer and the TiN/TaO_x interface or TiN electrode, played an important role in the emergence of resistive switching behavior.

CONFLICT OF INTEREST

Authors declare no conflict of interest.

DATA AVAILABILITY STATEMENT

The data that support the findings of this study are available from the corresponding author upon reasonable request.

ACKNOWLEDGEMENT

Authors acknowledge Julia Deuschle for FIB lamella preparation. Y. Eren Suyolcu and Peter A. van Aken acknowledges funding from the European Union's Horizon 2020 research and innovation program under grant agreement No. 823717–ESTEEM3. The authors thank the support from the Independent Research Fund Denmark, Grant No. 6111-00145B.

REFERENCES

- ¹ C.-W. Hsu, I.-T. Wang, C.-L. Lo, M.-C. Chiang, W.-Y. Jang, C.-H. Lin, and T.-H. Hou, in *2013 Symp. VLSI Technol.* (IEEE, Kyoto, Japan, 2013), pp. T166–T167.
- ² A.C. Torrezan, J.P. Strachan, G. Medeiros-Ribeiro, and R.S. Williams, *Nanotechnology* **22**, 485203 (2011).
- ³ S.P. Garg, N. Krishnamurthy, A. Awasthi, and M. Venkatraman, *J. Phase Equilibria* **17**, 63 (1996).
- ⁴ Y. Li, S. Sanna, K. Norrman, D.V. Christensen, C.S. Pedersen, J.M.G. Lastra, M.L. Traulsen, V. Esposito, and N. Pryds, *Appl. Surf. Sci.* **470**, 1071 (2019).
- ⁵ S.U. Sharath, M.J. Joseph, S. Vogel, E. Hildebrandt, P. Komissinskiy, J. Kurian, T. Schroeder, and L. Alff, *Appl. Phys. Lett.* **109**, (2016).
- ⁶ H. Jeon, J. Park, W. Jang, H. Kim, C. Kang, H. Song, H. Kim, H. Seo, and H. Jeon, *Phys. Status Solidi Appl. Mater. Sci.* **211**, 2189 (2014).
- ⁷ M.T. Brumbach, P.R. Mickel, A.J. Lohn, A.J. Mirabal, M.A. Kalan, J.E. Stevens, and M.J. Marinella, *J. Vac. Sci. Technol. A* **32**, 051403 (2014).
- ⁸ J. Hong, W. Jang, H. Song, C. Kang, and H. Jeon, *J. Korean Phys. Soc.* **66**, 721 (2015).
- ⁹ C. Chen, C. Song, J. Yang, F. Zeng, and F. Pan, *Appl. Phys. Lett.* **100**, (2012).
- ¹⁰ L. Goux, J.Y. Kim, B. Magyari-Kope, Y. Nishi, A. Redolfi, and M. Jurczak, *J. Appl. Phys.* **117**, 124501 (2015).
- ¹¹ L. Zhang, S. Member, R. Huang, S. Member, M. Zhu, and S. Qin, *IEEE Electron Device Lett.* **31**, 966 (2010).
- ¹² P.S. Dobal, R.S. Katiyar, Y. Jiang, R. Guo, and a S. Bhalla, *J Raman Spectrosc* **31**, 1061 (2000).
- ¹³ S. Lagergren and A. Magnéli, *Acta Chem. Scand.* **6**, 444 (1952).
- ¹⁴ C. Joseph, P. Bourson, and M.D. Fontana, *J. Raman Spectrosc.* **43**, 1146 (2012).
- ¹⁵ D. V. Christensen, M. von Soosten, F. Trier, T.S. Jespersen, A. Smith, Y. Chen, and N. Pryds, *Adv. Electron. Mater.* **3**, 1 (2017).
- ¹⁶ Y. Jiang, C.C. Tan, M.H. Li, Z. Fang, B.B. Weng, W. He, and V.Y.-Q. Zhuo, *ECS J. Solid State Sci. Technol.* **4**, N137 (2015).
- ¹⁷ H.-Y. Chen and F.-H. Lu, *J. Vac. Sci. Technol. A Vacuum, Surfaces, Film.* **23**, 1006 (2005).

SUPPLEMENTARY INFORMATION

The XRD data in Figure S 1a was collected in theta-2theta configuration, scanning from 20° to 80° with a step size of 0.01° (0.2 s/step). The grazing-incidence small angle scattering data in Figure S 1b to d were collected using the same diffractometer. The x-ray incident angles were set to 0.1° , 0.5° , and 1° , respectively. The detector scanned in 2θ range $20^\circ \leq 2\theta \leq 90^\circ$ with a step size of 0.02° (0.5 s/step).

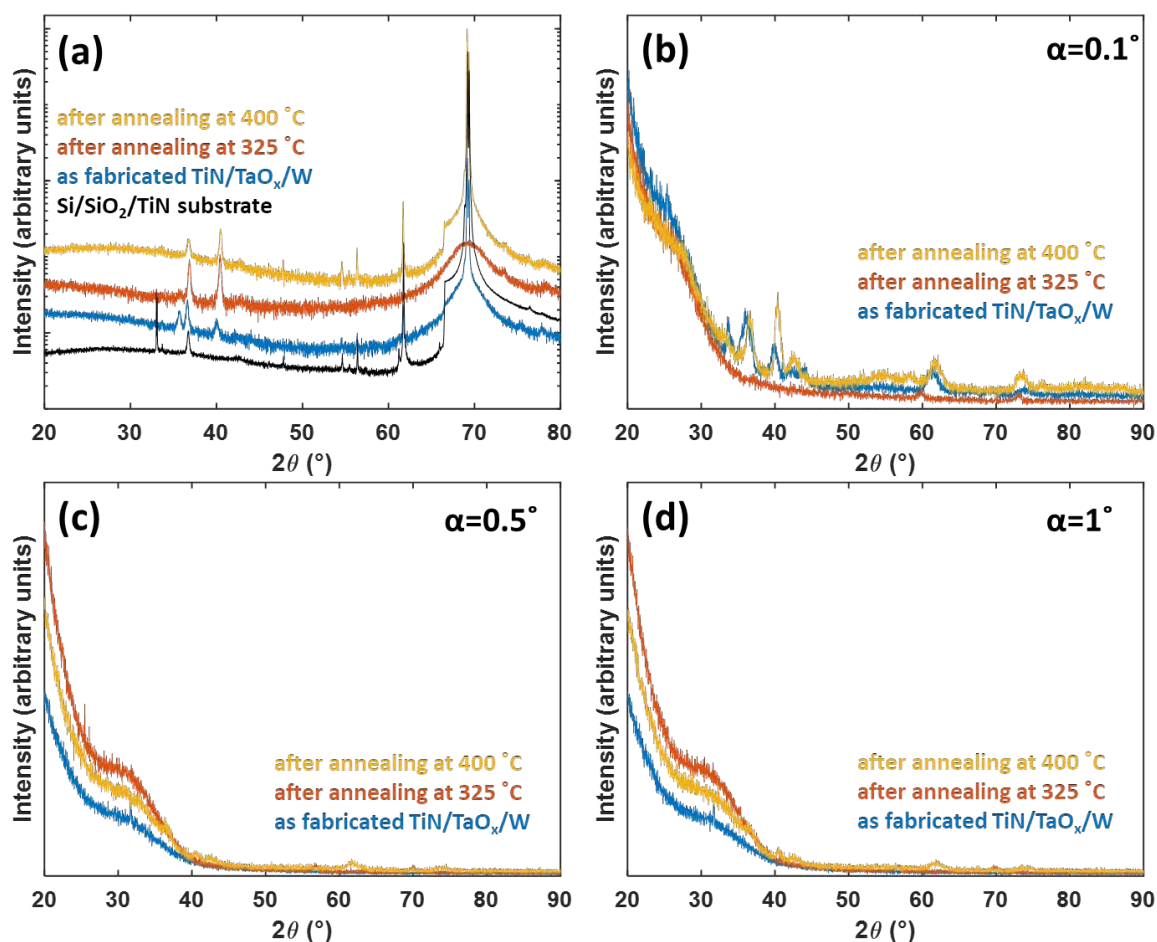


Figure S 1 X-ray diffraction (XRD) results of samples annealed at different temperatures. (a) XRD of samples under $\theta/2\theta$ method, (b), (c), and (d) are results for samples characterized using grazing incidence XRD with a grazing incident angle α of 0.1° , 0.5° , and 1° .

For TaO_x films grown at low P_{O_2} , more oxygen vacancies V_{O} are incorporated into the TaO_x film during deposition and thus leading to a more conductive electrical property. As fabricated devices start from already quite low initial resistances and external electrical field cannot switch the device to even lower or even higher resistance states. The devices are ‘stuck’ at low initial resistances states. Whereas for the device with TaO_x layer grown at high P_{O_2} , device initial resistance starts from high resistance state and can be switched to low resistance state after a forming process with a positive voltage applied to W top electrode. The device resistance can be switched back to a higher state when applying a negative voltage after the forming process. The devices showed bipolar resistive switching behavior. It shows that the initial oxygen content inside TaO_x layer will influence the devices initial resistances and the resistive switching behaviors dramatically (Figure S 2).

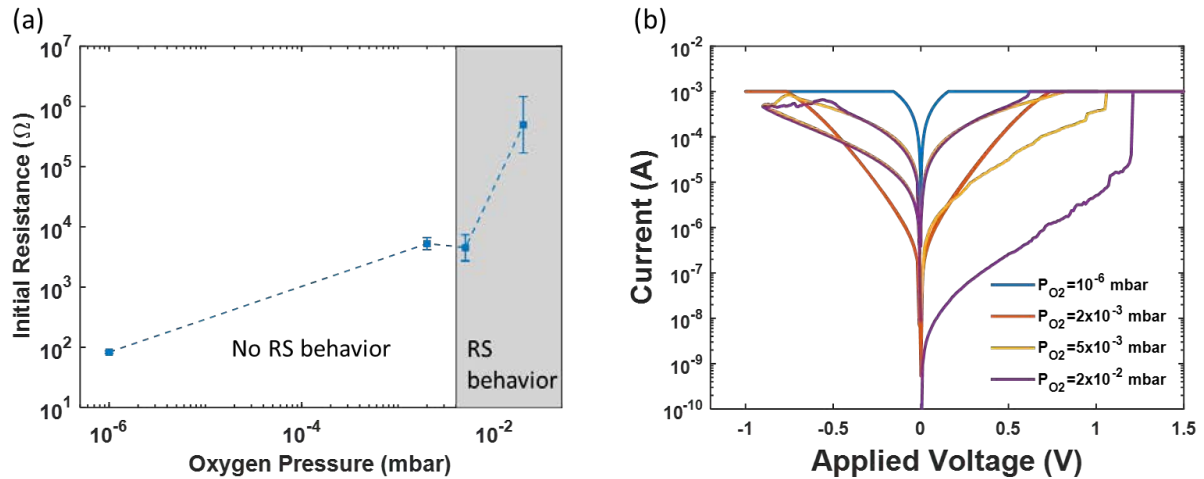


Figure S 2 Typical electrical properties of TiN/TaO_x/W structured devices. (a) During pulsed laser deposition (PLD) of TaO_x layer, as the oxygen partial pressure P_{O_2} vary from 10^{-6} mbar to 2×10^{-2} mbar, the initial resistances of devices increased about seven orders of magnitude (b) Typical I-V curves for devices with TaO_x layer deposited at different P_{O_2} . For TaO_x layer deposited at $P_{O_2} > 2 \times 10^{-3}$ mbar, the devices began to show resistive switching behavior. Inset of (a) is an illustration of device film stacks.

Y. Li, D. V. Christensen, S. Sanna, V. Esposito, and N. Pryds
The effect of external stimuli on the performance of memristive oxides
Book chapter in “Metal Oxides for Non-volatile Memory: Technology and Applications”, Elsevier (2020).



Early Autumn at Risø Campus DTU (19th September 2017)
Photo: Yang Li

The effect of external stimuli on the performance of memristive oxides

Yang Li, Dennis Valbjørn Christensen, Simone Sanna, Vincenzo Esposito, and Nini Pryds

Department of Energy Conversion and Storage, Technical University of Denmark

Abstract

This book chapter provides a comprehensive overview of the interrelationship between memristors properties and their responses to external stimuli such as electrical field, magnetic field, temperature, strain and radiation. The ability of a material to change properties in response to external stimuli is an attractive feature which is gaining attention across many different fields, especially for metal oxides, where it already finds uses in numerous applications, such as light-emitting diodes and photodetectors, chemical sensors, transistors, and nonvolatile memories. This book chapter introduces the concepts of stimuli-responsiveness for metal oxide based memristors, including the fundamental materials properties required for designing and understanding the new generation of memristors under the application of external stimuli. It provides readers with comprehensive scientific literature review on the principles and the developments of stimuli responsive memristor and presents several concrete examples showing the effect of external stimuli on the materials properties.

Introduction

The concept of memristor was first introduced and predicted by Leon Chua [1], [2] as the forth basic circuit element after resistor, capacitor, and inductor. It is based on a two terminal passive device linking the relationship between the charge q as time integral of current $I(t)$ and the generalized flux ϕ as time integral of voltage $V(t)$. If the resistance representing the ratio V/I depends on the charge $q(t)$ passed through the device, it becomes a memristance $M(q(t))$ according to

$$V(t) = M(q(t))/t$$

This theoretical concept was verified experimentally by R. Stanley Williams and his colleagues by fabricating nanoscale memristor based on TiO_2 thin films sandwiched between two electrodes.[3] The memristance, i.e. the property of a material which enables it to remember the last resistance it had before being shut off,

shows hysteretic behavior which can be exploited as non-volatile memory device. Memristors, which are also known as resistive switching memories, can be grouped in different categories depending on the underlying physical mechanism responsible for the non-volatile behavior: ferroelectric random access memory (FeRAM),[4], [5] magnetoresistive random access memory (MRAM),[6], [7] phase change memory (PCM),[8], [9] and resistance (switching) random access memory (RRAM).[10]–[13] In this chapter, we will focus on RRAM and provide an overview of how devices respond to various external stimuli (electrical field, magnetic field, temperature, strain and radiation) as well as explaining the physical mechanisms behind these observations. For the other types of novel non-volatile memory technologies mentioned above, the readers referred to many excellent reports including review papers and books[4]–[9] which will not be included in this book chapter.

A typical RRAM device exhibits a three-layered metal-insulator-metal (MIM) structure. The device switches under an electrical stimuli between two different resistance states, i.e. high resistance state (HRS or R_{OFF}) and low resistance state (LRS or R_{ON}) with a typical value of the resistance ratio R_{OFF}/R_{ON} exceeding 10.[13] Usually a “forming process” is required to trigger the resistive switching behavior in a device at the high initial resistance state (IRS). During the forming process of many resistive switching devices, conductive filaments are formed, connecting the top electrode (TE) and the bottom electrode (BE) of the device and switching the device to LRS. The following process of switching the device from LRS to HRS is called RESET while the opposite process from HRS to LRS is called SET. A compliance current (I_{CC}), i.e. the maximum current that can flow through a RRAM device during the forming or SET process, is applied to protect the device from hard breakdown. A typical device structure and I - V curve during switching process is as shown in Figure 1.

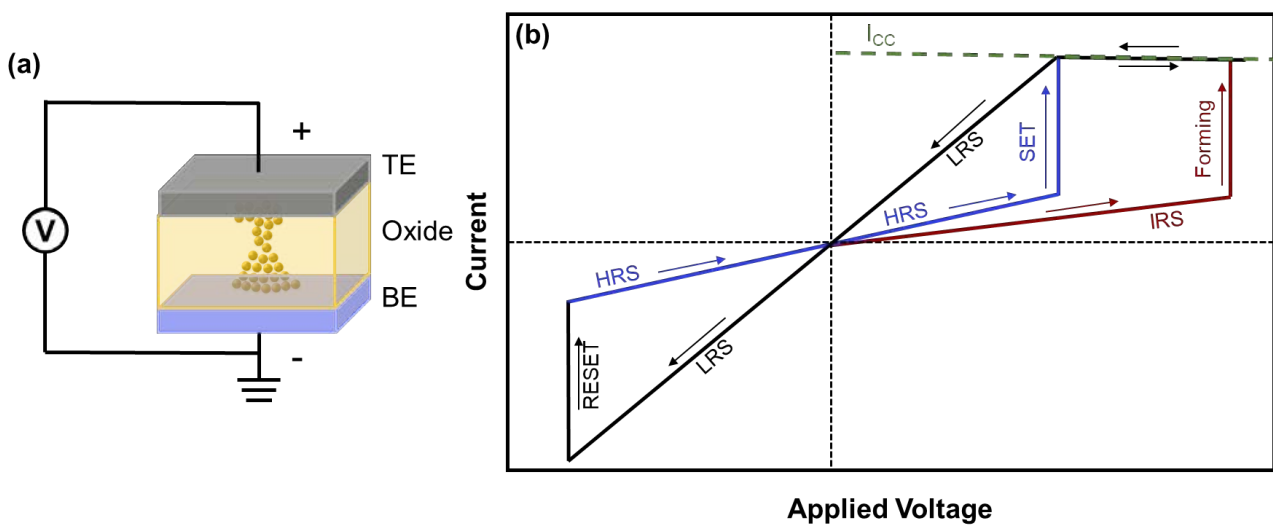


Figure 1 A schematic illustration of (a) metal-insulator-metal (MIM) structured RRAM device under electric field and (b) its switching process and the corresponding IV curve.

Redox-based ion-related RRAM devices include two types of memory devices: electrochemical metallization memories (ECM) and valance change memories (VCM).[13]–[16] More detailed explanation of RRAM devices and the corresponding switching mechanisms can be found in Refs.[10], [11], [17]–[24] In the remaining of the chapter, emphasis will be put on the effect of external stimuli on the device behavior.

1. Electrical field

External applied electrical field is the most basic and common method to tune the resistance states of RRAM devices. The ECM based device is a memory cell with a metal electrode supplying electrochemical active elements, such as Ag and Cu, and a counter inert electrode, such as Pt and W. The distance between the electrodes can be very small, e.g. a few nanometers to a few tens of nanometers. A conductive filament formed during the switching process consist of an active electrodeposition of metal bridging the two electrodes. The SET process of ECM involve three steps: (i) anodic dissolution of electrochemical active metal M ($M \rightarrow M^{z+} + ze^{-}$, with M^{z+} representing the metal cations in the resistive oxide thin film and e^{-} representing electrons), (ii) migration of the metal cations under the external electrical field, and (iii) reduction and electrocrystallization of M on the surface of inert electrode ($M^{z+} + ze^{-} \rightarrow M$). In the RESET process, the formed conductive filaments are dissolved partially under reverse external stimuli.[25] VCM device consists of electrodes which do not inject metal cations but rather form conductive filaments consist of oxygen vacancies V_{O} . The conductive filaments are driven by point defects, such as oxygen vacancies V_{O} . [26]–[28]

Direct experimental observations of conductive filaments were reported using different experimental methods, including energy dispersive X-ray spectroscopy (EDX),[29] scanning electron microscopy (SEM),[29] transmission electron microscopy (TEM),[26], [27], [30]–[34] scanning TEM (STEM),[35] conductive atomic force microscopy (CAFM),[36], [37] X-ray absorption spectroscopy,[28], [38] and scanning tunneling microscopy (STM).[39]

The formation and the dissolution dynamics of conductive filaments for Pt/SiO₂/Ag structured RRAM was studied by TEM, as shown in Figure 2 (a) to (c). Figure 2 (a) shows the initial device state without any conductive filaments inside SiO₂ layer (bright layer). During the forming process, conductive Ag filaments were formed, Figure 2 (b), and later dissolved during the RESET process, Figure 2 (c). A schematic illustration

of the Ag ions transport and reduction process which results in formation of dendrite shaped filaments is given in Figure 2 (d).[40]

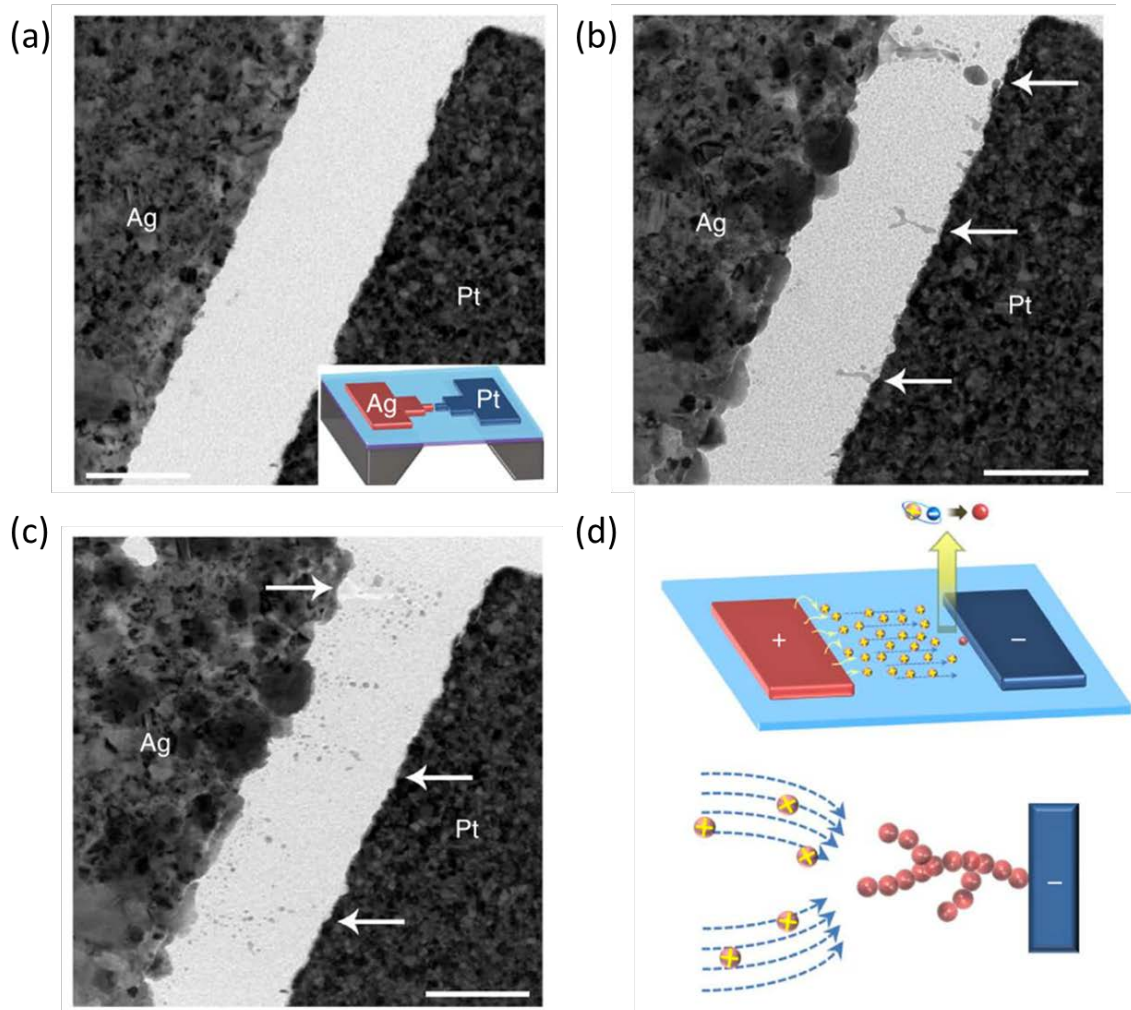


Figure 2 Observation of Ag conductive filament dynamics in SiO_2 -based RRAM. Scale bar, 200 nm. (a) TEM image of an as-fabricated Ag/SiO₂/Pt structured RRAM device with an inset showing the device structure schematic illustration. (b) TEM image of the same device after the forming process. The arrows highlight several representative filaments. (c) TEM image of the same device after RESET. (d) A schematic illustration of the conductive filament formation process under external electrical stimuli.[40]

The conductive filaments can be controlled by the compliance current in the SET process[41]–[46] and the stop voltage in the RESET process.[41], [42], [46]–[48] By limiting the compliance current (I_{CC}) during the SET process, it was shown possible to control the diameter of the conductive filament.[45], [49] In the RESET process, a depletion gap is formed and interrupted the conductive filament, i.e., the electric field drops across the gap region and induces an abrupt increase of cell resistance. The length (distance) of the depletion gap can be controlled by different RESET stop voltage.[25], [50] An example illustrating the control of the resistances by both limiting the compliance current in the SET process and the stop voltage in the RESET

process within one RRAM device is shown in Figure 3. Figure 3 (a) shows a circuit of one RRAM device connected in series with one transistor, which formed the so-called one transistor one RRAM (1T1R) structure. The transistor here is implemented in order to provide the possibility to control the compliance current. A TEM picture of the device is also provided in Figure 3 (a). By varying the compliance current from 100 μA to 1 μA , the intermediate resistance states (INRS) achieved after SET process varied from 1 k Ω to 1M Ω . This showed a relationship between the INRS and the compliance current I_{CC} of $\text{INRS} \propto \frac{1}{I_{CC}}$, Figure 3 (b). Figure 3 (c) shows different INRS achieved by varying RESET stop voltage, here the INRS was found to be $\text{INRS} \propto V_{RESET}$.

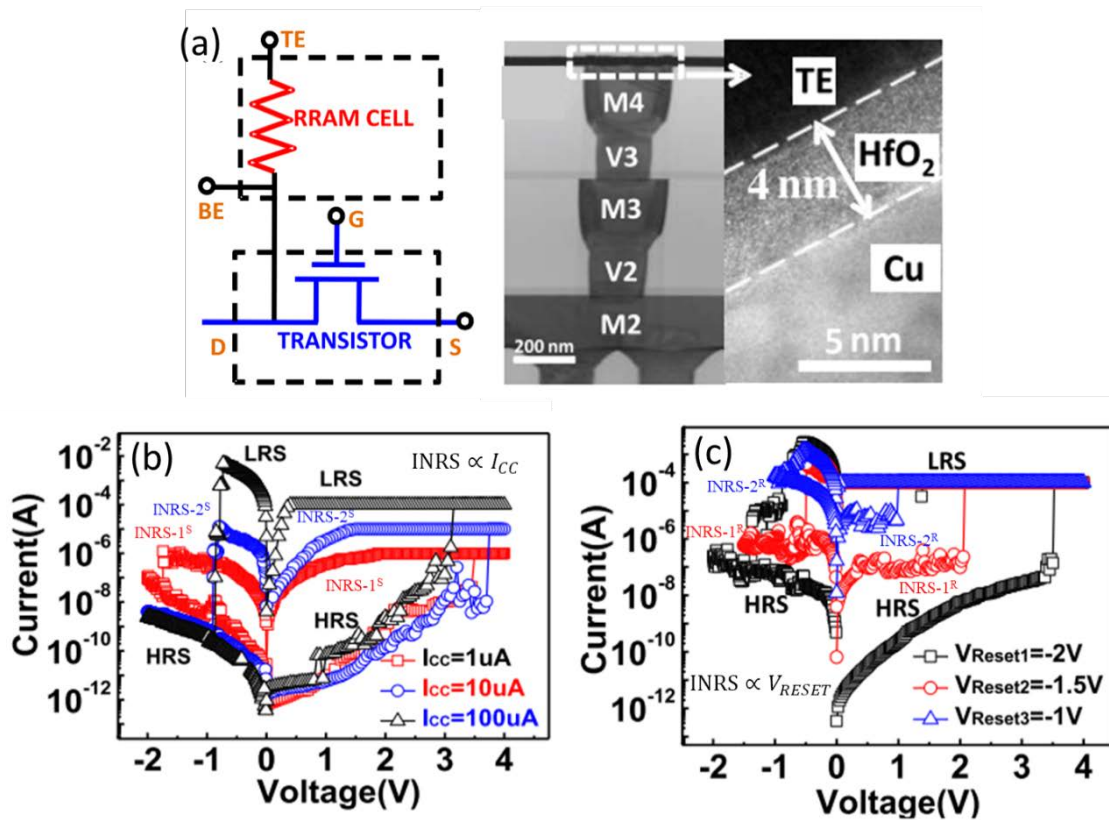


Figure 3 Multi-level storage obtained in (a) 1T1R structured RRAM by (b) different compliance current in SET process and (c) different sweep stop voltage in RESET process.[42]

The above example shown in Figure 3 used voltage sweep to switching the RRAM device. Besides voltage sweep, the external voltage can also be applied in a form of voltage pulse.[48], [51]–[57] Compared to voltage sweep switching, the voltage pulse switching method has several advantages, such as fast switching speed and low switching energy. For example, the fastest switching time by voltage pulse is about 100 ps for SET process and 120 ps for RESET process.[56] The switching energy consumption by voltage pulse is as low as less than 0.1 pJ per bit.[57] The voltage pulse width and amplitude can also influence the amplitude of the resistance change. Two examples illustrating the change of voltage pulse are shown in Figure 4 (a) and (b).

Figure 4 (a) shows that by increasing the amplitude of the RESET voltage pulse from -4.5 V to -6.5 V, the HRS increases.[58] Figure 4 (b) shows that by decreasing the voltage pulse width from 100 μ s to 100 ns in RESET process (or by decreasing the voltage pulse width from 100 ms to 10 μ s in SET process), the HRS decreases (or the LRS achieved increases).[59] Figure 4 shows the device structures (left) and the corresponding device responses under voltage pulse (right).

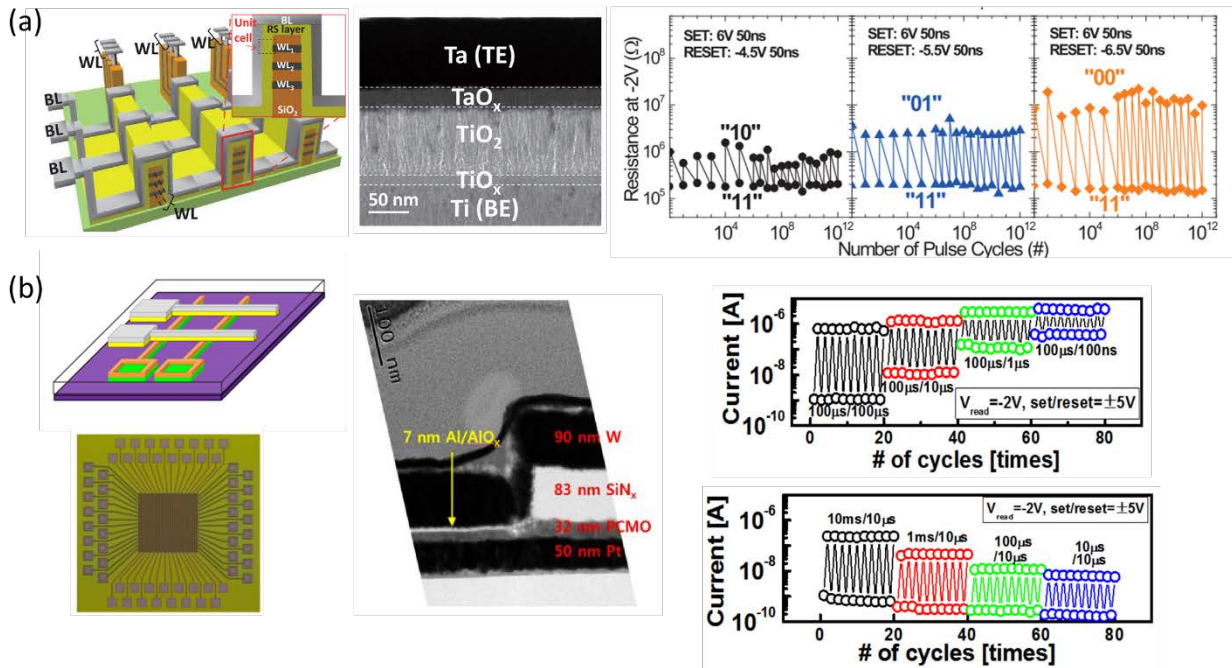


Figure 4 (a) In Ti/TiO_x/TiO₂/TaO_x/Ta RRAM, multiple resistance states, indicated by '11', '10', '01', '00', were achieved by using different voltage pulse heights in RESET process. An excellent endurance property of 10¹² cycles without obvious resistance degradation was also verified by using pulse switching mode.[58] (b) In Pt/PCMO/SiN_x/W RRAM, multiple high resistances or multiple low resistances were achieved by varying pulse widths in RESET and SET process, respectively.[59]

2. Magnetic field

The research question is whether resistive switching can be influenced by magnetic field? If the answer is positive, this can provide a unique opportunity to encode information in resistive switching with the help of magnetic modulation.[60] However, so far only few works have been focused on the responses of a device to external magnetic field.[60]–[65]

For ECM devices, such as Pt/TiO₂/Ni,[61] Pt/HfO₂/Ni,[62] and Pt/HfO₂/Co RRAM[63], the conductive filaments consist of magnetic metal ions such as Ni and Co. The anisotropic magnetoresistance (AMR) behavior in Pt/HfO₂/Ni device is shown in Figure 5.[61] The directions of the external magnetic field are shown in Figure 5 (d). Magnetic field of H_x and H_y are in plane of the substrate and perpendicular to the Ni top electrode,

i.e., H_z is perpendicular to the substrate. Magnetoresistance is defined as $\Delta R/R = [R(H) - R(H_0)]/R(H_0) \times 100(\%)$, where $R(H)$ is the resistance under the external magnetic field and $R(H_0)$ is the resistance at zero field. The AMR of device at LRS under different magnetic fields are as shown in Figure 5 (a) to (c). Low AMR value was observed with a relative resistance change of less than 0.5%. The observed AMR is induced by ferromagnetic conductive filaments formed during the LRS. Whereas no AMR was observed for devices at HRS (data not shown in original references).[61], [62]

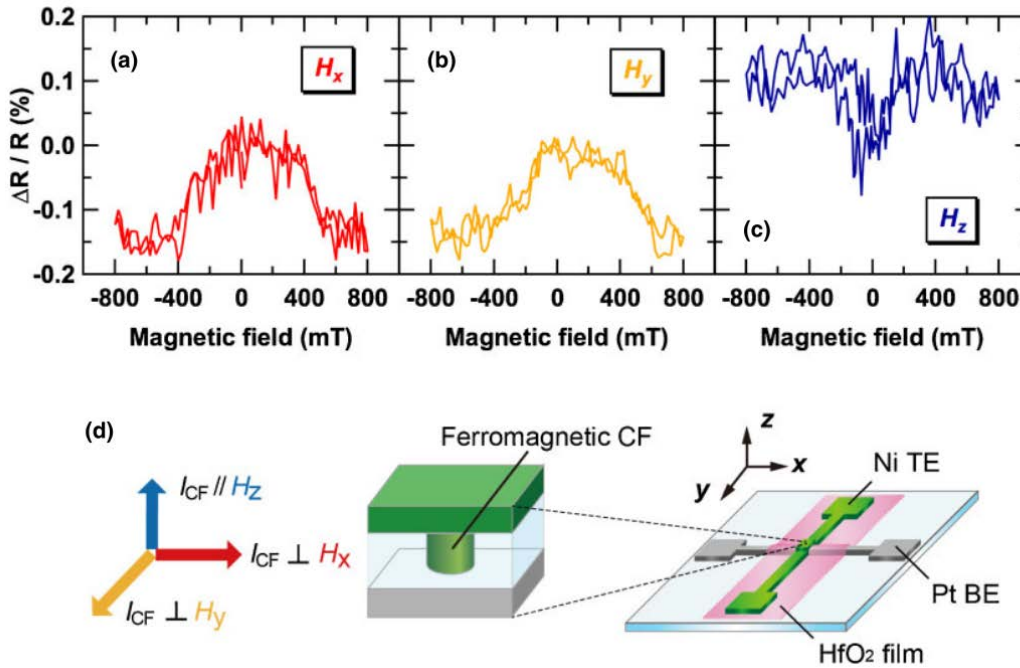


Figure 5 Anisotropic magnetoresistance (AMR) observed in Pt/TiO₂/Ni RRAM devices at LRS. The directions of the applied magnetic field are (a) H_x , (b) H_y , and (c) H_z as indicated in (d).[61]

For VCM devices, such as Pt/Co:ZnO/Pt,[60] Pt/Mg-substituted ZnO/Pt,[65] and Ag/BaTiO₃/FeMn/BaTiO₃/Ag,[64] the magnetization (or magnetic moment) and coercive field of the RRAM devices at both HRS and LRS were tested.[60], [65] The resistive switching was found to be controlled by magnetic fields.[64] A model of bound magnetic polarons (BMP), stemming from a coupling between the magnetic moments of the electrons and those of the magnetic ions, was used to explain the resistive switching as a function of magnetic modulation for the VCM.[60], [65], [66] As shown in Figure 6 (a), the device configuration consists of Pt/(Zn_{0.95}Co_{0.05})O/Pt and the resistive switching layer, (Zn_{0.95}Co_{0.05})O, is made of a diluted magnetic semiconductor (DMS). Figure 6 (b) and (c) show typical magnetization hysteresis loops of devices measured at HRS and LRS. The most eminent feature is that both the saturation magnetization (M_S) and coercive field (H_C) changed as the device switched between HRS and LRS. The M_S changed from 3.2 μemu to 5.8 μemu and the H_C changed from 65 kOe to 90 kOe as the RRAM switched from HRS to LRS,

respectively. Reversible control of M_S and H_C in a sequence of HRS/LRS cycles is shown in Figure 6 (d) and (e). The BMP mechanism is believed to be accounted for the observed ferromagnetism. The higher density of well-ordered V_O yields a larger volume occupied by BMPs, thus increasing the probability of transferring more Co^{2+} ions into the ferromagnetic domains and enhanced the ferromagnetism. While the model claimed remains phenomenological, the description appears reasonable and efforts to pursue these processes further are highly warranted.

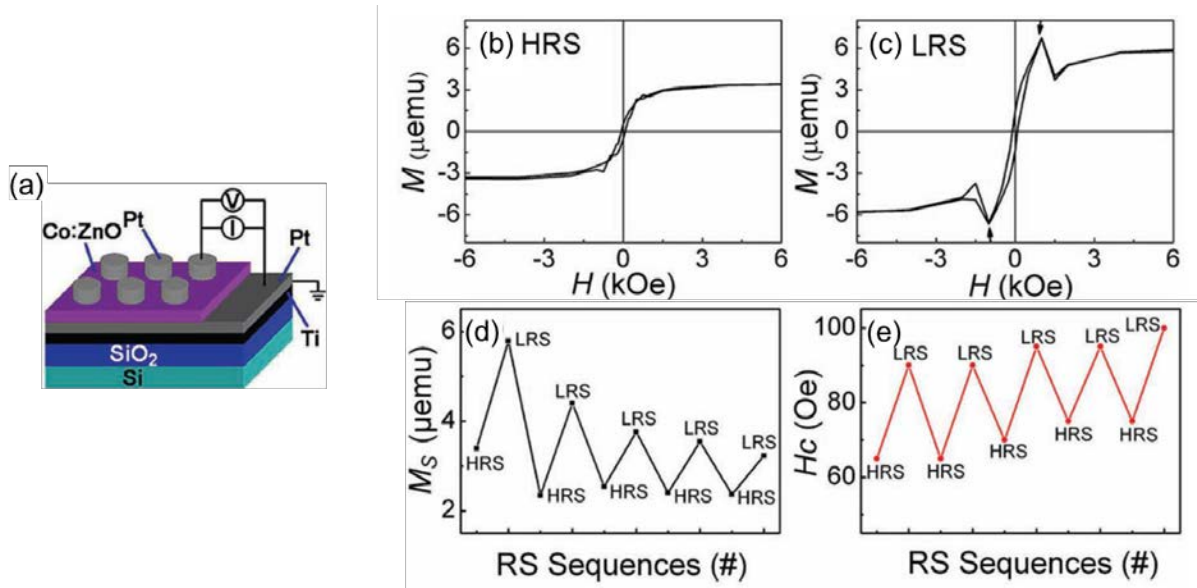


Figure 6 (a) A schematic illustration of Pt/(Zn_{0.95}Co_{0.05})O/Pt RRA device and measurement setup. Hysteresis loop measured at room temperature of RRAM devices at (b) HRS and (c) LRS. The magnetization M_S (d) and coercive field H_C (e) are altered reversibly when the resistance of RRAM switched between HRS and LRS.[60]

The desire is to achieve a multi-level or a multi-state storage by combining electrical and magnetic properties together however, a real uncoupled multi-level storage device has not yet been fully realized, since the magnetic properties are always coupled to the device resistance states. More detailed models of the physical mechanism are desirable to a better understanding the device behavior and its relation to magnetic stimuli.

3. Thermochemical treatments

In this part, we would like to discuss the thermochemical treatment which refers to annealing of post-deposited RRAM devices under a certain gas atmosphere at elevated temperatures. Depending on the gas type, temperature and treatment time, the thermochemical treatment can influence the device crystallinity,[67]–[69] defects concentration,[52], [70]–[74] and stoichiometry,[73] which will in turn affect the devices performances.

Thermochemical treatment can have a profound influence on the device crystallinity i.e., the degree of structural order. The Pt/TaO_x/W system after annealing at 964 °C for 30 min shows a change of the TaO_x layer structure from amorphous to polycrystalline β phase while the resistive switching showed negligible degradation.[67] For the TiN/HfO_x/TiN based system, only cubic HfO_x layer deposited at 350 °C showed resistive switching while the monoclinic HfO_x deposited at 400 °C did not show resistive switching.[75] Interestingly, in the Pt/HfO₂/Pt system, the monoclinic HfO_x also showed resistive switching.[69] For the Pt/La_{0.7}Ca_{0.3}MnO₃ (LCMO)/Ag system, the resistance switching took place only at the crystalline state of the LCMO and not in the amorphous state.[76]

During a thermochemical treatment, defects such as hydrogen ions or V_{O} , can be introduced into metal oxide. Annealing the TiN/Ta₂O₅/Ta in NH₃ at 400 °C for 5 min, introduced hydrogen into Ta₂O₅, see Figure 7 (a). The presence of hydrogen inside Ta₂O₅ decreased the forming voltage as well as the LRS of the device. Besides, the drift of both HRS and LRS to higher resistances is reduced after treatment with NH₃. Figure 7 (b) and (c) show the degradation of the resistance after 15 days for samples treated at 250 °C. However, devices which annealed with NH₃ showed less pronounced degradation of the resistance. The authors explained this behavior in the following way: annealing introduces H species which led to spontaneous formation of O-H bonds in Ta₂O₅. This process can be expressed using the Kröger–Vink notation by $\frac{1}{2}H_2(g) + O_{\text{O}}^x \rightleftharpoons HO_{\text{O}}^+ + e^-$, which shows that the formation of O-H act as donors i.e., leads to the generation of electrons (e^-). After heat treating the devices at 250 °C for 15 days, the introduction of H species led to a better thermal stability of both the HRS and the LRS. At elevated temperatures and over long time (15 days), the O-H bonds stabilized the V_{O} defects and improved the stability of the conductive filaments. In another example, it was shown that annealing of Al-doped ZnO/ZnO/Au in H₂ at 350 °C for 15 min introduced a layer with high concentration of V_{O} , which acted as oxygen reservoir.[71] This resulted in improvement of the $R_{\text{OFF}}/R_{\text{ON}}$ ratio from ~10 to 10⁴. In both Pt/Al₂O₃/Cu based ECM type and Pt/HfO₂/Zr based VCM type RRAM, annealing the devices in 1 MPa H₂ at 400 °C for 30 min lowered the forming voltage due to the generation of oxygen vacancies V_{O} and OH^- bounds, which assist the conductive filament formation.[70]

Thermochemical treatment can also result in stoichiometry changes. An example of such effect can be seen in the Pt/TaO_x/TiN system which was annealed in O₂ at 300 °C for 1 min. Here, the stoichiometry of TaO_x changed from TaO_{2-γ} to Ta₂O_{5-z} which has a profound effect on the device endurance i.e., changes from 27 cycles to more than 270 cycles, as shown in Figure 7 (d) to (e).

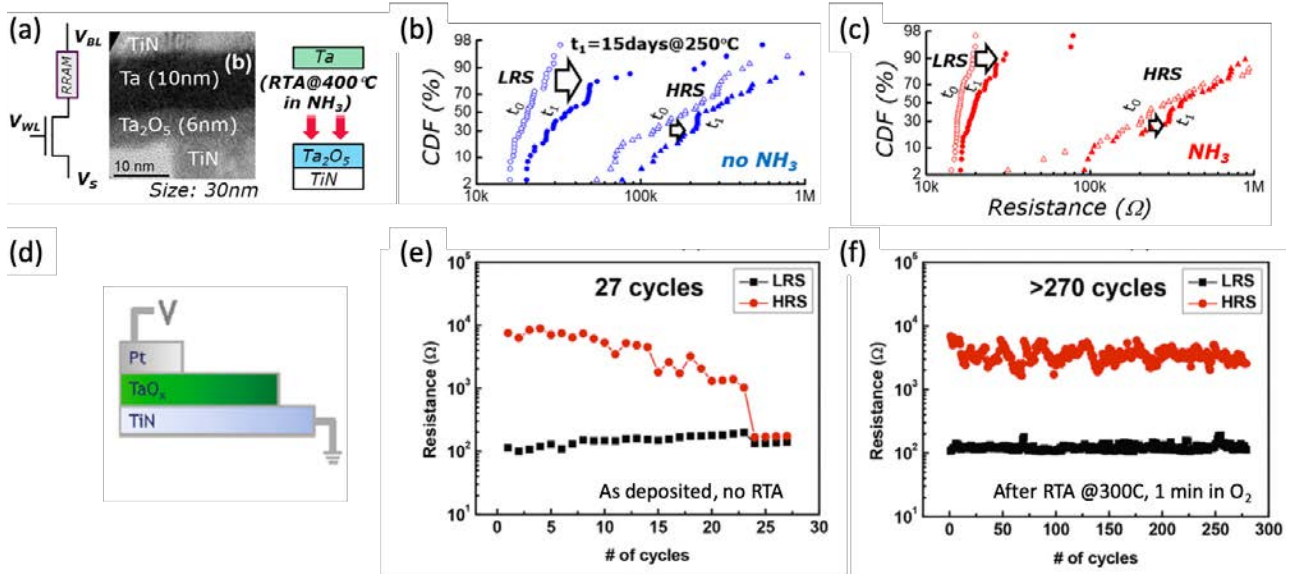


Figure 7 Rapid thermal annealing effect in TaO_x based RRAM devices. (a) Schematic illustration of TiN/Ta₂O₅/Ta RRAM and a TEM cross sectional view of the RRAM device, (b) resistance retention behavior in devices without NH₃ annealing, (c) resistance retention behavior in devices with NH₃ annealing.[72] (d) Schematic illustration of Pt/TaO_x/TiN RRAM, (e) endurance behavior without rapid thermal annealing (RTA), (f) endurance behavior after rapid thermal annealing.[73]

4. Strain

Due to the potential application of RRAM devices in electronics, roll-up displays, and wearable devices, the impact of stress and flexible (foldable or stretchable) RRAM devices have been widely studied and reported. Various substrates including paper,[77], [78] polyethersulfone (PES),[79]–[84] plastic,[85]–[88] polyimide,[89]–[91] poly-ethylene-naphthalate (PEN),[92] poly-ethylene-terephthalate (PET),[93]–[100] parylene,[101] polydimethylsiloxane (PDMS),[102] mica,[103] and water soluble substrates[104] have been used in flexible applications.

Exploring the feasibility of printable, foldable and stretchable devices and the effect of strain on the device is of particular interest and is a key parameter for tuning the functionality of the devices.[105] Three sources of stress can be applied to a device, i.e. stress caused by external mechanical deformation,[82] stress introduced by interfaces mismatch, i.e., heterostructure interfaces[105], [106] and weak points at grain boundaries,[107], and stress induced by doping.[108] Figure 8 shows schematic illustrations of two types of stress sources with (a) showing the mechanical bending stress[82] and (b) showing the stress introduced at heterostructure interfaces, either in multilayer (left) or vertical aligned (right) structure.[105] Doping is a very common and widely used way to influence the performance of the devices, but currently there are only a

few reports which explain or relate the stress causes by the doping to the device performance and therefore this not be discussed here.[109], [110], [119]–[122], [111]–[118]

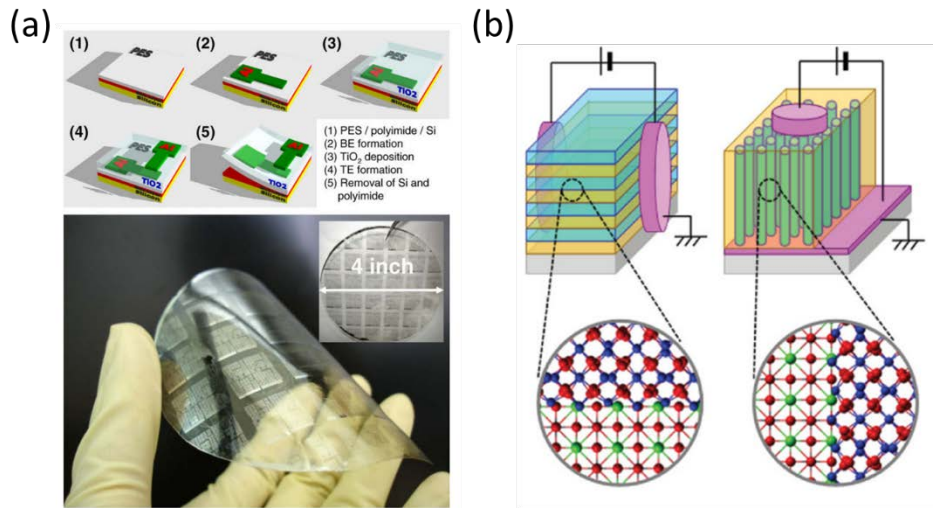


Figure 8 Two sources of stress applied to RRAM device: (a) the fabrication process flow of Al/TiO₂/Al structured RRAM on polyethersulfone (PES) and a photograph of the mechanical bending stress applied to RRAM devices;[82] (b) illustration of stress introduced by heterostructure interfaces inside RRAM device.[105]

The most commonly reported applied stress is bending, which is often characterized by the so-called mechanical flexibility and endurance. Mechanical flexibility of the device is commonly characterized by the bending radius R and bending angle θ , as illustrated in Figure 9. Mechanical endurance is characterized by the repeatability of the bending process, i.e. the number of bending cycles.

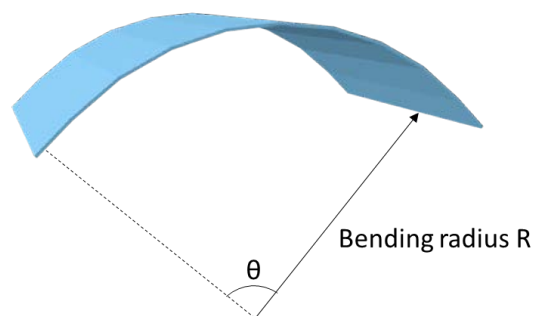


Figure 9 Common mechanical stress applied to RRAM devices with an illustration of bending radius R and bending angle θ .

Before reaching a critical crack initiation and propagation which lead to the failure of the device, most devices exposed to mechanical stress showed stable resistive switching, including single layered Al₂O₃, [79], [87] HfO₂, [98], [101], [104] TiO₂, [78], [82], [84], [86], [89], [97] ZnO, [80], [81], [99], [123] NiO, [94] Cu_xO, [88] WO₃·H₂O, [96] and α -IGZO, [85] bilayered Al₂O₃/HfO₂, [93] Zr_{0.5}Hf_{0.5}O₂/InGaZnO, [103] Al-In-O/InO_x, [124]

GeO_x/HfON,[90] and TaO_x/TiO₂.[91] Due to different ductility of the individual film, detachment of the films or formation of crack often happened under repetitive bending or varying strain conditions.[81], [96], [123] As the bending radius decreases (i.e., increasing the bending angle), cracks are initiated and propagated leading to deterioration of the resistive switching behavior. The crack density increases as the strain increases.[98] An example using the ITO/HfO_x/ITO device show that the relation between the bending radius and the strain as well as crack density are shown in Figure 10 (a) and (c). The strain was estimated by the relation $\varepsilon = t/2R$, where t is the thickness of the substrate and R is the bending radius.[98] As the bending radius decreased from flat state (∞) to 2 mm, the strain increased from 0% to 3.18%. The structure of the HfO_x layer is a mixed amorphous-nanocrystalline and the tensile stresses in HfO_x layer is found to be released by the presence of the amorphous components. As the crack density in the ITO bottom electrode increased from 0 to 35 mm⁻¹, the resistance of the ITO layer increased and the corresponding voltage required for RESET increased as well. At the critical bending radius of 2 mm, the applied voltage mainly dropped on the fractured bottom electrode and the voltage remained on the HfO_x layer is no longer sufficient to rupture the conductive filament. The devices failed to RESET and the R_{OFF}/R_{ON} ratio decreased to 0, as shown in Figure 10 (b) and (d).[98]

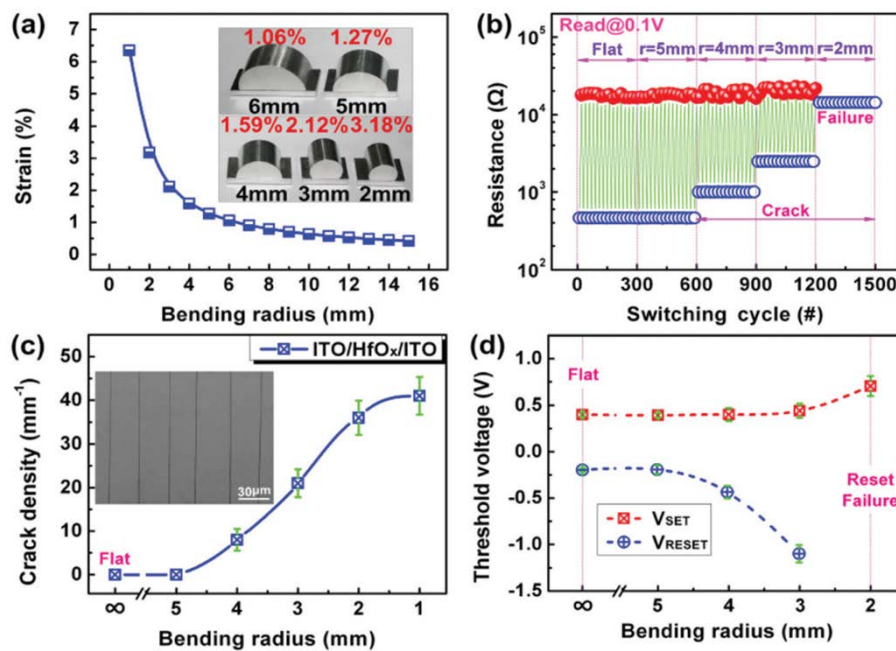


Figure 10 Mechanical flexibility of TIO/HfO_x/ITO structured RRAM device: (a) mechanical strain vs. bending radius.(b) resistance evolution as a function of the bending radius, (c) crack density vs. bending radius, and (d) switching voltages evolution as a function of the bending radius.[98]

The experimental setup of strained Ti/TiO₂/TaO_x/Ta device deposited on polyimide are shown in Figure 11 (a) and (b). In these experiments, both the LRS and HRS increased as the bending radius increased from a flat state to 10mm, see Figure 11 (c).[91] The physical mechanism behind the behavior of the device resistance under bending is still unclear.

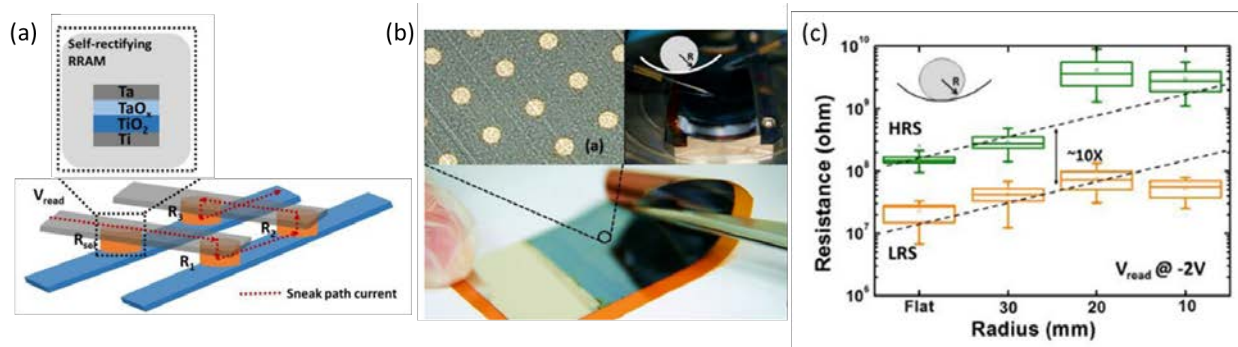


Figure 11 (a) Schematic illustration of device structure. (b) Image of fabricated RRAM devices, electrical measurement setup and flexible RRAM device. (c) Resistance evolution as the bending radius decreased.[91]

Experiments with ITO/HfO_x/ITO deposited on poly-ethylene-terephthalate (PET) showed no obvious degradation of the resistance after 2.4x10⁴ cycles of bending i.e., at a bending radius of 6 mm.[98] Whereas ITO/ZnO/ITO devices deposited on polyethersulfone (PES) began to show degradation of the resistance already after 10 cycles of bending, i.e., at a bending radius of 20 mm. The degradation of the resistance is caused by cracks formation in the ITO bottom electrode.[81] The number of bending cycles was improved from 10 to 10⁴ cycles for the PES/ITO/ZnO/ITO by inserting a ductile Ag layer between the ITO bottom electrode and the ZnO layer, as shown in Figure 12 (a). A record of 10⁵ bending cycles was measured for the Ni/GeO/HfON/TaN system, as shown in Figure 12 (b).[90] Both LRS and HRS remained stable after 10⁵ bending cycles, however, the reason for such improvement in the bending resistant was not explicitly explained. Other works [78], [94], [96], [98], [103], [123]–[125] also reported the mechanical robustness of the device by showing stable resistance states after many cycles of bending, yet currently the maximum bending cycles is still 10⁵.

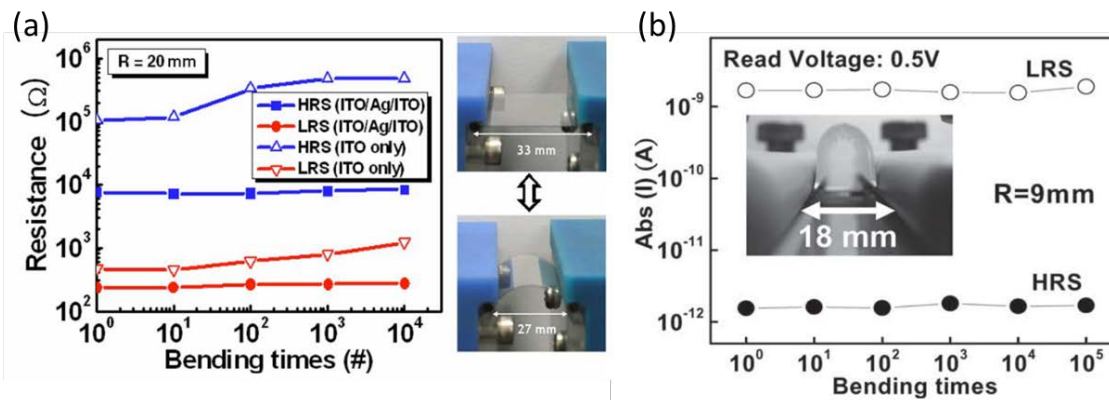


Figure 12 Mechanical endurance of RRAM devices. (a) ITO/ZnO/ITO structured RRAM devices showed severe resistance degradation after 10 times of bending due to the bottom electrode cracking. Improved mechanical endurance was achieved by inserting Ag into bottom electrode.[81] (b) TaN/HfON/GeO/Ni structured RRAM device showed robust LRS and HRS after 10^5 times of bending.[90]

Since a poor adhesion between the device and the substrates usually results in formation of cracks and detachment under repetitive bending, flexible materials rather than metal oxides are often used, e.g., organic materials[77], [102], [125], [126] and graphene oxide[83], [95], [100] based devices. Since this chapter is dealing mainly with metal oxide we will not discuss these type materials by rather referred the readers who are interested in these materials to the references above.

Besides bending, stress can also be introduced at the interfaces, such as multilayer heterostructures by mismatch of the different layers.[127], [128] Many studies in metal oxide heterostructures with variation of interfaces focused on tuning the ionic conductivity through lattice compressive or tensile strain caused by the mismatch between the layers.[129]–[132] For example, tuning the V_{O} mobility in $\text{Gd}_{0.1}\text{Ce}_{0.9}\text{O}_{2-\delta}/\text{Er}_2\text{O}_3$ heterostructures was reported to enhanced the mobility as the number of interfaces increase.[106] In this paper, the strain was systematically varied by increasing the number of individual layers of $\text{Gd}_{0.1}\text{Ce}_{0.9}\text{O}_{2-\delta}$ and Er_2O_3 from 1 to 60 while keeping the overall heterostructure at a constant thickness. By changing the compressive strain in these structures by more than 1.16%, the activation energy for oxygen vacancies migration was altered by 0.31 eV while the ionic conductivity increased. The same authors used the same system $\text{Gd}_{0.1}\text{Ce}_{0.9}\text{O}_{2-\delta}/\text{Er}_2\text{O}_3$ to fabricate RRAM device with side electrodes to study the stress effect on the performance of the device along the direction of the interfaces, Figure 13 (a). [106], [128], [133] The lattice mismatch between the $\text{Gd}_{0.1}\text{Ce}_{0.9}\text{O}_{2-\delta}$ and the Er_2O_3 interface led to an in-plane compressive strain in $\text{Gd}_{0.1}\text{Ce}_{0.9}\text{O}_{2-\delta}$, as shown in Figure 13 (b) and in the TEM image in Figure 13 (c) and (d). By increasing the number of interfaces from 6 to 60 while keeping the ceria-to-erbia ratio and the total film thickness constant, the device transformed from a volatile to a nonvolatile behavior. Hysteresis of the resistance during cycling was also observed and it was explained by the formation of filaments of ceria at the phase boundary with

eria. The authors speculate that the low mobility of oxygen ions was a results of compressive strain. The low mobility of oxygen vacancies does not allow fully oxidation Ce, which basically hindered the formation of conductive filaments, this retained the device kinetically frozen at LRS.

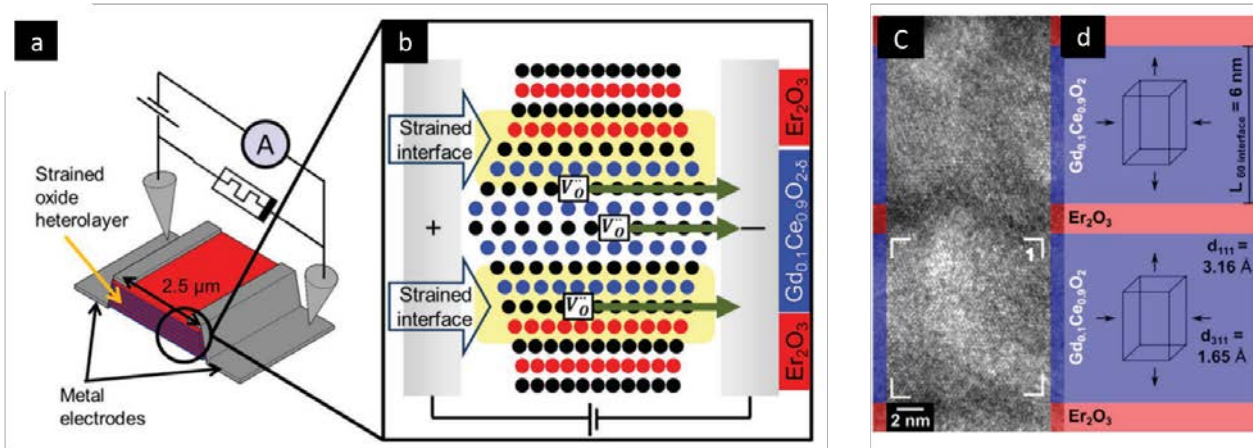


Figure 13 (a) a schematic illustration of device composed of $Gd_{0.1}Ce_{0.9}O_{2-\delta}/Er_2O_3$ heterostructures and the testing set up, (b) schematic view of one of the $Gd_{0.1}Ce_{0.9}O_{2-\delta}/Er_2O_3$ interface showing the lattice mismatch induced strain and the conduction channels of oxygen vacancies V_o , (c) bright field high resolution TEM image of a 60 interface sample, and (d) diagram illustration of the Miller plane spacing measurements and the in-plane compressive and out-of-plane tensile strain.[133]

5. Radiation

Radiation is another form of external stimuli which can affect the performance of the resistive switching device. External radiations often cause defects generation in the materials, such as electron-hole pairs[134], [135] and Frenkel defects,[136] or ion displacement,[137]–[139] which thereby effect the performance of the RRAM devices. A wide range of electromagnetic and particle radiations can affect the RS behavior of the materials, e.g. x-ray,[139]–[142] γ -ray,[75], [137], [150]–[153], [139], [143]–[149] ultraviolet light (UV),[140], [154] visible light,[155]–[157] protons,[139], [141], [142] α particles,[158]–[160] heavy ions,[161]–[164] and neutrons.[135], [138] Interestingly, in space application the failure of the RRAM devices can be caused by cosmic rays and radiations from the Van Allen radiation belts around the earth.[158], [165]

The effect of radiation can be categorized into two main types: (1) a cumulative effect and (2) a single-event effects (SEE). Cumulative effects are the device responses to total ionizing dose (TID) integrated over time. While SEEs are caused by a single, energetic particle and is characterized by an instantaneous failure mechanism.[158], [163], [165]–[168]

Total ionizing dose (TID) is characterized by absorbed dose, i.e., the energy absorbed by matter, with a unit called rad (an acronym for radiation absorbed dose). The effect of TID on RRAM devices were tested using γ -

ray generated by ^{60}Co source,[75], [137], [150]–[153], [139], [143]–[149] x-ray,[139]–[142] protons,[139], [141], [142] and EUV[140] as radiation sources. The responses of the device to TID depend on metal oxide materials, radiation dose and device dimensions. Different TID tolerance values were reported in different oxide based RRAM.[137], [148]–[150] A threshold TID to change device resistances or switching voltages was reported[140] and higher dose usually caused more severe device degradation.[140], [144], [147], [148] In Pt/HfO₂/Ti/Pt devices, the TID threshold for HRS change was reported to be 100 Mrad for EUV and 600 Mrad for x-ray.[140] The effect of γ -ray irradiation on the Mo/Ti/HfO₂/Au system is shown in Figure 14. Both HRS and LRS decreased with the increase the irradiation dose, i.e., ^{60}Co γ -ray, Figure 14 (b). In particular, more than 20% change in LRS, 20% change in forming voltage and 16% change in SET voltage were observed as the radiation dose exceeded 3 Mrad, see Figure 14 (c) and (d).[147] Here, the decrease in the forming voltage and SET voltage were explained by the increase of oxygen vacancies inside HfO₂ layer after radiation. In other experiments, the performance of the device as a response to radiation were explained by radiation-induced charge trapping inside the RRAM devices,[139], [143], [144] radiation-induced defects generation,[147], [150] and metal oxide phase transition.[148], [149]

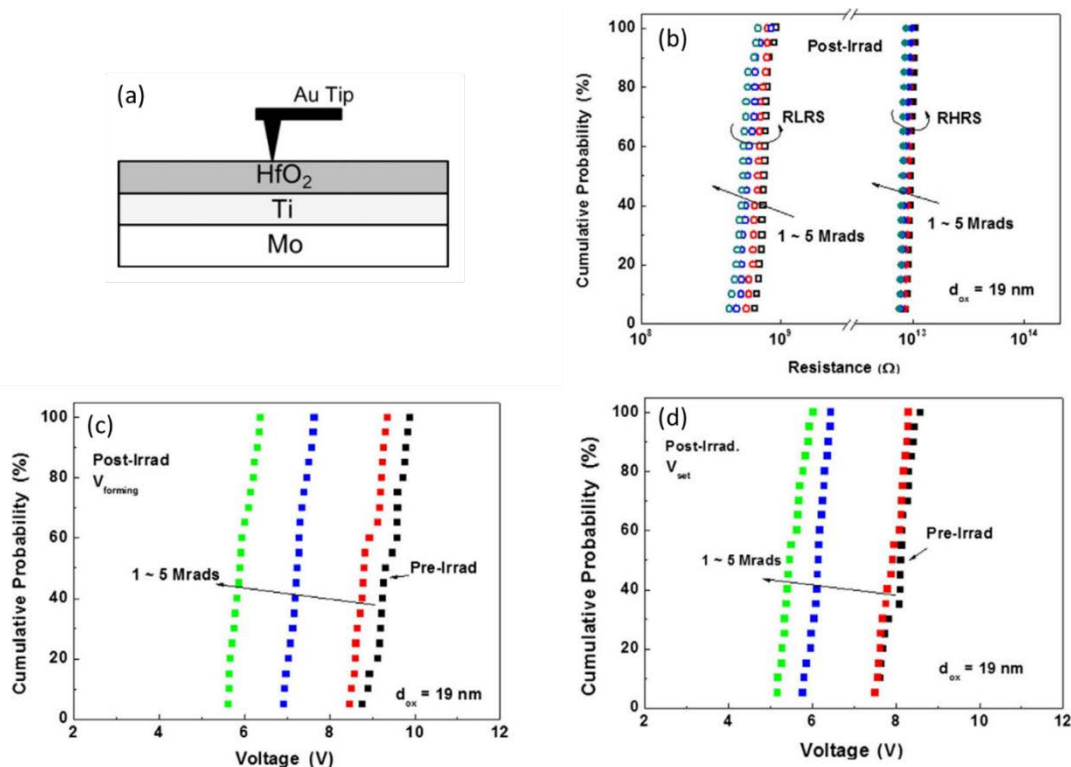


Figure 14 (a) Schematic illustration of Ti/HfO₂/Au RRAM device. ^{60}Co γ -ray irradiation effect on (b) resistance states, (c) forming voltage and (d) SET voltage in Ti/HfO₂/Au RRAM.[147]

Thinner oxide layer and smaller device area showed improved resilience to radiation, e.g. Pt/TaO_x/TiN RRAM devices as shown in Figure 15 (a). These devices with a thickness 25nm were exposed to 180 krad (Si) of γ -ray radiation.[143] Devices with the same area of 20 $\mu\text{m} \times 20 \mu\text{m}$, but a thicker, i.e. 50 nm, show a larger degradation of the HRS after radiation compared to a thinner samples i.e., 25 nm, see Figure 15 (b). This is explained by a electron-hole pair generation under γ -ray radiation where holes believed to be trapped. Holes are more likely to be trapped in thick oxide layer or near the oxide/metal electrode interface in this device. This was explained by the drift or hopping of holes under different built-in electric field caused by different oxide thickness. Here, the trapped holes in thick oxide may form a path for the electron transport, which resulted in a decreased HRS. Whereas holes tapped near interface in thin oxide are more easily to escape and tunnel through electrode, which impeded the formation of an electron conduction path in thin oxide. In the same structured devices with different area of 2 $\mu\text{m} \times 2 \mu\text{m}$, 20 $\mu\text{m} \times 20 \mu\text{m}$, and 80 $\mu\text{m} \times 80 \mu\text{m}$, higher HRS degradation are observed in larger area devices, as shown in Figure 15 (c), indicating an improved tolerance to irradiation as devices scale down.[143]

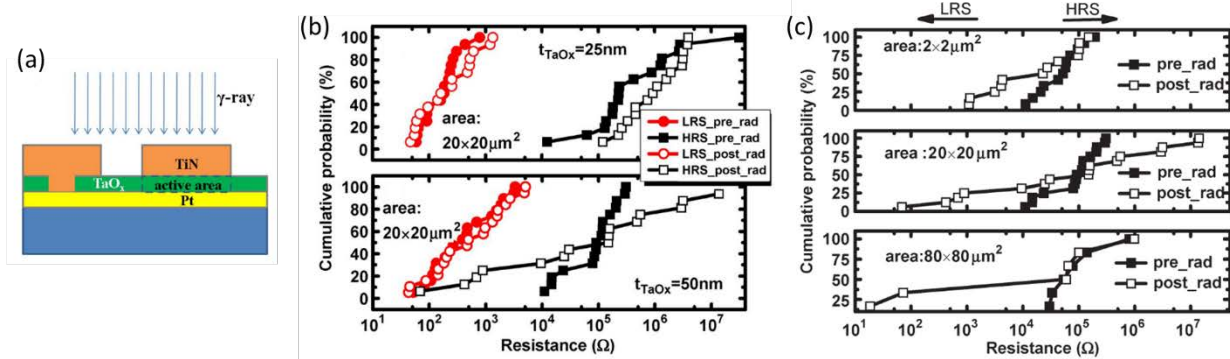


Figure 15 (a) A schematic illustration of 20 $\mu\text{m} \times 20 \mu\text{m}$ Pt/TaO_x/TiN RRAM device, (b) resistance degradation after radiation in devices of same area of 20 $\mu\text{m} \times 20 \mu\text{m}$ with 25-nm thick TaO_x and 50-nm thick TaO_x, respectively, (c) HRS degradation after radiation in devices of different area of 2 \times 2 μm , 20 \times 20 μm , and 80 \times 80 μm .[143]

RRAM devices were also reported to be resilient to a single-event effects (SEE). The TiN/HfO_x/Ti device was irradiated by heavy ions and showed no single event upset in the device.[163] The effects of SEE on the devices were also simulated based on the experimental results of TiN/TaO_x/Ta/TiN RRAM and the results indicated that the system is highly resistant to SEEs for over 30 years of operation.[167]

Radiation can also affect the device resistances through radiation induced metal-oxygen bond breaking,[155], [169] photon-excited oxygen ion migration,[156] and illumination generated electron-hole pairs.[157] Figure 16 (a) shows the effect of photo-radiation on the performance of RRAM devices for the ITO/ZnO nanorods/Au structured.[155] After treating the sample with a low surface-tension perfluorinated liquid, the

hydrothermally grown ZnO nanorods changed from hydrophilic to super hydrophobic. When submerged in water, a double layer containing water-air interface structure is formed due to the hydrophobic property of ZnO nanorods, as shown in Figure 16 (b). The air layer prevented the water from penetrating to the device and caused an operational failure or even more seriously, an electric shock. The water/air interface completely reflected the light when the incident angle is larger than the critical incident value of $\theta_c = 48.6^\circ$. When the angle of the light incident is larger than θ_c , the light is totally reflected and the device showed resistor-type behavior, as shown in Figure 16 (c). When the light incident angle is smaller than the critical angle θ_c , the light penetrates the water-air interface and the device showed memristor-type behavior, as shown in Figure 16 (d). The presence of light, triggered the resistive switching behavior due to the radiation induced desorption of chemisorbed oxygen ions from ZnO nanorods. This gave rise to selective illumination direction as a tuning parameter to trigger the RS.

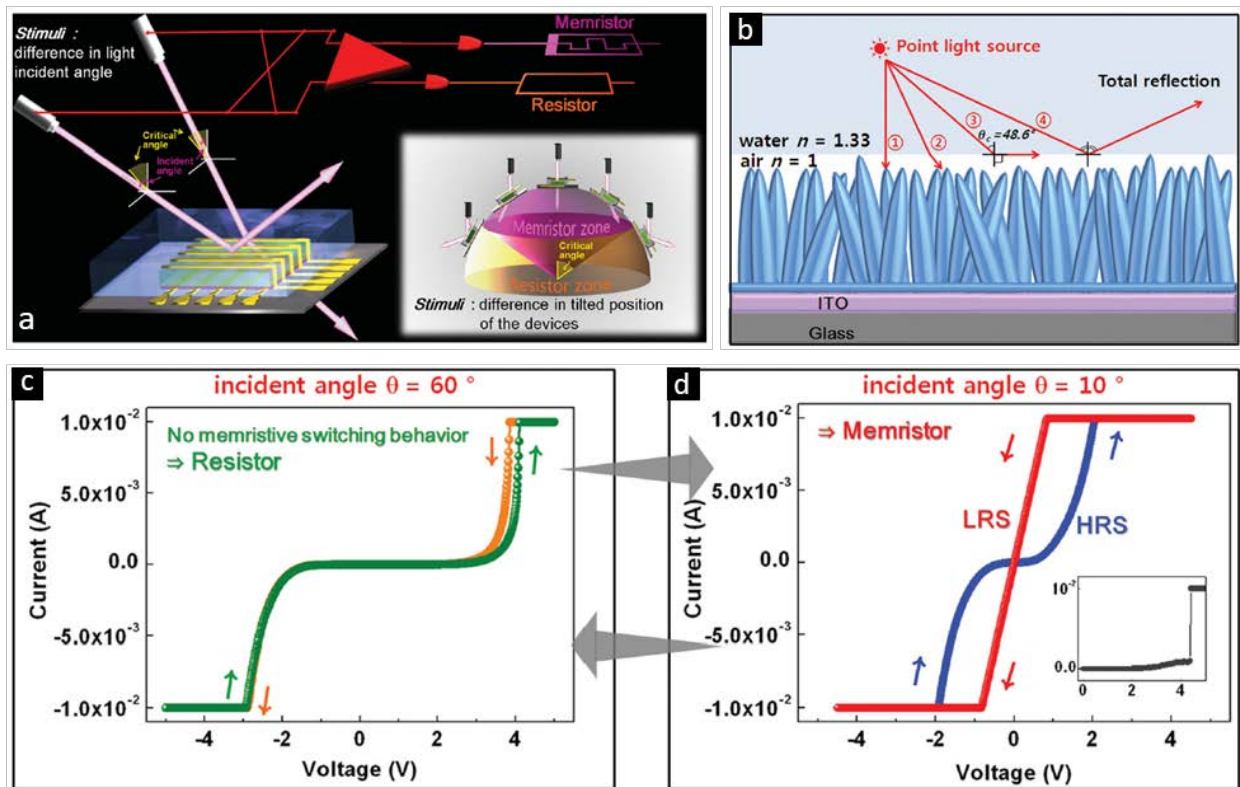


Figure 16 Light radiation (wavelength of 200 to 2500 nm) induced RS behavior inside the ITO/ZnO nanorods/Au structured RRAM devices. (a) Schematic diagram representing the concept of light controlled reversible device function between memristor-type behavior and resistor-type behavior, (b) schematic side view of RRAM device submerged in water with a total reflection at 48.6° , (c) when the incident angle is 60° , the light is total reflected and the device showed resistor-type behavior, (d) when the incident angle is 10° , the light can assist the oxygen inside ZnO nanorods and device showed memristor-type behavior. [155]

Light illumination can also influence the oxygen ion migration of the devices and lead to accelerated dissolution of the filaments. In TiN/HfO₂/diamond-coated Si tip RRAM device,[156] as shown in Figure 17 (a), light radiation caused current drop/RESET process inside the RRAM device. Under light illumination, the device current drops and the resistance increases, which indicates a conductive filament rupture process under illumination, as shown in Figure 17 (b). As the illumination intensity increases, the time it takes to RESET decreases. At an illumination intensity of 1 mW/cm², the device resistance can be modulated by controlling the exposure time, as shown in Figure 17 (c). The illumination induced drop in the resistance and it is due to the photons induced excitation of oxygen ions migration. During the formation of conductive filament (comprising oxygen vacancies) in the dark, Figure 17 (d), oxygen ions are populating the interstitial sites in the filament vicinity. Under light illumination, the interstitial oxygen ions migration is excited by photons, migrating and recombining with the filament vacancies. This lead to a conductive filament rupture, as shown in Figure 17 (e).

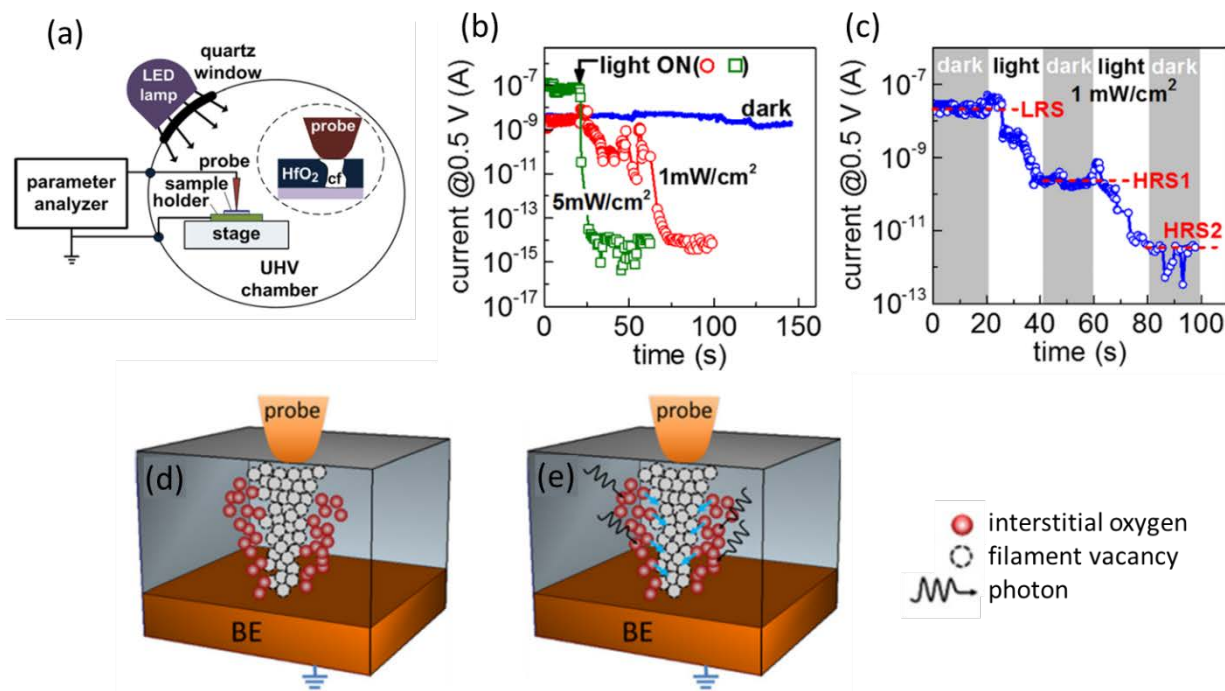


Figure 17 Light induced resistance modulation due to light excited oxygen ion movement. (a) Schematic illustration of the device structure and experimental setup used in this study. (b) Current drop (RESET) process speed dependence on illumination intensity, (c) different intermediate resistance states can be achieved by limiting the duration of exposure time. (d) Conductive filament comprising of oxygen vacancies under darkness, (e) photon excited oxygen migration and recombination with oxygen ions, which lead to conductive filament rupture under illumination.[156]

The behavior of Ti/BiFeO₃/ITO RRAM device under different light intensities [157] is shown in Figure 18 (a) and (b). As the light intensity increases, both SET voltage (V_{SET}) and RESET voltage (V_{RESET}) decreases, as

shown in Figure 18 (c). The HRS drops from 550 M Ω in the dark to about 1 M Ω under a light with intensity of 20 mW/cm², Figure 18 (d). The change in the HRS under light illumination were verified both in the dark and under light illumination repeatedly as shown in Figure 18 (e). Besides the switching properties, the device also showed a significant photoferroelectric effect where both ferroelectric polarization (P_r) and saturated ferroelectric polarization (P_s) increases as the light intensity increases, not shown here. The light induce modulation of the resistive switching was explained by the photo-generated polarized charges in the BiFeO₃ layer which cause an increase in the electric field in the opposite direction leading to a decrease in the HRS and the LRS.

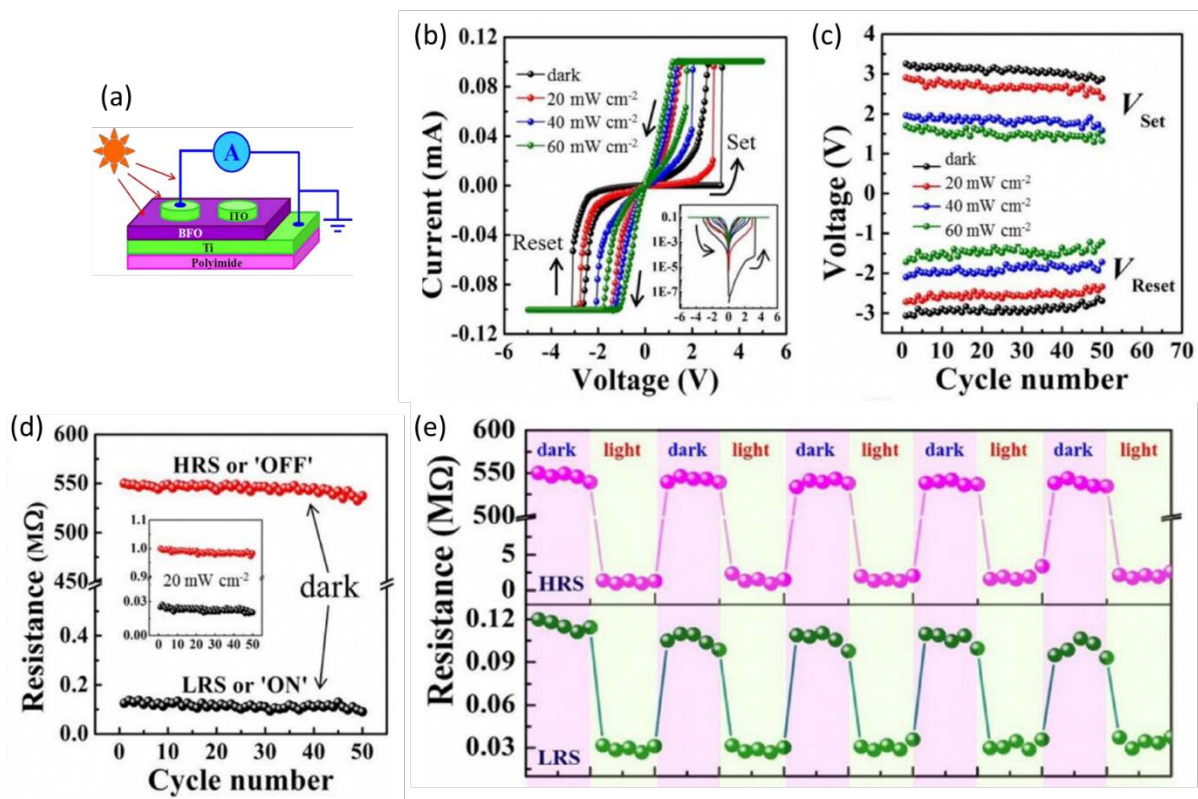


Figure 18 (a) Schematic device illustration of Ti/BFO/ITO RRAM, (b) I-V curve change under different light illumination conditions, (c) light radiation caused decrease of switching voltages, (d) light illumination decreased both HRS and LRS, (e) repeatable verification of resistance change in the dark and under light illumination condition which is explained by photo-generated polarized charges in BiFeO₃ layer.[157]

Outlook

Memristors materials capable of responses to external stimuli represent one of the most exciting and emerging areas of scientific interest and unexplored commercial applications. This provide the potential to modify the materials by applying external stimuli such as light, temperature, magnetic fields, electric fields

and stress. While there are many exciting challenges facing this field, there are a number of opportunities in design, synthesis, and engineering of memristor systems. However, this research topic is to a large extent still unexplored both experimentally and theoretically. This book chapter highlights the recent progress in stimuli-responsiveness of metal oxide based memristor. The demand for widespread research on development of stimuli-responsive memristors are requisite to understand and resolve the future challenges relating to the memristive switching dynamics which require higher resolutions in experiments and a larger degree of accuracy in modeling. This can lead to new and yet unexplored properties for future memory and computing technologies. Navigating this multi-dimensional space is an enormous task without an additional guidance. Therefore, combining in situ techniques and computational materials science to uncover the detailed switching mechanism is one of the key tools for understanding the responds of materials to multiple stimuli.

Acronyms list

FeRAM	Ferroelectric Random Access Memory
MRAM	Magnetoresistive Random Access Memory
PCM	Phase Change Memory
RRAM	Resistance (Switching) Random Access Memory
MIM	Metal-Insulator-Metal
IRS	Initial Resistance State
HRS/ R_{OFF}	High Resistance State
LRS/ R_{ON}	Low Resistance State
TE	Top Electrode
BE	Bottom Electrode
CC	Compliance Current
ECM	Electrochemical Metallization Memory
VCM	Valance Change Memory
EDX	Energy Dispersive X-Ray Spectroscopy
SEM	Scanning Electron Microscopy
TEM	Transmission Electron Microscopy
STEM	Scanning Transmission Electron Microscopy
CAFM	Conductive Atomic Force Microscopy

STM	Scanning Tunneling Microscopy
INRS	Intermediate Resistance State
DMS	Diluted Magnetic Semiconductor
AMR	Anisotropic Magnetoresistance
C-AFM	Conductive Atomic Force Microscope
BMP	Bound Magnetic Polarons
XPS	X-ray Photoelectron Spectroscopy
PEN	Poly-Ethylene-Naphthalate
PET	Poly-Ethylene-Terephthalate
PDMS	Polydimethylsiloxane
UV	Ultraviolet Light
SEE	Single-Event Effect
TID	Total Ionizing Dose

Symbols list

$I(t)$	Current as a function of time
ϕ	Generalized flux
$V(t)$	Voltage as a function of time
$q(t)$	Charge as a function of time
$M(q(t))$	Memristance
R_{OFF}	High resistance state
R_{ON}	Low resistance state
I_{CC}	Compliance current
M	Electrochemical active metal
M^{z+}	Metal cations
e^-	Electrons
$V_{\ddot{O}}$	Oxygen vacancy
H	Magnetic field
ΔR	Resistance difference
$R(H)$	Resistance under external magnetic field

$R(H_0)$	Resistance at zero field
M_S	Saturation magnetization
H_C	Coercive field
T_{crit}	Critical temperature
R	Bending radius
θ	Bending angle
ε	strain
t	Thickness of the substrate
θ_c	Critical incident value
P_r	ferroelectric polarization
P_s	saturated ferroelectric polarization

References

- [1] L. O. Chua, "Memristor—The Missing Circuit Element," *IEEE Trans. Circuit Theory*, vol. 18, no. 5, pp. 507–519, 1971.
- [2] L. O. Chua and S. M. Kang, "Memristive Devices and Systems," *Proc. IEEE*, vol. 64, no. 2, pp. 209–223, 1976.
- [3] D. B. Strukov, G. S. Snider, D. R. Stewart, and R. S. Williams, "The missing memristor found," *Nature*, vol. 453, no. 7191, pp. 80–83, 2008.
- [4] Y. Arimoto and H. Ishiwara, "Current Status of Ferroelectric Random-Access Memory," *MRS Bull.*, vol. 29, no. 11, pp. 823–828, 2004.
- [5] H. Ishiwara, M. Okuyama, and Y. Arimoto, *Ferroelectric random access memories: fundamentals and applications*, vol. 93. Springer Science & Business Media, 2004.
- [6] Z. H. U. Jian-Gang, "Magnetoresistive random access memory: The path to competitiveness and scalability," *Proc. IEEE*, vol. 96, no. 11, pp. 1786–1798, 2008.
- [7] D. Apalkov, B. Dieny, and J. M. Slaughter, "Magnetoresistive Random Access Memory," *Proc. IEEE*, vol. 104, no. 10, pp. 1796–1830, 2016.
- [8] M. Salinga *et al.*, "Monatomic phase change memory," *Nat. Mater.*, vol. 17, no. 8, pp. 681–685,

2018.

- [9] G. W. Burr *et al.*, "Recent Progress in Phase-Change Memory Technology," *IEEE J. Emerg. Sel. Top. Circuits Syst.*, vol. 6, no. 2, pp. 146–162, 2016.
- [10] B. Mohammad *et al.*, "State of the art of metal oxide memristor devices," *Nanotechnol. Rev.*, vol. 5, no. 3, pp. 311–329, 2016.
- [11] H. S. P. Wong *et al.*, "Metal-oxide RRAM," *Proc. IEEE*, vol. 100, no. 6, pp. 1951–1970, 2012.
- [12] Y. Li *et al.*, "Conductance Quantization in Resistive Random Access Memory," *Nanoscale Res. Lett.*, vol. 10, no. 1, 2015.
- [13] R. Waser, R. Dittmann, C. Staikov, and K. Szot, "Redox-based resistive switching memories nanoionic mechanisms, prospects, and challenges," *Adv. Mater.*, vol. 21, no. 25–26, pp. 2632–2663, 2009.
- [14] I. Valov, R. Waser, J. R. Jameson, and M. N. Kozicki, "Electrochemical metallization memories - Fundamentals, applications, prospects," *Nanotechnology*, vol. 22, no. 25, p. 254003, 2011.
- [15] I. Valov and M. N. Kozicki, "Cation-based resistance change memory," *J. Phys. D. Appl. Phys.*, vol. 46, no. 8, 2013.
- [16] J. J. Yang, I. H. Inoue, T. Mikolajick, and C. S. Hwang, "Metal oxide memories based on thermochemical and valence change mechanisms," *MRS Bull.*, vol. 37, no. 2, pp. 131–137, 2012.
- [17] M. A. Zidan, J. P. Strachan, and W. D. Lu, "The future of electronics based on memristive systems," *Nat. Electron.*, vol. 1, no. 1, pp. 22–29, 2018.
- [18] M. Yi *et al.*, "Temperature dependence of resistive switching behaviors in resistive random access memory based on graphene oxide film," *Nanotechnology*, vol. 25, no. 18, 2014.
- [19] B. Hudec *et al.*, "3D resistive RAM cell design for high-density storage class memory- a review," *Sci. China Inf. Sci.*, vol. 59, no. 6, pp. 1–21, 2016.
- [20] R. Waser, R. Dittmann, M. Salinga, and M. Wuttig, "Function by defects at the atomic scale - New concepts for non-volatile memories," *Solid. State. Electron.*, vol. 54, no. 9, pp. 830–840, 2010.
- [21] J. J. Yang, D. B. Strukov, and D. R. Stewart, "Memristive devices for computing," *Nat. Nanotechnol.*,

vol. 8, no. 1, pp. 13–24, 2013.

- [22] S. G. Hu *et al.*, “Review of nanostructured resistive switching memristor and its applications,” *Nanosci. Nanotechnol. Lett.*, vol. 6, no. 9, pp. 729–757, 2014.
- [23] S. Kim, J. Zhou, and W. D. Lu, “Crossbar RRAM arrays: Selector device requirements during write operation,” *IEEE Trans. Electron Devices*, vol. 61, no. 8, pp. 2820–2826, 2014.
- [24] I. Valov and T. Tsuruoka, “Effects of moisture and redox reactions in VCM and ECM resistive switching memories,” *J. Phys. D. Appl. Phys.*, vol. 51, no. 41, 2018.
- [25] S. Larentis, F. Nardi, S. Balatti, D. C. Gilmer, and D. Ielmini, “Resistive switching by voltage-driven ion migration in bipolar RRAM-Part II: Modeling,” *IEEE Trans. Electron Devices*, vol. 59, no. 9, pp. 2468–2475, 2012.
- [26] D.-H. Kwon *et al.*, “Atomic structure of conducting nanofilaments in TiO₂ resistive switching memory,” *Nat. Nanotechnol.*, vol. 5, no. 2, pp. 148–153, 2010.
- [27] G.-S. Park *et al.*, “In situ observation of filamentary conducting channels in an asymmetric Ta₂O_{5-x}/TaO_{2-x} bilayer structure,” *Nat. Commun.*, vol. 4, pp. 1–9, 2013.
- [28] S. Kumar *et al.*, “Direct Observation of Localized Radial Oxygen Migration in Functioning Tantalum Oxide Memristors,” *Adv. Mater.*, vol. 28, no. 14, pp. 2772–2776, 2016.
- [29] Y. Yang *et al.*, “Nonvolatile resistive switching in single crystalline ZnO nanowires,” *Nanoscale*, vol. 3, no. 4, pp. 1917–1921, 2011.
- [30] J. Yao, L. Zhong, D. Natelson, and J. M. Tour, “In situ imaging of the conducting filament in a silicon oxide resistive switch,” *Sci. Rep.*, vol. 2, pp. 1–5, 2012.
- [31] Q. Liu *et al.*, “Real-time observation on dynamic growth/dissolution of conductive filaments in oxide-electrolyte-based ReRAM,” *Adv. Mater.*, vol. 24, no. 14, pp. 1844–1849, 2012.
- [32] X. Tian *et al.*, “Filament growth dynamics in solid electrolyte-based resistive memories revealed by in situ TEM,” *Nano Res.*, vol. 7, no. 7, pp. 1065–1072, 2014.
- [33] G. S. Park, X. S. Li, D. C. Kim, R. J. Jung, M. J. Lee, and S. Seo, “Observation of electric-field induced Ni filament channels in polycrystalline Ni Ox film,” *Appl. Phys. Lett.*, vol. 91, no. 22, pp. 1–4, 2007.

- [34] Q. Liu *et al.*, "Controllable growth of nanoscale conductive filaments in solid-electrolyte-based ReRAM by using a metal nanocrystal covered bottom electrode," *ACS Nano*, vol. 4, no. 10, pp. 6162–6168, 2010.
- [35] J. Lee, C. Du, K. Sun, E. Kioupakis, and W. D. Lu, "Tuning Ionic Transport in Memristive Devices by Graphene with Engineered Nanopores," *ACS Nano*, vol. 10, no. 3, pp. 3571–3579, 2016.
- [36] U. Celano *et al.*, "Conductive-AFM tomography for 3D filament observation in resistive switching devices," *Tech. Dig. - Int. Electron Devices Meet. IEDM*, pp. 574–577, 2013.
- [37] U. Celano, Y. Yin Chen, D. J. Wouters, G. Groeseneken, M. Jurczak, and W. Vandervorst, "Filament observation in metal-oxide resistive switching devices," *Appl. Phys. Lett.*, vol. 102, no. 12, pp. 3–6, 2013.
- [38] J. P. Strachan *et al.*, "Spectromicroscopy of tantalum oxide memristors," *Appl. Phys. Lett.*, vol. 98, no. 24, 2011.
- [39] A. Wedig *et al.*, "Nanoscale cation motion in TaO_x, HfO_x and TiO_x memristive systems," *Nat. Nanotechnol.*, vol. 11, no. 1, pp. 67–74, 2016.
- [40] Y. Yang, P. Gao, S. Gaba, T. Chang, X. Pan, and W. Lu, "Observation of conducting filament growth in nanoscale resistive memories," *Nat. Commun.*, vol. 3, pp. 732–738, 2012.
- [41] W. Hu, L. Zou, C. Gao, Y. Guo, and D. Bao, "High speed and multi-level resistive switching capability of Ta₂O₅ thin films for nonvolatile memory application," *J. Alloys Compd.*, vol. 676, pp. 356–360, 2016.
- [42] X. Xu *et al.*, "Methodology for stability evaluation on the Multi-level storages of oxide-based conductive bridge RAM (CBRAM)," in *Proceedings of the International Symposium on the Physical and Failure Analysis of Integrated Circuits, IPFA*, 2015, vol. 2015-Augus, pp. 543–547.
- [43] Y. Li *et al.*, "Nonvolatile multilevel memory effect in Cu/Wo₃/pt device structures," *Phys. Status Solidi - Rapid Res. Lett.*, vol. 4, no. 5–6, pp. 124–126, 2010.
- [44] C. H. Hsu, Y. S. Fan, and P. T. Liu, "Multilevel resistive switching memory with amorphous InGaZnO-based thin film," *Appl. Phys. Lett.*, vol. 102, no. 6, pp. 1–4, 2013.
- [45] A. Prakash, J. Park, J. Song, J. Woo, E. J. Cha, and H. Hwang, "Demonstration of low power 3-bit

multilevel cell characteristics in a TaO_x-Based RRAM by stack engineering," *IEEE Electron Device Lett.*, vol. 36, no. 1, pp. 32–34, 2015.

- [46] Y. Qi, C. Z. Zhao, C. Liu, and Y. Fang, "Comparisons of switching characteristics between Ti/Al₂O₃/Pt and TiN/Al₂O₃/Pt RRAM devices with various compliance currents," 2018.
- [47] C. W. Hsu, T. H. Hou, M. C. Chen, I. T. Wang, and C. L. Lo, "Bipolar Ni/TiO₂/HfO₂/Ni RRAM with multilevel states and self-rectifying characteristics," *IEEE Electron Device Lett.*, vol. 34, no. 7, pp. 885–887, 2013.
- [48] S. Yu, Y. Wu, Y. Chai, J. Provine, and H. S. P. Wong, "Characterization of switching parameters and multilevel capability in HfO_x/AlO_x bi-layer RRAM devices," *Int. Symp. VLSI Technol. Syst. Appl. Proc.*, pp. 106–107, 2011.
- [49] D. Ielmini, "Modeling the universal set/reset characteristics of bipolar RRAM by field- and temperature-driven filament growth," *IEEE Trans. Electron Devices*, vol. 58, no. 12, pp. 4309–4317, 2011.
- [50] P. Huang *et al.*, "A physics-based compact model of metal-oxide-based RRAM DC and AC operations," *IEEE Trans. Electron Devices*, vol. 60, no. 12, pp. 4090–4097, 2013.
- [51] S. Long *et al.*, "Impact of program/erase operation on the performances of oxide-based resistive switching memory," *Nanoscale Res. Lett.*, vol. 10, no. 1, 2015.
- [52] S. Lee, J. B. Park, M. J. Lee, and J. J. Boland, "Multilevel resistance in ZnO nanowire memristors enabled by hydrogen annealing treatment," *AIP Adv.*, vol. 6, no. 12, 2016.
- [53] W. Wang *et al.*, "Learning of spatiotemporal patterns in a spiking neural network with resistive switching synapses," *Sci. Adv.*, vol. 4, no. 9, pp. 1–9, 2018.
- [54] D. Bhattacharjee, W. Kim, A. Chattopadhyay, R. Waser, and V. Rana, "Multi-valued and Fuzzy Logic Realization using TaO_x Memristive Devices," *Sci. Rep.*, vol. 8, no. 1, p. 8, 2018.
- [55] K.-P. Chang, Y.-C. Chen, W.-C. Chien, and E.-K. Lai, "Operating method of electrical pulse voltage for RRAM application," 8,134,865, 13-Mar-2012.
- [56] A. C. Torrezan, J. P. Strachan, G. Medeiros-Ribeiro, and R. S. Williams, "Sub-nanosecond switching of a tantalum oxide memristor," *Nanotechnology*, vol. 22, no. 48, p. 485203, 2011.

- [57] B. Govoreanu *et al.*, “10×10nm² Hf/HfO_x crossbar resistive RAM with excellent performance, reliability and low-energy operation,” in *International Electron Devices Meeting, IEDM*, 2011, pp. 729–732.
- [58] C.-W. Hsu *et al.*, “Self-Rectifying Bipolar TaO_x/TiO₂ RRAM with Superior Endurance over 10¹² Cycles for 3D High-Density Storage-Class Memory,” in *2013 Symposium on VLSI Technology (VLSIT)*, 2013, pp. T166–T167.
- [59] S. Park *et al.*, “RRAM-based synapse for neuromorphic system with pattern recognition function,” in *Technical Digest - International Electron Devices Meeting, IEDM*, 2012, pp. 10.2.1-10.2.4.
- [60] G. Chen, C. Song, C. Chen, S. Gao, F. Zeng, and F. Pan, “Resistive switching and magnetic modulation in cobalt-doped ZnO,” *Adv. Mater.*, vol. 24, no. 26, pp. 3515–3520, 2012.
- [61] S. Otsuka, Y. Hamada, T. Shimizu, and S. Shingubara, “Ferromagnetic nano-conductive filament formed in Ni/TiO₂/Pt resistive-switching memory,” *Appl. Phys. A Mater. Sci. Process.*, vol. 118, no. 2, pp. 613–619, 2014.
- [62] S. Otsuka, Y. Hamada, D. Ito, T. Shimizu, and S. Shingubara, “Magnetoresistance of conductive filament in Ni/HfO₂/Pt resistive switching memory,” *Jpn. J. Appl. Phys.*, vol. 54, no. 5, 2015.
- [63] L. Li *et al.*, “Anisotropic Magnetoresistance of Nano-conductive Filament in Co/HfO₂/Pt Resistive Switching Memory,” *Nanoscale Res. Lett.*, vol. 12, no. 1, pp. 10–15, 2017.
- [64] H. Li, S. Wu, P. Hu, D. Li, G. Wang, and S. Li, “Light and magnetic field double modulation on the resistive switching behavior in BaTiO₃/FeMn/BaTiO₃ trilayer films,” *Phys. Lett. Sect. A Gen. At. Solid State Phys.*, vol. 381, no. 25–26, pp. 2127–2130, 2017.
- [65] X. L. Wang, Q. Shao, C. W. Leung, R. Lortz, and A. Ruotolo, “Non-volatile, electric control of magnetism in Mn-substituted ZnO,” *Appl. Phys. Lett.*, vol. 104, no. 6, p. 062409, 2014.
- [66] D. R. Yakovlev and W. Ossau, “Magnetic Polarons,” in *Introduction to the Physics of Diluted Magnetic Semiconductors*, Berlin, Heidelberg: Springer, 2010, pp. 221–262.
- [67] C. Chen, C. Song, J. Yang, F. Zeng, and F. Pan, “Oxygen migration induced resistive switching effect and its thermal stability in W/TaO_x/Pt structure,” *Appl. Phys. Lett.*, vol. 100, no. 25, 2012.
- [68] N. S. Kamarozaman, M. F. M. Soder, M. Z. Musa, R. a Bakar, S. H. Herman, and M. Rusop, “Effect of

vol. 92, no. 22, pp. 1–4, 2008.

- [80] S. Kim, H. Moon, D. Gupta, S. Yoo, and Y. K. Choi, “Resistive switching characteristics of Sol-Gel Zinc oxide films for flexible memory applications,” *IEEE Trans. Electron Devices*, vol. 56, no. 4, pp. 696–699, 2009.
- [81] J. Won Seo *et al.*, “Transparent flexible resistive random access memory fabricated at room temperature,” *Appl. Phys. Lett.*, vol. 95, no. 13, pp. 1–4, 2009.
- [82] S. Kim, O. Yarimaga, S. J. Choi, and Y. K. Choi, “Highly durable and flexible memory based on resistance switching,” *Solid. State. Electron.*, vol. 54, no. 4, pp. 392–396, 2010.
- [83] H. Y. Jeong *et al.*, “Graphene oxide thin films for flexible nonvolatile memory applications,” *Nano Lett.*, vol. 10, no. 11, pp. 4381–4386, 2010.
- [84] H. Y. Jeong, Y. I. Kim, J. Y. Lee, and S. Y. Choi, “A low-temperature-grown TiO₂ based device for the flexible stacked RRAM application,” *Nanotechnology*, vol. 21, no. 11, p. 115203, 2010.
- [85] Y. C. Liu, Z. Q. Wang, Y. X. Liu, X. H. Li, H. Y. Xu, and X. T. Zhang, “Flexible Resistive Switching Memory Device Based on Amorphous InGaZnO Film With Excellent Mechanical Endurance,” *IEEE Electron Device Lett.*, vol. 32, no. 10, pp. 1442–1444, 2011.
- [86] S. Kim, H. Y. Jeong, S. K. Kim, S. Y. Choi, and K. J. Lee, “Flexible memristive memory array on plastic substrates,” *Nano Lett.*, vol. 11, no. 12, pp. 5438–5442, 2011.
- [87] Y. W. Dai *et al.*, “Complementary resistive switching in flexible RRAM devices,” *IEEE Electron Device Lett.*, vol. 35, no. 9, pp. 915–917, 2014.
- [88] H. G. Yoo, S. Kim, and K. J. Lee, “Flexible one diode-one resistor resistive switching memory arrays on plastic substrates,” *RSC Adv.*, vol. 4, no. 38, pp. 20017–20023, 2014.
- [89] J. J. Huang, Y. M. Tseng, W. C. Luo, C. W. Hsu, and T. H. Hou, “One selector-one resistor (1S1R) crossbar array for high-density flexible memory applications,” *Tech. Dig. - Int. Electron Devices Meet. IEDM*, pp. 31.7.1-31.7.4, 2011.
- [90] C. H. Cheng, F. S. Yeh, and A. Chin, “Low-power high-performance non-volatile memory on a flexible substrate with excellent endurance,” *Adv. Mater.*, vol. 23, no. 7, pp. 902–905, 2011.

- [91] C. Chou, C. Hsu, C. Chang, and T. Hou, "Self-Rectifying Ta/TaO_x/TiO₂/Ti Cell for High-Density Flexible RRAM," in *2014 International Conference on Solid State Devices and Materials*, 2014, pp. 422–423.
- [92] J. Jang, F. Pan, K. Braam, and V. Subramanian, "Resistance switching characteristics of solid electrolyte chalcogenide Ag₂Se nanoparticles for flexible nonvolatile memory applications," *Adv. Mater.*, vol. 24, no. 26, pp. 3573–3576, 2012.
- [93] R.-C. Fang, Q.-Q. Sun, P. Zhou, W. Yang, P.-F. Wang, and D. W. Zhang, "High-performance bilayer flexible resistive random access memory based on low-temperature thermal atomic layer deposition," *Nanoscale Res. Lett.*, vol. 8, no. 1, p. 92, 2013.
- [94] S. Kim *et al.*, "Flexible Crossbar-Structured Resistive Memory Arrays on Plastic Substrates via Inorganic-Based Laser Lift-Off," *Adv. Mater.*, vol. 26, no. 44, pp. 7418–7418, 2014.
- [95] A. Midya, N. Gogurla, and S. K. Ray, "Flexible and transparent resistive switching devices using Au nanoparticles decorated reduced graphene oxide in polyvinyl alcohol matrix," *Curr. Appl. Phys.*, vol. 15, no. 6, pp. 706–710, 2015.
- [96] L. Liang *et al.*, "Vacancy associates-rich ultrathin nanosheets for high performance and flexible nonvolatile memory device," *J. Am. Chem. Soc.*, vol. 137, no. 8, pp. 3102–3108, 2015.
- [97] K. N. Pham, V. D. Hoang, C. V. Tran, and B. T. Phan, "TiO₂ thin film based transparent flexible resistive switching random access memory," *Adv. Nat. Sci. Nanosci. Nanotechnol.*, vol. 7, no. 1, p. 015017, 2016.
- [98] J. Shang *et al.*, "Highly flexible resistive switching memory based on amorphous-nanocrystalline hafnium oxide films," *Nanoscale*, vol. 9, no. 21, pp. 7037–7046, 2017.
- [99] B. Sun *et al.*, "A flexible nonvolatile resistive switching memory device based on ZnO film fabricated on a foldable PET substrate," *J. Colloid Interface Sci.*, vol. 520, pp. 19–24, 2018.
- [100] L. Wu *et al.*, "Flexible, multilevel, and low-operating-voltage resistive memory based on MoS₂-rGO hybrid," *Appl. Surf. Sci.*, vol. 463, no. July 2018, pp. 947–952, 2019.
- [101] X. Zhao *et al.*, "Flexible cation-based threshold selector for resistive switching memory integration," *Sci. China Inf. Sci.*, vol. 61, no. 6, pp. 0–8, 2018.
- [102] M. Yang *et al.*, "Stretchable and conformable synapse memristors for wearable and implantable

- electronics," *Nanoscale*, vol. 10, no. 38, pp. 18135–18144, 2018.
- [103] X. Yan *et al.*, "Flexible memristors as electronic synapses for neuro-inspired computation based on scotch tape-exfoliated mica substrates," *Nano Res.*, vol. 11, no. 3, pp. 1183–1192, 2018.
- [104] H. Bae *et al.*, "Physically Transient Memory on a Rapidly Dissoluble Paper for Security Application," *Sci. Rep.*, vol. 6, no. December, pp. 1–7, 2016.
- [105] S. Lee *et al.*, "Novel electroforming-free nanoscaffold memristor with very high uniformity, tunability, and density," *Adv. Mater.*, vol. 26, no. 36, pp. 6284–6289, 2014.
- [106] S. Schweiger, M. Kubicek, F. Messerschmitt, C. Murer, and J. L. M. Rupp, "A microdot multilayer oxide device: Let us tune the strain-ionic transport interaction," *ACS Nano*, vol. 8, no. 5, pp. 5032–5048, 2014.
- [107] Y. Shi *et al.*, "In Situ Demonstration of the Link Between Mechanical Strength and Resistive Switching in Resistive Random-Access Memories," *Adv. Electron. Mater.*, vol. 1, no. 4, p. 1400058, 2015.
- [108] S. Ambrogio, S. Balatti, S. Choi, and D. Ielmini, "Impact of the mechanical stress on switching characteristics of electrochemical resistive memory," *Adv. Mater.*, vol. 26, no. 23, pp. 3885–3892, 2014.
- [109] Y. Y. Chen *et al.*, "Tailoring switching and endurance / retention reliability characteristics of HfO₂ / Hf RRAM with Ti, Al, Si dopants," *Dig. Tech. Pap. - Symp. VLSI Technol.*, no. 59, pp. 1–2, 2014.
- [110] B. Traore *et al.*, "On the Origin of Low-Resistance State Retention Failure in HfO₂-Based RRAM and Impact of Doping/Alloying," *IEEE Trans. Electron Devices*, vol. 62, no. 12, pp. 4029–4036, 2015.
- [111] S. H. Misha *et al.*, "Effect of nitrogen doping on variability of TaO_x-RRAM for low-power 3-bit MLC applications," *ECS Solid State Lett.*, vol. 4, no. 3, pp. P25–P28, 2015.
- [112] H. Xu *et al.*, "Effect of Co doping on unipolar resistance switching in Pt/Co:ZnO/Pt structures," *J. Alloys Compd.*, vol. 658, pp. 806–812, 2016.
- [113] N. Sedghi *et al.*, "The role of nitrogen doping in ALD Ta₂O₅ and its influence on multilevel cell switching in RRAM," *Appl. Phys. Lett.*, vol. 110, no. 10, pp. 1–6, 2017.

- [114] L. F. Liu *et al.*, "Gd doping improved resistive switching characteristics of TiO₂-based resistive memory devices," *Jpn. J. Appl. Phys.*, vol. 47, no. 4 PART 2, pp. 2701–2703, 2008.
- [115] B. Gao *et al.*, "Oxide-based RRAM: Uniformity improvement using a new material-oriented methodology," *Dig. Tech. Pap. - Symp. VLSI Technol.*, pp. 30–31, 2009.
- [116] H. Zhang *et al.*, "Ionic doping effect in ZrO₂ resistive switching memory," *Appl. Phys. Lett.*, vol. 96, no. 12, pp. 98–101, 2010.
- [117] C. Y. Liu, X. J. Lin, H. Y. Wang, and C. H. Lai, "Improved resistive switching dispersion of NiO_x thin film by Cu-doping Method," *Jpn. J. Appl. Phys.*, vol. 49, no. 5 PART 1, pp. 0565071–0565074, 2010.
- [118] B. Gao *et al.*, "Oxide-based RRAM: Physical based retention projection," *2010 Proc. Eur. Solid State Device Res. Conf. ESSDERC 2010*, pp. 392–395, 2010.
- [119] H. Zhang *et al.*, "Gd-doping effect on performance of HfO₂ based resistive switching memory devices using implantation approach," *Appl. Phys. Lett.*, vol. 98, no. 4, pp. 1–4, 2011.
- [120] C. S. Peng, W. Y. Chang, Y. H. Lee, M. H. Lin, F. Chen, and M. J. Tsai, "Improvement of resistive switching stability of HfO₂ films with Al doping by atomic layer deposition," *Electrochem. Solid-State Lett.*, vol. 15, no. 4, pp. 88–90, 2012.
- [121] K. C. Chang *et al.*, "The effect of silicon oxide based RRAM with tin doping," *Electrochem. Solid-State Lett.*, vol. 15, no. 3, pp. 65–68, 2012.
- [122] N. Raghavan *et al.*, "Stochastic variability of vacancy filament configuration in ultra-thin dielectric RRAM and its impact on OFF-state reliability," *Tech. Dig. - Int. Electron Devices Meet. IEDM*, pp. 21.1.1-21.1.4, 2013.
- [123] F. M. Simanjuntak, D. Panda, K. H. Wei, and T. Y. Tseng, "Status and Prospects of ZnO-Based Resistive Switching Memory Devices," *Nanoscale Res. Lett.*, vol. 11, no. 1, 2016.
- [124] W. Duan *et al.*, "Solution processed flexible resistive switching memory based on Al-In-O self-mixing layer," *J. Appl. Phys.*, vol. 124, no. 10, pp. 1–10, 2018.
- [125] Y. Cai, J. Tan, L. Yefan, M. Lin, and R. Huang, "A flexible organic resistance memory device for wearable biomedical applications," *Nanotechnology*, vol. 27, no. 27, 2016.

- [126] T. Y. Wang *et al.*, "An organic flexible artificial bio-synapses with long-term plasticity for neuromorphic computing," *Micromachines*, vol. 9, no. 5, 2018.
- [127] C. Korte, J. Keppner, A. Peters, N. Schichtel, H. Aydin, and J. Janek, "Coherency strain and its effect on ionic conductivity and diffusion in solid electrolytes - an improved model for nanocrystalline thin films and a review of experimental data," *Phys. Chem. Chem. Phys.*, vol. 16, no. 44, pp. 24575–24591, 2014.
- [128] S. Schweiger and J. L. M. Rupp, *Strain and interfaces for metal oxide-based memristive devices*. Elsevier Inc., 2018.
- [129] J. L. M. Rupp, S. Schweiger, and F. Messerschmitt, "Strained multilayer resistive-switching memory elements." Washington, DC: U.S. Patent and Trademark Office, Aug-2017.
- [130] S. Azad *et al.*, "Nanoscale effects on ion conductance of layer-by-layer structures of gadolinia-doped ceria and zirconia," *Appl. Phys. Lett.*, vol. 86, no. 13, p. 131906, 2005.
- [131] J. Garcia-Barriocanal *et al.*, "Colossal Ionic Conductivity at Interfaces of Epitaxial $\text{ZrO}_2\text{:Y}_2\text{O}_3\text{/SrTiO}_3$ Heterostructures," *Science*, vol. 321, no. 5889, pp. 676–680, 2008.
- [132] S. Sanna, V. Esposito, A. Tebano, S. Licocchia, E. Traversa, and G. Balestrino, "Enhancement of ionic conductivity in sm-doped ceria/yttria-stabilized zirconia heteroepitaxial structures," *Small*, vol. 6, no. 17, pp. 1863–1867, 2010.
- [133] S. Schweiger, R. Pfenninger, W. J. Bowman, U. Aschauer, and J. L. M. Rupp, "Designing Strained Interface Heterostructures for Memristive Devices," *Adv. Mater.*, vol. 29, no. 15, 2017.
- [134] K. H. Chen *et al.*, "Illumination effect on bipolar switching properties of Gd:SiO₂ RRAM devices using transparent indium tin oxide electrode," *Nanoscale Res. Lett.*, vol. 11, no. 1, pp. 2–6, 2016.
- [135] K. W. Hsu, H. Ren, R. J. Agasie, S. Bian, Y. Nishi, and J. L. Shohet, "Effects of neutron irradiation of ultra-thin HfO₂ films," *Appl. Phys. Lett.*, vol. 104, no. 3, pp. 1–4, 2014.
- [136] A. Mehonic, T. Gerard, and A. J. Kenyon, "Light-activated resistance switching in SiO_x RRAM devices," *Appl. Phys. Lett.*, vol. 111, no. 23, p. 233502, 2017.
- [137] J. Holt, N. Cady, and J. Yang-Scharlotta, "Radiation testing of tantalum oxide-based resistive memory," in *2015 IEEE International Integrated Reliability Workshop (IIRW)*, 2015, pp. 155–158.

- [138] A. N. Mikhaylov *et al.*, "Field- and irradiation-induced phenomena in memristive nanomaterials," *Phys. Status Solidi*, vol. 13, no. 10–12, pp. 870–881, 2016.
- [139] M. J. Marinella *et al.*, "Initial Assessment of the Effects of Radiation on the Electrical Characteristics of TaO_x Memristive Memories," *IEEE Trans. Nucl. Sci.*, vol. 59, no. 6, pp. 2987–2994, 2012.
- [140] B. Y. Tsui, K. C. Chang, B. Y. Shew, H. Y. Lee, and M. J. Tsai, "Investigation of radiation hardness of HfO₂ resistive random access memory," in *Proceedings of Technical Program - 2014 International Symposium on VLSI Technology, Systems and Application, VLSI-TSA 2014*, 2014, pp. 1–2.
- [141] J. S. Bi *et al.*, "The impact of X-ray and proton irradiation on HfO₂/Hf-based bipolar resistive memories," *IEEE Trans. Nucl. Sci.*, vol. 60, no. 6, pp. 4540–4546, 2013.
- [142] S. L. Weeden-Wright *et al.*, "TID and Displacement Damage Resilience of 1T1R HfO₂/Hf Resistive Memories," *IEEE Trans. Nucl. Sci.*, vol. 61, no. 6, pp. 2972–2978, 2014.
- [143] L. Zhang *et al.*, "Total ionizing dose (TID) effects on TaO_x-based resistance change memory," *IEEE Trans. Electron Devices*, vol. 58, no. 8, pp. 2800–2804, 2011.
- [144] Y. L. Wu, C. Y. Huang, and J. J. Lin, "Effects of radiation on the bipolar resistive switching characteristics of Al/HfO₂/ITO structure," in *2012 IEEE 11th International Conference on Solid-State and Integrated Circuit Technology*, 2012, pp. 1–3.
- [145] R. Fang *et al.*, "Total ionizing dose effect of γ -ray radiation on the switching characteristics and filament stability of HfO_x resistive random access memory," *Appl. Phys. Lett.*, vol. 104, no. 18, 2014.
- [146] F. Yuan, S. Shen, and Z. Zhang, " γ -ray irradiation effects on TiN/HfO_x/Pt resistive random access memory devices," in *IEEE Aerospace Conference Proceedings*, 2015, pp. 1–7.
- [147] S. H. Lin, Y. L. Wu, Y. H. Hwang, and J. J. Lin, "Study of radiation hardness of HfO₂-based resistive switching memory at nanoscale by conductive atomic force microscopy," *Microelectron. Reliab.*, vol. 55, no. 11, pp. 2224–2228, 2015.
- [148] K. Agashe *et al.*, "Effect of gamma irradiation on resistive switching of Al/TiO₂/n⁺ Si ReRAM," *Nucl. Instruments Methods Phys. Res. Sect. B Beam Interact. with Mater. Atoms*, vol. 403, pp. 38–44, 2017.
- [149] W. Duan, J. Wang, and X. Zhong, "The effect of γ -rays irradiation on the electrical properties of WO_x

film-based memory cells," *EPL (Europhysics Lett.)*, vol. 119, no. 2, p. 27003, 2017.

- [150] H. García *et al.*, "Electrical Characterization of Defects Created by γ -Radiation in HfO_2 -Based MIS Structures for RRAM Applications," *J. Electron. Mater.*, vol. 47, no. 9, pp. 5013–5018, 2018.
- [151] N. Arun, K. V. Kumar, A. P. Pathak, D. K. Avasthi, and S. V. S. N. Rao, "Hafnia-based resistive switching devices for non-volatile memory applications and effects of gamma irradiation on device performance," *Radiat. Eff. Defects Solids*, vol. 173, no. 3–4, pp. 239–249, 2018.
- [152] N. Arun, K. Vinod Kumar, A. Mangababu, S. V. S. Nageswara Rao, and A. P. Pathak, "Influence of the bottom metal electrode and gamma irradiation effects on the performance of HfO_2 -based RRAM devices," *Radiat. Eff. Defects Solids*, vol. 174, no. 1–2, pp. 66–75, 2019.
- [153] J. Bi, Y. Duan, F. Zhang, and M. Liu, "Total ionizing dose effects of 1 Mb HfO_2 -Based resistive-random-access-memory," *Proc. Int. Symp. Phys. Fail. Anal. Integr. Circuits, IPFA*, vol. 2018-July, pp. 1–4, 2018.
- [154] K. C. Liu, W. H. Tzeng, K. M. Chang, Y. C. Chan, and C. C. Kuo, "Effect of ultraviolet light exposure on a HfO_x RRAM device," *Thin Solid Films*, vol. 518, no. 24, pp. 7460–7463, 2010.
- [155] J. Park, S. Lee, J. Lee, and K. Yong, "A light incident angle switchable ZnO nanorod memristor: Reversible switching behavior between two non-volatile memory devices," *Adv. Mater.*, vol. 25, no. 44, pp. 6423–6429, 2013.
- [156] Y. Zhou *et al.*, "White-light-induced disruption of nanoscale conducting filament in hafnia," *Appl. Phys. Lett.*, vol. 107, no. 7, pp. 0–5, 2015.
- [157] B. Sun, M. Tang, J. Gao, and C. M. Li, "Light-Controlled Simultaneous Resistive and Ferroelectricity Switching Effects of BiFeO_3 Film for a Flexible Multistate High-Storage Memory Device," *ChemElectroChem*, vol. 3, no. 6, pp. 896–901, 2016.
- [158] R. C. Baumann, "Radiation-induced soft errors in advanced semiconductor technologies," *IEEE Trans. Device Mater. Reliab.*, vol. 5, no. 3, pp. 305–315, 2005.
- [159] H. J. Barnaby *et al.*, "Impact of alpha particles on the electrical characteristics of TiO_2 memristors," *IEEE Trans. Nucl. Sci.*, vol. 58, no. 6 PART 1, pp. 2838–2844, 2011.
- [160] W. M. Tong *et al.*, "Radiation hardness of TiO_2 memristive junctions," *IEEE Trans. Nucl. Sci.*, vol. 57,

no. 3 PART 3, pp. 1640–1643, 2010.

- [161] B. V. Mistry, S. J. Trivedi, U. V. Chhaya, S. A. Khan, D. K. Avasthi, and U. S. Joshi, “RRAM properties of swift heavy ion irradiated Ag/In₂O₃/Pt/Si heterostructures,” *Radiat. Eff. Defects Solids*, vol. 168, no. 7–8, pp. 625–629, Aug. 2013.
- [162] M. Alayan *et al.*, “Experimental and Simulation Studies of the Effects of Heavy-Ion Irradiation on HfO₂-Based RRAM Cells,” *IEEE Trans. Nucl. Sci.*, vol. 64, no. 8, pp. 2038–2045, 2017.
- [163] M. Alayan *et al.*, “Heavy-ion upset immunity of RRAM cells based on thin HfO₂ layers,” in *16th European Conference on Radiation and Its Effects on Components and Systems (RADECS)*, 2016, pp. 1–5.
- [164] F. Tan *et al.*, “Investigation on the response of TaO_x-based resistive random-access memories to heavy-ion irradiation,” *IEEE Trans. Nucl. Sci.*, vol. 60, no. 6, pp. 4520–4525, 2013.
- [165] P. E. Dodd and L. W. Massengill, “Basic mechanisms and modeling of single-event upset in digital microelectronics,” *IEEE Trans. Nucl. Sci.*, vol. 50 III, no. 3, pp. 583–602, 2003.
- [166] Y. Gonzalez-Velo, H. J. Barnaby, and M. N. Kozicki, “Review of radiation effects on ReRAM devices and technology,” *Semicond. Sci. Technol.*, vol. 32, no. 8, p. 083002, 2017.
- [167] Z. Ye, R. Liu, J. L. Taggart, H. J. Barnaby, and S. Yu, “Evaluation of Radiation Effects in RRAM-Based Neuromorphic Computing System for Inference,” *IEEE Trans. Nucl. Sci.*, vol. 66, no. 1, pp. 97–103, 2019.
- [168] W. G. Bennett *et al.*, “Single- and Multiple-Event Induced Upsets in HfO₂/Hf 1T1R RRAM,” *IEEE Trans. Nucl. Sci.*, vol. 61, no. 4, pp. 1717–1725, 2014.
- [169] C. C. Shih *et al.*, “Resistive switching modification by ultraviolet illumination in transparent electrode resistive random access memory,” *IEEE Electron Device Lett.*, vol. 35, no. 6, pp. 633–635, 2014.

C. S. Pedersen, J. H. Chang, **Y. Li**, N. Pryds, and J. M. G. Lastra
Phase separation and mixing in amorphous tantalum-oxide from first
principles
Submitted to Nanoscale (2020)



Winter Snow at Risø Campus (8th March 2018)
Photo: Yang Li

Cite this: DOI: 00.0000/xxxxxxxxxx

Phase separation in amorphous tantalum-oxide from first principles[†]

Christian Søndergaard Pedersen, Jin Hyun Chang*, Yang Li, Nini Pryds, Juan Maria Garcia Lastra*

Received Date

Accepted Date

DOI: 00.0000/xxxxxxxxxx

The transition between Ta₂O₅ and TaO₂ governs resistive switching in tantalum-oxide-based resistive random access memory. Despite its importance, the Ta₂O₅–TaO₂ transition is scarcely described in the literature in part because the tantalum-oxide layer in devices is amorphous, which makes it difficult to characterize. In this paper, we use first-principles calculations to construct the convex hull of the amorphous Ta₂O_{5-x} system for $0 \leq x \leq 1$ and show that oxygen-deficient tantalum oxide phase separates into Ta₂O₅ and TaO₂. In addition, our work challenges the conventional interpretation of X-ray Photoelectron Spectroscopy (XPS) spectra of the Ta 4f orbitals. Specifically, we find that TaO₂ exhibits both the Ta⁴⁺ peak associated with TaO₂ and the Ta⁵⁺ peak normally associated with Ta₂O₅. While our simulated Ta₂O₅ peak originates from a narrow range of oxidation states, the TaO₂ peak comes from disproportionated Ta atoms with Bader charges ranging from +3 to +1, the lowest of which are well below Ta atoms in crystalline TaO. Finally, we demonstrate that the XPS blueshift of around 1 eV observed experimentally in amorphous Ta₂O₅ with respect to crystalline Ta₂O₅ comes from both the presence of under-coordinated Ta atoms and longer Ta–O bond distances in the amorphous system. Our simulated XPS analysis shows that amorphous XPS spectra may be more complex than previously thought, and hence caution should be applied when assigning XPS peaks to oxidation states.

1 Introduction

Resistive switching devices constitutes an important research topic within the general area of random access memory (RAM) technology.^{1,2} Since Chua proposed the “memristor” — memory resistor — in 1971,³ researchers have demonstrated memory resistive properties in Metal/Metal-oxide/Metal devices^{4,5} using semiconducting and insulating transition metal oxides such as TiO₂,⁴ HfO₂,^{6,7} and Ta₂O₅⁸ as the active layer. The switching mechanism in these layers is initiated by applying a large electric field across the device. This leads to the creation and subsequent migration of oxygen vacancy (v_{O}) defects, and eventually to the growth of nanoscale filaments of oxygen-deficient and conductive regions through the device.^{9–11}

Tantalum pentoxide (Ta₂O₅) is one of the key candidate material for the switching layer of memristive switching devices. In a direct comparison to TiO₂, which was the first material to be linked to memristive switching,⁴ Ta₂O₅ shows five times greater ionic mobility^{4,12} and, by extension, may yield greater switching speed and lower power consumption.¹³ Additionally, a switching endurance exceeding 10¹² cycles has been demonstrated without

device breakdown.¹⁴

Structurally, Ta₂O₅ thin films fabricated at low to room temperature are amorphous,^{15–17} which make them difficult to study on a theoretical level. Nevertheless, previous *ab initio* Molecular Dynamics (AIMD) studies based on Density Functional Theory (DFT) have provided in-depth investigations of amorphous tantalum oxide. Utilising the atomic-level information offered by DFT, researchers have described atomic arrangements surrounding singular v_{O} 's,¹⁸ density-of-states spectra of several TaO_x stoichiometries,¹⁹ electrical conductivity of TaO_x,²⁰ and formation energy of v_{O} 's in Ta₂O₅ close to a Ta-Ta₂O₅ interface.²¹ To our knowledge, however, neither experiment nor simulation has thus far attempted to map the Ta₂O₅–TaO₂ transition which governs resistive switching in TaO_x devices.

One reason for this is that determining the exact composition of amorphous materials is a non-trivial task, which is highly dependent on fabrication parameters.¹⁷ Several studies have applied X-ray Photoelectron Spectroscopy (XPS) to obtain binding energies (BEs) for especially the Ta 4f orbitals.^{17,22–27} Usually, the resultant spectra are deconvoluted using Gaussian/Lorentzian functions^{17,24,26,27} assigned either to different oxidation states of Ta or to different stoichiometries. The two assignments can be used interchangeably since the stoichiometries Ta₂O₅, TaO₂, Ta₂O₃, TaO, Ta₂O and Ta respectively correspond to the oxidation states +5, +4, +3, +2, +1, and 0. A compositional analysis can

* Department of Energy Conversion and Storage, Technical University of Denmark, DK-2800 Kgs. Lyngby, Denmark. E-mail: jchang@dtu.dk, jmgl@dtu.dk

† Electronic Supplementary Information (ESI) available. See DOI: 00.0000/00000000.

be performed based on the relative areas underneath the fitting functions. However, the XPS spectra of amorphous materials are more complex compared to crystalline materials, which exhibit well-defined patterns.

In this study, we zoom in on the transition between Ta_2O_5 and TaO_2 , which is the range of compositions where resistive switching takes place. We use DFT to investigate amorphous $\text{Ta}_2\text{O}_{5-x}$ (a- $\text{Ta}_2\text{O}_{5-x}$), sampling fourteen different snapshots for each of six different compositions with $0 \leq x \leq 1$. We draw the convex hull for the Ta_2O_5 – TaO_2 transition and confirm that the hull consists of these two stoichiometries, with Ta_6O_{13} being another possible meta-stable intermediate phase. Further, we simulate XPS spectra for each stoichiometry and show that the XPS spectrum of TaO_2 shows both Ta^{5+} and Ta^{4+} peaks, the latter of which comes from disproportionated atoms with a wide range of oxidation states. Finally, by fitting Gaussian components to our oxidation state spectra and our XPS spectra, we establish a linear correlation between the Gaussian peak locations. These conclusions aid the understanding of XPS results of a- Ta_2O_5 and of amorphous materials in general.

2 Methods

All calculations employed DFT as implemented in the Vienna Ab initio Simulation Package (VASP),^{28–31} Ta and O atoms used Projector Augmented Wave (PAW) pseudopotentials³² with valence electron configurations of $5p^65d^36s^2$ and $2s^42p^4$, respectively. Calculations used the Perdew-Burke-Ernzerhof (PBE) Generalized Gradient Approximation (GGA)³³ to describe the exchange-correlation functional except where noted otherwise. The convergence threshold of the electronic structure iterations was set to 10^{-5} eV.

Amorphous systems of $\text{Ta}_2\text{O}_{5-x}$, $x \in \{0.00, 0.33, 0.50, 0.67, 0.80, 1.00\}$ were generated using AIMD. Beginning with the primitive cell of λ - Ta_2O_5 suggested by Lee *et al.*³⁴, we created a $2 \times 2 \times 3$ orthogonal supercell containing 48 Ta atoms and 120 O atoms; same size as those used by Bondi *et al.*^{18,20} and Guo and Robertson.³⁵ Oxygen atoms were subsequently deleted randomly to obtain 8, 12, 16 and 24 vacancies. We expanded each lattice vector by a factor of 1.06, which was chosen to match the experimental density for a- Ta_2O_5 of $6.88 \times 10^3 \text{ kg/m}^3$.³⁶ The expanded cell vectors were kept fixed throughout the duration of the MD simulations.

The amorphous structure generation used the following melt-and-quench procedure: 1) equilibration at 5000 K for 10 ps, 2) further equilibration and extraction of in total 14 structure snapshots per stoichiometry in intervals of 2 ps following the initial equilibration, 3) quenching of each snapshot from 5000 K to 300 K, and 4) equilibration for 2 ps at 300 K. The MD simulations used a low-accuracy/high-speed setup with a cutoff energy of 300 eV and sampling only the Γ point. The time step was 1 fs for equilibrations and 2 fs for quenching.

Following the AIMD procedure, we increased the cutoff energy to 520 eV and k point sampling to $(2 \times 2 \times 2)$ and performed full

DFT relaxations of ionic positions and lattice vectors[‡]. Atomic forces were converged to within $0.025 \text{ eV}/\text{\AA}$, which resulted in little change to the cell volume, and thus density. We performed a high-precision calculation of the optimised structures using the hybrid functional of Heyd-Ernzerhof-Scuseria (HSE06).^{37–39} Due to their high computational demands, these calculations sampled only the Γ point. Following these calculations, the BEs of the Ta 4f orbitals were computed using the initial state approximation, which involves recalculating the Kohn–Sham eigenvalues of the core states after a self-consistent calculation of the valence charge density. The HSE06-calculated wave functions served as the basis for a Bader charge analysis⁴⁰ using the program developed by Henkelmann *et al.*[§]

In addition to our amorphous systems, we performed PBE relaxation followed by HSE06 calculations of the following crystalline structures: λ - Ta_2O_5 , rutile TaO_2 , corundum Ta_2O_3 , rock-salt TaO, and BCC Ta. These calculations used the same setup as the DFT calculations of the amorphous systems with a k point sampling density of at least $3.6 k$ points per \AA^{-3} .

3 Results and Discussion

3.1 Energetic Stability and Structural Analysis

We first examine the phase change between Ta_2O_5 and TaO_2 as well as differences in the Ta–O bonding. Fig. 1 presents the convex hull, cumulative distribution function (CDF) for Ta–O bonds limited to the sixth nearest neighbour, and a histogram of Ta coordination numbers for all simulated systems (radial distribution functions can be found in Fig. S2†). The total energies making up the hull are extracted from the HSE06 calculations and subsequently normalised to 24 formula units (f.u.). Our high sampling of fourteen structures per stoichiometry allows us to visualise the energy variance, providing reassurance that our convex hull is accurate.

The convex hull in Fig. 1(a) shows a preference for phase separation into Ta_2O_5 and TaO_2 . However, while Ta_3O_7 ($x = 0.33$), Ta_4O_9 ($x = 0.50$), and $\text{Ta}_{12}\text{O}_{25}$ ($x = 0.80$) lie on average more than 0.6 eV above the hull, Ta_6O_{13} ($x = 0.67$) is considerably lower at only 0.11 eV above the hull. Our calculations show a clear divide into high-energy and low-energy stoichiometries, and we expect some degree of similarity between the three low-energy stoichiometries.

To investigate what the three low-energy stoichiometries (Ta_2O_5 , Ta_6O_{13} , and TaO_2) have in common, we consider the CDF for the Ta–O bonds in the atomic structures of Fig. 1(a). Since Ta is 6-fold coordinated in most, if not all, stable and metastable crystalline TaO_x phases, we limit our investigation to exactly the sixth-nearest neighbour. The resultant spectra are shown in Fig. 1(b). All systems are characterised by an ascent beginning at $\sim 2.0 \text{\AA}$ and ending at $\sim 2.5 \text{\AA}$. Therefore, we use 2.5\AA as the cutoff radius for when an O atom counts towards the coordination number of a Ta atom. The height of the ini-

‡ Despite the relaxation of the lattice vectors, the average density of the final Ta_2O_5 geometry was still similar to the experimental density (see Fig. S1†).

§ <http://theory.cm.utexas.edu/henkelman/code/bader/>

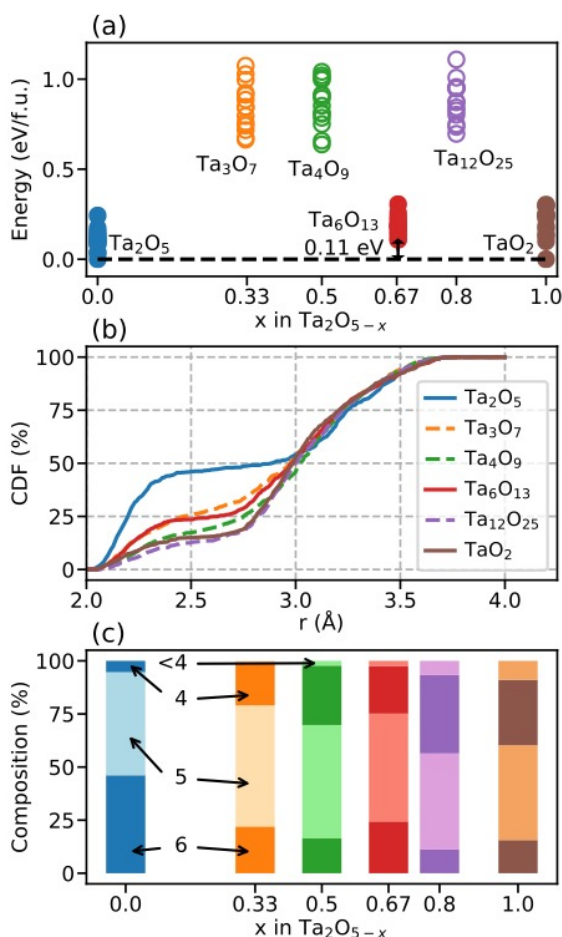


Fig. 1 (a) Convex hull for the a-Ta₂O₅-TaO₂ system. (b) CDF for sixth-nearest O neighbours of Ta atoms; inset zooms in on the 2.0 Å – 2.5 Å range. (c) Histogram of the coordination number of Ta atoms in each stoichiometry. Colour coding is consistent throughout.

tial ascent thus describes the ratio of fully 6-fold coordinated Ta atoms, and the low-energy systems are characterised by relatively larger quantities of fully-coordinated Ta atoms than are seen for the high-energy systems. Within this picture, it is also clear that over 50% of Ta atoms are under-coordinated in all stoichiometries, including a-Ta₂O₅. We further illustrate the trends in coordination numbers in Fig. 1(c) by plotting coordination numbers 6, 5, 4, and < 4 in a cumulative histogram. In particular, Ta₆O₁₃ and TaO₂ shows higher 6-fold coordination and lower 4-fold coordination than stoichiometries with slightly greater oxygen content.

It is worth mentioning that the low-energy stoichiometries exist in crystalline form. Although no Ta₆O₁₃ phase exists, Ta shares periodic table Group 5 with vanadium, which has a phase with stoichiometry V₆O₁₃.⁴¹ In this phase, V is also 6-fold coordinated. No metal in Group 5 has oxides with the formula unit for any of our high-energy stoichiometries. This analogy underlines the importance of 6-fold coordination for the stability of Ta ions in amorphous as well as crystalline TaO_x.

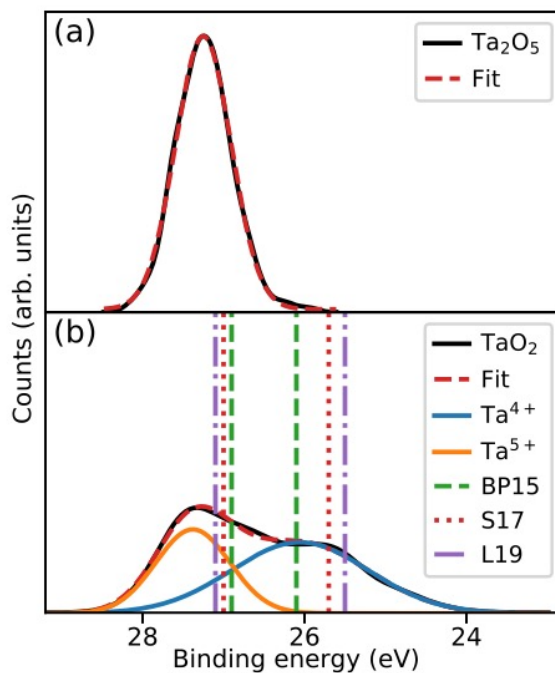


Fig. 2 As-calculated XPS spectra (black curves) and Gaussian fit (red dashed curves) for (a) a-Ta₂O₅ and (b) a-TaO₂. TaO₂ in (b) also includes deconvoluted Gaussians (orange and blue curves) as well as the Ta⁵⁺ and Ta⁴⁺ peak locations of Benito and Palacio²⁶ (BP15), Simpson *et al.*²⁷ (S17) and Li *et al.*¹⁷ (L19), presented as vertical lines.

3.2 XPS Spectra

In this section, we present simulated XPS spectra for our systems and compare them to the experimental XPS spectra reported by Benito and Palacio,²⁶ Simpson *et al.*,²⁷ and Li *et al.*¹⁷. To this end, we calculate the energies of the core electrons of the Ta 4f orbital, which correspond to measuring their BEs, thus simulating an XPS spectrum.

We ‘calibrated’ our XPS results in two ways prior to making any comparisons. We benchmarked our 4f binding energy spectra for the crystalline λ phase³⁴ of Ta₂O₅ (19.1 eV) against the Ta_{7/2}⁵⁺ peak reported by Ho *et al.*²⁴ for crystalline Ta₂O₅. The reported XPS peak value is 26.2 eV; hence we shifted all our XPS spectra uniformly by 26.2 eV – 19.1 eV = 7.1 eV. Such a shift is customary, and even necessary, in order to compare DFT-calculated XPS results to experiment.⁴² Additionally, we remark that realistic XPS spectra are usually obtained at room temperature, whereas DFT calculations are performed at 0 K. We applied Gaussian broadening to our data to overcome this difference, using a broadening width obtained from the energy spectrum of 2000 AIMD iterations at 300 K using a 520 eV cutoff energy and (2 × 2 × 2) *k* point grid. With these two alterations, we proceed to discuss our XPS spectra and compare them to the aforementioned experimental results.

Fig. 2(a) presents our calculated XPS spectrum for a-Ta₂O₅ with a single Gaussian function fitted to it. The fit is near perfect, signifying that the XPS spectrum comes from atoms with uniform oxidation states. The spectrum of a-TaO₂ in Fig. 2(b), by contrast, shows two peaks and has been deconvoluted using two Gaussian functions. We compare these to the peak locations reported by

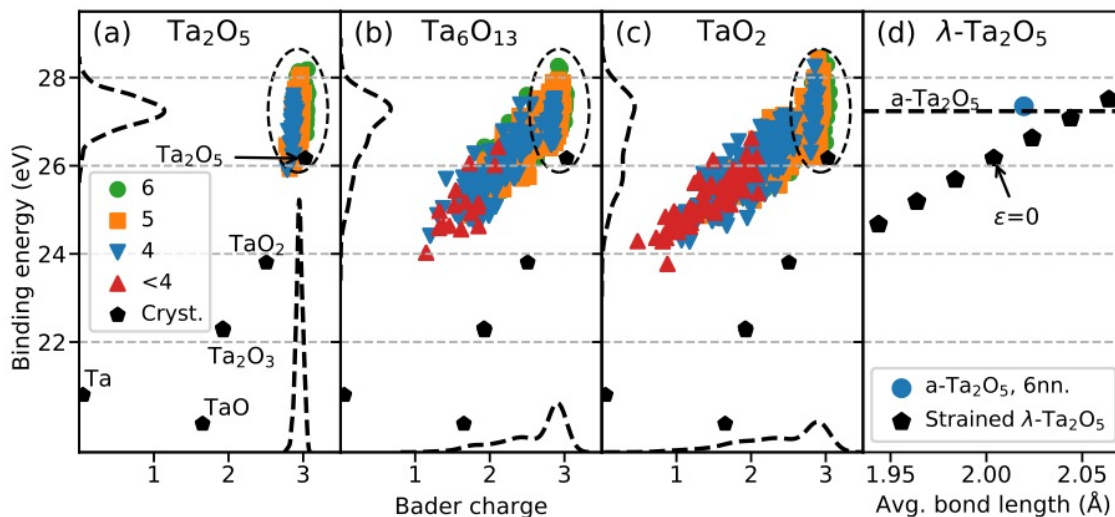


Fig. 3 Binding energy versus Bader charge for amorphous (a) Ta_2O_5 , (b) Ta_6O_{13} , and (c) TaO_2 . Green/orange/blue/red markers represent Ta atoms that are 6/5/4/<4-fold coordinated, respectively. (d) shows λ - Ta_2O_5 compressed/expanded up to 3%. The blue circle represents the average binding energy and average bond length for all 6-fold coordinated Ta atoms in a- Ta_2O_5 .

Benito and Palacio,²⁶ Simpson *et al.*,²⁷ and Li *et al.*,¹⁷ and find our peaks to lie at slightly greater (0.1 – 0.2 eV) binding energies than the results of Simpson *et al.* and Li *et al.*, with very similar spacing between peaks. Apart from matching experiments, we highlight the XPS spectrum of TaO_2 as a particularly important result. Even in a sample with nominal Ta oxidation state of +4, the Ta^{5+} peak is visibly present. Additionally, the Ta^{4+} curve is significantly wider than the Ta^{5+} curve, which contradicts the deconvolutions performed in the previous experimental studies.^{17,26,27} For this reason, we recommend caution when using deconvoluted XPS spectra to perform compositional analyses on amorphous a- TaO_x samples, and likely for other amorphous metal-oxide samples.

3.3 Bader analysis

Our CDF spectra showed how a significant fraction of Ta atoms in all samples are under-coordinated; i.e. less than 6 oxygen neighbours within 2.5 Å. We now examine the connection between the Ta coordination numbers, BEs, and Bader charges (which provide an indication of oxidation state). Fig. 3(a-c) shows the as-calculated Ta 4f binding energies plotted against their corresponding Bader charges for the three low-energy stoichiometries (Ta_2O_5 , Ta_6O_{13} , TaO_2). Atoms are colour- and shape-coded according to the number of oxygen neighbours within 2.5 Å. Also shown are five points corresponding to crystalline Ta–O phases and elemental Ta, along with kernel density estimates of the Bader charges (horizontal axis) and BEs (vertical axis). Discussions henceforth are limited to the low-energy stoichiometries.

For stoichiometric Ta_2O_5 , the observed XPS peak comes from a narrow range of Bader charges centered at roughly +3, which is consistent with the results of Xiao and Watanabe.¹⁹ Any slight variation in Bader charge is clearly related to the coordination number of number of Ta, visible as discernible regions of different colours. As O deficiency increases, the Bader charge spectrum

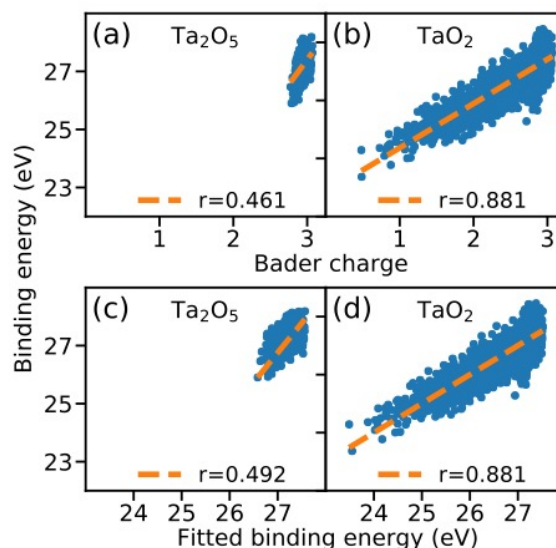


Fig. 4 (a-b): Linear fit of binding energy to Bader charge for a- Ta_2O_5 (a) and a- TaO_2 (b). (c-d): Corrected fit based on Ebadi *et al.*⁴³ for the same data as the upper row.

becomes smeared out in direction towards lower positive charge; i.e. Ta atoms retain more of their valence electrons. However, a significant part of the Ta_2O_5 spectrum — highlighted by the dashed ellipsis — remains even for TaO_2 . Evidently for $x > 0$, a- $\text{Ta}_2\text{O}_{5-x}$ becomes disproportionated, which is the origin of the dual peak spectrum we observe for TaO_2 .

In comparison with crystalline phases, the Ta atoms of the amorphous structures exhibit much higher BEs even at lower oxidation states. For Ta_2O_5 , the calculated difference between the BE of the Ta 4f orbitals in the crystalline phase and the center of the Gaussian peak of the amorphous phase is around 1 eV, in excellent agreement with the experimental difference (compare the results of the amorphous phase by Benito and Palacio,²⁶ Simp-

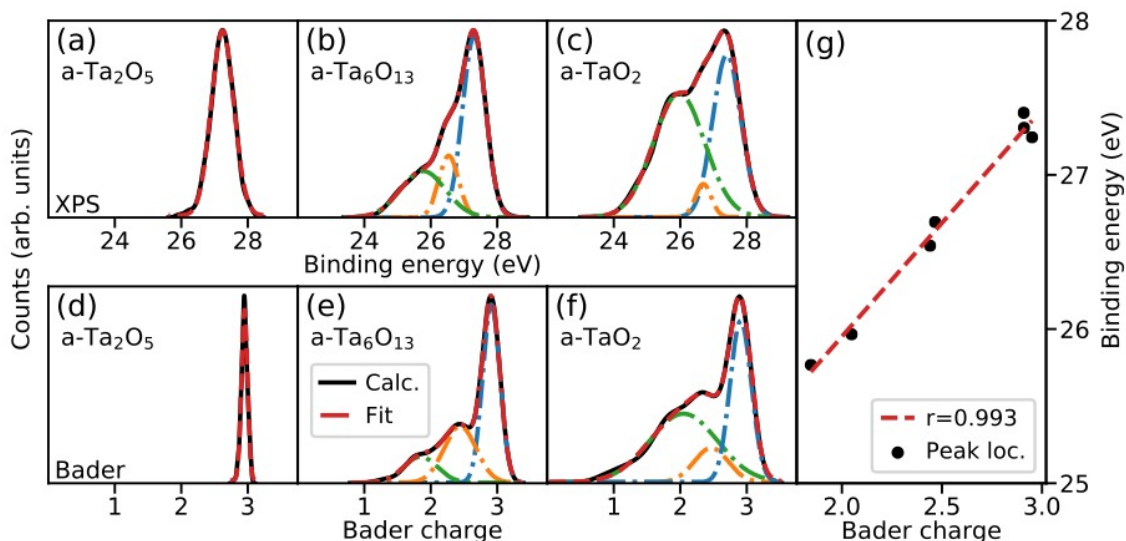


Fig. 5 (a-c) As-calculated (black), fitted (red), and deconvoluted (blue/orange/green) XPS spectra. (d-f) Same treatment for Bader charge spectra. (g) Comparison of Bader/XPS peak locations. Scales differ between y axes.

son *et al.*,²⁷ Li *et al.*,¹⁷ with those for the crystalline phase by Ho *et al.*²⁴). For lower Ta oxidation states, the differences in BEs between amorphous samples and their crystalline counterparts become even more pronounced. This phenomenon can be understood by comparing the coordination number of Ta atoms between the crystalline and amorphous phases. While Ta is always 6-fold coordinated for crystalline phases, every considered amorphous phase shows a large degree of under-coordination, especially for Ta atoms with lower oxidation states.

The change in coordination number is not the only cause of the difference in BEs between amorphous and crystalline phases. In Fig. 3(d), we show the variation of the BE peak for crystalline Ta₂O₅ when varying the lattice parameter of the crystal (which is equivalent to varying the average Ta–O distances). We scan the variation of the Ta 4f binding energy in the range from $\varepsilon = -0.03$ to $\varepsilon = +0.03$, where ε is the relative expansion factor applied to the lattice parameters. We observe a quasi-linear correlation in the investigated region between the BE of Ta 4f orbitals and average Ta–O bond length, which is consistent with the expected reduction of the Coulombic repulsion between the Ta 4f electron and the oxygen ligands when the Ta–O distance increases. We observe that the average Ta–O distances for the 6-fold coordinated Ta atoms in Ta₂O₅ is ~ 2 pm larger than in crystalline λ -Ta₂O₅ (at $\varepsilon = 0$). Thus, we do not only attribute the blueshift in BEs in the amorphous samples to under-coordinated Ta atoms, but also to the increase in the Ta–O distances for 6-fold coordinated Ta atoms in amorphous samples relative to crystalline ones.

We now examine the relation between Bader charge and BE hinted at in Fig. 3 in detail. For the crystalline phases plotted in Fig. 3(a-c), there appears to be a linear relation between BE and Bader charge. Hence, in Fig. 4(a-b), we present a simple linear fit between BE and Bader charge for amorphous Ta₂O₅ and TaO₂. For a-Ta₂O₅, the linear fit performs poorly, achieving a correlation coefficient r of 0.461. The correlation is greater ($r = 0.881$) in a-TaO₂ due to the smeared Bader charge spectrum. In

Fig. 4(c-d), we attempt to improve the linear fit by incorporating a term describing differences in the coordination number and in the Ta–O distances. We use the term suggested by Ebadi *et al.*,⁴³ which is expressed as

$$BE_A = \beta_0 q_A + \beta_1 \sum_{i \neq A} \frac{q_i}{r_{iA}} + \beta_2, \quad (1)$$

where subscripts A and i respectively represent Ta ions and their 6 nearest O neighbours in our implementation, q is Bader charge, r is distance between i and A, and $\beta_{0,1,2}$ are fitting parameters to be determined. This model improves the correlation coefficient for a-Ta₂O₅ to 0.492 but has no impact on a-TaO₂ ($r = 0.881$). We conclude that the correlation between BE and Bader charge in both a-Ta₂O₅ and a-TaO₂ is more complex than can be accounted for in the above models (in contrast, the model of Ebadi *et al.*⁴³ performs well for the crystalline phases; see Fig. S4†).

Instead, we decompose the Bader charge and XPS spectra of Fig. 3 (black dashed curves) into Gaussian components in order to compare the peak locations. We find that the best fit is achieved using a single Gaussian function for a-Ta₂O₅ and three Gaussian functions for a-Ta₆O₁₃ and a-TaO₂. We plot the decomposed BE peak values vs. the Bader charge peak values in Fig. 5(g), and achieve a clear linear correlation with $r = 0.993$. We conclude that the XPS/Bader charge spectra of amorphous tantalum oxide are best understood as statistical entities, even when complete knowledge of the atomic arrangements is available.

4 Conclusions

We have used AIMD and DFT to sample amorphous and oxygen-deficient Ta₂O₅. We have analyzed our a-Ta₂O_{5-x} systems with respect to relative formation energy, CDF, XPS, Bader charge, and coordination numbers. By drawing a convex hull over all 84 included structures, we show that oxygen-deficient a-Ta₂O₅ will preferentially separate into a-Ta₂O₅ and a-TaO₂. Additionally, the hitherto unknown stoichiometry of a-Ta₆O₁₃ showed ener-

gies significantly lower than other intermediate stoichiometries, which is linked to the existence of a vanadium-oxide phase with stoichiometry V_6O_{13} . Our CDF spectra showed that stoichiometries with relatively low energy contain higher proportions of Ta atoms with six O neighbours within a radius of 2.5 Å.

By using Bader charges to model oxidation states explicitly, we found that Ta atoms in amorphous TaO_2 were divided into two different Bader charge spectra: one representing oxidation state +5 contributing to the Ta^{5+} peak, and one with a wide range of oxidation states contributing to the Ta^{4+} peak. Unlike the crystalline TaO_2 with a nominal Ta oxidation state +4, amorphous TaO_2 possesses disproportionated Ta atoms which make such a description less accurate. Our finding that the XPS spectrum of amorphous TaO_2 contains both Ta^{4+} and Ta^{5+} peaks challenges the conventional view of a- TaO_x spectra. Our results suggest that only the Ta_2O_5 stoichiometry may be reduced to a single oxidation state (+5). This finding is important for researchers wishing to use XPS spectra to estimate the composition of amorphous TaO_x samples, and conceivably samples of other amorphous metal-oxides as well. Finally, we determined the origin of the experimentally observed blueshift of the Ta 4f XPS peaks in amorphous Ta_2O_5 relative to its crystalline counterpart. The presence of under-coordinated Ta atoms and the longer Ta–O distances in amorphous TaO_x leads to lower Coulomb repulsion and hence higher binding energies.

As a final remark, we decompose our calculated XPS and Bader charge spectra in Gaussian components and find a linear correlation between peak locations. The correlation strength of this Gaussian model exceeds the strength of a linear model accounting for Coulomb interactions with the sixth nearest neighbours, suggesting that the more accurate way to analyse amorphous materials is by using statistical models.

Conflicts of interest

There are no conflicts to declare.

Acknowledgements

The authors acknowledge support from the Independent Research Fund Denmark (DFF), Grant No. 6111-00145B. Additionally, the authors thank Henrik Høgh Kristoffersen of DTU Physics for valuable counsel.

References

- 1 H. Akinaga and H. Shima, *Proceedings of the IEEE*, 2010, **98**, 2237–2251.
- 2 I. H. Inoue and A. Sawa, *Functional Metal Oxides: New Science and Novel Applications*, 2013, **11**, 443–463.
- 3 L. Chua, *IEEE Transactions on Circuit Theory*, 1971, **18**, 507–519.
- 4 D. B. Strukov, G. S. Snider, D. R. Stewart and R. S. Williams, *Nature*, 2008, **453**, 80–3.
- 5 H. S. Wong, H. Y. Lee, S. Yu, Y. S. Chen, Y. Wu, P. S. Chen, B. Lee, F. T. Chen and M. J. Tsai, *Proceedings of the IEEE*, 2012, **100**, 1951–1970.
- 6 Y. Hou, U. Celano, L. Goux, L. Liu, A. Fantini, R. Degraeve, A. Youssef, Z. Xu, Y. Cheng, J. Kang, M. Jurczak and W. Vandervorst, *Applied Physics Letters*, 2016, **108**, 1–6.
- 7 A. K. Singh, S. Blonkowski and M. Kogelschatz, *Journal of Applied Physics*, 2018, **124**, year.
- 8 M.-J. Lee, C. B. Lee, D. Lee, S. R. Lee, M. Chang, J. H. Hur, Y.-B. Kim, C.-J. Kim, D. H. Seo, S. Seo, U.-I. Chung, I.-K. Yoo and K. Kim, *Nature Materials*, 2011, **10**, 625–630.
- 9 S. Kumar, C. E. Graves, J. P. Strachan, E. M. Grafals, A. L. D. Kilcoyne, T. Tylliszczak, J. N. Weker, Y. Nishi and R. S. Williams, *Advanced Materials*, 2016, **28**, 2772–2776.
- 10 D.-H. Kwon, K. M. Kim, J. H. Jang, J. M. Jeon, M. H. Lee, G. H. Kim, X.-S. Li, G.-S. Park, B. Lee, S. Han, M. Kim and C. S. Hwang, *Nature nanotechnology*, 2010, **5**, 148–153.
- 11 K.-L. Lin, T.-H. Hou, J. Shieh, J.-H. Lin, C.-T. Chou and Y.-J. Lee, *Journal of Applied Physics*, 2011, **109**, 084104.
- 12 M. S. Mattsson, G. A. Niklasson, K. Forsgren and A. Hårsta, *Journal of Applied Physics*, 1999, **85**, 2185–2191.
- 13 P. W. C. Ho, F. O. Hatem, H. A. F. Almurib and T. Nandha Kumar, *IEEE International Conference on Electronic Design*, 2014, 249 – 254.
- 14 C. Hsu, I. Wang, C. Lo, M. Chiang, W. Jang, C. Lin and T. Hou, 2013 Symposium on VLSI Technology, 2013, pp. T166–T167.
- 15 C. Joseph, P. Bourson and M. D. Fontana, *Journal of Raman Spectroscopy*, 2012, **43**, 1146–1150.
- 16 Y. Yang, S. Choi and W. Lu, *Nano Letters*, 2013, **13**, 2908–2915.
- 17 Y. Li, S. Sanna, K. Norrman, D. V. Christensen, C. S. Pedersen, J. M. G. Lastra, M. L. Traulsen, V. Esposito and N. Pryds, *Applied Surface Science*, 2019, **470**, 1071–1074.
- 18 R. J. Bondi, B. P. Fox and M. J. Marinella, *Journal of Applied Physics*, 2016, **119**, 124101.
- 19 B. Xiao and S. Watanabe, *Nanoscale*, 2014, **6**, 10169–10178.
- 20 R. J. Bondi, M. P. Desjarlais, A. P. Thompson, G. L. Brennecke and M. J. Marinella, *Journal of Applied Physics*, 2013, **114**, 203701.
- 21 R. J. Bondi and M. J. Marinella, *Journal of Applied Physics*, 2015, **117**, 085308.
- 22 G. E. Mcguire, G. K. Schweitzer and T. A. Carlson, *Inorganic Chemistry*, 1973, **12**, 2450–2453.
- 23 D. D. Sarma and C. N. R. Rao, *Journal of Electron Spectroscopy and Related Phenomena*, 1980, **20**, 25–45.
- 24 S. F. Ho, S. Contarini and J. W. Rabalais, *The Journal of Physical Chemistry*, 1987, **91**, 4779–4788.
- 25 J. H. Thomas and L. H. Hammer, *Journal of The Electrochemical Society*, 1989, **136**, 2004.
- 26 N. Benito and C. Palacio, *Applied Surface Science*, 2015, **351**, 753 – 759.
- 27 R. Simpson, R. G. White, J. F. Watts and M. A. Baker, *Applied Surface Science*, 2017, **405**, 79 – 87.
- 28 G. Kresse and J. Hafner, *Phys. Rev. B*, 1993, **47**, 558–561.
- 29 G. Kresse and J. Hafner, *Phys. Rev. B*, 1994, **49**, 14251–14269.
- 30 G. Kresse and J. Furthmüller, *Computational Materials Science*, 1996, **6**, 15 – 50.

- 31 G. Kresse and J. Furthmüller, *Phys. Rev. B*, 1996, **54**, 11169–11186.
- 32 P. E. Blöchl, *Phys. Rev. B*, 1994, **50**, 17953–17979.
- 33 J. P. Perdew, K. Burke and M. Ernzerhof, *prl*, 1996, **77**, 3865–3868.
- 34 S.-H. Lee, J. Kim, S.-J. Kim, S. Kim and G.-S. Park, *arXiv e-prints*, 2013, arXiv:1305.4425.
- 35 Y. Guo and J. Robertson, *Microelectronic Engineering*, 2015, **147**, 254 – 259.
- 36 S. Kakio, K. Hosaka, M. Arakawa, Y. Ohashi and J. Kushibiki, *Japanese Journal of Applied Physics*, 2012, **51**, 07GA01.
- 37 J. Heyd, G. E. Scuseria and M. Ernzerhof, *The Journal of Chemical Physics*, 2003, **118**, 8207–8215.
- 38 J. Heyd, G. E. Scuseria and M. Ernzerhof, *The Journal of Chemical Physics*, 2006, **124**, 219906.
- 39 J. Heyd and G. E. Scuseria, *The Journal of Chemical Physics*, 2004, **121**, 1187–1192.
- 40 R. F. W. Bader, *Atoms in Molecules: A Quantum Theory*, Oxford University Press, 1st edn, 1994.
- 41 K. Kosuge, S. Kachi, H. Nagasaki and S. Minomura, *Journal of the Physical Society of Japan*, 1965, **20**, 178–179.
- 42 J. M. García-Lastra, P. L. Cook, F. J. Himpsel and A. Rubio, *The Journal of Chemical Physics*, 2010, **133**, 151103.
- 43 M. Ebadi, A. Nasser, M. Carboni, R. Younesi, C. F. N. Marchiori, D. Brandell and C. M. Araujo, *The Journal of Physical Chemistry C*, 2019, **123**, 347–355.

Supplementary Information for:
Phase separation in amorphous tantalum-oxide from first
principles

Christian Søndergaard Pedersen Jin Hyun Chang* Yang Li Nini Pryds
Juan Maria Garcia Lastra*

* *Department of Energy Conversion and Storage, Technical University of Denmark, DK-2800 Kgs. Lyngby, Denmark. E-mail: jchang@dtu.dk, jmgla@dtu.dk*

S1 Density of amorphous tantalum oxide

Fig. S1 plots the density of each individual calculation in a box plot, grouped by stoichiometry. The average Ta_2O_5 -density from our calculations lie very close to the experimental density, $6.88 \times 10^3 \text{ kg/m}^3$, of amorphous Ta_2O_5 .¹ Decreasing oxygen content leads to increasing average density, with TaO_2 having a density of $7.06 \times 10^3 \text{ kg/m}^3$. No order seems to govern the density of the lowest-energy structure (visualized as blue circles) in relation to the mean.

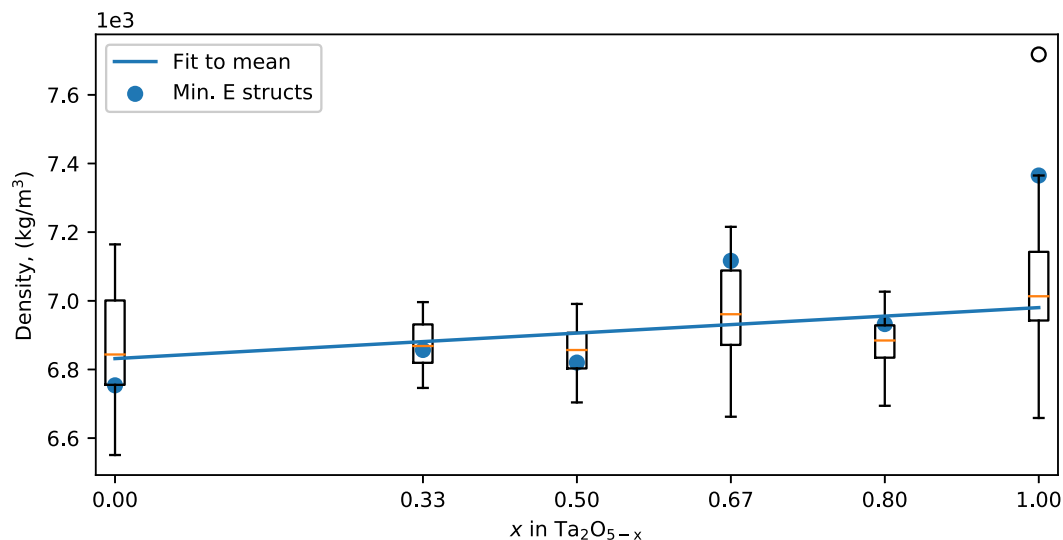


Figure S1: Boxplot of density versus oxygen content and a trend line to the mean values. Densities of the minimum-energy structure are shown for each stoichiometry.

S2 Radial distribution function

The radial distribution function (RDF) is plotted in Fig. S2. The spectra are drawn based on the equilibrations at 300 K and averaged over each time step of every individual structure; i.e. 28 000 time steps per stoichiometry. Vertical lines provide comparison to bond lengths from our calculations of crystalline phases. The appearance of a peak in the Ta–Ta spectrum as the vacancy concentration (i.e., x in $\text{Ta}_2\text{O}_{5-x}$) increases is consistent with the results of Xiao and Watanabe.²

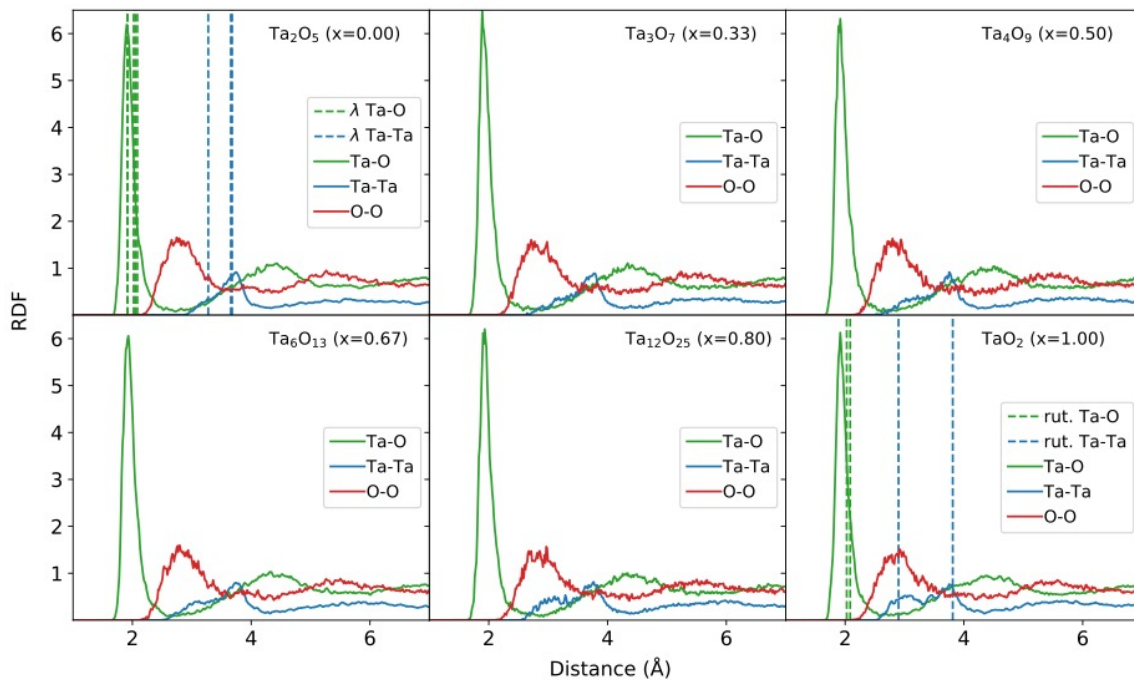


Figure S2: RDF spectra for all considered stoichiometries.

S3 Solid solution vs. phase separated XPS spectra

In Fig. S3, we compare the as-calculated XPS spectra (solid solution) to the spectra obtained as a linear expansion of the stoichiometric Ta_2O_5 and TaO_2 spectra (phase separated). This corresponds to examining a solid solution of oxygen vacancies versus phase-separated sample with the same stoichiometry. As seen in Fig. S3(b-e), the curves do not match. Therefore, we expect our as-calculated XPS curves of $\text{Ta}_2\text{O}_{5-x}$, to look different from experimentally obtained curves of similar stoichiometries.

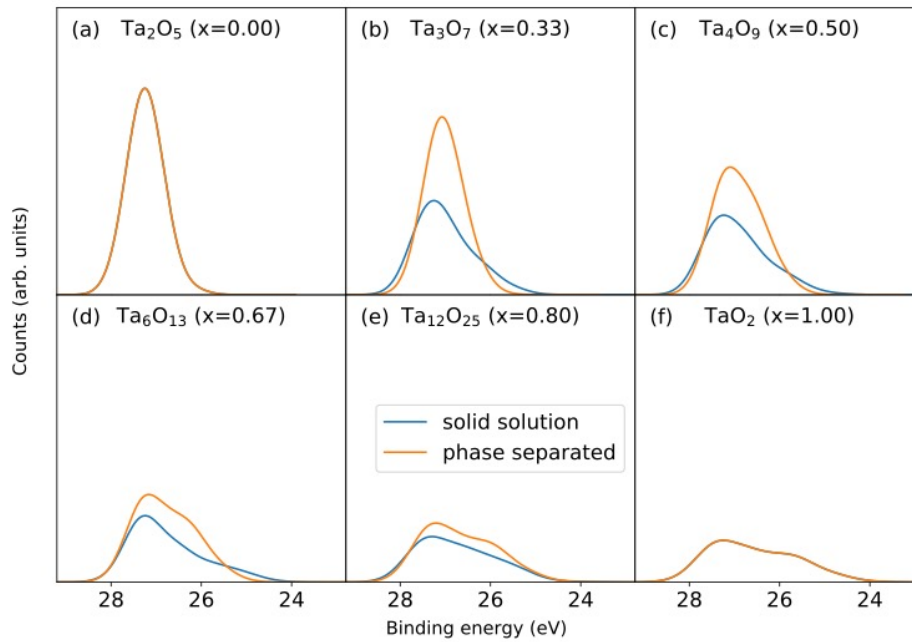


Figure S3: XPS spectra for solid solution (blue) and for phase separation (orange). All y axes have the same scale. Legend of (e) applies to (a-f).

S4 Relation between BE and Bader charge for crystalline TaO_x

This section presents a simple linear fit as well as the a fit incorporating the expression by Ebadi *et al.*,³

$$\text{BE}_A = \beta_0 q_A + \beta_1 \sum_{i \neq A} \frac{q_i}{r_{iA}} + \beta_2. \quad (\text{S1})$$

We limit the second term to include only the six nearest oxygen neighbours of tantalum atoms. Fig. S4 shows how the correction improves the fit for crystalline λ -Ta₂O₅, rutile-TaO₂, corundum-Ta₂O₃ and rocksalt-TaO. A near-perfect correlation is obtained for these systems.

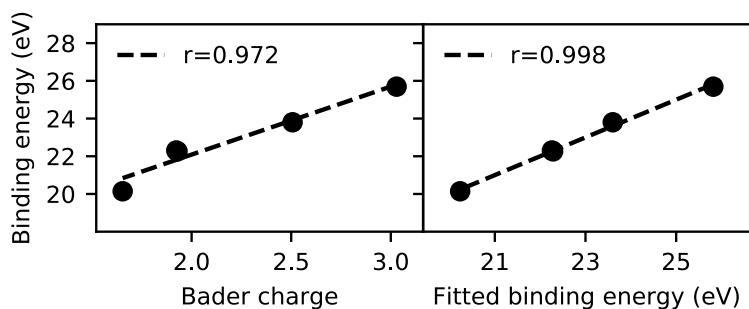


Figure S4: (left) Linear fit of BE to Bader charge for crystalline TaO_x-phases. (right) Corrected fit based on Ebadi *et al.*³ for the same data.

References

- S1 S. Kakio, K. Hosaka, M. Arakawa, Y. Ohashi and J. Kushibiki, *Japanese Journal of Applied Physics*, 2012, **51**, 07GA01.
- S2 B. Xiao and S. Watanabe, *Nanoscale*, 2014, **6**, 10169–10178.
- S3 M. Ebadi, A. Nasser, M. Carboni, R. Younesi, C. F. N. Marchiori, D. Brandell and C. M. Araujo, *The Journal of Physical Chemistry C*, 2019, **123**, 347–355.